UNIVERSITÀ DEGLI STUDI DI MILANO

Scuola di Dottorato in Fisica, Astrofisica e Fisica Applicata
Dipartimento di Fisica

Corso di Dottorato in Fisica, Astrofisica e Fisica Applicata
Ciclo XXX

Neutrinos and the Large Scale Structure of the Universe

Settore Scientifico Disciplinare FIS/05

Supervisors: Prof. Julien Bel (CPT, Marseille)

Dott. Carmelita Carbone (INAF/UniMi, Milan)

Internal Supervisor: Prof. Davide Maino

Coordinatore: Prof. Francesco Ragusa

Tesi di Dottorato di:

Matteo Zennaro

Anno Accademico 2016/2017

Final examination:

Date 18/12/2017

Università degli Studi di Milano, Dipartimento di Fisica, Milano, Italy

Cover illustration:
Matteo Zennaro
Internal illustrations:
Matteo Zennaro
Template design:
Anna Lisa Varri

MIUR subjects:
FIS/05

Contents

List of Figures

List of Tables

Introduction

Cosmology is currently living a rather exciting season, as many experiments and surveys have just ended or are about to end, providing us with data of unprecedented quality, and many more are about to begin, prospecting an even more substantial improvement coming in the next future. The former list comprises experiments such as the Planck satellite (Planck Collaboration et al., 2013, 2015), or galaxies redshift surveys such as BOSS (Dawson et al., 2013), eBOSS (Dawson et al., 2016), VIPERS (Guzzo et al., 2014), etc... The latter group includes spectroscopic redshift surveys such as spectro-Euclid, DESI and PFS, and photometric surveys such as J-PAS, LSST, DES or photo-Euclid.

Together with precise observations, however, to maximally extract cosmological information, also accurate theoretical modelling is required. While the ΛCDM model has received in recent years many confirmations, becoming in fact the standard cosmological model, it is still far from being either perfect or complete.

On the one hand, modelling the small, nonlinear scales, where structures such as clusters and galaxies form, is of paramount importance, but rather difficult. A large amount of information is encompassed in such range of scales, in particular regarding the peculiar velocities of these objects, the details of the virialization of dark matter haloes, its connections with baryon physics, and the physics of galaxy formation.

On the other hand, extremely large scales have been probed only through the observation of the cosmic microwave background (CMB), and therefore general relativity on cosmological scales has not still received robust confirmations from observations of the large scale structure (LSS). This in principle leaves some room for modifications of the laws of gravity, provided that on galactic scales general relativity is recovered.

On a more fundamental side, the two main components of the current standard model, the cold dark matter and the dark energy, are still unknown. The desired properties of cold dark matter are very clear in the model: it must be heavy to become nonrelativistic very early, and very weakly interacting to be almost pressureless and not emit. However, no candidate particle has been detected yet. Dark energy as well is poorly understood. Such mechanism is invoked to model the accelerated expansion the universe is undergoing right now, and is described as a fluid with negative pressure and equation of state $w = -1$. However, the profound nature of this mechanism is not clear. Moreover, even in this standard fluid description of dark energy, its properties have not been characterised precisely enough, and, for example, the equation of state could be evolving in time.

Next generation surveys have been designed to shed light into these issues, but this will happen only if theory will join the effort and push the predictive power of models. In order to obtain accurate predictions, one must consider also that accounting for the presence of cosmological massive neutrinos modifies several cosmological observables. Therefore, in recent years, the study of the effects of neutrinos has gained more and more importance and, now, neutrinos can no longer be neglected when considering the standard picture.

The presence of massive neutrinos modifies the expansion rate of the universe, shifting the time when the radiation energy density fell below the matter energy density. They also modify the number of relativistic species present in the universe, N_{eff}, which affects the Cosmic Microwave Background angular power spectrum. Moreover being very likely light particles, neutrinos are characterised by large thermal velocities that prevent them from clustering on small scales, inducing a overall suppression of the matter clustering on the same scales.

However, not only neutrinos must be accounted for in order not to introduce systematic errors in theoretical models, but Cosmology can also help constraining some of their properties, which are still open questions in fundamental Physics. As a matter of fact, the number of neutrino species, their total mass and hierarchy can be constrained fitting cosmological observations.

Neutrinos, in the Standard Model of Particle Physics, are predicted to be massless. They come in three flavours, one per each of the leptons of the SM, namely an electronic neutrino, a muonic neutrino and a tauonic neutrino, $\nu_e,\ \nu_\mu,\ \nu_\tau$. Wolfgang Pauli was the first, in 1930, to propose the presence of neutrinos to satisfy energy, momentum and spin conservation laws in β-decay events of the kind

$$n \longrightarrow p^+ + e^- + \bar{\nu}_e, \tag{1}$$

but they were not directly observed until the experiment of Cowan et al. (1956), whose work was later awarded a Nobel prize. Yet, the experiments active in the 60s, that tried to measure neutrinos produced in the p-p chain in the sun, posed another challenge, when the observed neutrino fluxes were around one third of expectations.

The solution to the missing neutrino problem resides in considering a non-diagonal mixing matrix, which makes neutrinos oscillate from one flavour to the other. The theoretical formalism of neutrino flavour oscillation in vacuum was developed by Pontecorvo in the 60s, and the generalization to oscillations in matter was presented as the MSW effect (Wolfenstein, 1978; Mikheyev and Smirnov, 1985).

The non-diagonal terms of the mixing matrix are interpreted as mass, leading to the evidence that neutrinos must be massive. Experiments measuring neutrino oscillations, such as Kamiokande, SNO, Super-Kamiokande, measuring the mass splitting of neutrino mass eigenstates, have bound the lower limit of the sum of neutrino masses,

$$M_\nu = \sum_i m_\nu > 0.06\ \text{eV} \tag{2}$$

at 95% level (Gonzalez-Garcia et al., 2014; Forero et al., 2014; Esteban et al., 2017). However, oscillation experiments provide no upper bound to the total neutrino mass.

Experiments investigating β-decay offer a different approach to measure the neutrino mass spectrum, in principle being capable of setting an upper bound to the total mass. For example, in the Mainz neutrino experiment, the energy spectrum of neutrinos is inferred by measuring the energy carried by the electrons produced in decays like

$$^3_1\text{T} \quad \longrightarrow \quad ^3_2\text{H}^+ + e^- + \bar{\nu}_e. \tag{3}$$

Results from this experiment (Kraus et al., 2005) have set an upper bound on the electronic neutrino mass of

$$m(\nu_e) < 2.2\ \text{eV} \tag{4}$$

at 95% confidence level. Other future experiments, as well based on tritium decay, are expected to increase sensitivity by at least an order of magnitude, such as KATRIN, whose expected sensitivity is ~ 0.2 eV. Other experiments, like PTOLEMY, aim at a slightly different strategy: instead of studying the β-decays coming from a laboratory source of tritium, PTOLEMY is designed to directly detect cosmological neutrinos, exploiting the process of neutrino capture on tritium,

$$\nu_e +^3_1 \mathrm{T} \quad \longrightarrow \quad {}^3_2\mathrm{He}^+ + e^- . \tag{5}$$

In this experiment two populations of electrons are collected, the one coming from the neutrino capture, and the other coming from the natural β-decay of the tritium source. The comparison of the two populations is expected to allow us to detect the cosmic neutrino background and constrain the total neutrino mass.

However, current cosmological data can already constraint the value of the total neutrino mass. From CMB temperature and polarization anisotropies, the upper bound at 95% level has been found to be $M_\nu = \sum m_\nu < 0.49$ eV (Planck Collaboration et al., 2015). Galaxy clustering measurements, analyised jointly with CMB data, have provided even more stringent constraints, for example Pellejero-Ibanez et al. (2016) found $M_\nu < 0.22$ eV at 95% level. Also fitting the 1D power spectra of distant quasars (the Lyman-α forest) has provided very tight constraints on the 95% upper bound of the neutrino total mass, such as $M_\nu < 0.12$ eV (Palanque-Delabrouille et al., 2015).

In this work I will present some aspects of the effects of neutrinos on the large scale structure of the universe, aiming both at improving the cosmological model and at constraining the neutrino total mass through cosmology.

In Chapter 1 I will introduce some of the tools that I have used. In particular, I will focus on the statistical properties of random a field, the fluid description of the linear growth of perturbations, and some approaches to describe nonlinearities. Section 1.3 will be entirely devoted to neutrinos, their effect on the background and on the growth of fluctuation, once again described as an expanding perturbed fluid. I will present, in the last part of this chapter, the matter power spectrum in the presence of massive neutrinos.

In Chapter 2, I will present my work on understanding and possibly correcting systematic errors introduced, by some common approximations, in cosmological simulations that include a neutrino component. I will employ a two-fluid approximation to produce rescaled power spectra to be used for the generation of initial conditions that correct for the unavoidable approximations employed in Newtonian N-body codes.

In chapter 3, I will present my work on the clustering ratio, a cosmological observable that I extended to neutrino cosmologies. I will show here the optimal scales needed to maximise neutrino effects in the clustering ratio, while minimizing potential uncertainties. I will then apply the clustering ratio to observed data, end to a Euclid-like synthetic galaxy catalogue to investigate its constraining power.

Finally, chapter 4 will be devoted to the description of my work about populating dark matter + neutrino N-body simulations with galaxies, in order to study the linear and nonlinear bias between galaxies and the underlying matter distribution.

CHAPTER 1

The concordance model of Cosmology

Since the beginning of the Twenties, new means to measure the distance of far-way objects have opened our eyes to an unexpectedly vast cosmos. In particular, the velocity-distance relation, intensively studied by Edwin Hubble, not only was a powerful tool to create the first 3-dimensional galaxy maps, but was also an evidence of the fact that our universe is *expanding*. More recently, thanks to yet another method to measure distances, which exploits SuperNova explosions as standard candles, such expansion was shown to be *accelerated*, a discovery worth a Nobel prize (Riess et al., 1998; Perlmutter et al., 1999).

Cosmology precisely aims at describing the geometrical properties, the dynamics and the evolution of such an expanding universe. The assumption on which the cosmological model is based upon, called *the cosmological principle*, states that the universe, on sufficiently large scales, is isotropic and homogeneous in a statistical sense. If it is so, then the expansion appears in every direction of the sky to each possible observer, wherever they might be located.

The current cosmological model describes a universe that, starting as extremely hot and dense, expands and cools down as time passes by. The primeval density fluctuations, whose amplitude is enhanced during a early-phase called *inflation*, are the seeds driving the growth of structures. A confirmation of the inflationary model is provided by the Cosmic Microwave Background (CMB), the radiation produced at the time when photons and baryons, which in the early universe formed a ionized plasma, decoupled, and photons became free to travel. This radiation has a temperature that is extremely isotropic, which corroborates the cosmological principle. Moreover, the observation of the distribution of galaxies in space (in the late-time universe) shows us a picture that, albeit granular and complex on small scales, is very homogeneous on scales larger that $\sim 150\, h^{-1}$ Mpc (Marinoni et al., 2012), corroborating the assumption of homogeneity.

However, CMB temperature shows some anisotropies, which are the imprint of the density perturbations present in the photon-baryon plasma right before the time of decoupling. Such fluctuations are very small, of order $\Delta T/T \sim 10^{-5}$, and, on large scales, are distributed in very good agreement with the spectrum of fluctuations expected to be generated in the inflationary phase (Planck Collaboration et al., 2013, 2015).

In this work I will focus on the universe after the time the CMB was emitted. In this respect, the small temperature fluctuations in the CMB constitute the initial conditions for the gravity-driven growth of matter perturbations, which eventually forms collapsed structures. In this chapter I will review the fundamental aspects of the cosmological model needed to describe the Large Scale Structure of the universe.

1.1 Background properties of the universe and their evolution

Einstein's field equation In the standard ΛCDM model, gravity is described by means of Einstein's General Relativity. The field equations link the geometry of the universe to its mass-energy content (the stress-energy tensor $T_{\mu\nu}$), and have the form

$$R_{\mu\nu} - \frac{1}{2} g_{\mu\nu} R + g_{\mu\nu}\Lambda = \frac{8\pi G}{c^4} T_{\mu\nu}, \tag{1.1}$$

where $R_{\mu\nu}$ is the Ricci tensor, R the Ricci scalar, accounting for the local curvature of the universe, and $g_{\mu\nu}$ is the metric. Λ is called the *cosmological constant*, which, having inverse sign with respect to the effects of gravity, describes the (accelerated) expansion of the universe. In fact, before observations showed that the universe is undergoing an accelerated expansion, the cosmological constant had already been introduced by Einstein, with the purpose of making the universe static.

We still need to specify how to describe the space-time, *i.e.* we need to choose a metric. The metric adopted to describe the universe must obey the cosmological principle, therefore must be invariant under rotations and translations. It must also be able to describe a expanding (or contracting) space-time. The most general metric that satisfies these requirements is the one derived by Friedman, Lemaître, Robertson and Walker (called the FLRW metric). The line element of this metric, valid for a class of comoving observers, in hyperspherical coordinates reads

$$\mathrm{d}s^2 = -c^2 \mathrm{d}t^2 + a^2(t) \left\{ \mathrm{d}x^2 + \mathcal{S}_K^2(r)(\mathrm{d}\vartheta^2 + \sin^2\vartheta \, \mathrm{d}\varphi^2) \right\}, \tag{1.2}$$

where angular distances depend on the curvature through the term

$$\mathcal{S}_K(x) = \begin{cases} \sin(\sqrt{|k|}x)/\sqrt{|k|} & \text{if } K = -1 \\ x & \text{if } K = 0 \\ \sinh(\sqrt{k}x)/\sqrt{k} & \text{if } K = +1, \end{cases} \tag{1.3}$$

in which $K = \{-1, 0, 1\}$ correspond to a negatively curved, flat and positively curved universe respectively.

The spatial term is modulated by the scale factor $a(t)$, that accounts for the expansion of the space-time. The normalized expansion rate $H \equiv \dot{a}/a$ is called the Hubble rate (or Hubble function). The quantity k is linked to the curvature of the universe. If we choose it to have units of length^{-2}, it can be written as

$$k = \frac{Kc^2}{a_0^2 H_0^2}, \tag{1.4}$$

where $a_0 = a(t = t_0)$ and $H_0 = \dot{a}_0/a_0$ are the scale factor and the Hubble rate at the present time. With this choice x has units of length, $a(t)$ is dimensionless, and we can fix the value of the scale factor today to $a_0 = 1$. In this case, the spatial term,

$$\mathrm{d}\Sigma^2 = \left\{ \mathrm{d}x^2 + \mathcal{S}_K^2(x)(\mathrm{d}\vartheta^2 + \sin^2\vartheta \, \mathrm{d}\varphi^2) \right\}, \tag{1.5}$$

measures *comoving distances*, which are distances projected on the coordinate system today.

For example, the comoving radial distance between two events can be expressed as

$$x = \int_{t_1}^{t_2} \frac{c \, \mathrm{d}t}{a(t)}. \tag{1.6}$$

Since the comoving distance is projected on the distance scale today, to obtain the corresponding proper distance at an earlier time we need to rescale the comoving distance using the scale factor at the time of interest

$$r = a(t)\, x. \tag{1.7}$$

Since physical scales, therefore, depend on time, also the wavelength of light will be affected depending on the time of its emission.

Cosmological redshift. In an expanding universe, the light emitted by a source at a given wavelength will be stretched as the space-time itself expands. As a consequence, the farther away a source is from us, the more the light it emits is shifted towards the red end of the spectrum.

A far-away source emits two wave-crests at different times, t_e and $t_e + \lambda_e/c$. The two waves, which travel the same (comoving) distance x and keep the same relative phase, are received at times t_0 and $t_0 + \lambda_0/c$ by an observer today. As a consequence,

$$x = \int_{t_e}^{t_0} \frac{c\,\mathrm{d}t}{a(t)} = \int_{t_e+\lambda_e/c}^{t_0+\lambda_0/c} \frac{c\,\mathrm{d}t}{a(t)}. \tag{1.8}$$

This implies that

$$\int_{t_e}^{t_e+\lambda_e/c} \frac{\mathrm{d}t}{a(t)} = \int_{t_0}^{t_0+\lambda_0/c} \frac{\mathrm{d}t}{a(t)}. \tag{1.9}$$

We can consider the period of this waves way smaller that the expansion rate of the universe, and, in each interval, factor the $a(t)$ term out of the integral,

$$\frac{1}{a(t_e)} \int_{t_e}^{t_e+\lambda_e/c} \mathrm{d}t = \frac{1}{a(t_0)} \int_{t_0}^{t_0+\lambda_0/c} \mathrm{d}t \quad \Rightarrow \quad \frac{\lambda_e}{a(t_e)} = \frac{\lambda_0}{a(t_0)}, \tag{1.10}$$

which means that ratio between the observed wavelength and the emitted one is equal to the ratio between the scale factor of the universe at the time of observation and the one at emission. As the definition of redshift is

$$z \equiv \frac{\lambda_0 - \lambda_e}{\lambda_e}, \tag{1.11}$$

and assuming $a(t_0) = 1$,the scale factor of the universe can be linked to the redshift of the light emitted by a source at time t as

$$a(t) = \frac{1}{1+z}\ . \tag{1.12}$$

Such relation is extremely powerful as it allows us to link a quantity measurable to great precision, the redshift of the emitted light of galaxies, to the size the universe had when this light was emitted. Moreover, if we know the evolution of the scale factor $a(t)$ in time, we can link the redshift to the time at which the object emitted the light we measure and, therefore, exploiting the integral presented in Eq. 1.6, to the comoving radial distance of the observed object from us. As a consequence, describing the time evolution of the scale factor $a(t)$, the velocity with which it changes $\dot{a}(t)$ and its acceleration $\ddot{a}(t)$ is of paramount importance.

Friedmann equations. To find the time evolution of the scale factor we need to solve the field equations, Eq. 1.1. They can be explicitly written introducing the metric, Eq. 1.2. From the initial 10 equations, only 2 independent equations are left (one coming from the time-time components and one coming from the space-space components), commonly referred to as the Friedmann equations. The first Friedmann equation describes the expansion rate of the universe and reads

$$\left(\frac{\dot{a}}{a}\right)^2 = \frac{8\pi G}{3}\rho - \frac{kc^2}{a^2} + \frac{\Lambda c^2}{3}, \tag{1.13}$$

where $\rho = \sum \rho_i$ is the total mass-energy density coming from the stress-energy tensor (*i.e.* the sum of the densities of all the species present in the universe).

The second Friedman equation, instead, describes the acceleration of the scale factor and reads

$$\frac{\ddot{a}}{a} + \frac{1}{2}\left(\frac{\dot{a}}{a}\right)^2 = -\frac{4\pi G}{c^2}p - \frac{1}{2}\frac{kc^2}{a^2} + \frac{\Lambda c^2}{2}\,, \tag{1.14}$$

where p is the total pressure, $p = \sum p_i$, which, for a perfect fluid with no shear, is linked to the total mass-energy density through an equation of state of the kind

$$p = w\,\rho\,c^2. \tag{1.15}$$

The interpretation of the acceleration becomes easier if we look at the linear combination of the first and second Friedmann equations, which is

$$\frac{\ddot{a}}{a} = -\frac{4\pi G}{3}\left(\rho + 3\frac{p}{c^2}\right) + \frac{\Lambda c^2}{3}\,. \tag{1.16}$$

The presence of mass-energy makes the expansion decelerate, eventually causing the universe to contract. The cosmological constant has opposite sign. If it exactly compensate the amount of matter and positive pressure, it makes the universe static (which we know is not the case in reality). However, if its value dominates on the other term, it can make the universe expand, with a positive acceleration of the scale factor.

In Eq.s 1.13-1.16 the terms regarding the cosmological constant can be absorbed in the total density and pressure introducing the energy density

$$\rho_\Lambda = \frac{\Lambda\,c^2}{8\pi G} \tag{1.17}$$

and the pressure

$$p_\Lambda = -\rho_\Lambda\,c^2. \tag{1.18}$$

In the same fashion the energy density of curvature can be introduced

$$\rho_k = \frac{3\,k\,c^2}{8\pi G a^2}, \tag{1.19}$$

allowing us to absorb the curvature term into the total density. A quite general expression of the total density comprehends, therefore, the contribution of radiation, matter, curvature and cosmological constant,

$$\rho(a) = \sum_i \rho_i(a) = \rho_r(a) + \rho_m(a) + \rho_k(a) + \rho_\Lambda(a). \tag{1.20}$$

Looking at Eq. 1.13 (in which I am now absorbing the cosmological constant in the total density, but leaving the curvature density explicit) and recalling the definition of Hubble rate, $H \equiv \dot{a}/a$, it can be rewritten as

$$1 + \frac{kc^2}{a^2 H^2} = \frac{8\pi G}{3H^2}\rho, \tag{1.21}$$

where on the left hand side I have isolated the geometrical properties of the universe and on the right hand side its energy density. An important limiting case is given by a universe with total energy density

$$\rho_{\rm crit} = \frac{3H^2}{8\pi G}, \tag{1.22}$$

that must therefore have a flat geometry, with $k = 0$. Such limiting value of the density is called *critical density*. In a ΛCDM universe with present day $H = 67~{\rm km~s^{-1}~Mpc^{-1}}$, the critical density has value $\rho_{\rm crit} \simeq 1.25 \times 10^{11}~{\rm M_\odot~Mpc^{-3}}$.

The different components of the universe contribute with different relative abundance to the total energy density. We can define the normalized energy density

$$\Omega_i(t) \equiv \frac{\rho_i(t)}{\rho_{\rm crit}(t)}, \tag{1.23}$$

leading to the fact that, in a flat universe,

$$\sum_i \Omega_i(t) = 1. \tag{1.24}$$

In a non flat universe, instead,

$$1 - \Omega_k(t) = \sum_i \Omega_i(t). \tag{1.25}$$

To completely describe the evolution of the Hubble rate in time, we still need to describe the evolution of the energy density of the different species in the universe. To this end, we can start from the first Friedmann equation, Eq. 1.13, differentiate it with respect to time,

$$2H(t)\left(\frac{\ddot{a}}{a} - H^2(t)\right) = \frac{8\pi G}{3}\dot{\rho}, \tag{1.26}$$

and plug the second Friedman equation, Eq. 1.16, into it, obtaining

$$\dot{\rho}(t) = -3~H(t)\left[\rho(t) + \frac{p(t)}{c^2}\right], \tag{1.27}$$

which is called the *fluid equation*. If the different species in the universe can be described as perfect, non-interacting fluids (for example there is no matter conversion into photons or vice versa), then Eq. 1.27 is valid for each species separately.

Such equation can be expressed in a more useful way by recalling that $p = w~\rho~c^2$ and turning derivatives in time into derivatives with respect to the scale factor of the universe. By integrating this differential equation, the evolution of a fluid with equation of state w_i in an expanding universe is generally described as a function of the scale factor of the universe itself as

$$\rho_i(a) = \rho_{i,0}~a^{-3~(w_i+1)}. \tag{1.28}$$

In the standard ΛCDM model the universe contains photons and massless neutrinos (that often go under the umbrella term *radiation*); pressureless dust, which we generally call *matter*, is in fact composed of cold dark matter, supposed to be pressureless to very good approximation, and baryonic matter, which instead, on small scales, does not truly satisfy this approximation; a dark energy component, that in the standard picture is associated to a *cosmological constant*, described by a fluid with negative pressure. In addition, to the *curvature* of the universe, for the sake of simplicity, can be associated a density and a pressure, treating it as an additional fluid. Applying Eq. 1.28 to these different fluid and schematically representing their evolution in the following table we obtain:

radiation	$w_r = 1/3$	$\rho_r = \rho_{r,0}\, a^{-4}$
matter	$w_m = 0$	$\rho_m = \rho_{m,0}\, a^{-3}$
curvature	$w_k = -1/3$	$\rho_k = \rho_{k,0}\, a^{-2}$
cosmological constant	$w_\Lambda = -1$	$\rho_\Lambda = \rho_{\Lambda,0}$

Using the results in this table, we can conclude that the early universe, when the scale factor a was very small, was dominated by the radiation component. It was then dominated by matter for some time until the curvature energy density (if any) became the leading term in the total energy budget. Finally the cosmological constant becomes important only at late times.

From Eq. 1.13, the Hubble rate at a given time – and therefore at a given value of the scale factor a or of the redshift z – can be written as

$$H^2(a) = \frac{8\pi G}{3} \sum_i \rho_i. \tag{1.29}$$

Exploiting the definition given in Eq. 1.23 we can rewrite it as a function of the energy density parameters today,

$$H^2(a) = H_0^2 \sum_i \frac{\rho_i(a)}{\rho_{c,0}} = H_0^2 \sum_i \Omega_{i,0}\, a^{-3(w_i+1)}, \tag{1.30}$$

where $H_0^2 = 8\pi G \rho_{\mathrm{crit},0}/3$ is the present day expansion rate. Therefore

$$H(a) = H_0 \left\{ \Omega_{r,0}\, a^{-4} + \Omega_{m,0}\, a^{-3} + \Omega_{k,0}\, a^{-2} + \Omega_{\Lambda,0} \right\}^{1/2} \tag{1.31}$$

is the expression of the Hubble rate in a standard ΛCDM cosmology. H_0 and the Ω_i can be considered as cosmological parameters, linked to the abundance of each species, which are not given theoretically but can be determined fitting cosmological observations. For example, the measurement of the present-day temperature of the CMB, $T_{\gamma,0} = (2.72548 \pm 0.00057)$ K (Fixsen, 2009), gives a radiation density parameter of $\Omega_{r,0} h^2 = (2.473 \pm 0.002) \times 10^{-5}$. note that this value is multiplied by h^2, where $h \equiv H_0/100$, in order to express it irrespective to the actual value of the Hubble parameter. The fit of the temperature and polarization anisotropy angular power spectrum measured by the Planck satellite gives, when the universe is assumed to be flat, (Planck Collaboration et al., 2015)

$$\begin{aligned}
\Omega_b h^2 &= 0.02225 \pm 0.00016 \\
\Omega_c h^2 &= 0.1193 \pm 0.0014 \\
\Omega_m &= 0.3156 \pm 0.0091 \\
\Omega_\Lambda &= 0.6844 \pm 0.0091 \\
H_0 &= (67.27 \pm 0.66)\ \mathrm{km\ s^{-1}\ Mpc^{-1}},
\end{aligned} \tag{1.32}$$

where errors are 68% limits. When also the curvature parameter is free to vary it has a constraint $\Omega_k = -0.040^{+0.038}_{-0.041}$, this time at 95% level, which is very well consistent with a flat universe.

In Fig. 1.1 I show the evolution of the different components of a flat universe, whose present-day densities have been chosen to reproduce the results by Planck, *i.e.* $\Omega_{r,0} = 9.3049 \times 10^{-5}$, $\Omega_{m,0} = 0.3156$ and $\Omega_{\Lambda,0} = 0.6844$.

This figure clearly shows that in the early universe the energy budget was dominated by the radiation component. Around redshift $z \sim 3800$, the energy density associated to radiation fell below the energy density of matter. For this reason, subsequent times are called the matter-dominated era. Photons of the CMB are emitted in this epoch, at redshift $z \sim 1100$. At the time of CMB emission, photons and baryons decouple. In the next section we will see that this marks the time when baryons become free to fall in the potential wells created by the cold dark matter. Therefore, in the matter dominated universe matter perturbations are free to grow and form the structures that today we observe. Finally, at redshift $z \sim 0.32$, the matter energy density falls below that of dark energy. The present day universe is, as a matter of fact, dominated by cosmic accelera-

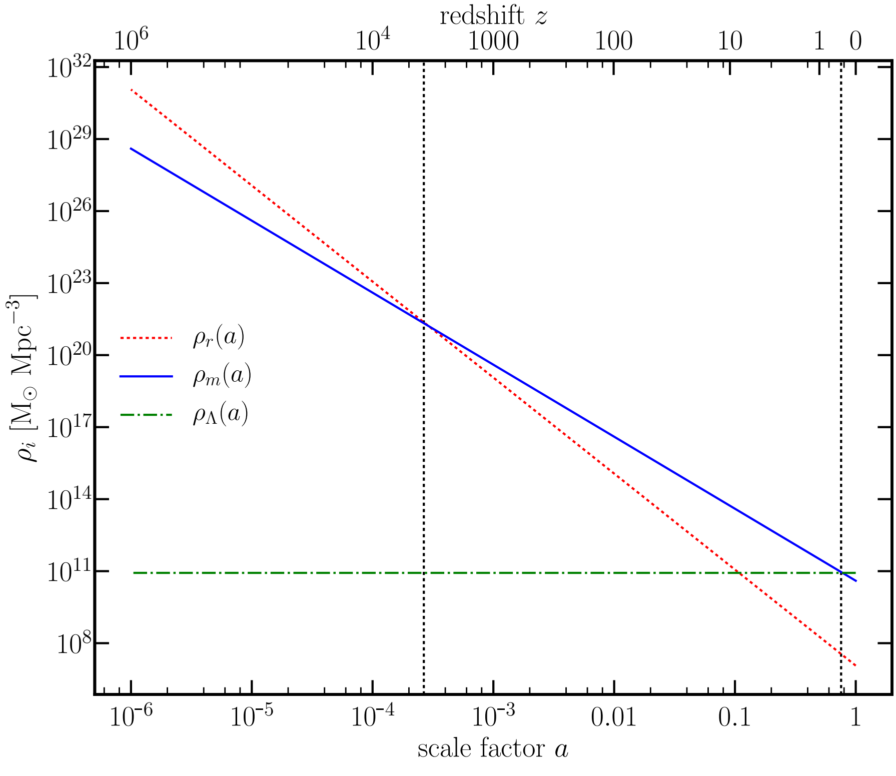

Figure 1.1: The matter density associated to radiation, pressureless matter and cosmological constant as a function of the scale factor of the universe (axis below) or redshift (axis above). The present-day values of these parameters have be taken to been chosen to give a flat universe with $\Omega_{r,0} = 9.3049 \times 10^{-5}$, $\Omega_{m,0} = 0.3156$ and $\Omega_{\Lambda,0} = 0.6844$. The two vertical lines mark the time of matter-radiation equality and of dark energy-matter equality.

tion.

Despite the cosmological constant being the standard mechanism invoked to explain the accelerated expansion of the universe, it is not the only possibility. Non-minimal modifications to Einstein's gravity are under investigation and represent valid alternatives to the standard scenario. However, they are beyond the scope of the present work.

In the next section, I will review the formalism of structure formation that describes the growth of matter perturbations in the matter dominated era.

1.2 The inhomogeneous universe

The overdensity field. Up to now we have only considered the smooth background of the universe, intended as the superposition of the different fluids associated to the different components, whose evolution only depends on time. However, we expect to find perturbations growing and propagating on top of that.

In particular, in the inflationary framework, the original quantum fluctuations present in the primeval energy density are stretched during inflation and leave a characteristic distribution of perturbations, distributed according to a power law.

When describing perturbation of a relativistic fluid, relativistic effects cannot be neglected, and the common approach is to write the phase-space distribution function of the species of interest (photons, neutrinos...) and solve the Einstein-Boltzmann equation numerically (Seljak and Zaldarriaga, 1996; Lewis et al., 2000; Lesgourgues, 2011a). As in this work I am mainly interested in matter perturbations, however, I will follow the custom of the field and adopt a fluid description, modelling CDM and baryons as two fluids, whose perturbations expand as waves and obey the conservation of mass and momentum. In this framework, gravity is well described in Newtonian terms (Peebles, 1980) and the fluid feels its own self-gravitation through the Poisson equation.

Given a fluid with average background density $\bar{\rho}(t)$, an overdensity is defined as

$$\delta(\boldsymbol{r},t) \equiv \frac{\rho(\boldsymbol{r},t)}{\bar{\rho}(t)} - 1. \tag{1.33}$$

Equations of motion. To describe the evolution of the overdensity field we need to start from the fluid equations that guarantee the conservation of mass (continuity equation) and momentum (Euler equation) and that describe its auto-gravitation (Poisson equation). An additional assumption is that of *single stream*, which ensures that only one velocity vector can be associated to each point in space. In the physical spatial coordinates $\boldsymbol{r}$ and cosmic time t, with $\boldsymbol{v} \equiv \mathrm{d}\boldsymbol{r}/\mathrm{d}t$, these equations read

$$\begin{cases} \dfrac{\partial \rho}{\partial t} + \boldsymbol{\nabla}_r \cdot (\rho \boldsymbol{v}) = 0 \\ \dfrac{\partial \boldsymbol{v}}{\partial t} + (\boldsymbol{v} \cdot \boldsymbol{\nabla}_r)\boldsymbol{v} = -\dfrac{1}{\rho}\boldsymbol{\nabla}_r P - \boldsymbol{\nabla}_r \varphi_{\mathrm{tot}} \\ \nabla_r^2 \varphi_{\mathrm{tot}} = 4\pi G \rho. \end{cases} \tag{1.34}$$

However, it is better to pass from physical coordinates, $\boldsymbol{r}$, to the comoving ones, $\boldsymbol{x}$. They are linked through $\boldsymbol{r} = a(t)\ \boldsymbol{x}$, where $a(t)$ is the scale factor at the considered time. This is very important since the physical velocity contains both the contribution due to the expansion of the background and the proper motion,

$$\boldsymbol{v} = \dot{a}\boldsymbol{x} + a\dot{\boldsymbol{x}} = aH\boldsymbol{x} + \boldsymbol{u}\ , \tag{1.35}$$

where $\boldsymbol{u}$ is called the *peculiar velocity*.

In the new coordinate system, we need to change derivatives with respect to spatial coordinates and time according to

$$\boldsymbol{\nabla}_r \to \frac{1}{a}\boldsymbol{\nabla}_x \qquad \text{and} \qquad \frac{\partial}{\partial t} \to \frac{\partial}{\partial t} - H\, \boldsymbol{x} \cdot \boldsymbol{\nabla}_x \tag{1.36}$$

respectively, where $\boldsymbol{\nabla}_x$ denotes derivatives with respect to the $\boldsymbol{x}$ coordinates. Since in what follows spatial derivatives will always be wrt the comoving coordinates, I will drop the subscript, so that $\boldsymbol{\nabla} = \boldsymbol{\nabla}_x$.

Using these new coordinates we can rewrite the set of equations presented in 1.34. Since we are interested in the evolution of perturbations, we can write densities, velocities, pressures and the gravitational potential in the form

$$\begin{aligned} &\rho(\boldsymbol{x}, t) = \bar{\rho}(t)[1 + \delta(\boldsymbol{x}, t)]\ , \\ &\boldsymbol{v} = aH\boldsymbol{x} + \boldsymbol{u}\ , \\ &P = \bar{p} + \delta p\ , \\ &\varphi_{\text{tot}} = \frac{2\pi G\bar{\rho}r^2}{3} + \varphi\ , \end{aligned} \tag{1.37}$$

where δ, $\boldsymbol{u}$, δp and φ represent the perturbations over the smooth background. Note that the factor $2\pi G\bar{\rho}r^2/3$ in the gravitational potential guarantees its Laplacian to be $4\pi G\bar{\rho}$. The resulting set of equations is

$$\begin{cases} \dfrac{\partial \delta}{\partial t} + \dfrac{1}{a}\boldsymbol{\nabla} \cdot [(1+\delta)\, \boldsymbol{u}] = 0 \\ \dfrac{\partial \boldsymbol{u}}{\partial t} + H\boldsymbol{u} + \dfrac{1}{a}(\boldsymbol{u} \cdot \boldsymbol{\nabla})\boldsymbol{u} = -\dfrac{\boldsymbol{\nabla} p}{a\bar{\rho}(1+\delta)} - \dfrac{1}{a}\boldsymbol{\nabla}\varphi \\ \nabla^2\varphi = 4\pi G\bar{\rho}a^2\delta\ . \end{cases} \tag{1.38}$$

In Euler's equation still appears a pressure gradient term. This can be expanded considering that pressure variations in principle depended on density and entropy,

$$\delta p = \frac{\partial p}{\partial \rho}\, \delta\rho + \frac{\partial p}{\partial s}\, \delta s = c_s^2\, \delta\rho \tag{1.39}$$

where $\delta s = 0$ because we are considering adiabatic perturbations.

The pressure gradient term, anyway, is often neglected. CDM, whatever candidate particle we consider, is thought to only interact via gravity and the weak force, with extremely small cross section (whose exact value depends on the considered candidate). For this reason the interaction rate of CDM falls below the expansion rate of the universe very early, allowing us to consider CDM as a pressureless fluid almost at all times.

For baryons this is not the case. As long as they are coupled to photons in the primeval plasma, the radiation pressure prevents them from collapsing and makes perturbations oscillate with a characteristic speed of sound

$$c_s^2 \simeq \frac{\partial P_\gamma}{\partial(\rho_b + \rho_\gamma)}\Big|_S = \frac{c^2}{3}\left(1 + \frac{3}{4}\frac{\rho_b}{\rho_\gamma}\right)^{-1}\ . \tag{1.40}$$

However, after baryons decouple from photons, such pressure becomes negligible. For this reason, being I interested in the growth of matter perturbations after the epoch of recombination, I will consider the baryon fluid as pressureless.

Linear perturbation theory. The simplest possible way to solve these equations consists in linearising them. In the linear regime overdensities are very small, meaning that $\delta \ll 1$. Furthermore, only first order terms in δ and $\boldsymbol{u}$ will be considered. Under these assumption Eq.s 1.38 become

$$\begin{cases} \dfrac{\partial \delta}{\partial t} + \dfrac{1}{a}\boldsymbol{\nabla}\cdot\boldsymbol{u} = 0 \\ \dfrac{\partial \boldsymbol{u}}{\partial t} + H\boldsymbol{u} = -\dfrac{c_s^2 \boldsymbol{\nabla}\delta}{a\bar{\rho}} - \dfrac{1}{a}\boldsymbol{\nabla}\varphi \\ \nabla^2\varphi = 4\pi G\bar{\rho}a^2\delta \ . \end{cases} \tag{1.41}$$

These equations are independent, and we can combine them by taking the divergence of the Euler equation and plugging the other two in it. First we obtain

$$\begin{cases} \dfrac{\partial \delta}{\partial t} + \dfrac{\vartheta}{a} = 0 \\ \dfrac{\partial \vartheta}{\partial t} + H\vartheta = -\dfrac{c_s^2 \nabla^2\delta}{a\bar{\rho}} - \dfrac{1}{a}\nabla^2\varphi \\ \nabla^2\varphi = 4\pi G\bar{\rho}a^2\delta \ , \end{cases} \tag{1.42}$$

where $\vartheta \equiv \nabla \cdot \boldsymbol{u}$. Recombining them, we obtain the linear equation of growth of fluctuations

$$\frac{\partial^2 \delta}{\partial t^2} + 2H\frac{\partial \delta}{\partial t} = \frac{c_s^2 \nabla^2 \delta}{a^2 \bar{\rho}} + 4\pi G\bar{\rho}\delta \ . \tag{1.43}$$

When $c_s = 0$, this is the equation of an harmonic oscillator, where the right-hand side, gravity, ‘compresses the spring’, while the expansion of the universe, which enters through the term in H, is the friction contrasting the contraction of the spring itself. On the other hand, when $c_s \neq 0$, oscillations are damped by the pressure support.

To explicitly see the scale of the suppression, we can perturb this equation with a plane wave

$$\psi(\boldsymbol{x}, t) = \psi_0 \, e^{i(\boldsymbol{k}\cdot\boldsymbol{x} - \omega t)}. \tag{1.44}$$

We are left with the following dispersion relation,

$$\omega^2 + 2i\omega H = \frac{c_s^2}{a^2}k^2 - 4\pi G\rho. \tag{1.45}$$

Since we are interested in the propagation of pressure waves, which we expect to occur on time scales much smaller than the expansion of the universe itself, we consider at each redshift $H \ll \omega$, hence

$$\omega^2 = \frac{c_s^2}{a^2}k^2 - 4\pi G\rho. \tag{1.46}$$

The oscillatory solutions have $\omega^2 > 0$, and correspond to waves whose gravitational collapse is contrasted by the pressure support of the fluid. On the other hand, solutions with $\omega^2 < 0$ correspond to overdensities that grow exponentially in time, meaning that such solutions correspond to the gravitational collapse of these perturbations. The case when gravity and pressure are balanced corresponds to $\omega = 0$ and gives a characteristic wave-mode,

$$k_{\mathrm{J}}(a) = \sqrt{\frac{4\pi G\rho(a)a^2}{c_s^2}}, \tag{1.47}$$

corresponding to waves with wavelength $\lambda_{\mathrm{J}} = 2\pi/k_{\mathrm{J}}$. This is usually called the Jeans scale (Jeans, 1902). Perturbative waves with wavelength larger than this ($k \ll k_{\mathrm{J}}$) have $\omega^2 < 0$ and are therefore free to grow under the effect of gravity. On the other hand, waves with wavelength smaller than the Jeans scale ($k \gg k_{\mathrm{J}}$) have $\omega^2 > 0$, and are therefore in a oscillatory regime, with gravity and pressure contrasting each other.

While this ideal plane-wave perturbation is very informative on the physics of the growth of a density perturbation, it is very common in cosmology to describe the same effect in terms of decomposition in Fourier modes of the overdensity δ. The advantage of this approach is that, describing perturbations as a superposition of waves, allows us to investigate how different scales differently contribute to the total inhomogeneity. To this purpose, I define the Fourier couple

$$\hat{\delta}(\boldsymbol{k}) = \int \frac{\mathrm{d}^3 r}{(2\pi)^3}\, e^{-i\boldsymbol{k}\cdot\boldsymbol{r}}\, \delta(\boldsymbol{r}), \qquad \delta(\boldsymbol{r}) = \int \mathrm{d}^3 k\, e^{i\boldsymbol{k}\cdot\boldsymbol{r}}\, \hat{\delta}(\boldsymbol{k}). \tag{1.48}$$

This defines the convention on the normalization of the Fourier transform that I adopt throughout this work. Moreover, note that quantities with a hat ($\hat{\cdot}$) are in Fourier space, while quantities without it are in configuration space.

Taking the Fourier transform of Eq 1.43 we obtain

$$\begin{aligned} \frac{\partial^2 \hat{\delta}(\boldsymbol{k})}{\partial t^2} + 2H\frac{\partial \hat{\delta}(\boldsymbol{k})}{\partial t} &= 4\pi G\bar{\rho}(a)\hat{\delta}(\boldsymbol{k})\left[1 - \frac{c_s^2 k^2}{4\pi G\bar{\rho}(a)a^2}\right] \\ &= 4\pi G\bar{\rho}(a)\hat{\delta}(\boldsymbol{k})\left[1 - \frac{k^2}{k_{\mathrm{J}}^2}\right], \end{aligned} \tag{1.49}$$

which corresponds to the result shown before. Once again, for perturbations described by Fourier modes with $k \ll k_{\mathrm{J}}$ the pressure support is negligible, and the growth is only driven by the gravitational collapse. For perturbations with $k \gg k_{\mathrm{J}}$, however, the growth is contrasted by the pressure term.

The details of the propagation of perturbations through density waves that move with velocity c_s depends on the characteristics of the species considered. When baryons were coupled with photons, c_s was the one presented in Eq. 1.40. At that time, therefore, baryon perturbations would oscillate on scales smaller than the sound horizon of the photon-baryon plasma, which poses a problem for explaining the formation of small scale structures.

For this reason, another matter component must be present, which is dark matter. However, if dark matter was hot (*i.e.* it became non-relativistic *after* it decoupled), its sound horizon would coincide with the speed of light, and, according to Eq. 1.43, fluctuations would be damped on scales smaller than this. Once again, this prevents small-scale fluctuations from forming and growing, which would leave us with a top-down scenario, where only large perturbations grow and then fragment to form smaller structures. Yet, cosmology heads towards a bottom-up scenario, where the extremely small perturbations imprinted in the CMB grow and form matter haloes and galaxies.

This can be achieved if the dark matter is cold. In this case, it becomes non-relativistic before decoupling. Moreover, to very good approximation, it is pressureless. In such conditions, $c_s = 0$ for this species, meaning that, in the epoch when matter energy-density dominates the energetic budget of the universe, while the photon-baryon fluid oscillates, the CDM fluid has perturbations that are free to grow. After photon decoupling, baryons lose the radiation pressure support, and their sound speed falls to (almost) zero. For this reason, in the subsequent epoch, baryons are free to fall into the potential wells previously created by the cold dark matter Peebles (1980).

If $c_s = 0$, the evolution of density perturbations is self-similar. This means that the perturbation at a given time can be written as

$$\delta(t) = D(t)\delta_0 \,, \tag{1.50}$$

where δ_0 is the value of the perturbation at an arbitrary time (for convenience usually chosen to be the present time), and $D(t)$ is the *growth factor*, *i.e.* a time dependent function that encloses the evolution in the given cosmology. The growth factor D therefore is as well a solution of Eq. 1.43.

This is not the case (as will be clear in section 1.3) when $c_s \neq 0$. In this case we can expect the growth to be scale dependent, to account for the damping induced by the pressure support.

1.2.1 Description of the growth of fluctuations on nonlinear scales

Small scales, below a few Megaparsecs, are interested by a nonlinear growth of density perturbations. This is due to the fact that collapsing objects, which dominate on such scales, are characterised by high values of the density contrast, $\delta > 1$, and large velocities, induced by the in-halo virialization. For these reasons, Eq. 1.38 cannot be linearised and, therefore, lacks an analytic solution.

There are many possible approaches to try to describe structure formation and evolution on these scales. One is to apply a power series development to the equations in 1.38 and solve for increasingly higher orders, as is common in perturbation theory. Another way is to try to solve the nonlinear equations numerically through numerical simulations.

Nonlinear perturbation theory

The perturbation theory approach (following Bernardeau et al., 2002; Scoccimarro, 2004; Crocce and Scoccimarro, 2006) starts from the fluid equations, Eq. 1.38. Since the nonlinear growth of fluctuations becomes important in the matter dominated universe, I will present here the simplified case in which $\Omega_m = 1$ (corresponding to a Einstein-de Sitter universe). For convenience of writing, we can define a new time variable

$$\eta = \ln a \tag{1.51}$$

and a normalized velocity

$$\boldsymbol{v} = -\frac{\boldsymbol{u}}{\mathcal{H}}, \tag{1.52}$$

that corresponds to a normalized divergence of the velocity field,

$$\Theta = -\frac{\vartheta}{\mathcal{H}}, \tag{1.53}$$

where $\mathcal{H}(a) = aH(a)$. Poisson equation can be recast as

$$\nabla^2\phi = 4\pi G\rho\delta = \frac{3}{2}\mathcal{H}^2\delta \tag{1.54}$$

With these definitions, the equation of motion can be recast in

$$\begin{cases} \dfrac{\partial\delta}{\partial\eta} - \Theta = \boldsymbol{\nabla}\cdot(\delta\boldsymbol{v}) \\ \dfrac{\partial\Theta}{\partial\eta} - \dfrac{3}{2}\delta + \dfrac{1}{2}\Theta = \boldsymbol{\nabla}[(\boldsymbol{v}\cdot\boldsymbol{\nabla})\boldsymbol{v}]. \end{cases} \tag{1.55}$$

The equation of motion in Fourier space look like

$$\begin{cases} \dfrac{\partial \hat{\delta}(\boldsymbol{k})}{\partial \eta} - \hat{\Theta}(\boldsymbol{k}) = \mathcal{F}\{\boldsymbol{\nabla} \cdot (\delta \boldsymbol{v})\} \\ \dfrac{\partial \hat{\Theta}(\boldsymbol{k})}{\partial \eta} - \dfrac{3}{2}\hat{\delta}(\boldsymbol{k}) + \dfrac{1}{2}\hat{\Theta}(\boldsymbol{k}) = \mathcal{F}\{\boldsymbol{\nabla}[(\boldsymbol{v} \cdot \boldsymbol{\nabla})\boldsymbol{v}]\}, \end{cases} \tag{1.56}$$

where quantities with a hat ($\hat{\cdot}$) are in Fourier space. Both the right-hand sides comprehend multiplications of densities and velocities. This means that, in Fourier space, we expect these terms to become convolutions. Therefore, the main consequence of non linearising the equations of motion is that now it is no longer possible to describe the evolution of densities and velocities on each scale independently, while, in fact, different modes are coupled and power leaks into the small scales.

The first mode coupling term in Fourier space can be explicitly written as

$$\mathcal{F}\{\boldsymbol{\nabla} \cdot (\delta \boldsymbol{v})\} = \iint \mathrm{d}^3k_1\, \mathrm{d}^3k_2\, \delta_D(\boldsymbol{k}_{12} - \boldsymbol{k})\, \frac{\boldsymbol{k}_{12} \cdot \boldsymbol{k}_2}{k_2^2}\, \hat{\delta}(\boldsymbol{k}_1)\, \hat{\Theta}(\boldsymbol{k}_2), \tag{1.57}$$

where I adopted the convention that $\boldsymbol{k}_{12} \equiv \boldsymbol{k}_1 + \boldsymbol{k}_2$. The second mode coupling term, becomes

$$\mathcal{F}\{\boldsymbol{\nabla}[(\boldsymbol{v} \cdot \boldsymbol{\nabla})\boldsymbol{v}]\} = \iint \mathrm{d}^3k_1\, \mathrm{d}^3k_2\, \delta_D(\boldsymbol{k} - \boldsymbol{k}_{12})\, \frac{(\boldsymbol{k}_1 \cdot \boldsymbol{k}_2)(\boldsymbol{k}_{12} \cdot \boldsymbol{k}_2)}{k_1^2 k_2^2}\, \hat{\Theta}(\boldsymbol{k}_1)\hat{\Theta}(\boldsymbol{k}_2). \tag{1.58}$$

We are therefore left with the following system of equations

$$\begin{cases} \dfrac{\partial \hat{\delta}(\boldsymbol{k})}{\partial \eta} - \hat{\Theta}(\boldsymbol{k}) = \displaystyle\iint \mathrm{d}^3k_1\, \mathrm{d}^3k_2\, \delta_D(\boldsymbol{k}_{12} - \boldsymbol{k})\, \frac{\boldsymbol{k}_{12} \cdot \boldsymbol{k}_2}{k_2^2}\, \hat{\delta}(\boldsymbol{k}_1)\, \hat{\Theta}(\boldsymbol{k}_2) \\ \dfrac{\partial \hat{\Theta}(\boldsymbol{k})}{\partial \eta} - \dfrac{3}{2}\hat{\delta}(\boldsymbol{k}) + \dfrac{1}{2}\hat{\Theta}(\boldsymbol{k}) = \displaystyle\iint \mathrm{d}^3k_1\, \mathrm{d}^3k_2\, \delta_D(\boldsymbol{k} - \boldsymbol{k}_{12})\, \frac{(\boldsymbol{k}_1 \cdot \boldsymbol{k}_2)(\boldsymbol{k}_{12} \cdot \boldsymbol{k}_2)}{k_1^2 k_2^2}\, \hat{\Theta}(\boldsymbol{k}_1)\hat{\Theta}(\boldsymbol{k}_2). \end{cases} \tag{1.59}$$

Since the left-hand side of this equation does not contain time-dependent parameters, we can seek recursive solutions for the purely growing mode for both the density contrast and the divergence of the velocity field in Fourier space. They have the form

$$\begin{cases} \hat{\delta}^n(\boldsymbol{k}) = \displaystyle\int \mathrm{d}^3q_1 \dots \mathrm{d}^3q_n\, \delta_D(\boldsymbol{k} - \boldsymbol{q}_{1\dots n})\, F_n(\boldsymbol{q}_1 \dots \boldsymbol{q}_n)\, \hat{\delta}^L(\boldsymbol{q}_1) \dots \hat{\delta}^L(\boldsymbol{q}_n) \\ \hat{\Theta}^n(\boldsymbol{k}) = \displaystyle\int \mathrm{d}^3q_1 \dots \mathrm{d}^3q_n\, \delta_D(\boldsymbol{k} - \boldsymbol{q}_{1\dots n})\, G_n(\boldsymbol{q}_1 \dots \boldsymbol{q}_n)\, \hat{\delta}^L(\boldsymbol{q}_1) \dots \hat{\delta}^L(\boldsymbol{q}_n), \end{cases} \tag{1.60}$$

where δ^L is the linear density contrast, which is a solution of Eq. 1.43. F_n and G_n are the kernels that include the nonlinear mode coupling.

It is not obvious that this series converges to the true nonlinear density contrast evolution. Moreover, the physically motivated description of matter as a fluid will inevitably break down below a certain scale (for example, inside haloes the velocity dispersion can become quite important).

Numerical N-body Simulations

The other, essential method to investigate the nonlinear evolution of the matter field is given by numerical simulations.

N-body simulations assume a fluid description of dark matter. The dark matter fluid is sampled with a set of macro-particles (each particle with mass of the order of millions of solar masses or more). At the initial time of the simulation, the particles must reproduce a given initial setup. To do so, the simplest method is to place these particles on a regular grid and compute initial displacements such that the resulting particle distribution has the same power spectrum as the desired one. Such displacements can be computed in Lagrangian perturbation theory, since this approach is devised to describe the final positions and velocities of a set of particles in terms of their initial positions. In this case, initial positions ($\boldsymbol{q}$) are the grid points. Stopping the expansion at the first order, the so called Zel'dovich approximation is obtained (Zel'dovich, 1970), which describes the displacements $\boldsymbol{\psi}$ to be applied to the grid points in terms of the local density at each original location $\delta(\boldsymbol{q})$ and the growing solution of the growth factor $D(a)$ (which is a solution of Eq. 1.43). This displacement is defined by (see for example Bernardeau et al., 2002)

$$\delta(\boldsymbol{x}) = -\boldsymbol{\nabla} \cdot \boldsymbol{\psi} \, . \tag{1.61}$$

Moreover, imposing the continuity equation, also peculiar velocities in the final position can be obtained solving

$$\boldsymbol{u} = -a \, H(a) \, f(a) \, \boldsymbol{\psi} \, , \tag{1.62}$$

where $f \equiv \partial \ln D / \partial \ln a$ is the growth rate. Moreover, more refined results can be achieved adding higher order information, for example stopping at second order in the expansion (2LPT) or at third order (3LPT). This can alleviate possible transients introduced in the initial conditions, since the higher the PT order employed, the more rapidly such transients decay (Scoccimarro, 1998; Crocce et al., 2006).

There exist also other methods to set-up the initial particle distribution, such as the glass method proposed by White (1994). In this case, instead of beginning with particles on a grid, they are first distribute as a Poisson sampling, and then evolved with a gravitational force with inverted sign until residual forces have become negligible. At this point, this particles can be initialized to reproduce the required initial power spectrum. The main advantage is given by the fact that the evolved simulation will not carry any trace of the initial regular grid, thus avoiding the emergence of a non-Poisson shot noise.

At this point, the actual simulation can start. It follows the gravitational evolution of this set of particles, computing, at each new time step, the force exerted on each particle and consequently updating its position and velocity. Several strategies exist to limit the required computational expense, which can easily become prohibitive if the direct computation of the force between a particle and all the others is attempted (particle-particle algorithms) . One of the cheapest and fastest techniques to overcome this problem is to assign particles, at each time, to a density grid, that can be then Fourier transformed to solve Poisson's equation in Fourier space (avoiding in this way the need to take derivatives). Once the grid is set-up, the force on each particle can be computed (particle-mesh algorithms, Klypin and Shandarin (1983); White et al. (1983)). This method, albeit fast, has an accuracy that largely depends on the resolution of the chosen grid. One attempt at speeding up calculations while keeping grid-resolution effects under control is given by the P3M (particle-particle, particle-mesh) algorithm (Eastwood et al., 1984; Efstathiou et al., 1985). In this case, for each particle the force exerted by nearby neighbours is computed directly (particle-particle), while for the long-range force a particle-mesh algorithm is applied. Yet another method is to employ hierarchical trees (Appel, 1985; Barnes and Hut, 1986; Dehnen, 2000) to resolve the force on a almost particle-by-particle basis for particles in the vicinity, using instead larger and larger blocks of particles (collapsed in their center of mass) for distant contributions. A successful combination is the so called TreePM hybrid method (Xu, 1995), that uses the tree algorithm to compute the short-range force acting on each particle and the particle-mesh technique to compute long-range forces.

These methods have made possible studying the fully nonlinear evolution of the dark matter distribution. On the one hand they allow us to test the limits of validity of perturbative approaches Crocce and Scoccimarro (2006). On the other hand, specific fitting formulae can be calibrated to reproduce such nonlinearities (such as the `halofit` fitting formula Smith et al., 2003; Takahashi et al., 2012).

1.3 Cosmological neutrinos

In the ΛCDM model neutrinos have usually been considered to be massless, neglecting their peculiar behaviour but for their contribution to radiation. In fact, as I will briefly review in this section, the effects that the presence of massive neutrinos induce on the evolution of the universe (and on the cosmological observables that we ultimately measure) is far from tiny. Only fairly recently, thanks to the increasing precision in cosmological measurements that calls for models as accurate as possible, neutrinos have drawn a fair amount of attention, to the point of becoming, nowadays, part of the standard picture. Lesgourgues and Pastor (2006, 2012, 2014) presented extensive reviews about cosmological neutrinos, which go beyond what is needed in this work.

The effects of neutrinos can be divided into two general categories: the modifications they induce on the background evolution of the universe and the imprint they leave on the growth of structures.

1.3.1 Effects on the background

The background evolution of the universe is governed by the evolution of the energy densities of the different species that compose it. The Hubble rate, the normalized velocity of the expansion, is the function we use to parametrize the evolution of the energetic budget of the universe. Therefore, to properly include neutrinos in the Hubble rate, we need to understand the evolution of their energy-density parameter.

In the early universe neutrinos are a relativistic species (with kinetic energy way larger than rest-mass energy) and their momenta are distributed according to a Fermi-Dirac distribution function. For neutrinos of mass m_ν, momentum $\boldsymbol{p}$ and temperature T_ν it reads

$$f_\nu(\boldsymbol{x}, \boldsymbol{p}, z) = \frac{1}{e^{pc/k_\mathrm{B} T_\nu} + 1}, \tag{1.63}$$

where $T_\nu(z)$ is the neutrino temperature at redshift z, c the speed of light and k_B the Boltzmann constant. In principle, in the momentum distribution function we should also include the chemical potential, but it has been shown to be negligible for cosmological neutrinos (see for example Dolgov et al., 2002; Wong, 2002; Abazajian et al., 2002).

The goal of this section is to write the proper Hubble rate for a cosmology including massive neutrinos. I will start explicitly deriving the photon energy density, since neutrino evolution is often expressed in terms of corrections to the photon evolution. I will then fix two fundamental times: the redshift of the neutrino decoupling and the redshift of their non-relativistic transition. After this, I will derive the neutrino mass-energy density $\rho_\nu(z)$ and density parameter normalized to the critical density $\Omega_\nu(z)$. The latter is the key quantity that enters the Hubble rate in presence of neutrinos.

Photon density

It is often useful to express the neutrino energy density and temperature in terms of the photon energy density and temperature. To this purpose we need to start from the photon phase-space distribution function, in this case a Bose-Einstein distribution,

$$f_\gamma(\boldsymbol{x},\boldsymbol{p},z) = \frac{1}{e^{pc/k_\mathrm{B}T_\gamma}-1}. \tag{1.64}$$

The photon number density and energy density are then given by the two following equations,

$$\begin{aligned} n_\gamma(z) &= g_\gamma \int \frac{\mathrm{d}^3p}{(2\pi\hbar)^3}\, f_\gamma(\boldsymbol{x},\boldsymbol{p},z) \\ \varepsilon_\gamma(z) &= g_\gamma \int \frac{\mathrm{d}^3p}{(2\pi\hbar)^3}\, f_\gamma(\boldsymbol{x},\boldsymbol{p},z)E(\boldsymbol{p}) = g_\gamma \int \frac{\mathrm{d}^3p}{(2\pi\hbar)^3}\, \frac{pc}{e^{pc/k_\mathrm{B}T_\gamma}-1}. \end{aligned} \tag{1.65}$$

Here $g_\gamma = 2$ is the state degeneracy of photons, which accounts for the two possible polarizations. The factor $(2\pi\hbar)^3$ comes from Heisenberg's uncertainty principle and marks the minimum volume element required to know at the same time the photon position and momentum. Note that the usual (mass-like) photon density is recovered as $\rho_\gamma = \varepsilon_\gamma/c^2$.

The last integral in Eq. 1.65 can be conveniently manipulated defining $x \equiv pc/k_\mathrm{B}T_\gamma$,

$$\rho_\gamma(z) = \frac{g_\gamma}{2\pi^2\hbar^3c^5}\,[k_\mathrm{B}T_\gamma(z)]^4 \int_0^\infty \mathrm{d}x\, \frac{x^3}{e^x-1}, \tag{1.66}$$

where the change of coordinates is made possible by the assumption that momenta are isotropically distributed. Now the solution can be given in terms of the Riemann-Zeta function and the Γ function, obtaining

$$\rho_\gamma = \frac{g_\gamma}{2\pi^2\hbar^3c^5}\,[k_\mathrm{B}T_\gamma(z)]^4\zeta(4)\Gamma(4) = \left(\frac{\pi^4}{15}\right)\frac{g_\gamma}{2\pi^2\hbar^3c^5}\,(k_\mathrm{B}T_{\gamma,0})^4(1+z)^4. \tag{1.67}$$

As a consequence, once the value of the photon temperature today is fixed, the photon energy density at all times is automatically given. The temperature of the CMB has been measured to exquisite precision, $T_{\gamma,0} = (2.72548 \pm 0.00057)$ K (Fixsen, 2009). In the rest of this work I will always assume $T_{\gamma,0} = 2.7255$ K.

Finally,

$$\Omega_\gamma(z) = \frac{\rho_\gamma(z)}{\rho_\mathrm{crit}(z)} = \frac{8\pi G}{3H^2(z)}\left(\frac{\pi^4}{15}\right)\frac{g_\gamma}{2\pi^2\hbar^3c^5}\,(k_\mathrm{B}T_{\gamma,0})^4(1+z)^4 \tag{1.68}$$

is the photon energy density parameter normalized to the critical density of the universe. By parametrizing the Hubble constant today as $H_0 = h\ 100\ \mathrm{km\,s^{-1}\,Mpc^{-1}}$, the photon energy density parameter today can be expressed as

$$\Omega_{\gamma,0}h^2 = 2.469\times10^{-5}, \tag{1.69}$$

where I have introduced all the values of the physical constants, photon degeneracy parameter an photon temperature today.

Neutrino decoupling and non-relativistic transition

Neutrinos decouple when their interaction rate falls below the expansion rate of the universe. The neutrino interaction rate can be written as

$$\Gamma = n_\nu \left\langle v \, \sigma_\nu(E) \right\rangle , \tag{1.70}$$

where n_ν is the neutrino number density, v the velocity of the particle and $\sigma_\nu(E)$ the energy-dependent cross section. Assuming that their only channel of interaction is through weak force, their cross-section has the form

$$\sigma = \frac{G_F^2 \, (k_B T_{\rm bg})^2}{\pi (\hbar c)^4}, \tag{1.71}$$

where G_F is the Fermi coupling. By equating the interaction rate Γ and the expansion rate of the universe H, we obtain that neutrinos decouple when the background temperature is around $T_{\rm bg} \simeq 1 \ {\rm MeV}$. This roughly corresponds to a redshift

$$1 + z_{\rm dec} \simeq 10^9. \tag{1.72}$$

As the universe expands and the background temperature drops down, the kinetic energy of neutrinos eventually becomes lower than their rest-mass. By equating $m_\nu c^2 \simeq T_{\nu,0}(1+z)$ we find the redshift when neutrinos turned non-relativistic,

$$1 + z_{\rm nr} \simeq 1890 \left[\frac{m_\nu}{1 \ {\rm eV}} \right] . \tag{1.73}$$

Here I have assumed that the neutrino temperature today is $T_{\nu,0} = 1.95 \ {\rm K}$. In appendix A I present a derivation of the neutrino to photon temperature ratio, justifying this number. There I also briefly discuss the limitations of modelling neutrino decoupling like a instantaneous event and the most common corrections employed to alleviate them.

The interesting fact is that neutrinos are hot, meaning that when they decouple they are still relativistic. As a consequence, we expect we can use equation 1.63 to describe the distribution of neutrino momenta even after they become non-relativistic, since this phase-space distribution function remains frozen for all times after neutrino decoupling.

Neutrino density

Starting from the phase-space distribution function in Eq. 1.63, the neutrino number density can be written as

$$n_\nu(\boldsymbol{x}, z) = 2 \int \frac{{\rm d}^3 p}{(2\pi\hbar)^3} \, f_\nu(\boldsymbol{x}, \boldsymbol{p}, z), \tag{1.74}$$

and their energy density is

$$\rho_\nu(\boldsymbol{x}, z) = \frac{2}{c^2} \int \frac{{\rm d}^3 p}{(2\pi\hbar)^3} \, f_\nu(\boldsymbol{x}, \boldsymbol{p}, z) \, E(\boldsymbol{p}) = \frac{2}{c^2} \int \frac{{\rm d}^3 p}{(2\pi\hbar)^3} \, \frac{\sqrt{p^2 c^2 + m_\nu^2 c^4}}{e^{pc/k_B T_\nu} + 1} \, . \tag{1.75}$$

Note that the phase-space distribution used here is the one valid for relativistic neutrinos. This is justified because, as seen in the previous section, neutrinos become non-relativistic after decoupling, which freezes their momentum distribution to the relativistic one.

In order to link the neutrino density to the photon one we are missing the relation between neutrino and photon temperature. The two temperatures can be linked as

$$T_\nu(z) = \Gamma_\nu T_\gamma(z), \tag{1.76}$$

where the value of Γ_ν is derived in appendix A. The neutrino density can therefore be expressed in terms of the photon one as

$$\rho_\nu(z) = \left(\frac{15}{\pi^4}\right)\Gamma_\nu^4 \rho_\gamma(z)\mathcal{F}(y), \tag{1.77}$$

where

$$\mathcal{F}(y) = \int \mathrm{d}x \frac{x^2\sqrt{x^2+y^2}}{e^x+1}, \quad y \equiv \frac{m_\nu c^2}{k_B T_{\nu,0}(1+z)}. \tag{1.78}$$

The parameter y depends on time, with $y \ll 1$ corresponding to times when neutrinos are relativistic, and $y \gg 1$ describing non-relativistic neutrino. The non-relativistic transition occurs when $y \sim 1$.

Equation 1.77 has two interesting limiting cases. At early times neutrinos are relativistic and we can consider $m_\nu \ll T_{\nu,0}(1+z)$,

$$\lim_{y\to 0} \mathcal{F}(y) = \frac{7}{8}\zeta(4)\Gamma(4) = \frac{7}{8}\frac{\pi^4}{15}. \tag{1.79}$$

In this case the early time neutrino density is given by

$$\rho_\gamma^{\mathrm{et}}(z) = \frac{7}{8}\Gamma_\nu \rho_\gamma(z) \propto (1+z)^4 \tag{1.80}$$

and neutrinos evolve like radiation. In this regime, the density parameter of radiation in the universe, Ω_r, is given by the sum of the photon density parameter and the neutrino one. The neutrino density parameter for the relativistic case is directly derived by Eq. 1.80. As a consequence, for $N_\nu^{\mathrm{rel}} = 3$ massless neutrinos, the radiation density parameter reads

$$\Omega_r(z) = \Omega_\gamma(z)\left[1 + N_\nu^{\mathrm{rel}}\frac{7}{8}\Gamma_\nu^4\right]. \tag{1.81}$$

Here, following appendix A, we should use the value of Γ_ν that accounts for the reheating given by the $e^\pm$ recombination in the non-instantaneous decoupling scenario. It is customary, though, to use use instead the neutrino to photon temperature ratio obtained in the case of instantaneous decoupling, $\Gamma_\nu = (4/11)^{4/3}$, and absorb the correction in the number of relativistic species, that therefore becomes an *effective number of relativistic species*,

$$N_{\mathrm{eff}} = \frac{N_\nu \Gamma_\nu^4}{(4/11)^{4/3}} = 3.046. \tag{1.82}$$

This leads to the customary formula for the radiation density parameter in case of relativistic neutrinos

$$\Omega_r(z) = \Omega_\gamma(z)\left[1 + N_{\mathrm{eff}}\frac{7}{8}\left(\frac{4}{11}\right)^{4/3}\right]. \tag{1.83}$$

The late-time limit of equation 1.77 corresponds to non-relativistic neutrinos with $m_\nu \gg T_{\nu,0}(1+z)$,

$$\lim_{y\to\infty} \mathcal{F}(y) = y\frac{3}{2}\zeta(3). \tag{1.84}$$

The late-time neutrino density therefore reads

$$\rho_\nu^{\rm lt}(z) = \left(\frac{15}{\pi^4}\right) \Gamma_\nu^4 \frac{3}{2}\zeta(3)\ [y\ \rho_\gamma(z)] \propto m_\nu\ (1+z)^3. \tag{1.85}$$

At late times neutrinos therefore evolve like matter. In this regime, they contribute to the gravitational potential, and modify the growth of matter perturbations.

Their present time density parameter, accounting for all the neutrino species, can be approximated from Eq. 1.85 as

$$\Omega_{\nu,0} = \frac{\sum \rho_{\nu_i}^{lt}}{\rho_{\rm crit}(z=0)} = \zeta(3)\frac{4G(k_b\ T_{\nu,0})^3}{\pi\ H^2\ \hbar^3\ c^5}\ M_\nu, \tag{1.86}$$

which becomes, after introducing the values of the different physical constants,

$$\Omega_{\nu,0}\ h^2 = \frac{M_\nu}{93.14\ {\rm eV}}\ . \tag{1.87}$$

In Fig. 1.2 I show the evolution of the neutrino density and of the two limiting cases presented above, as a function of redshift.

We can now combine the neutrino and radiation density previously computed to express the redshift dependent Hubble function in cosmologies that include massive neutrinos.

We can express the neutrino density from Eq. 1.77 as a density parameter in units of the critical density of the universe, obtaining

$$\Omega_\nu(z) = \left(\frac{15}{\pi^4}\right)\Gamma_\nu^4 \Omega_\gamma(z)\mathcal{F}(y). \tag{1.88}$$

The Hubble function at each redshift can therefore be expressed as

$$H^2(z) = H_0^2\left\{\Omega_{\gamma,0}(1+z)^4 + \Omega_\nu(z)E^2(z) + \Omega_{cb,0}(1+z)^3 + \Omega_\Lambda\right\}. \tag{1.89}$$

Written this way, the $\Omega_\nu(z)$ term automatically accounts, at each redshift, for both the fraction of neutrinos that are still relativistic (and that add on top of the photon density term) and for the fraction that is already non-relativistic.

1.3.2 Fluid description of neutrino perturbations

The growth of neutrino perturbation can be described adopting a fluid formalism, as much as it is customary with CDM. Unlike CDM, though, we expect we will need a pressure term to model the small scale behaviour of neutrinos. While the description of the evolution of perturbations in the presence of massive neutrinos dates to back to Bond et al. (1980); Ma and Bertschinger (1995); Wong (2008), the description of cosmic neutrinos as a fluid has first been introduced in Shoji and Komatsu (2010) and employed, more recently, in Blas et al. (2014).

Such a neutrino fluid will obey the usual fluid equations, which here will be considered in their linearised form (valid for small overdensities and velocities), see Eq. 1.41. In the framework of a fluid description, we need to understand how to treat the speed of sound that appears in these equations. We can introduce the pressure of the neutrino fluid, linked to its density though an equation of state, such as

$$p_\nu = w_\nu \rho_\nu c^2, \tag{1.90}$$

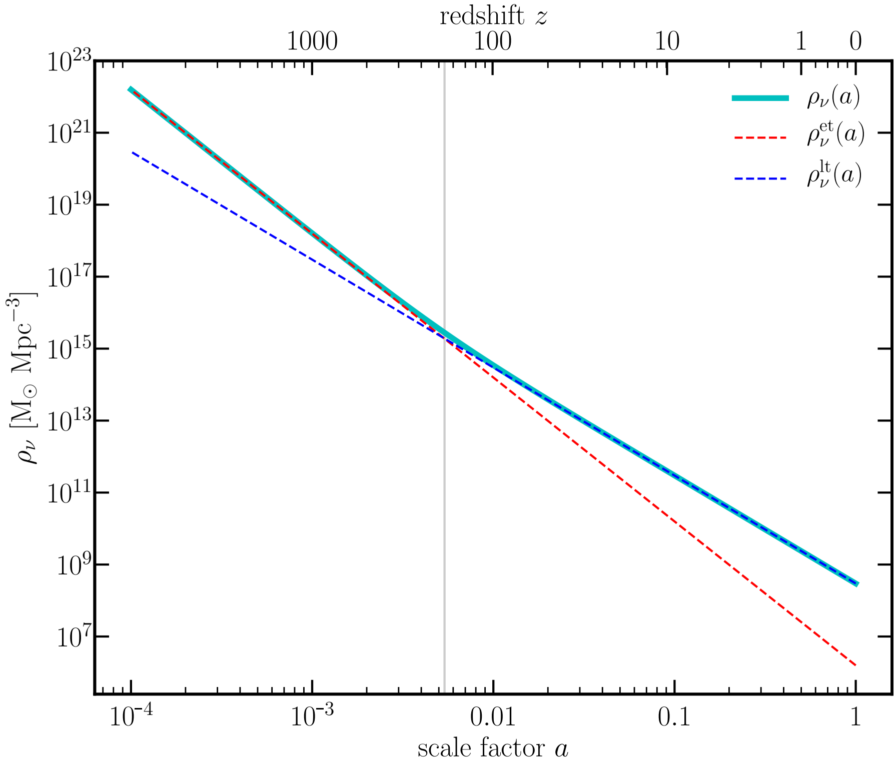

Figure 1.2: The evolution of the neutrino density with the scale factor a (axis below) and redshift z (axis above). Here a neutrino of mass $m_\nu = 0.1$ eV is considered. The cyan solid line shows the correct solution for $\rho_\nu(z)$, while the red and blue dashed lines respectively show the early and late time limit of the correct solution. The early time limit is proportional to $(1+z)^4$, underlining that at early times neutrinos are relativistic and behave like radiation. The late time limit, instead, is proportional to $(1+z)^3$, following the same evolution of radiation. The gray vertical line marks the non-relativistic transition for neutrinos of this given mass.

where w_ν is uniquely defined by the equation

$$\mathrm{d}\ln\rho_\nu = (1+3w_\nu)\,\mathrm{d}\ln a, \tag{1.91}$$

where a is the scale factor of the universe. Thanks to the latest equation, we can obtain

$$w_\nu = \frac{1}{3}\left[1 - y\frac{\mathcal{G}(y)}{\mathcal{F}(y)}\right], \tag{1.92}$$

where y is the same defined in Eq. 1.2, $y \equiv m_\nu/k_\mathrm{B}T_\nu$, and I have defined

$$\mathcal{G}(y) = y\int_0^\infty \mathrm{d}x\,\frac{x^2(x^2+y^2)^{-1/2}}{e^x+1}. \tag{1.93}$$

Note that when we take the early-time limit of 1.92, with $y \to 0$ and $\mathcal{G}(y) \to 0$, we obtain $w_\nu^\mathrm{et} \to 1/3$. On the other hand the late-time limit has $y \to \infty$ and $\mathcal{G}(y) \to 3\zeta(3)/2$ and results in $w_\nu^\mathrm{lt} \to 0$. Consistently with what we said before, the early-time behaviour of neutrinos is that of a radiative species, while at late times they behave as pressureless dust.

Having introduced an effective neutrino pressure, we need to define the speed at which pressure waves propagate in the neutrino fluid, namely the speed of sound. Under the assumption that there are no entropy perturbations, we can express the speed of sound as

$$c_\nu = \sqrt{\frac{\partial p_\nu}{\partial \rho_\nu}} \simeq 134.423\,(1+z)\left[\frac{1\,\mathrm{eV}}{m_\nu}\right]\ \mathrm{km\,s^{-1}}, \tag{1.94}$$

see for example Blas et al. (2014).

The speed of sound of neutrinos introduces a typical scale, called free streaming scale. Below this scale, neutrino velocities prevent them from clustering, as they freely stream through the gravitational potential wells without being trapped. On scales larger than that of free streaming, however, they follow the same evolution driven by the CDM fluid and their growth is indistinguishable.

In the fluid formalism the free streaming scale is the scale where pressure and gravity are balanced. We can refer to Eq. 1.47 to see that, for a neutrino fluid, the effective Jeans length, called in this case the free-streaming scale, is

$$k_\mathrm{fs} = \sqrt{\frac{4\pi G\rho a^2}{c_\nu^2}} = \sqrt{\frac{3}{2}\frac{\Omega_m a^2 H^2}{c_\nu^2}}. \tag{1.95}$$

Since we characterised neutrino pressure, we are now able to express what fraction of the whole neutrino distribution is non-relativistic at all times. In Newtonian terms, we expect only this fraction to contribute to gravity. This can be done considering that the fraction of neutrinos that contributes to the energy budget of relativistic species, at each redshift, is given by

$$\Omega_\nu^\mathrm{rel}(z) = 3w_\nu(z)\Omega_\nu(z), \tag{1.96}$$

where $\Omega_\nu(z)$ is computed according to Eq. 1.77 and $w_\nu(z)$ according to Eq. 1.92. As a consequence, the fraction of non-relativistic neutrinos at each redshift is given by

$$\Omega_\nu^\mathrm{nr}(z) = \left[1 - 3w_\nu(z)\right]\Omega_\nu(z). \tag{1.97}$$

The effective matter density parameter therefore is

$$\Omega_m(z) = \Omega_{cdm}(z) + \Omega_b(z) + [1 - 3w_\nu(z)]\,\Omega_\nu(z) \tag{1.98}$$

Note that this scale does not only affect the growth of neutrino perturbations. As a matter of fact, if we considered the coupled growth of two fluids, one composed of dark matter (CDM and baryons) and the other one of neutrinos, it is described by the system of equations

$$\begin{cases} \dfrac{\partial^2\delta_{cb}}{\partial t^2} + 2H(a)\dfrac{\partial\delta_{cb}}{\partial t} & = \dfrac{3}{2}\Omega_m H^2(a)\delta_{\rm tot}(a) \\ \dfrac{\partial^2\delta_\nu}{\partial t^2} + 2H(a)\dfrac{\partial\delta_\nu}{\partial t} & = \dfrac{c_s^2}{a^2}\nabla^2\delta_\nu(a) + \dfrac{3}{2}\Omega_m H^2(a)\delta_{\rm tot}(a)\,. \end{cases} \tag{1.99}$$

where $\delta_{\rm tot} = (1 - \mathfrak{f}_\nu)\delta_{cb} + \mathfrak{f}_\nu\delta_\nu$ is the growth factor of the total matter component, Ω_m is the one defined in Eq. 1.98, accounting only for the non-relativistic fraction of matter in the universe at any given redshift. Both the solutions for δ_{cb} and δ_ν obtained from this set of equations are scale dependent, meaning that the free streaming of neutrino through the growing matter perturbations also affects the evolution of dark matter overdensities.

1.4 Random fields

The fluid description adopted up to now is a very powerful tool to model the evolution of overdensities in the universe. However, it is ultimately impossible to follow any single perturbation. For this reason, we must adopt a statistical description of the evolution of matter fluctuations. To this end, cosmological fields (such as the overdensity, or the velocity of a cosmological fluid) can be described as random fields, which evolve in time.

A random field is fully characterized by its n-point probability distribution. The 1-point moments of a random field ϕ at a given position can be written as

$$\langle\phi^n\rangle = \int \mathrm{d}\phi\, p(\phi)\,\phi^n\,. \tag{1.100}$$

where $p(\phi)$ is the *probability density distribution* of the field. The mean value of the field is its first 1-point moment, $\bar{\phi} = \langle\phi\rangle$, while its variance is related to the second and first moment according to $\sigma_\phi^2 = \left\langle\phi^2\right\rangle - \langle\phi\rangle^2$. Hear the brackets $\langle\ \rangle$ denote ensemble averages.

These 1-point moments describe punctual properties of the field. If the field is statistically homogeneous, they do not depend on the position. However, we are also interested in studying possible correlations between points that are spatially distributed. The 2-point moment considers the field in two different positions $\boldsymbol{r}_1$ and $\boldsymbol{r}_2$, and is defined as

$$\langle\phi^n(\boldsymbol{r}_1)\phi^m(\boldsymbol{r}_2)\rangle = \int \mathrm{d}\phi(\boldsymbol{r}_1)\,\mathrm{d}\phi(\boldsymbol{r}_2)\,p(\phi(\boldsymbol{r}_1),\phi(\boldsymbol{r}_2))\,\phi^n(\boldsymbol{r}_1)\phi^m(\boldsymbol{r}_2)\,. \tag{1.101}$$

In general, for a moment of order higher than 1, we can provide a *cluster expansion* (Fry, 1984), that is it can be expressed as a combination of moments of lower or equal order. For the 2-point moment of order $n = 1$ and $m = 1$, the cluster expansion reads

$$\langle\phi(\boldsymbol{r}_1)\phi(\boldsymbol{r}_2)\rangle = \langle\phi(\boldsymbol{r}_1)\rangle\,\langle\phi(\boldsymbol{r}_2)\rangle + \langle\phi(\boldsymbol{r}_1)\phi(\boldsymbol{r}_2)\rangle_c\,, \tag{1.102}$$

where $\langle\phi(\boldsymbol{r}_1)\phi(\boldsymbol{r}_2)\rangle_c$ is the *connected expectation value*, also called the *cumulant moment*, *i.e.* the term of the expansion that does not depend on any lower order. In case of a field with null mean, the 2-point moment corresponds to its connected part. The connected part of the 2-point moment is also called the *2-point correlation function*, ξ. It represents the excess probability of finding a non-zero correlation between two given points. Under the assumption that the universe is homogeneous, the correlation function only depends on the distance between the two points, $\langle\phi(\boldsymbol{r}_1)\phi(\boldsymbol{r}_2)\rangle_c = \xi(\boldsymbol{r}_1 - \boldsymbol{r}_2)$. If, in addition, the field is isotropic, then the correlation function only depends on the modulus of the distance between the points, $\langle\phi(\boldsymbol{r}_1)\phi(\boldsymbol{r}_2)\rangle_c = \xi(|\boldsymbol{r}_1 - \boldsymbol{r}_2|)$.

The generic n-point moment (of order n) is given by

$$\langle\phi(\boldsymbol{r}_1)\dots\phi(\boldsymbol{r}_n)\rangle = \int \mathrm{d}\phi(\boldsymbol{r}_1)\dots\mathrm{d}\phi(\boldsymbol{r}_n)\, p(\phi(\boldsymbol{r}_1),\dots,\phi(\boldsymbol{r}_n))\ \phi(\boldsymbol{r}_1)\dots\phi(\boldsymbol{r}_n). \tag{1.103}$$

Whatever the order, performing the cluster expansion, the connected part of each moment can be found, which allows us to define n-point correlation functions.

In the particular case of a Gaussian random field, which is a random field whose probability density function is Gaussian, the field is completely described by its mean and 2-point correlation function, and all higher-order cumulant moments are zero.

1.4.1 The matter power spectrum

It is often very useful to perform the statistical analysis of the overdensity field in Fourier space. As a matter of fact, viewing the overall field as a superposition of waves gives us information about the *relative contribution* to the overall inhomogeneity of each different scale. The adopted convention for the Fourier transform is the one introduced in 1.48.

When we compute the 2-point correlation function of the overdensity field in Fourier space we obtain

$$\begin{aligned}\left\langle\hat\delta(\boldsymbol{k}_1)\hat\delta(\boldsymbol{k}_2)\right\rangle &= \int\frac{\mathrm{d}^3r_1}{(2\pi)^3}\int\frac{\mathrm{d}^3r_2}{(2\pi)^3}\, e^{-i\boldsymbol{k}_1\cdot\boldsymbol{r}_1}e^{-i\boldsymbol{k}_2\cdot\boldsymbol{r}_2}\ \langle\delta(\boldsymbol{r}_1)\delta(\boldsymbol{r}_2)\rangle \\ &= \delta_D(\boldsymbol{k}_1+\boldsymbol{k}_2)\int\frac{\mathrm{d}^3r}{(2\pi)^3}\, e^{-i\boldsymbol{k}_1\cdot\boldsymbol{r}}\ \xi(\boldsymbol{r}) \\ &= \delta_D(\boldsymbol{k}_1+\boldsymbol{k}_2)P(\boldsymbol{k}_1),\end{aligned} \tag{1.104}$$

where δ_D is the Dirac delta, $\boldsymbol{r}\equiv\boldsymbol{r}_1-\boldsymbol{r}_2$ is the separation in configuration space, and

$$P(\boldsymbol{k}) \equiv \int\frac{\mathrm{d}^3r}{(2\pi)^3}\, e^{-i\boldsymbol{k}\cdot\boldsymbol{r}}\ \xi(\boldsymbol{r}) \tag{1.105}$$

is the *power spectrum*. Just like the correlation function, also the power spectrum, whenever the additional assumption of isotropy is verified, only depends on the modulus of the distance between the two wavenumbers in Fourier space.

From Eq. 1.104 we can see that, in linear theory, there is no mode coupling in Fourier space, and the evolution of each mode can be described independently. The power spectrum in linear theory can in general be predicted numerically, solving the Einstein-Boltzmann equation for all the species considered in the universe. There exist some publicly available codes that undertake this task (Seljak and Zaldarriaga, 1996; Lewis et al., 2000; Lesgourgues, 2011a).

Moreover, we can apply the results obtained in standard perturbation theory (Eq. 1.60) and expand $\hat\delta(\boldsymbol{k})$ in a power series. In this case, we can expect that the mode coupling introduced by the kernels will transfer power from large-scale modes into the small scales. The accuracy of the perturbative approach can therefore be tested by comparing the power spectrum predicted in this way with the matter power spectrum measured in dark matter cosmological simulation.

1.4.2 Estimation of the matter power spectrum in N-body simulations

Numerical simulations provide us with positions and velocities of a set of dark matter macroparticles, evolved in time from an initial setup. As a consequence, we need to estimate the power spectrum from a discrete collection of particles $\{\boldsymbol{x}_1, \ldots, \boldsymbol{x}_{Np}\}$, distributed in a finite volume V. For simplicity, let the volume be a cubical box of side L. the fundamental frequency of the box is given by

$$k_f = \frac{2\pi}{L}, \tag{1.106}$$

and represents the largest scale contained in the given volume. We are going to decompose density fluctuations in the box in terms of a discrete set of Fourier modes, $\boldsymbol{k} = \boldsymbol{n}\, k_f$, obtaining

$$\delta(\boldsymbol{k}) = \int_V \frac{\mathrm{d}^3 x}{(2\pi)^3} e^{-i\boldsymbol{k}\cdot\boldsymbol{x}} \delta(\boldsymbol{x}) \,, \qquad \delta(\boldsymbol{x}) = k_f^3 \sum_{\boldsymbol{k}} e^{i\boldsymbol{k}\cdot\boldsymbol{x}} \hat{\delta}(\boldsymbol{k}) \,. \tag{1.107}$$

The overdensity in configuration space is given by

$$\delta(\boldsymbol{x}) = \frac{1}{\bar{n}} \sum_{i=1}^{N_p} \delta^D(\boldsymbol{x} - \boldsymbol{x}_i) - 1 \,, \tag{1.108}$$

where δ^D is a Dirac delta and $\bar{n} = N_p/V$. Its Fourier transform consequently reads

$$\hat{\delta}(\boldsymbol{k}) = \frac{1}{(2\pi)^3} \left[\frac{1}{\bar{n}} \sum_{i=1}^{N_p} e^{-i\boldsymbol{k}\cdot\boldsymbol{x}_i} - \delta^K_{\boldsymbol{k}} \right] , \tag{1.109}$$

where δ^K is a Kronecker delta (since here the wavemodes are discrete). It follows that (Peebles, 1980; Jing, 2005; Sefusatti et al., 2016)

$$\langle \delta(\boldsymbol{k}_1)\delta(\boldsymbol{k}_2) \rangle = \frac{\delta^K_{\boldsymbol{k}_1+\boldsymbol{k}_2}}{k_f^3} \left[P(\boldsymbol{k}_1) + \frac{1}{(2\pi)^2 \bar{n}} \right] . \tag{1.110}$$

The second term in the parenthesis is called the *shot noise* and represents the autocorrelation of each point with itself. It is constant term (white noise) and arises from the discreteness of the particle distribution. In order to estimate the power spectrum, we need to correct for this spurious contribution by subtracting it, for example defining the estimator

$$\tilde{P}(k) = k_f^3 \left[|\delta(\boldsymbol{k})|^2 - \frac{1}{N_p} \right] , \tag{1.111}$$

while the true power spectrum is given by $P = \left\langle \tilde{P} \right\rangle$.

Moreover, in a finite box, high frequency modes can be determined to much better precision than low frequency ones. This effect is usually called *cosmic variance*. To visualize it, we can think that, when computing the power spectrum in the discrete Fourier space, considering circular bins centred in the fundamental frequency and of given size Δk, there will be fewer points falling the in bins close to k_f, and more and more points in farther away bins. It can be quantified when we compute the covariance between the k bins of the power spectrum,

$$\begin{aligned} C_{ij} &= \langle P(k_i)P(k_j)\rangle - \langle P(k_i)\rangle \langle P(k_j)\rangle \\ &= \frac{2\delta^K_{ij}}{N_{k_i}}\, P^2(k_i) + k_f^3 \bar{T}(k_i, k_j)\ , \end{aligned} \tag{1.112}$$

where δ^K_{ij} is a Kronecker delta, N_{k_i} is the number of wavemodes in the i-th bin, and $\bar{T}(k_i, k_j)$ is the bin-averaged trispectrum (see for example Scoccimarro et al., 1999). For a Gaussian overdensity field the trispectrum is zero, and the covariance matrix of the power spectrum is diagonal. However, the gravitational growth of fluctuations induces non-gaussianities that in principle require to account also for the non-diagonal terms.

1.4.3 Effects of neutrinos on the matter power spectrum

Combining the effects of neutrinos on the background evolution and on the growth of matter perturbations, we expect the matter power spectrum to display a suppression of the power on scales smaller than the free streaming scale at the time neutrinos became non-relativistic. This is indeed what can be observed in Fig. 1.3, for the matter power spectrum computed in linear theory.

The neutrino suppression is effective on scales below the scale of the neutrino free streaming at the time they became non-relativistic. Such scale moves towards higher wavemodes for neutrinos of larger mass, because they become non-relativistic earlier. Moreover, the suppression is larger for heavier neutrinos. The reason is that more massive neutrinos become non-relativistic earlier, and therefore their free streaming is integrated over a longer time.

The presence of massive neutrinos therefore introduces a peculiar scale dependence already in the linear power spectrum (and in the growth factor) of density fluctuation. Such scale dependence also modifies small-scale, coherent velocities, hence introducing as well a scale dependence in the growth rate of structures. Moreover, such peculiar scale dependence evolves with redshift.

Such scale dependence is visible also in the nonlinear power spectrum. For example, Fig. 1.4 shows the total matter power spectrum measured in three simulations of the DEMNUni project (the details of these simulations will be presented in section 2.6) with $M_\nu = \{0, 0.16, 0.32\}$ eV. On top of the suppression predicted in linear theory, the fully nonlinear power spectrum shows an additional, spoon-like suppression in the power on scales $k \sim 1\ h\,\mathrm{Mpc}^{-1}$, which is induced by the presence of neutrinos.

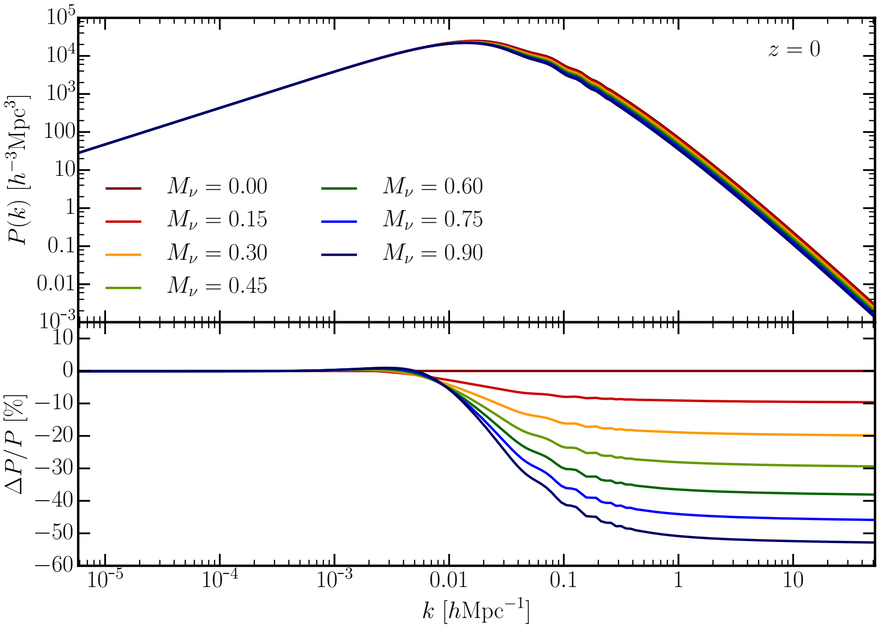

Figure 1.3: The linear matter power spectrum in the presence of massive neutrinos. Different colours correspond to different neutrino masses. The lower panel shows the ratio between the matter power spectrum in the massive neutrino cases with respect to the standard ΛCDM case. The matter power spectrum is suppressed by the presence of neutrinos on scales below the scale of neutrino free streaming at the time they became non-relativistic. Such scale moves to smaller scales for larger neutrino masses. Moreover, the suppression is larger for larger neutrino masses.

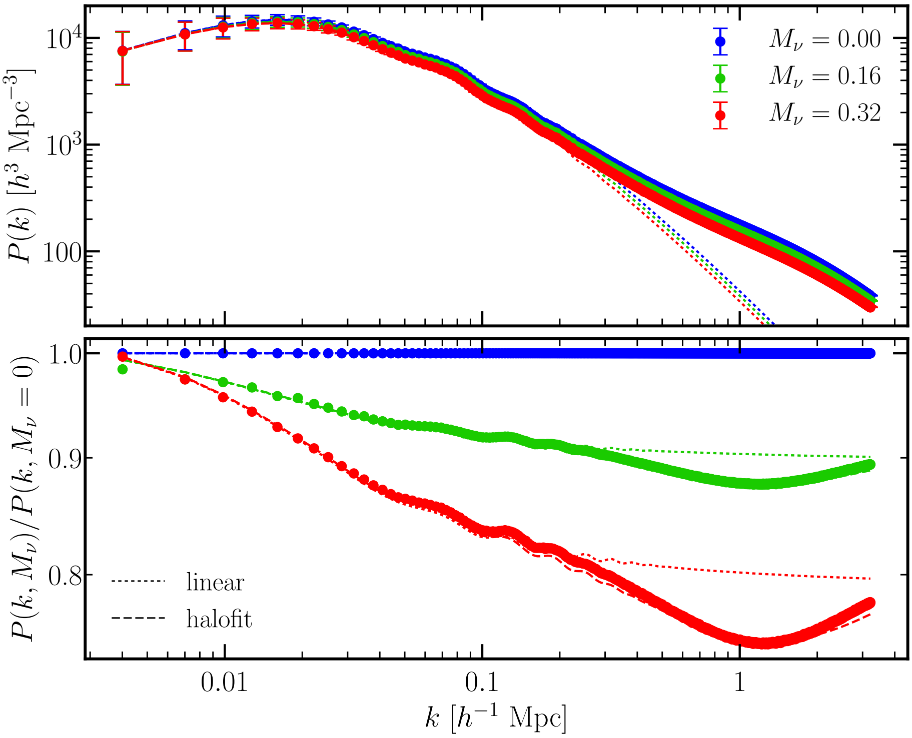

Figure 1.4: *Upper panel:* The nonlinear matter power spectrum in the presence of massive neutrinos, measured in three of the DEMNUni simulations with $M_\nu = \{0, 0.16, 0.32\}$ eV (corresponding to blue, green and red respectively) at redshift $x = 0.48551$. *Lower panel:* the ratio between the power spectrum measured in cosmologies with non-zero neutrino mass with respect to the ΛCDM case. In both panels, dotted lines show linear theory predictions, while dashed lines show a nonlinear prediction obtained with `halofit`.

CHAPTER 2

Initial conditions for simulations of massive neutrino cosmologies

In section 1.3 we have seen that massive neutrinos do modify both the expansion history of the universe and the distribution and clustering properties of the matter contained in it. Although such differences from a standard ΛCDM model appear already at linear level, to fully characterize measurable neutrino effects we need to explore the nonlinear power spectrum of matter and galaxies in presence of massive neutrinos.

Generally, given the impracticability of an analytic approach to solve the fully nonlinear fluid equations, either semi-analytic techniques or a numerical approach must be adopted. In particular, N-body simulations allow for solving the gravity-driven evolution of a given CDM distribution down to very small scales, that, depending on the resolution of the specific simulation, can correspond to 1 or a few $h^{-1}\,\mathrm{Mpc}$ ($k \simeq$ 1-5 $h\,\mathrm{Mpc}^{-1}$). For this reason N-body simulations are regarded as the state-of-the-art technique to study the late-time small-scale nonlinear evolution of CDM in the standard ΛCDM model.

To reach the same level of accuracy in describing the nonlinear growth of structures when we consider the presence of massive neutrinos, the most natural thing is to include neutrinos in N-body simulations. There are many possible techniques to do so. Given that neutrino clustering on small scales is strongly suppressed, one can solve the neutrino potential at linear level on a grid and add it to the force computed on the CDM particles, as in the so-called *grid-based* approach (Brandbyge and Hannestad, 2009). On the other hand, in the *particle-based* approach, neutrinos are regarded as an additional particle species that, unlike CDM, includes a thermal component in its initial velocities (Brandbyge et al., 2008; Viel et al., 2010; Villaescusa-Navarro et al., 2013; Castorina et al., 2015; Carbone et al., 2016). Also hybrid versions of grid-based and particle-based methods exist, as presented in Brandbyge et al. (2010), or combinations of the particle-based method with semi-analytic models (Ali-Haïmoud and Bird, 2013). Other relevant possible implementations include the method employed by Agarwal and Feldman (2011) and Upadhye et al. (2014), who consider only CDM particles but perturb a fraction of them according to neutrino and baryon transfer functions, or the method presented in Banerjee and Dalal (2016), that combines N-body and fluid techniques.

The particle-based method, even if, for its discrete nature, is plagued by shot noise, has been shown to allow for describing neutrino effects at nonlinear level (Bird et al., 2012; Villaescusa-Navarro et al., 2013) and, at the same time, studying the relative velocity of neutrinos and CDM (Inman et al., 2015).

In the particle-based approach the starting point is an initial distribution of particles, usually chosen to describe a universe at an early enough time to consider its fluctuations still small, or, in other words, to be still described by linear theory. Such initial distribution is then evolved computing, at each step, the Newtonian force among the particles. The codes that implement this method, therefore, work in the Newtonian framework and do not include any relativistic feature. This can represent a problem when setting the initial conditions for the CDM particle distribution, since linear theory solutions are often provided by codes that solve the Einstein-Boltzmann equation, for CDM and baryons, in a given gauge in GR.

The standard procedure for running particle-based simulations, at least for ΛCDM cosmologies, consists in the following five steps:

1. Choose a target linear power spectrum, commonly at redshift $z = 0$
2. Compute the linear Newtonian growth factor $D(z = z_{\text{initial}})$
3. Scale the target power spectrum back in time $P_{\text{initial}}(k) = D^2(z_{\text{initial}})P_{\text{target}}(k)$
4. Use the initial power spectrum to draw initial displacements and velocities of particles
5. Start the actual simulation, which evolves the initial particle distribution down to the target redshift computing the intra-particle force with the method of choice.

Being the growth factor Newtonian, the rescaling procedure is consistent with the dynamics of the simulation itself, and the so-obtained initial power spectrum $P_{\text{initial}}(k)$ is constructed to converge (at linear level, i.e. on large scales) to the target power spectrum, once it has been evolved by the simulation. We can therefore expect such rescaled initial power spectrum to differ from the power spectrum computed by a Boltzmann code at the same redshift.

2.1 Rescaling in the presence of massive neutrinos

The problem when adding massive neutrinos is how to compute the Newtonian growth factor to perform the rescaling. The scale independent ΛCDM growth factor cannot be used in this case, as it would miss the characteristic scale dependence induced by the presence of neutrinos.

To avoid this issue a possible solution (Viel et al., 2010; Bird et al., 2012; Villaescusa-Navarro et al., 2013; Ali-Haïmoud and Bird, 2013; Rossi et al., 2014) is to directly use the output power spectrum of a Boltzmann code at redshift $z = z_{\text{initial}}$ to compute displacements and velocities of the particles at the initial redshift. However, while including the correct scale dependence induced by neutrinos, this method introduces three possible systematic errors in the simulations:

1. The initial power spectrum of the simulation is in a given GR gauge (usually the synchronous gauge), but, when evolved by the Newtonian simulation, the final power spectrum departs from the $z = 0$ power spectrum computed by a Boltzmann code in the same gauge;
2. The neutrino-induced power suppression in the initial power spectrum is computed by the Boltzmann code by integrating the neutrino distribution function; typical N-body simulation codes, instead, assume all particles to be non-relativistic, including neutrinos; therefore, when evolved with a Newtonian code, the neutrino scale dependence, correct at the initial redshift, does not reproduce the one computed with a Boltzmann code at lower redshifts;

3. Massive neutrinos modify the expansion rate of the universe, as shown in Eq. 1.89; typically in N-body codes, as neutrinos are considered non-relativistic at all times, the Hubble function is computed consequently; anyway there is usually the possibility to provide a tabulated custom Hubble function, where the effects of neutrinos can be included.

Such considerations led me and my working group to quantify the systematic effects introduced in simulation of cosmologies with massive neutrinos by many common approximations assumed when setting initial conditions and, at the same time, to devise a possible workaround. This work has been published in Zennaro et al. (2017).

The key idea of the method proposed in this paper is to employ a two-fluid formalism to describe the joint evolution of CDM and neutrino density perturbations in a Newtonian framework. This allows us to compute the Newtonian, scale-dependent growth factor and growth rate that can be used to scale a $z = 0$ power spectrum back in time consistently with the simulation dynamics, without losing information about the neutrino scale dependence.

2.2 Implementation of the fluid approximation

In order to solve the system of fluid equations needed to obtain the required Newtonian growth rates and growth factors, I have implemented a Runge-Kutta solver. The code, named `reps` (**re**scaled **p**ower **s**pectra for initial conditions in cosmologies with massive neutrinos), is publicly available from `https://www.github.matteozennaro/reps`. It works with a parameter file (examples are provided) that allows the user to choose the cosmological parameters, the initial redshift, and the intermediate redshifts at which outputs are requested. The boundary conditions needed for the solutions of the differential equations can be directly provided by the user or computed automatically, letting `reps` call an external build of either `camb` or `class`.

Even if for most purposes just two fluids are enough to set initial conditions for simulations (namely CDM+baryons and neutrinos), `reps` solves a 3-fluid system, keeping CDM and baryons as separate, pressureless fluids. This approximations, that cannot capture the details of the baryon small-scale physics, is still useful to disentangle, at first order, the different amplitudes of baryons and CDM at relatively small redshift.

Therefore, the system of equations solved by `reps` reads, at each fixed time,

$$\begin{cases} D_b'(k) &= -\Theta_b(k) \\ \Theta_b'(k) &= A\ \Theta_b(k) - B\ [\mathfrak{f}_\nu D_\nu(k) + (1-\mathfrak{f}_\nu) D_{cb}(k)] \\ D_c'(k) &= -\Theta_c(k) \\ \Theta_c'(k) &= A\ \Theta_c(k) - B\ [\mathfrak{f}_\nu D_\nu(k) + (1-\mathfrak{f}_\nu) D_{cb}(k)] \\ D_\nu'(k) &= -\Theta_\nu(k) \\ \Theta_\nu'(k) &= A\ \Theta_\nu(k) - B\ \left[\left(\mathfrak{f}_\nu - \frac{k^2}{k_{\rm FS}^2}\right) D_\nu(k) + (1-\mathfrak{f}_\nu) D_{cb}(k)\right] \ . \end{cases} \tag{2.1}$$

Primed quantities are derived with respect to the scale factor $a(t)$. The convention adopted here is that $D_i(k, z)$ represents the growth factor for the i-th species, and $\Theta_i(k, z)$ is linked to the growth rate of the same species via

$$f_i(k, z) = -\frac{\Theta_i(k, z)}{D_i(k, z)}. \tag{2.2}$$

I have also introduced, for simplicity of writing, the functions $A(z)$ and $B(z)$, which only depend on time. The first one comes from the derivative of the Hubble function,

$$\begin{aligned} A(z) &= 1 - 2\left(\frac{\mathrm{d}H/\mathrm{d}t}{H}\right)^2 \\ &= \frac{1}{2}\left\{\Omega_{cb}(z) + 2\Omega_r(z)\left[1 + 3w_X(z)\right]\Omega_X(z) + \left[1 + 3w_\nu(z)\right]\Omega_\nu(z) - 2\right\}. \end{aligned} \tag{2.3}$$

The second function comes from the Poisson equation and accounts for the background potential sourcing gravity. In a Newtonian framework, only non-relativistic matter contributes to gravity. For this reason, in the function $B(z)$ we must only include the density fractions of cold matter and the non-relativistic fraction of neutrinos. As a consequence, using Eq. 1.92, we can write

$$B(z) = \frac{3}{2}\Omega_m^{\mathrm{nr}}(z) = \frac{3}{2}\left\{\Omega_{cb}(z) + \left[1 - 3w_\nu(z)\right]\Omega_\nu(z)\right\}. \tag{2.4}$$

The solution is performed using the Fehlberg-Runge-Kutta method of fourth order, with Dormand-Prince coefficients. This means that given a generic Cauchy's problem

$$\begin{cases} \dfrac{\mathrm{d}y}{\mathrm{d}x} = F(x, y) \\ y(x_0) = y_0, \end{cases} \tag{2.5}$$

the solutions at each subsequent time step $x_{n+1} = x_n + h$ is obtained by evaluating the slope of the function in four middle points,

$$\begin{aligned} K_1 &= F(x_n, y_n)\, h \\ K_2 &= F(x_n + \frac{h}{2}, y_n + \frac{K_1}{2})\, h \\ K_3 &= F(x_n + \frac{h}{2}, y_n + \frac{K_2}{2})\, h \\ K_4 &= F(x_n + h, y_n + K_3)\, h, \end{aligned} \tag{2.6}$$

and the new evaluation of the function is given by

$$y_{n+1} = y_n + \frac{K_1 + 2K_2 + 2K_3 + K_4}{6}. \tag{2.7}$$

Finally, we need to provide the boundary conditions. For a two-fluid problem (which will be the one of interest in rest of this chapter), these are given in terms of the initial values for the growth rate of the cold matter component,

$$f_{cb}(a) \equiv \frac{\mathrm{d}\ln D_{cb}(a)}{\mathrm{d}\ln a} \tag{2.8}$$

and of neutrinos

$$f_\nu(a) \equiv \frac{\mathrm{d}\ln D_\nu(a)}{\mathrm{d}\ln a} \tag{2.9}$$

along with the ratio between neutrino and cold matter perturbations

$$\beta(a) \equiv \frac{D_\nu(a)}{D_{cb}(a)}. \tag{2.10}$$

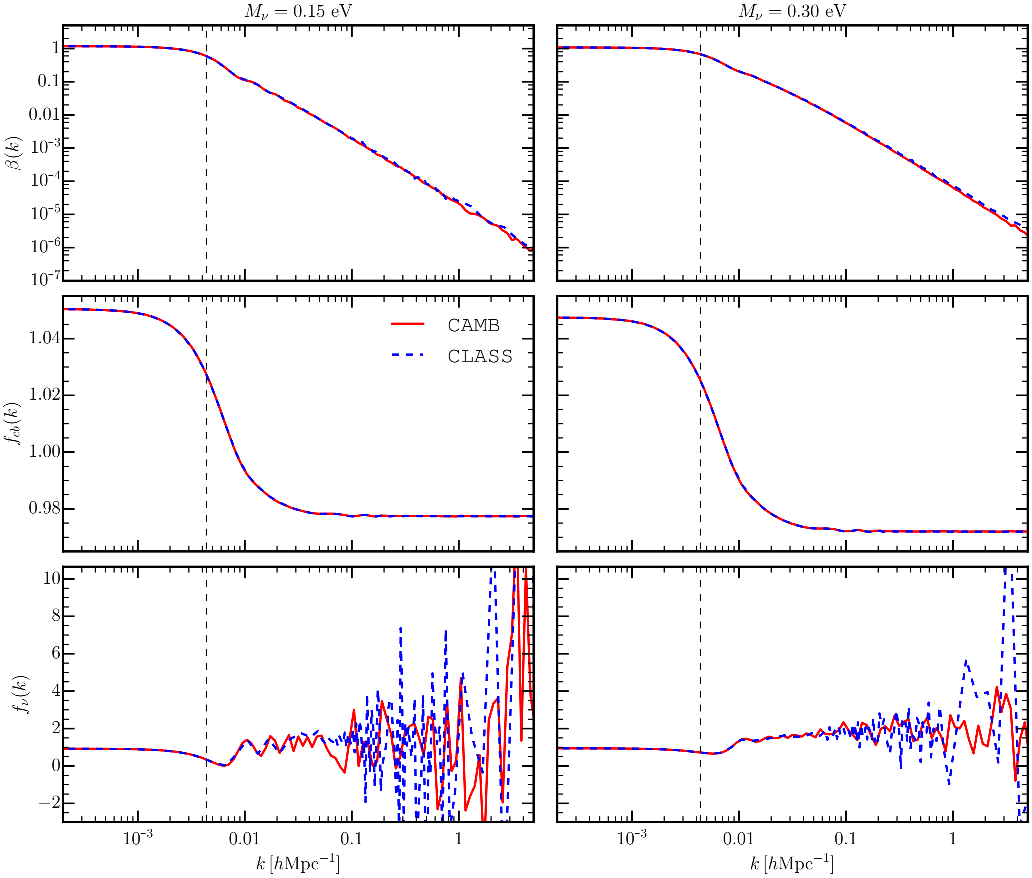

Figure 2.1: The boundary conditions needed for solving the fluid, newtonian equations in the presence of neutrinos. The two columns correspond to $M_\nu[\mathrm{eV}] = \{0.15, 0.30\}$, while the rows show the neutrino to cold matter ratio, $\beta = D_\nu/D_{cb}$, the cold matter growth rate, f_{cb}, and the neutrino growth rate, f_ν. Different colors/line styles correspond to the results obtained with `camb` (solid red lines) and `class` (dashed blue lines). The vertical black dashed line marks the scale of the horizon at $z = 99$.

We find four independent solutions that we linearly combine by imposing the conditions

$$\begin{aligned} &\text{at } z = 0 \quad && (1 - \mathfrak{f}_\nu)\, D_{cb} + \mathfrak{f}_\nu\, D_\nu \equiv D_m \equiv 1, \\ &\text{at } z = z_i \quad && \begin{cases} \beta D_{cb} - D_\nu = & 0, \\ \Theta_{cb} + f_{cb} D_{cb} = & 0, \\ \Theta_\nu + f_\nu D_\nu = & 0, \end{cases} \end{aligned} \tag{2.11}$$

where we have set the amplitude of the total matter growth factor at $z = 0$ equal to unity, since we will be interested in rescaling the power spectrum at that redshift. Fig. 2.1 shows an example of the required boundary conditions, generated both with `camb` and `class`.

The boundary conditions for the three-fluid case are the growth rates of baryons, cold dark matter and neutrinos, along with the baryon to cold dark matter and neutrino to cold dark matter ratios at the initial redshift, combined in the vary same way as in the two-fluid case.

2.3 Validation against Boltzmann codes

The first thing needed to proceed with the rescaling method is to make sure that the fluid description is adequate enough to describe the growth of matter perturbations in linear regime. To this end I will present some comparisons between the solutions obtained adopting the two-fluid formalism and the ones obtained by two well known public Boltzmann solvers, `camb` (Lewis et al., 2000) and `class` (Lesgourgues, 2011a). As the two codes present some inherent differences, and are parameterised in slightly different ways, in figure 2.2 I check that the settings I am adopting for `camb` and `class` really do correspond to the same cosmology. This is confirmed by the fact that the ratios between power spectra for different species and at different redshifts are always compatible with the comparisons presented in Lesgourgues (2011b) and Lesgourgues and Tram (2011). In particular, The two codes agree on the CDM and total matter power spectra at 10^{-4} level at almost all scales in the ΛCDM case, and their agreement is better than $\sim 0.2\%$ for $k < 1\ h\,\mathrm{Mpc}^{-1}$ when massive neutrinos are included.

In Fig.s 2.3-2.4 I am showing the comparison between the power spectra obtained with the fluid approximation with `camb` and `class` respectively. The rescaled power spectra are normalized to match the total matter power spectrum computed by the Boltzmann code at redshift $z = 0$.

Overall the fluid approximation is able to recover the Boltzmann solutions, in both cases, at 10^{-4} level. Some discrepancies, however, appear:

1. On very large scales the effect of having employed a Newtonian approximation appears. In particular, on near-horizon and over-horizon scales, the Boltzmann codes correctly include the effects of radiation perturbations in the chosen gauge (in this setting, the synchronous gauge), while the fluid approximation does not. This mismatch amounts to $\sim 10\%$ on very large scales at $z = 99$, maximal because of my choice of normalizing the spectra zt $z = 0$.

2. On intermediate scales, within the horizon but for $k \lesssim 10\ h\,\mathrm{Mpc}^{-1}$, the fluid approximation agrees with Boltzmann solutions at $0.01 - 0.02\%$ level.

3. On very small scales, $k \geq 10\ h\,\mathrm{Mpc}^{-1}$, the two-fluid approximation breaks down. The level of discrepancy increases as the considered scale increases. This is due to

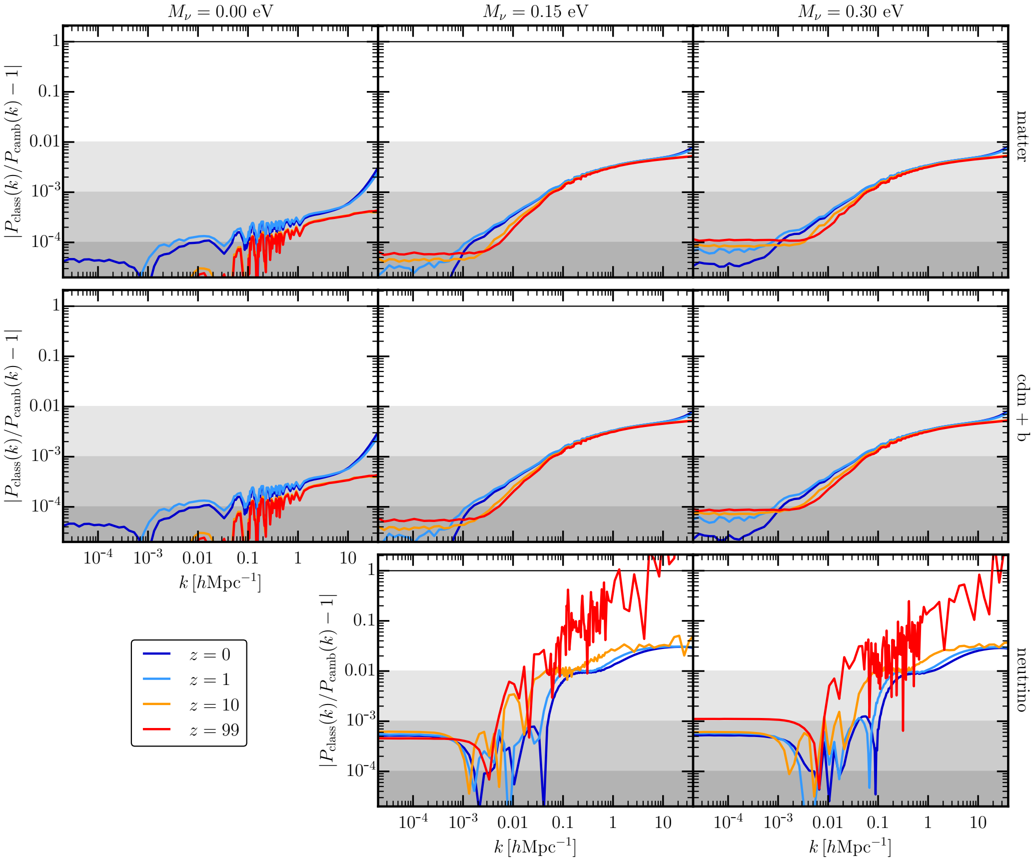

Figure 2.2: Comparison between power spectra obtained with `camb` and `class`. Columns correspond to cosmologies with three choices of total neutrino mass $M_\nu[\text{eV}] = \{0, 0.15, 0.30\}$, while rows correspond to the total matter, cold matter and neutrino power spectrum respectively. For total matter and cold matter the agreement between the two codes is compatible with what presented in the comparison paper. For neutrinos, it is below $\sim 0.2\%$ for $k < 1\ h\ \text{Mpc}^{-1}$.

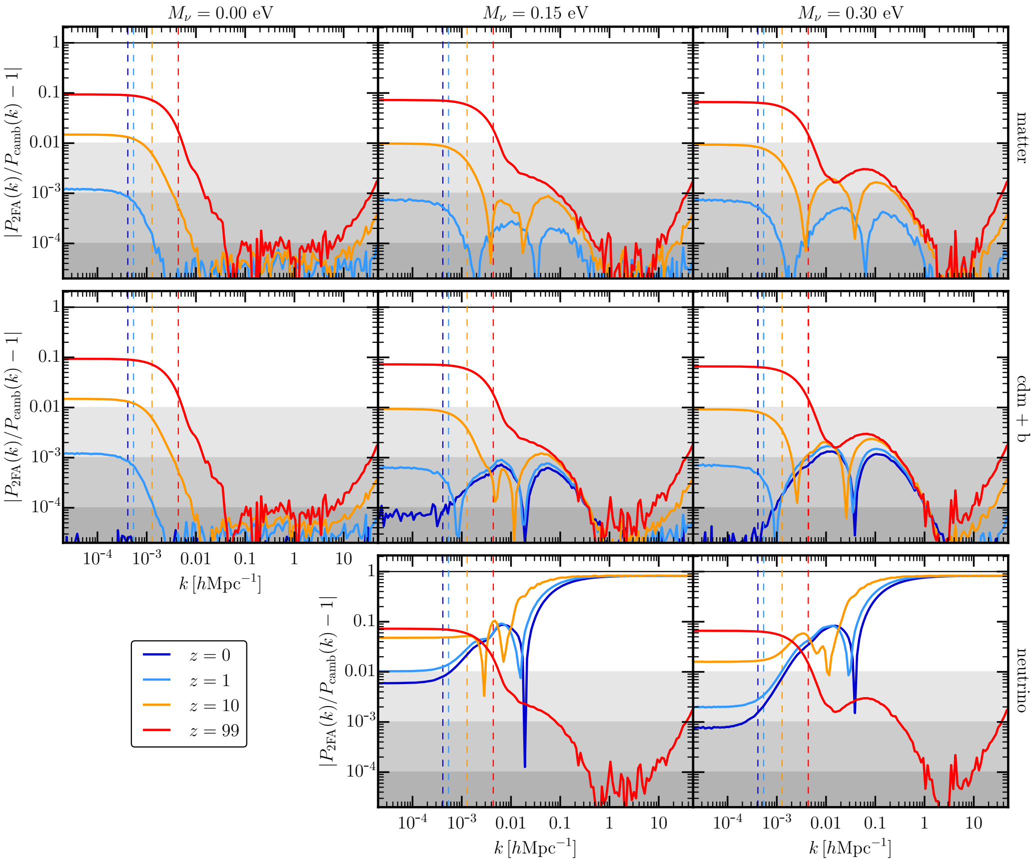

Figure 2.3: Validation of the fluid approximation against the solutions provided by the `camb` code.

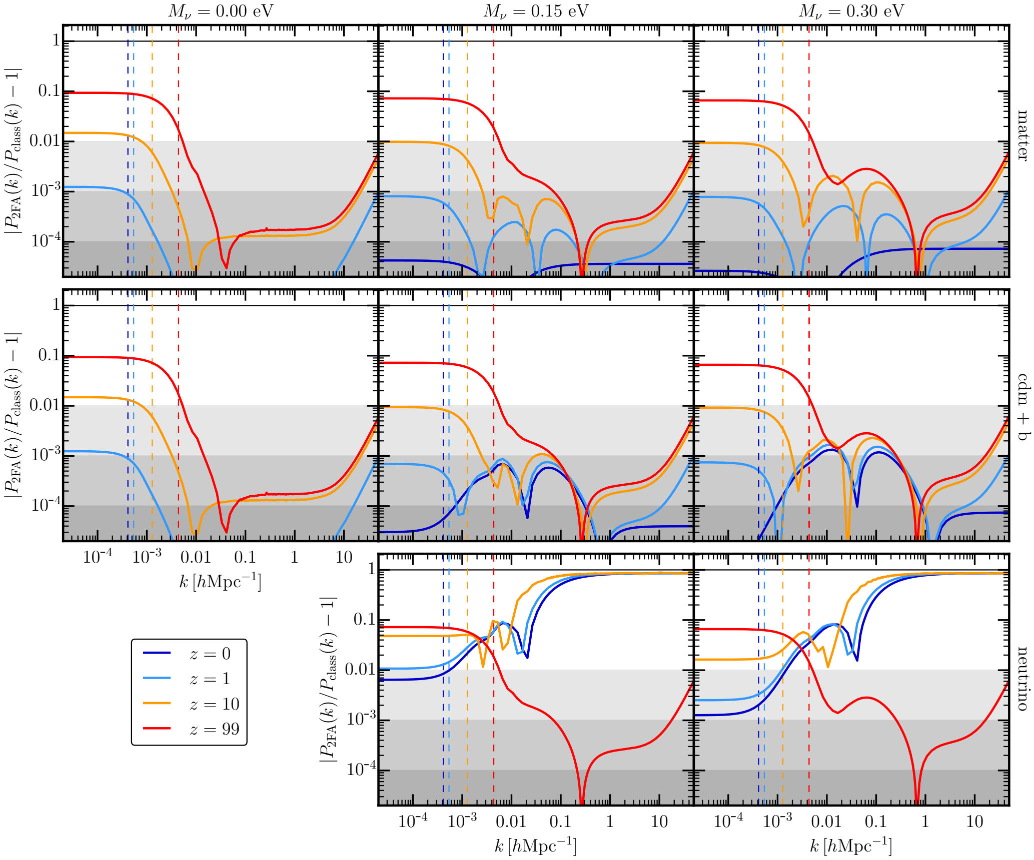

Figure 2.4: Validation of the fluid approximation against the solutions provided by the `class` code.

Scenario	Ω_γ	Ω_ν^r	$f = \mathrm{d}\ln D/\mathrm{d}\ln a$	$B(a)$
S1: No photons, f constant	0	0	$\Omega_m^{0.55} \simeq 1$	correct
S2: No photons + $f(k)$	0	0	correct	correct
S3a: f constant, $f = \Omega_m^{0.55}$	correct	correct	$\Omega_m^{0.55}$	correct
S3b: f constant, asymptotic value	correct	correct	asymptotic	correct
S4: Constant mass neutrino particles	correct	correct	correct	$\Omega_m = (\Omega_{cb,0} + \Omega_{\nu,0})a^{-3}$
S5: No relativistic neutrinos	correct	0	correct	$\Omega_m = (\Omega_{cb,0} + \Omega_{\nu,0})a^{-3}$

Table 2.1: Different scenarios of the considered, possible approximations in the initial conditions and in the Hubble expansion. $B(a)$ is the source term of the gravitational potential in the Newtonian approximation defined in Eq. 2.4. When it is correct, Ω_m includes only the actual non-relativistic fraction of neutrinos; otherwise, *all* neutrino perturbations are considered as non-relativistic (irrespective of possible relativistic tails) and always act as sources of gravity.

the term accounting for the neutrino effective sound speed, which is proportional to the wavenumber k, hence becoming more relevant on small scales. However, the fluid approximation is still reliable up to $k \sim 50\ h\ \mathrm{Mpc}^{-1}$, being the relative difference still below $0.1 - 0.2\%$.

An important point is that the agreement found for the cold and total matter components between the fluid approximation and the Boltzmann codes, is not confirmed for the neutrino component. In particular, at $k \sim 0.1\ h\ \mathrm{Mpc}^{-1}$ the neutrino power spectrum differs from both `camb` and `class` by $\sim 100\%$. In fact the agreement with the neutrino power spectrum largely depends on the version and on the choice of precision parameters of the Boltzmann codes. Yet, this is not of great importance as no observable or relevant quantity is exclusively dependent on the neutrino perturbations, that only provide, for instance, sub-percent corrections to the total matter power spectrum. Moreover, the solution at the initial redshift (which is the one used for setting the initial conditions for simulations) is always correct and shares the same level of accuracy as the CDM component, since discrepancies arise only in the the evolution of the initial power spectrum and grow with time.

2.4 Potential systematic errors from initial conditions

The two-fluid approach allows for investigating the effect of some common approximations adopted in the setting of initial conditions. The different choices of setup for the initial conditions can in fact be evolved to low redshift solving the set of differential equations presented in the previous sections. Being in the Newtonian framework, they mimic the evolution of a N-body simulations, but at the linear level.

Table 2.1 summarizes the different scenarios I will consider. Some of them refer only to cosmologies with a non-zero neutrino mass. Others, however, are more general and also apply to standard ΛCDM cosmologies.

The reference growth factor and growth rates are computed in the optimal setup, which does not include any approximation apart from those unavoidable in a Newtonian, fluid description.

I obtain the growth factor and growth rate of each species, normalized to match the reference power spectra at redshift $z = 99$. In this way departures from the reference solution appear in the $z = 0$ evolved power spectrum. Results are therefore given in term of the ratios

$$\frac{D^2_{cb}(k,z=0)}{D^2_{cb,\,\mathrm{ref}}(k,z=0)}\,, \quad \frac{D^2_{\nu}(k,z=0)}{D^2_{\nu,\,\mathrm{ref}}(k,z=0)}\,, \tag{2.12}$$

while the total matter growth factor $D_m(k,z)$ is obtained as

$$D_m(k,z) = (1-\mathfrak{f}_\nu)\,D_{cb}(k,z) + \mathfrak{f}_\nu\,D_\nu(k,z)\,. \tag{2.13}$$

for both the reference and approximated solutions.

More in detail, the considered scenarios are presented in the following. Each of them is shown in Fig. 2.5.

S1: no radiation and constant, initial growth rates

In the first scenario I neglect the radiation contribution to the Hubble expansion setting

$$\Omega_{\gamma,0} = 0, \tag{2.14}$$

in Eq. 1.89 and we impose the constant values for the growth rate

$$f_{cb} = f_\nu = \Omega_m^{0.55}(z_i) \simeq 1 \tag{2.15}$$

in the initial conditions, Eq. 2.11, at $z_i = 99$. The combination of these two assumptions is due to the second being a consequence of the first, for ΛCDM cosmologies, since $\Omega_m(z_i) \simeq 1$ when no radiation is present. In massive neutrino cosmologies this is not strictly true because of the scale-dependence of the growth rate and it therefore represents a further approximation for these models.

In general a larger density of relativistic species leads to a smaller growth of matter fluctuations. For this reason we expect a higher amplitude of the power spectrum when we neglect the contribution of radiation to the background. This indeed is what we see in Fig. 2.5 for S1, where the amplitude of the power spectrum at all scales that were within the horizon at z_i, is larger than the reference case at $z = 0$ by $3-4\%$. Moreover, since we are neglecting the scale-dependence of the growth rate in the initial conditions, we see that the error induced presents, in turn, a peculiar scale-dependence at large but still observable scales.

S2: no radiation

In the second scenario we consider the case of using the correct growth rate even when there is no radiation in the background; to this purpose, we compute the Hubble function setting

$$\Omega_{\gamma,0} = 0, \tag{2.16}$$

in Eq. 1.89. The growth rates are computed as numerical derivatives of the power spectrum at the initial redshift (*i.e.* numerically solving Eq.s (2.8-2.9) on each scale). In this case the resulting error is clearly scale-independent but still corresponds to more than 2% on the low redshift ΛCDM matter power spectrum, reduced to around 1.5% in the massive neutrino case, due to the different effective number of relativistic neutrinos contributing to radiation.

S3: constant growth rate, f

The third scenario is, in a sense, the opposite of the previous one, as we consider the effect of using the correct background evolution (with radiation and with the proper contribution of relativistic neutrinos, as in Eq. 1.89) keeping the growth rate fixed (*i.e.* scale independent). In one case, that we call S3a, the constant value of the growth rate is given by the approximation

$$f_{cb} = f_{\nu} = \Omega_m^{0.55}(z_i)\,, \quad \mathrm{scale-independent.} \tag{2.17}$$

which is valid in a ΛCDM cosmology with no radiation in the background (though we do have radiation in the background). Here the approximation has actually three implications: *(i)* the scale independence does not account for relativistic effects on large scales, such as the contribution of radiation perturbations, *(ii)* the scale independence does not account for the suppression induced by neutrinos at small scales, *(iii)* this approximate value is valid only with no radiation in the background. The main discrepancy from the correct low redshift power spectrum appears at near-horizon scales, which are affected by about $5-6\%$. On the contrary, for scales within the horizon this approximation results in a discrepancy of $\sim 0.3\%$ in the ΛCDM case, but becomes more pronounced, *and relevant*, being above the percent level, in presence of massive neutrinos.

It is possible, of course, to consider a similar scenario in which the growth rates are again scale-independent, but they assume the correct asymptotic value of the cold matter growth rate within the horizon. To do so we numerically compute the growth rate as in Eq. 2.8, considering only the asymptotic value towards small scales (therefore, well within the horizon). We note that for the ΛCDM case, this procedure corresponds to the approximation $f \simeq \Omega_m^{0.667}$. In this case, that we name S3b, in the evolved $z=0$ power spectrum, only scales above horizon show a discrepancy with respect to the Boltzmann solution (of the same amplitude as in S3a), while scales within the horizon agree at 0.01% level. The slight difference between case S3a and S3b for scales above horizon in the massive neutrino cosmologies is due to the residual systematic error induced by the fact that the asymptotic value for neutrinos ignores their scale dependence.

S4: constant mass neutrino particles

This approximation, as the following one, is specific to massive neutrinos models. In fact, at redshifts as high as $z_i \simeq 100$, there is still a significant tail of relativistic neutrinos that does not contribute to the gravitational potential. Particle-based N-body simulations, however, assume massive neutrinos to be non-relativistic (*i.e.* matter) at all redshifts $z \leq z_i$. Avoiding this approximation would require to allow the mass of neutrino particles to vary in time. To the best of our knowledge, however, no code in the literature considered this possibility.

To reproduce this scenario, therefore, we modify the function $B(a)$ defined in Eq. 2.4, which is the source of gravity in the Newtonian approximation,

$$B(a) = -\frac{3}{2}\Omega_m(a), \tag{2.18}$$

using

$$\Omega_m(a) = (\Omega_{cb,0} + \Omega_{\nu,0})\, a^{-3} \tag{2.19}$$

instead of 1.98. This means that in computing neutrino overdensities all neutrinos are treated as non-relativistic particles. On the other hand, we do not modify the Hubble rate

$H(a)$ and the function $A(a)$ (which only depends on the Hubble rate and its first derivative), defined in Eq. 1.89 and 2.3 respectively, in order to fully account for relativistic neutrinos in the background.

This approximation results in a negligible error on the power spectrum of the CDM component at low redshift. The effect is larger on the neutrino component, and therefore on the total matter power spectrum. Nonetheless, as neutrinos weight considerably less that CDM, even on the total matter power spectrum the effect is sub-percent.

S5: no relativistic neutrinos

Finally we consider *all* effects of neglecting the relativistic neutrino fraction, that is both on the perturbations (Poisson equation) as on the Hubble expansion, treating neutrinos as a non-relativistic species *also* in the background, as usually done in the literature. To do so, we extend the approximations described in S4 to the computation of the Hubble rate and of the function $A(a)$ (Eq. 2.3). This means that in this case we always use

$$\Omega_\nu(a) = \Omega_{\nu,0}\, a^{-3} \tag{2.20}$$

and

$$w_\nu(a) = 0. \tag{2.21}$$

The resulting error is only slightly larger than the one of S4, however, our solution is affected by numerical instabilities in the neutrino sector of the coupled differential equations.

From this exercise we conclude that, on the scales that at $z = z_i$ were within the horizon, the greater impact ($> 1\%$) comes from neglecting the scale dependence in the initial growth rate of the cold matter perturbations and neglecting the radiation contribution to the Hubble function. We should notice, in addition, that their combined effect can sum up to an appreciable level, even when individual errors are sub-percent.

2.5 Initial conditions for accurate N-body simulations

2.5.1 Method

Considering the effects of all the possible approximations from the previous section, I propose a method to set-up initial conditions for N-body simulations that include massive neutrinos employing a rescaling technique that minimizes systematic deviations from predictions at low redshift. In particular, solving the fluid equations employing the same dynamics and limitations unavoidable in N-body simulations (Newtonian framework, fixed mass neutrino particles…), while at the same time matching the rescaled power spectra to the desired $z = 0$ linear prediction, provides us with the initial redshift spectra to be used to compute initial displacements and velocities.

The power spectrum of cold matter at the initial redshift of the simulation can be written as

$$P_{cb}(k, z_i) = \frac{D^2_{cb,2FA}(k, z_i)}{D^2_{cb,2FA}(k, 0)} P^B_{cb}(k, 0), \tag{2.22}$$

where the superscript B refers to the power spectrum obtained with a Boltzmann code.

Such initial power spectra differ from the solutions of a Boltzmann code, as they scaled back in time using different physics. However, when they are evolved in the simulation, they converge to the expected low redshift power spectra, directly computed with a Boltzmann code.

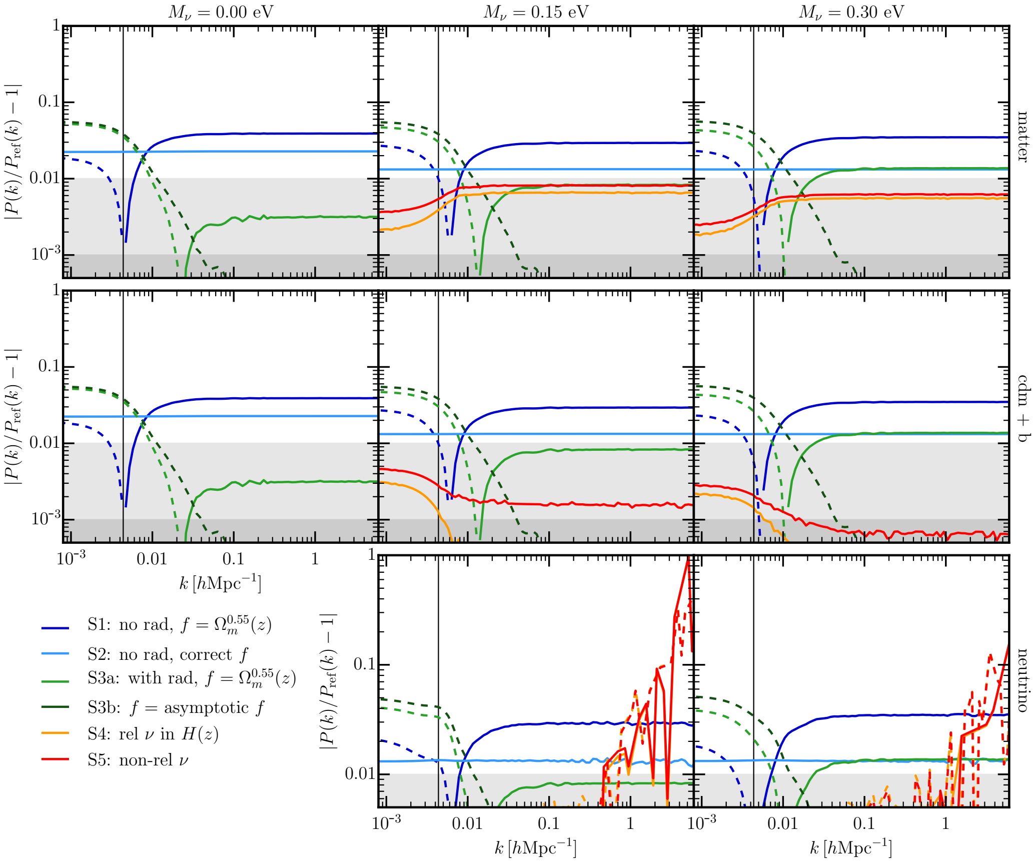

Figure 2.5: The impact of five common approximations assumed in simulations on the linear power spectrum at $z = 0$ with respect to a reference power spectrum. The vertical gray line marks the scale of the horizon at $z_i = 99$. The reference power spectrum is the one computed with the two-fluid approximation, with no further approximation (*i.e.* it is the power spectrum shown in figure 2.3, that agrees with the output of the Boltzmann codes apart from the fact of being in Newtonian limit). *Blue lines* show the effect of neglecting photons in the background in combination with using the ΛCDM approximated growth rate $f = \Omega_m^{0.55} \simeq 1$ (scenario S1). *Light blue lines* show the impact on the low redshift power spectrum of neglecting photons but using the correct, scale dependent growth rate (scenario S2). Note that, in the left panel, besides photons, we do not take into account massless (hence relativistic) neutrinos. If we do the contrary and we include photons in the background but use the ΛCDM parametrization for the growth rate (scenario S3a) we obtain the *light green lines*, while a scenario with scale-independent growth rates where the value is the correct one within the horizon is shown as scenario S3b (dark green lines). *Orange lines* show the impact of including the relativistic fraction of neutrinos in the background, but not in the computation of the peculiar gravitational potential, an unavoidable approximation in particle-based simulations where neutrinos are implemented as particles with constant mass (S4). Finally, *red lines* refer to S5, where we treat neutrinos as a completely non-relativistic specie.

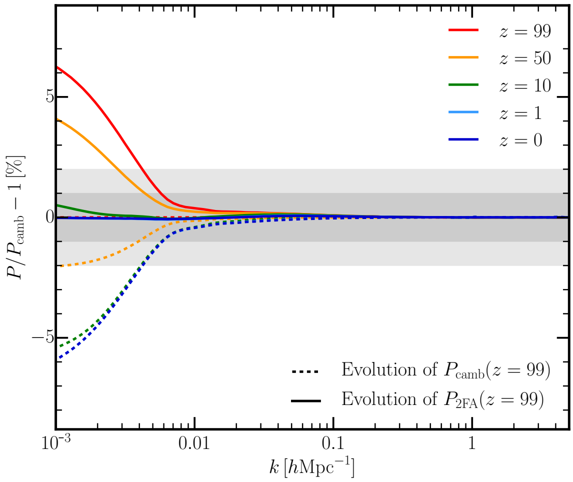

Figure 2.6: The evolution of two different initial linear power spectra at $z = 99$: one is directly taken from `camb`, the other one is obtained with the proposed method, *i.e.* the $z = 0$ power spectrum from `camb` has been rescaled to the initial redshift with the two-fluid approximation. The two spectra are then evolved forward using the two-fluid approximation, thus mimicking the linear (Newtonian) evolution in a simulation. In the first case, dashed lines, by construction at high redshift the evolved power spectrum coincides with that from the Boltzmann code, but differs from it at low redshift (reaching a lack of power $> 5\%$ at large scales at $z = 0$). On the other hand, our rescaling (solid lines) introduces a discrepancy at high redshift and large scales (due to the fact that in our Newtonian approximation all photon perturbations are inevitably neglected), but allows us to recover a sub-percent agreement with the linear power spectrum from a Boltzmann code at lower redshifts ($z < 10$).

Fig. 2.6 shows the difference between setting the initial conditions directly with a Boltzmann code or with the rescaling procedure. In this case I show results obtained using `camb`, with a total neutrino mass $M_\nu = 0.15$ eV, but the same holds for `class`.

In the first case (dashed lines in the plot) the power spectrum at initial redshift by construction corresponds with the Boltzmann code predictions. However, as redshift increases, the evolved power spectrum departs from the prediction, reaching a $\sim 6\%$ lack of power on large scales. This is due to the combination of the Newtonian nature of the evolution, and the non-relativistic approximation adopted for neutrino particles, in accordance to most N-body codes.

On the other hand, in the second case, the power spectrum at the initial redshift shows the expected mismatch from the Boltzmann code solution. However, as the spectrum is evolved in the Newtonian framework, it converges to the Boltzmann power spectrum, with sub-percent accuracy for $z < 10$.

It is important to note that this procedure introduces a scale dependent correction on large scales and high redshift. This spurious, albeit motivated, excess of power can in principle interfere with the nonlinear growth of structures, since it blends together the contributions of different modes. However, nonlinearities become important at low redshifts and small scales, and therefore we expect the rescaling technique not to modify the fully nonlinear growth, since for $z < 10$ the effects of the rescaling have completely decayed.

To show that this method allows us to recover the correct nonlinear power, I tested the method with N-body simulation.

2.5.2 Tests with simulations

I have analysed a set of N-body simulations produced by F. Villaescusa-Navarro, both with and without massive neutrinos. I provided the initial conditions set using the rescaling procedure presented above, testing, for the neutrino case, both the scenario S4 (rescaling for a simulation with Hubble function that does not include the relativistic evolution of the neutrino density) and S5 (rescaling for a simulation that employs the correct Hubble function, for example reading it from a table).

The simulations have been run using the TreePM code GADGET-III (Springel, 2005). The size of the periodic simulation box in all our simulations is set to 2 $h^{-1}\mathrm{Gpc}$. We have run simulations for three different cosmological models: a massless neutrino cosmology and two models with massive neutrinos corresponding to $M_\nu = 0.15$ eV and $M_\nu = 0.3$ eV. The relatively large values of M_ν are justified by the purpose to test our method. All simulations share the value of the following cosmological parameters: $\Omega_m = \Omega_{cb} + \Omega_\nu = 0.3175$, $\Omega_b = 0.049$, $\Omega_\Lambda = 0.6825$, $h = 0.6711$, $n_s = 0.9624$ and $A_s = 2.13 \times 10^{-9}$. In the models with massive neutrinos we set $\Omega_c = \Omega_m - \Omega_\nu$, where $\Omega_\nu = M_\nu/(93.14\,\mathrm{eV}\,h^2)$. We notice that, since all models have the same normalization of the amplitude of the linear power spectrum at the epoch of the CMB, the value of σ_8 will be different in each model: $\sigma_8 = 0.834,\ 0.801,\ 0.760$ for the models with $M_\nu = 0.0,\ 0.15,\ 0.30$ eV, respectively.

We follow the evolution of 768^3 CDM particles, plus 768^3 neutrino particles in the models with massive neutrinos, from $z = 99$ down to $z = 0$. In order to carry out convergence tests, we have also run a second set of simulations with 512^3 CDM and neutrino particles. The gravitational softening length is set to $1/40$ of the mean interparticle distance, both for CDM and neutrino particles.

Initial conditions are generated at $z = 99$ by displacing and assigning peculiar velocities to particles, that initially are located on a regular grid, using the Zel'dovich approximation. For neutrino particles we also add a thermal velocity component. The am-

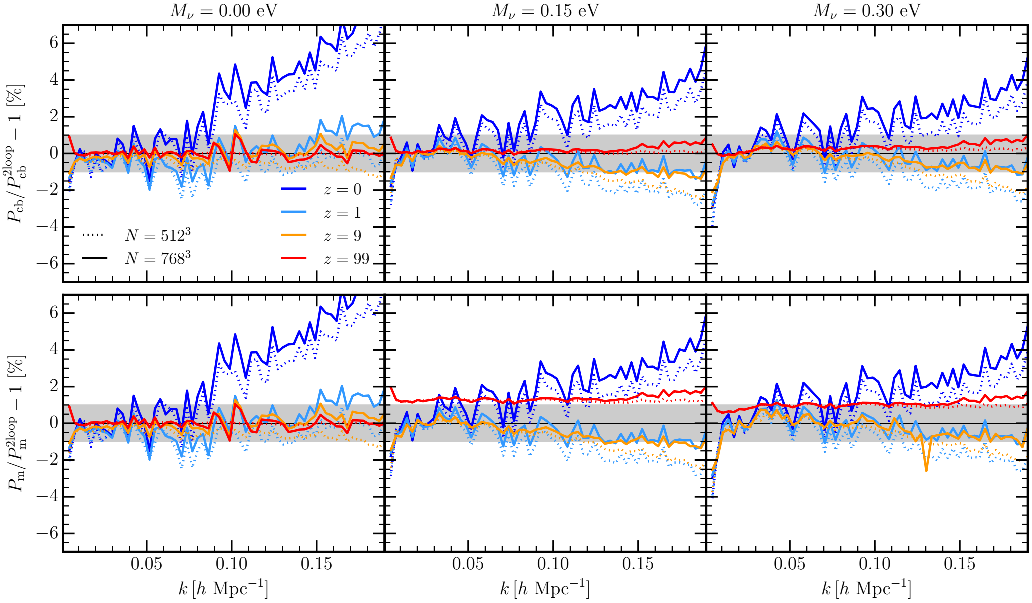

Figure 2.7: Ratio of the power spectra measured in the simulations to nonlinear predictions for ΛCDM (left panels) and massive neutrinos, $M_\nu = 0.15$ eV (middle panels) and $M_\nu = 0.3$ eV (right panels). Nonlinear predictions are computed from the linear outputs of `camb`, applying 2-loop corrections computed with the code `RegPT` for the CDM+baryon component only. The top panels show the power spectra of the cold dark matter component, while the bottom ones show the total matter power spectra. Colours from blue to red correspond to different redshifts, namely $z = 0, 1, 9, 99$. Solid lines refer to the simulations with $N = 2 \times 768^3$ particles, while dotted lines to the simulation with $N = 512^3$ particles.

plitude of the thermal velocities is determined by randomly sampling the Fermi-Dirac distribution of the corresponding model while the direction is taken randomly within the sphere. Thermal velocities dominate neutrino dynamics during the first time-steps, having a dispersion roughly five orders of magnitude larger than the dispersion of peculiar neutrino velocities. Instead of sampling the modes amplitude in Fourier-space using a Rayleigh distribution (as in a Gaussian distribution), we collapse the distribution to its mean value. It can be shown that a simulation run with the initial conditions generated in that way will have the correct 2-point statistics with a lower variance (Angulo and Pontzen, 2016).

The displacements and peculiar velocities are computed taking into account the scale-dependent growth factor and growth rate using the procedure described in the previous section. We have modified the N-GENIC code to achieve this. In the simulations with massive neutrinos we have generated the initial conditions for the scenarios S4 and S5 (see table **??**). The simulations have been run using a tabulated Hubble function, that is different for each model and scenario, that controls the time evolution of the background in the simulations.

I show in Fig. 2.7 the relative error between the power spectra of total matter, $P_m(k)$, and cold matter, $P_{cb}(k)$, measured in the simulations and their corresponding nonlinear predictions, for $M_\nu = \{0, 0.15, 0.30\}$ eV.

Nonlinear predictions have been obtained feeding the `camb` power spectra to the code REGPT (Taruya et al., 2012), implementing the multipoint propagator expansion of

Bernardeau et al. (2008). In particular, the prediction is computed at the 2-loop level. Following Castorina et al. (2015), nonlinear corrections in the presence of massive neutrinos are applied only to the cold matter component, as the neutrino auto power spectrum and the cold-neutrino cross power spectrum are well described with linear theory at all redshifts.

The spectra obtained from the simulations show a 1% agreement with predictions at all redshifts but $z = 0$ for the more resolved case ($N = 768^3$ particles, solid curves in the figure). Regarding the $z = 0$ power spectrum, 2-loop regularized perturbation theory, such as the one employed here, is known to underestimate the nonlinear power spectrum (Taruya et al., 2012). An interesting feature is that, in the cases with massive neutrinos, perturbation theory is more able to reproduce the nonlinear low-redshift spectrum. This is a consequence of the neutrinos smoothing the gravitational potential, hence producing a more linear growth of structures.

Regarding the effect of the choice of resolution, Fig. 2.7 shows that, as expected, a lower mass resolution results in less accurate estimations of the power spectra. In this case, at redshifts higher than 0, the agreement between measures and prediction is at $\sim 2\%$ level. Moreover, the presence of massive neutrinos seems to worsen the resolution effect. For example, there is a residual resolution effect on mildly nonlinear scales in the case with nonzero neutrino mass, that dos not cancel out even in the most resolved case presented here. However, the trend passing from $N = 512^3$ to $N = 768^3$ particles is clearly of alleviating this problem. Moreover, for higher resolution simulations (like those in Castorina et al., 2015; Carbone et al., 2016), this discrepancy disappears.

The main point of this figure is that the excess of power introduced in the initial conditions at $z = 99$ completely corrects the large scale effects due to the Newtonian nature of the simulation, and allows for recovering, for neutrino N-body simulations, the same level of accuracy as in a standard ΛCDM simulation.

This results hold both for the simulations set-up within scenario S4 and S5. The two scenarios differ at large scales, the second beeing closer to the Boltzmann code power spectrum, as neutrinos enter the Hubble function with no approximation. In this case, at the initial redshift, the discrepancy from `camb` amounts to 0.05% at $k \sim 0.1\,h\,\mathrm{Mpc}^{-1}$. At the same scale, the S4 scenario results in a mismatch of $\sim 2\%$. However, whatever the choice of the scenario for the rescaling, once the spectra are evolved in a consistent way, they both converge to the expected power spectrum. As a matter of fact, the difference between the spectra in the simulation started with S4 and S5 at $z = 0$ is less than 0.05% for both neutrino masses.

On last remark regards the total matter power spectrum measured in the simulations with massive neutrinos. From figure 2.7 it seems not to agree, at high redshift, with the theoretical prediction, while on the same scale P_{cb} has sub-percent agreement. Moreover, such discrepancy disappears moving to lower redshifts. This apparent discrepancy is present because the simulation treats neutrinos as completely non-relativistic particles, while the prediction accounts for their relativistic tail. The total matter power spectrum can be written as

$$P_m(z) = [1 - \mathfrak{f}_\nu(z)]^2 P_{cb}(z) + 2\mathfrak{f}_\nu(z)[1 - \mathfrak{f}_\nu(z)] P_{cb,\nu}(z) + \mathfrak{f}_\nu^2(z) P_\nu(z) \tag{2.23}$$

where $\mathfrak{f}_\nu$ is the neutrino fraction. The simulation uses as a neutrino fraction

$$\mathfrak{f}_\nu = \frac{\Omega_{cb,0}(1+z)^3}{\Omega_{\nu,0}(1+z)^3} = \frac{\Omega_{cb,0}}{\Omega_{\nu,0}}, \tag{2.24}$$

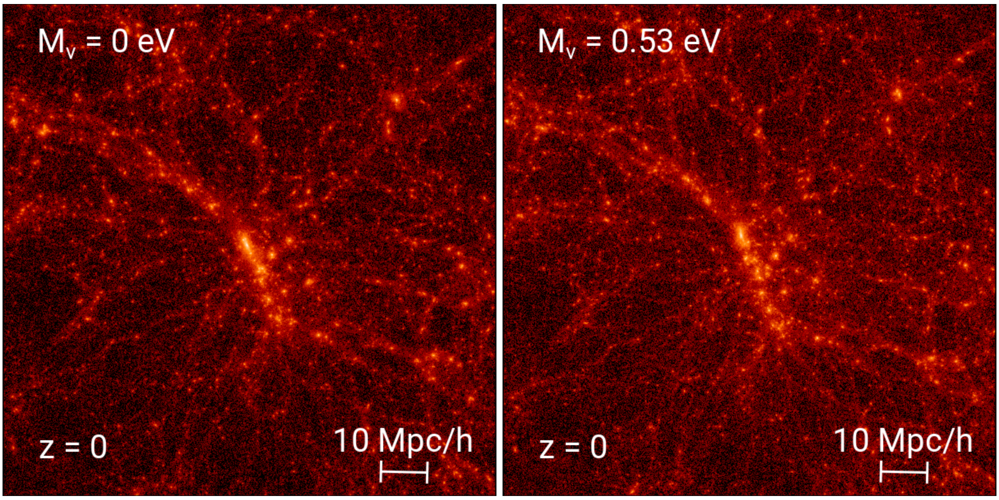

Figure 2.8: The largest halo in the first set of the DEMNUni simulations, on the left in the realization without massive neutrinos and on the right in the case with $M_\nu = 0.53$ eV. The image shows a cube centered in the center of mass of the halo and with side $100\ h^{-1}$ Mpc. Even by eye, the neutrinoless case appears more clustered and nonlinear, while the case with massive neutrinos shows a smoother matter distribution. This picture has been produced with `SPLASH` (Price, 2007).

while the prediction is computed using the redshift dependent

$$\mathfrak{f}_\nu(z) = \frac{\Omega_{cb}(z)}{\Omega_\nu(z)}, \tag{2.25}$$

where $\Omega_\nu(z)$ is computed solving Eq. 1.88. Combining the measurements of the different components using the latter definition of $\mathfrak{f}_\nu$ makes this mismatch completely disappear. However, I present measurements as they are, since the former definition of the neutrino fraction is consistent with the physics implemented in the simulation.

2.6 Application to the DEMNUni simulations

The Dark Energy and Massive Neutrino simulations (DEMNUni, Castorina et al., 2015; Carbone et al., 2016) are a set of large N-body simulations that explore different choices of neutrino total mass and of dynamical dark energy parameters w_0 and w_a, where the equation of state of dark energy is always $w = w_0 + (1-a)\, w_a$. They have been produced by Carmelita Carbone at the CINECA supercomputing facility.

The first set of 4 simulations is mainly focused on the effects of massive neutrinos, exploring the range $M_\nu = \{0, 0.17, 0.3, 0.53\}$ eV. Each simulation has a box size of $2000\ h^{-1}$ Mpc and contains 2048^3 cold matter particles and, if present, 2048^3 neutrino particles. The softening length is set at $20\ h^{-1}$ kpc, and the mass of the cold matter particle is around $8.27 \times 10^{10}\ h^{-1}\ \mathrm{M}_\odot$. As an example of the insight on the neutrino effects that these simulations provide, in figure 2.8 I show the same dark matter halo at $z = 0$ in the realization with $M_\nu = 0$ eV and $M_\nu = 0.53$ eV. Already by eye, the case with nonzero neutrino mass shows a smoother distribution of dark matter, whereas the ΛCDM case shows a more clustered and nonlinear structure.

The second set of simulations is more focused on the interplay between neutrinos and dynamical dark energy. In this case, 10 simulations explore the possible combinations of

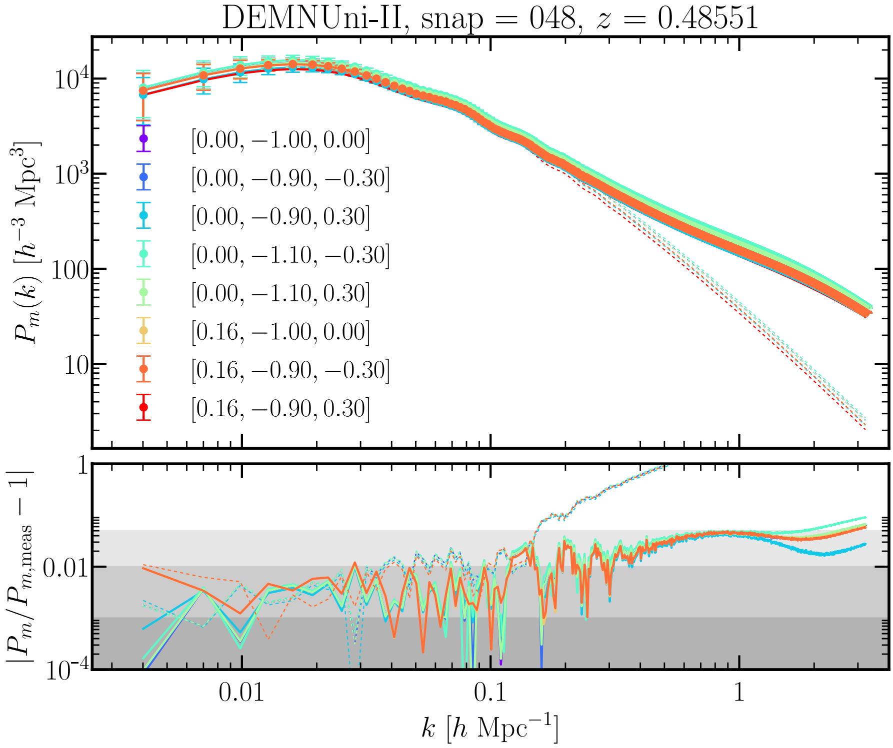

Figure 2.9: The matter power spectrum at $z \simeq 0.5$ measured in the DEMNUni simulations and compared to linear predictions from `camb` and nonlinear predictions obtained with `halofit`. Different colors correspond to different combinations of $[M_\nu, w_0, w_a]$. In the bottom panel, solid lines are ratios with respect to the nonlinear prediction while dotted lines refer to the linear theory.

$M_\nu = \{0, 0.16\}$ eV, $w_0 = \{-1.1, -1, -0.9\}$ and $w_a = \{0, \pm 0.3\}$. The simulation box side, number of particles, softening and mass resolution are the same as in the previous set.

For this second set of simulations, I have produced the rescaled power spectra employing the technique described in the present chapter. As a result, this is the first large set of simulations including massive neutrinos that can be directly compared to theoretical predictions computed by a Boltzmann code, with sub-percent accuracy.

As an example, I report in Fig. 2.9 the matter power spectrum measured at $z \simeq 0.5$ in the different cosmologies of the second set of DEMNUni simulation, and in Fig. 2.10 the mass function of spherical overdensities (defined with respect to δ_{200}, the overdensity 200 times denser than the mean) and of FoF haloes, fitted with the models of Tinker et al. (2008) and Crocce et al. (2010) respectively.

As these spectra and mass function show, some of these combinations of cosmological parameters can mimic a ΛCDM universe, despite being, in terms of parameters, quite far from that. Hence the importance of accurate simulations to address possible degeneracies and study combinations of cosmological probes that are capable of breaking them.

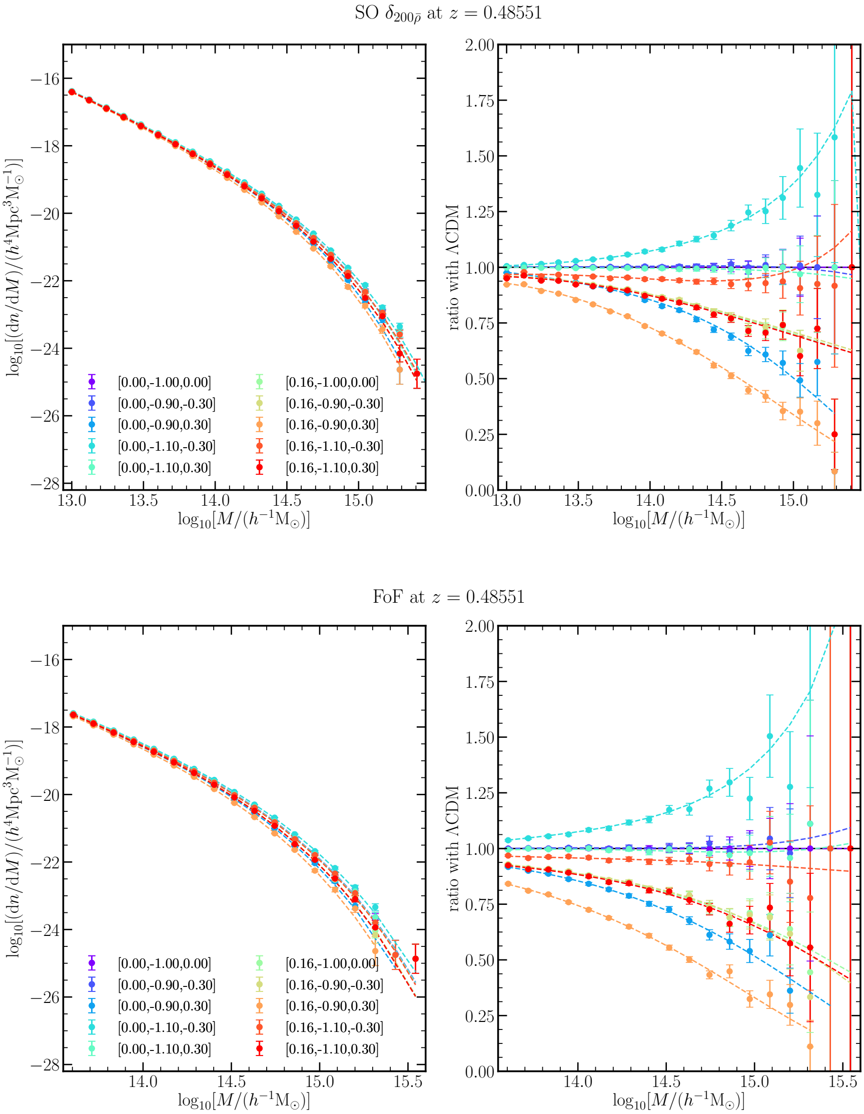

Figure 2.10: The mass function, at $z \simeq 0.5$, of spherical overdensities (defined by a contrast 200 times denser than the average) and of FoF haloes, in the upper and lower panels respectively. While plots on the left show the actual mass function, plots on the right show ratio taken respect the ΛCDM case. The model fitted to the SOs is the one by Tinker et al. (2008), while FoF groups are fitted following Crocce et al. (2010).

CHAPTER 3

The galaxy clustering ratio

In Chapter 1 we have seen that it is possible to predict many statistical properties (the variance, two-point correlation function and/or power spectrum, and also higher order statistics) of the matter field. However it cannot be *directly* observed. In fact, we must rely on the observation of galaxies and clusters of galaxies, which form in the densest peaks of the matter overdensity field and, as a consequence, represent a biased sampling of the underlying matter distribution.

One of the challenges of present-day Cosmology is, therefore, to connect the predictions of the clustering properties of matter to the measured galaxy clustering. This task is made even more difficult to accomplish since, on small scales, the biasing function might be extremely complicated to predict, being modified by nonlinearities of the matter field, nonlinearities of the galaxy formation processes and stochasticity of the sampling.

One possible approach to tackle such a problem is to try to parametrize the bias and fit it to observations. In this case, it can be considered as a nuisance parameter that is eventually marginalized over. On the other hand, one can search for cosmological observables which are blind to such small scale complications. The latter option, which is the main topic of the present chapter, complements, without substituting, the other approach. In fact, the next chapter, 4, will present some work on the modelling of the nonlinear galaxy bias.

A possible approach to describe the biasing function is the one proposed by Fry and Gaztanaga (1993). It consists in considering that the matter overdensity δ can be mapped into the galaxy overdensity δ_g with a local, deterministic function F, such that

$$\delta_g(\boldsymbol{x},t) = F(\delta(\boldsymbol{x},t)) \; . \tag{3.1}$$

Assuming that the function F is smooth enough, it can be Taylor expanded as

$$\delta_g(\boldsymbol{x},t) = \sum_{i=0}^{\infty} \frac{b_i}{i!}\, \delta^i(\boldsymbol{x},t), \tag{3.2}$$

where the b_i coefficients are called bias parameters of order i. The zeroth-order term guaranties that, whatever the order we choose to stop the expansion, the mean of the galaxy density contrast is zero, thus

$$\delta_g(\boldsymbol{x},t) \simeq \sum_{i=0}^{N} \frac{b_i}{i!}\, \delta^i(\boldsymbol{x},t), \quad \text{with} \quad b_0 = -\sum_{i=2}^{N} \frac{b_i}{i!}\, \left\langle \delta^i \right\rangle . \tag{3.3}$$

Although recent studies have shown that this is not the most accurate approach, it nevertheless offers a good description of the bias (Bel and Marinoni, 2014). For a more comprhensive review on bias see, e.g., Desjacques et al. (2016).

3.1 Definitions

In this section I will always consider the *smoothed density field*. As a matter of fact, we want to link the matter overdensities $\delta(\boldsymbol{x})$ to the overdensities in the discrete galaxy distribution $\delta_g(\boldsymbol{x})$. While the former can be obtained as a theoretical prediction, it is not possible to measure the latter. A more feasible approach is to measure, instead of the overdensity in a point, the overdensity in a sphere.

Assuming there is a mean density $\bar{N}$ of galaxies (or, for this matter, any structure) in the universe, then the overdensity of galaxies in a sphere of radius R is given by

$$\delta_{g,R}(\boldsymbol{x},t) = \frac{N_{g,R}(\boldsymbol{x},t)}{\bar{N}_{g,R}(t)} - 1, \tag{3.4}$$

where $N_{g,R}(\boldsymbol{x},t)$ is the number of galaxies in a sphere centred in $\boldsymbol{x}$ and of radius R, and $\bar{N}_{g,R} = \bar{N}_g\ 4\pi R^3/3$ is the mean number of galaxies in a sphere of radius R.

At this point, also for the matter field we must define a smoothed overdensity, which corresponds to applying a top-hat filtering to the matter overdensity field. It can be written as

$$\delta_R(\boldsymbol{x}) = \int \delta(\boldsymbol{x})\, W\left(\frac{|\boldsymbol{x}-\boldsymbol{x}'|}{R}\right) \mathrm{d}^3x', \tag{3.5}$$

where

$$W\left(\frac{r}{R}\right) = \frac{1}{\frac{4}{3}\pi G R^3} \begin{cases} 1 & r \le R \\ 0 & \text{otherwise}\ . \end{cases} \tag{3.6}$$

Thinking the matter overdensity field as a superposition of waves, this corresponds to a low-pass filter that selects only the waves with wavelength smaller than the size of the sphere. On the other hand, since we collapse all the information of the sphere in one point, when looking at the smoothed overdensity field we expect to have lost all the information coming from scales smaller than the size fo the spheres. As a consequence, fixing a smoothing scale corresponds to fixing the minimum scale from which we can extract information.

In Fourier space the top-hat window function becomes a modulation,

$$\hat{W}(k,R) = \frac{3[\sin(kR) - kR\ \cos(kR)]}{(kR)^3} = \frac{3}{kR} j_1(kR), \tag{3.7}$$

j_1 being the first order Bessel function.

In the framework of the hierarchical growth of fluctuations, in which smaller perturbations sum up to create larger ones, each higher order statistics can be expressed in terms of combinations of lower order ones. The cumulant

$$\langle \delta_R^n \rangle_c = S_n\ \sigma_R^{2(n-1)} \tag{3.8}$$

and

$$\left\langle \delta_{i,R}^n \delta_{j,R}^m \right\rangle_c = C_{nm}\ \xi_R(r)\ \sigma_R^{2(n+m-2)} \tag{3.9}$$

In general, one can predict the variance and 2-point correlation function of the smoothed overdensity field as given by

$$\sigma_R^2 = 4\pi \int_0^\infty k^2 \mathrm{d}k\ P(k)\ \hat{W}^2(kR)\ , \tag{3.10}$$

$$\xi_R(r) = 4\pi \int_0^\infty k^2 \mathrm{d}k\, P(k)\, \hat{W}^2(kR)\, j_0(kr), \tag{3.11}$$

where $j_0(x) = \sin x/x$ is the zeroth order Bessel function.

Bel and Marinoni (2014) defined the clustering ratio as the ratio between the correlation function and the variance of the smoothed field,

$$\eta_R(r) \equiv \frac{\xi_R(r)}{\sigma_R^2}\ . \tag{3.12}$$

In the remaining part of this section I will review some of the main features of the clustering ratio, which have been already studied in detail, in ΛCDM cosmologies, in the paper cited above.

Defining a quantity as a ratio has several advantages regarding the bias. When the filtering scale is large enough, one can truncate the bias expansion at leading order. In this case, the galaxy power correlation functions can be linked to the matter correlation function through

$$\xi_{g,R}(r) = b_1^2 \xi_R(r), \tag{3.13}$$

while the variance follows

$$\sigma_{g,R}^2 = b_1^2 \sigma_R^2. \tag{3.14}$$

As a consequence, the galaxy clustering ratio smoothed on this scale ends up being an unbiased quantity,

$$\eta_{g,R}(r) \equiv \eta_R(r), \tag{3.15}$$

the clustering ratio of galaxies being exactly the same as the one predicted for matter.

Relaxing the linear assumption, but still employing the local deterministic bias model, using the hierarchic relations that connect higher order statistics to variances and correlation functions presented in Eq.s 3.8-3.9, one can obtain, at second order,

$$\eta_{g,R}(r) \sim \eta_R(r) - \left\{ (S_{3,R} - C_{12,R}) c_2 + \frac{1}{2} c_2^2 \right\} \xi_R(r) + \frac{1}{2} c_2^2\, \eta_R(r)\, \xi_R(r), \tag{3.16}$$

where $c_2 \equiv b_2/b_1$ and $S_{3,R}$ and $C_{12,R}$ come from the hierarchic relations. Expression 3.16 can be employed to asses the contribution of higher order corrections. With a large enough smoothing scale R, the second order terms are suppressed and the clustering ratio is unbiased. In addition, note that possible non-local contributions would only modify c_2 in the above expression (Bel et al., 2015).

The evolution in time of the clustering ratio is given by the combined evolution of the correlation function and of the variance. In general, they are very simple to compute in linear theory, but become more tricky when nonlinearities are considered.

In linear theory, the growth of an overdensity is simply parametrized using its growth factor $D(z)$ (see Eq. 1.50). The evolution of the linear matter power spectrum can be written, as a consequence, as

$$P(k, z) = D^2(z)\, P(k, z = 0). \tag{3.17}$$

This allows us to write the variance and correlation function according to

$$\begin{aligned} \sigma_R^2(z) &= \sigma_8^2(z = 0)\, D^2(z)\, \mathcal{F}_R\ , \\ \xi_R(r) &= \sigma_8^2(z = 0)\, D^2(z)\, \mathcal{G}_R\ , \end{aligned} \tag{3.18}$$

where

$$\begin{aligned} \mathcal{F}_R &= \frac{\int_0^\infty k^2 \mathrm{d}k \; P(k) \hat{W}^2(kR)}{\int_0^\infty k^2 \mathrm{d}k \; P(k) \hat{W}^2(kr_8)} \,, \\ \mathcal{G}_R(r) &= \frac{\int_0^\infty k^2 \mathrm{d}k \; P(k) \hat{W}^2(kR) \, j_0(kr)}{\int_0^\infty k^2 \mathrm{d}k \; P(k) \hat{W}^2(kr_8)} \,. \end{aligned} \tag{3.19}$$

The clustering ratio can therefore be written as the ratio

$$\eta_R(r) = \frac{\mathcal{G}_R(r)}{\mathcal{F}_R}, \tag{3.20}$$

which does not depend on redshift.

However, the nonlinear evolution of the power spectrum introduces a slight dependence of the clustering ratio on redshift. In Fig. 3.1 I show that such evolution, albeit weak, is nevertheless detectable when the softening scale decreases. Nevertheless, it allows to easily compare the clustering properties at high and low redshift.

Finally, we must consider the observational effect introduced by the peculiar velocities of galaxies. In fact, galaxies not only move because they are dragged by the expansion of the space-time, but also posses peculiar motions due to the shape of the gravitational potential in which they are embedded. In particular we expect to see a bulk motion of galaxies, attracted towards the overdense regions of the universe. At the same time, in the high density, virialized regions, we expect galaxies to acquire thermal velocities, that can be even larger than their cosmological recession velocity. The former, known as the Kaiser effect (Kaiser, 1987), is well described in linear theory. The latter, instead, stems from the nonlinear growth of collapsing regions, and therefore is much harder to describe.

As a consequence of these two effects, when we measure the redshift of a galaxy, instead of observing its cosmological redshift, z_{cosmo}, we see the sum of z_{cosmo} and the apparent redshift due to the Doppler effect induced by the peculiar motion of the galaxy,

$$z_{\text{obs}} = z_{\text{cosmo}} + z_{\text{pec}}. \tag{3.21}$$

Using redshift measures to assign distances to galaxies, therefore, we displace such galaxies along the line of sight. This effect introduces distortions in the measured correlation function and power spectrum of galaxies, known as *redshift space distortions*. Due to redshift space distortions we cannot consider the observed 2-point statistics of galaxies to be isotropic.

Being the clustering ratio a smoothed observable, small scale modes are washed away. Therefore, by accurately choosing the smoothing radius R, one can neglect the nonlinear effect, and only take into consideration the Kaiser effect (Kaiser, 1987). In addition, when measuring the clustering ratio in redshift space I will always consider the average over all the angles, thus, in Eq. 3.20, I will replace the configuration space power spectrum with the monopole of the redshift space power spectrum in the Kaiser limit,

$$P_0^s(k) = \frac{1}{2} \int_{-1}^{+1} P^s(\boldsymbol{k}) \; \mathrm{d}\mu = \left[1 + \frac{2}{3} f + \frac{1}{5} f^2 \right] \; P^r(k), \tag{3.22}$$

where μ is the angle between the line of sight and the wavemode $\boldsymbol{k}$, f is the growth rate and $P^r(k)$ is the real space linear power spectrum. A desivation of this formula is

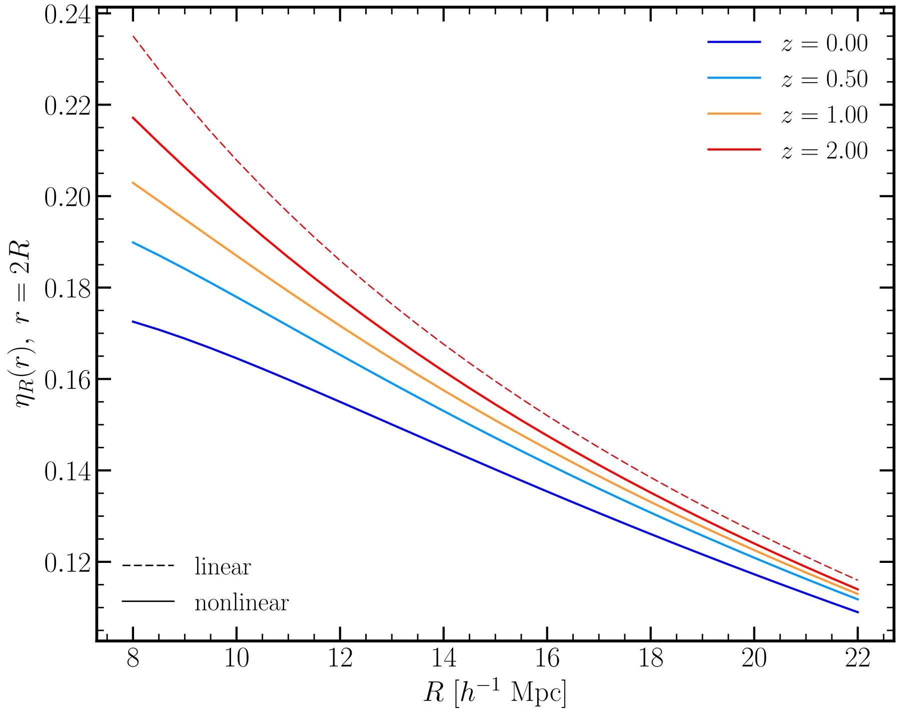

Figure 3.1: The evolution of the clustering ratio with redshift. The clustering ratio is plotted as a function of the smoothing scale R. Different colors correspond to different redshifts from $z = 0$ to 10. When computed in linear theory (dotted lines) the clustering ratio shows no redshift evolution, and all the curves lay on on top of the other. Adding nonlinearities (dashed lines) introduces a weak, but detectable, redshift dependence.

presented in appendix B. The clustering ratio in redshift space on linear scales therefore becomes

$$\eta^s_R(r) = \frac{\xi^s_R(r)}{\sigma^{2,s}_R} = \frac{\left[1+\frac{2}{3}f+\frac{1}{5}f^2\right]\xi_R(r)}{\left[1+\frac{2}{3}f+\frac{1}{5}f^2\right]\sigma^2_R} = \frac{\xi_R(r)}{\sigma^2_R} = \eta_R(r), \tag{3.23}$$

which is the same as in real space.

The clustering ratio, as shown by Bel and Marinoni (2012), can be estimated with a count-in-cell method. Assuming spherical cells, with mean number of objects per cell given by $\bar{N}$, then the discrete density contrast is

$$\delta_N = \frac{N_i}{\bar{N}} - 1, \tag{3.24}$$

where N_i is the number of objects in the i-th cell.

The estimator of the variance in this case is

$$\tilde{\sigma}^2_R = \frac{1}{p}\sum_{i=1}^{p}\delta_i^2 \tag{3.25}$$

and the one of the correlation function is

$$\tilde{\xi}_R(r) = \frac{1}{pq}\sum_{i=1}^{p}\sum_{j=1}^{q}\delta_i\delta_j\ , \tag{3.26}$$

where δ_i and δ_j are separated by a distance r. Thus, the estimator of the clustering ratio reads

$$\tilde{\eta}_R(r) = \frac{\tilde{\xi}_R(r)}{\tilde{\sigma}^2_R}. \tag{3.27}$$

Here we are dealing with discrete quantities, therefore we need to properly account for the shot noise. We imagine to be dealing with a continuous stochastic field $\lambda(\boldsymbol{x})$ that we want to smooth and discretize to reproduce our situation. The density of this field in a sphere of radius R centered in a point $\boldsymbol{x}$ is

$$\Lambda(\boldsymbol{x}) = \int_{V_{\rm sphere}} \lambda(\boldsymbol{x}')\mathrm{d}^3x', \tag{3.28}$$

while we call the mean density in a sphere $\bar{\Lambda}$. The density contrast of this smoothed field is

$$\delta(\boldsymbol{x}) = \frac{\Lambda(\boldsymbol{x})}{\bar{\Lambda}} - 1. \tag{3.29}$$

The discretization of this field can be modelled as a Poisson process with intensity function λ and intensity measure Λ. In this context Λ is the number of points expected in the bounded region of radius R. The factorial moments for a Poisson point process are given by

$$\left\langle \Lambda^k \right\rangle = \langle N(N-1)\dots(N-k+1)\rangle = \left\langle (N)^k_f \right\rangle \tag{3.30}$$

and for the two point statistics

$$\left\langle \Lambda^k(\boldsymbol{x}_1)\Lambda^q(\boldsymbol{x}_2)\right\rangle = \left\langle (N_1)^k_f (N_2)^q_f \right\rangle. \tag{3.31}$$

For the variance we have

$$\langle \delta(\boldsymbol{x})^2 \rangle = \frac{\langle \Lambda^2 \rangle}{\langle \Lambda \rangle^2} - 1 = \frac{\langle N(N-1) \rangle}{\langle N \rangle^2} = \frac{\langle N^2 \rangle}{\langle N \rangle^2} - \frac{1}{\langle N \rangle} - 1 = \frac{1}{p} \sum_{i=1}^{p} \delta_i - \frac{1}{\bar{N}}. \tag{3.32}$$

This is telling us that we need to correct the estimator of the variance to subtract the shot noise contribution, that is given by the inverse of the mean number of objects per spheres. Quite sensibly, a sparser sample gives rise to a larger shot noise, while a very dense sample results less affected.

On the other hand, for the 2-point statistics we have

$$\langle \delta(\boldsymbol{x}_1) \delta(\boldsymbol{x}_2) \rangle = \frac{\langle \Lambda^1(\boldsymbol{x}_1) \Lambda^1(\boldsymbol{x}_2) \rangle}{\langle \Lambda \rangle^2} - 1 = \frac{\langle N_1^1 N_2^1 \rangle}{\langle N \rangle^2} - 1 = \frac{1}{pq} \sum_{i=1}^{p} \sum_{j=1}^{q} \delta_i \delta_j, \tag{3.33}$$

hence we can conclude that the correlation function does not need a correction, as long as the spheres used to compute it do not overlap.

I implemented the count-in-cell method in a C code. The smoothed variance is computed filling the volume with spherical cells on a regular grid. The radius of each of these spheres is equal to the chosen smoothing radius. To compute the smoothed correlation function, I surround each cell on the grid (called seed) with a motif of 18 cells that are isotropically distributed around the seed, the distance of their centers from the center of the seed being equal to the chosen correlation length.The grid of seed cells is chosen to guarantee that all the cells in the motif fall within the considered volume.

3.2 Clustering ratio and neutrinos

In chapter 1.3 I have introduced the effects that massive neutrinos induce on the background evolution and on the growth of structures in the universe. In particular, one of the most notable consequences is the emergence of a characteristic scale dependence in the clustering properties of matter and galaxies, due to the neutrino free streaming. This implies that, comparing two cosmologies with same Ω_m and no other difference except from the presence of massive neutrinos, the clustering on large scale is the same, while on scales smaller than the free streaming scale, λ_{FS}, the clustering in the neutrino cosmology is suppressed compared to the standard case.

Such suppression of power is the key signature of the presence of massive neutrinos since, for the scales on which it takes place and the shape of the transition, it is in principle distinguishable from other possible scale dependencies, like the one induced by baryons on very small scales (see for example Mummery et al., 2017).

However, the presence of a scale dependence in the growth factor, could spoil the good properties of the clustering ratio, namely its very weak dependence on redshift, bias, redshift-space and distortions. For this reason I have employed the DEMNUni simulations (introduced in section 2.6) produced by Carmelita Carbone (Castorina et al., 2015; Carbone et al., 2016) to test the behaviour of the clustering ratio in the presence of neutrinos.

3.2.1 Bias

To test whether its independence from bias is kept by the clustering ratio also in cosmologies with massive neutrinos, I have first looked into the behaviour of the linear bias in the DEMNUni simulations. The linear bias can be obtained both from the smoothed

Bin	M_{min} $[10^{12} h^{-1}\ \mathrm{M}_{\odot}]$	M_{max} $[10^{12} h^{-1}\ \mathrm{M}_{\odot}]$
0	0.58	1.16
1	1.16	2.32
2	2.32	3.28
3	3.28	4.64
4	4.64	6.55
5	6.55	9.26
6	9.26	30
7	30	100
8	100	–

Table 3.1: Mass bins defined to compare the behaviour of the clustering ratio in different bias regimes, depending on the mass of the tracer.

correlation function and from the smoothed variance of the halo (friends-of-friends) distribution, namely

$$b_h = \sqrt{\frac{\xi_{R,h}(r)}{\xi_{R,\mathrm{theo}}(r)}} \tag{3.34}$$

and

$$b_h = \sqrt{\frac{\sigma^2_{R,h}(r)}{\sigma^2_{R,\mathrm{theo}}}}\ . \tag{3.35}$$

In order for the clustering ratio to be unbiased, they must coincide.

In principle this can depend on the considered choice of smoothing radius R, but also on the mass of the tracer. As a matter of fact, tracers of different mass evolve in different ways, thus giving rise to differences in the biasing function to be applied to the underlying matter field. To compare these cases and check which are the bias regimes in which the local, linear bias approximation breaks down, I have divided the DEMNUni halo catalogues according to the mass bins shown in table 3.1.

			bin 0	bin 1	bin 2	bin 3	bin 4	bin 5	bin 6	bin 7	bin 8
FoF	$z = 0.48551$	$M_\nu = 0.00$ eV	0	0	2902221	3509393	2402274	1708375	2878557	758008	145410
		$M_\nu = 0.17$ eV	0	0	3152025	3178910	2430866	1667315	2712374	690356	122241
		$M_\nu = 0.30$ eV	0	0	3116471	3269324	2263001	1642694	2589654	634844	104539
		$M_\nu = 0.53$ eV	0	0	3273517	3026718	2144285	1501769	2334332	532432	76127
	$z = 1.05352$	$M_\nu = 0.00$ eV	0	0	2571902	3039264	2003119	1358767	2044706	389064	38299
		$M_\nu = 0.17$ eV	0	0	2713196	2674546	1958721	1277479	1836860	328973	28852
		$M_\nu = 0.30$ eV	0	0	2620295	2674912	1767015	1218810	1679768	283298	22244
		$M_\nu = 0.53$ eV	0	0	2619539	2335248	1570202	1036782	1386909	206588	13059
SO	$z = 0.48551$	$M_\nu = 0.00$ eV	453415	2973241	2783664	2361431	1669494	1210036	2064503	527389	88178
		$M_\nu = 0.17$ eV	471602	2993986	2904400	2118437	1668026	1166042	1917029	470522	72097
		$M_\nu = 0.30$ eV	486007	2997527	2842491	2159522	1559049	1112575	1806821	424202	60046
		$M_\nu = 0.53$ eV	508713	3259563	2582711	1956593	1424500	1014066	1587591	343288	41497
	$z = 1.05352$	$M_\nu = 0.00$ eV	363148	2449897	2433901	2030689	1373779	952365	1446087	263959	22482
		$M_\nu = 0.17$ eV	359806	2376103	2479355	1766898	1330746	885172	1280841	218832	16462
		$M_\nu = 0.30$ eV	354938	2304946	2374992	1750620	1206312	819053	1157522	184575	12287
		$M_\nu = 0.53$ eV	341645	2359735	2069025	1500656	1039892	694588	932357	130319	6834

Table 3.2: Population of the 9 mass bins for he Friend-of-Friends (FoF) and spherical overdensities with respect to the critical density (SO) at redshift $z = 0.48551$ and $z = 1.05352$.

Table 3.2 shows how such mass bins are populated by haloes identified with the firends-of-friends algorithm and by spherical overdensities. For the friends-of-friends haloes, due to the minimum number of particles required to recognize a halo (in this case $N_{p,\min} = 32$), the first two mass bins are empty. However, for haloes identified as spherical overdensities, there is no such hard cut, the only limit being given by the mass resolution of the simulation. For this reason, spherical overdensities do populate also the first two mass bins.

Figures 3.2 ans 3.3 show the linear bias obtained from the correlation function and variance measured in simulations at redshift $z \simeq 0.5$ and $z \simeq 1$ respectively. Moreover they also show the measured clustering ratio compared to theoretical predictions. Each of these quantities is shown both for the standard ΛCDM case, and for the case with $M_\nu = 0.53$ eV, *i.e.* the most extreme case available.

The linear bias in these figures is obtained with respect to the nonlinear theoretical prediction from dark matter (`halofit`). This means that, in the massive neutrino case, I am using the prediction for cold dark matter + baryons, and not the one for total matter (see for example Castorina et al., 2015). The bias appears to be flat with respect to scale for all the mass bins to very good accuracy. The clustering ratio, at redshift $z \sim 0.84$ is very well described by the theoretical prediction, up to 3% accuracy on all scales, for the low-mass bins, while the two highest-mass bins are well described at 10% level. This in general is due to the fact that these mass bins represent extreme values of the linear bias. Moreover such bins are also affected by larger statistical errors, as they contain fewer objects.

Quite notably, the case with $M_\nu \neq 0$ shows an even higher concordance between measures and predictions, probably due to the more linear growth of structures in the presence of massive neutrinos.

Things are a little different at higher redshift. As a matter of fact, even if for the low-mass bins the concordance between measures and predictions is very high (better than at lower redshift, because of smaller and more regular nonlinearities), the two highest-mass bins are in complete disagreement with predictions. This is most likely due to lack of mass resolution in the simulations. As a matter of fact, moving back in time, we expect that not enough haloes of such masses have formed in the simulation. Moreover, in the massive neutrino case, we expect an even more sever lack of high-mass haloes at high redshift, which is confirmed also in Fig. 3.3.

To isolate the dependence of the clustering ratio on the mass of the considered tracer, in Fig. 3.4 and 3.5 I fix the smoothing scale to $R = 16\ h^{-1}\ \mathrm{Mpc}$ and the correlation length as $r = 2R = 32\ h^{-1}\ \mathrm{Mpc}$ and plot the clustering ratio in the different mass bins. In particular Fig. 3.4 uses the friends-of-friends haloes, while Fig. 3.5 uses spherical overdensities. Both figures once again shown that, as redshift increases, the high-mass bins not only exhibit larger statistical error (due to being sparsely populated) but also a significant systematic error.

3.2.2 Redshift-space distortions

To test the clustering ratio in redshift space, starting from the FoF and spherical overdensity catalogues in real space, I have constructed the redshift space catalogues. To do so I have chosen the z-direction as the line-of-sight direction, implicitly assuming a plane-parallel approximation, thus considering the whole box placed along the line of sight.

Employing this approximation, assuming the simulation box has cartesian coordinates (r_x, r_y, r_z), one only has to modify the r_z coordinate of the catalogue according to

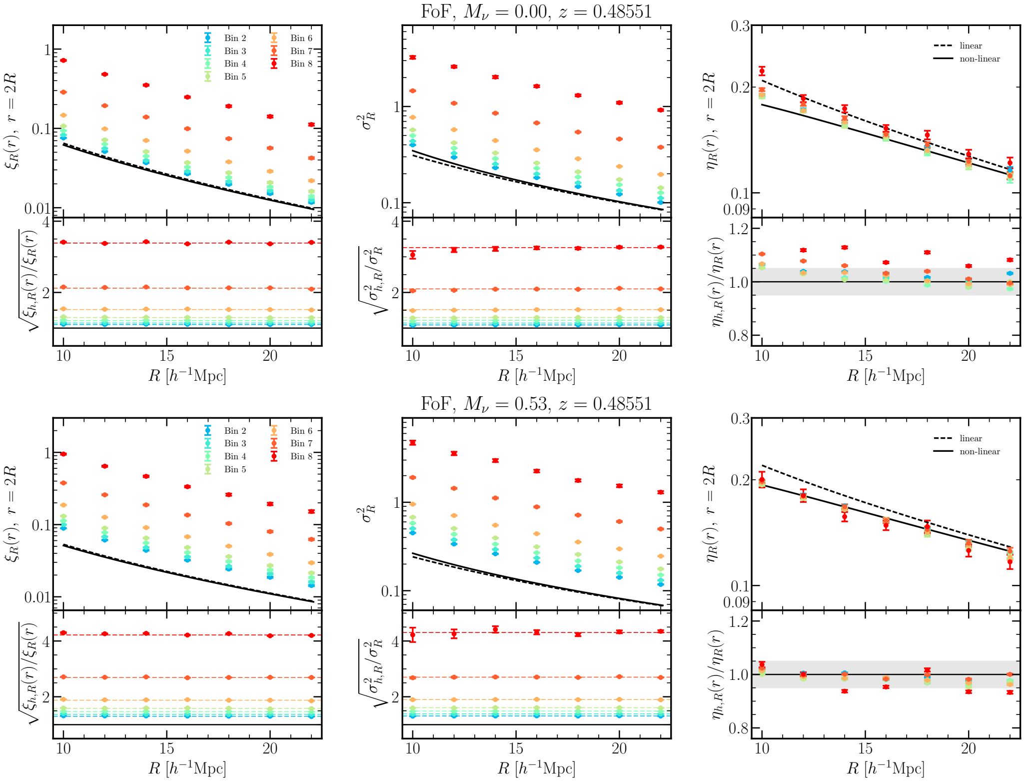
FoF, $M_\nu = 0.00$, $z = 0.48551$

FoF, $M_\nu = 0.53$, $z = 0.48551$

Figure 3.2: The linear bias as a function of the smoothing scale for the different mass bins defined in table 3.1, obtained using the correlations function (on the left) and the variance (central panel) of the haloes (friends of friends) in the DEMNuni simulations with $M_\nu = 0$ and 0.53 eV (above and below respectively) at redshift $z = 0.48551$. The panel on the right shows the clustering ratio. Both the bias from the correlation function and from the variance are flat to very good approximation (the flat lines shown are obtained fitting a straight line to the bias in the range $16 \le R/(h^{-1}\ \mathrm{Mpc}) \le 22$). Black lines are theoretical predictions in linear (dashed) and nonlinear (solid) theory. The bias is defined here wrt nonlinear theory. The clustering ratio agrees at 3% level with the predictions for the low-mass bins, while the high-mass bins agree on at 10% level. These is probably due to both the extreme bias of these objects and their sparsity, the former introducing a systematic effect and the latter a large statistical error.

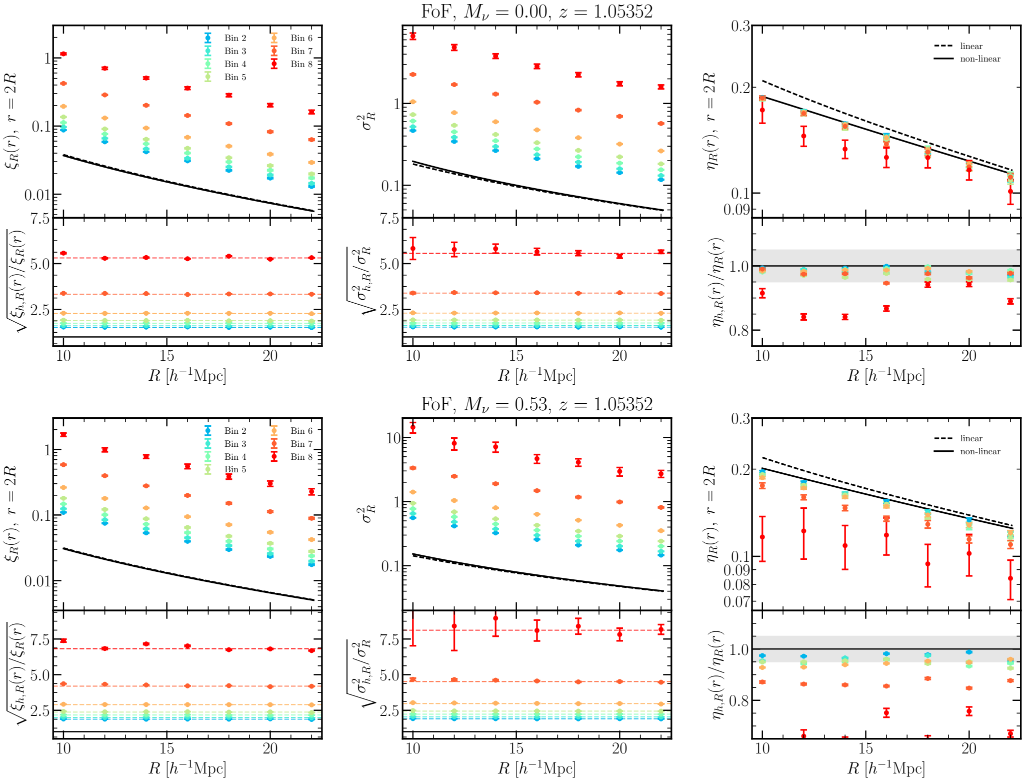

Figure 3.3: Same as in figure 3.2 but for redshift $z = 1.05352$. Again the clustering ratio, in the low-mass bins, agrees very well with the theoretical preditions. Moving towards tracers of higher mass, even if the accuracy of the description decreases, it is still acceptable (at 10% level). The highest mass bins, however, is completely discordant from the predictions, probably because of mass-resolution effects (at this redshift the simulation has not formed enough haloes of this mass). This consideration is supported also by the fact that the mismatch with theory increases with the neutrino mass.

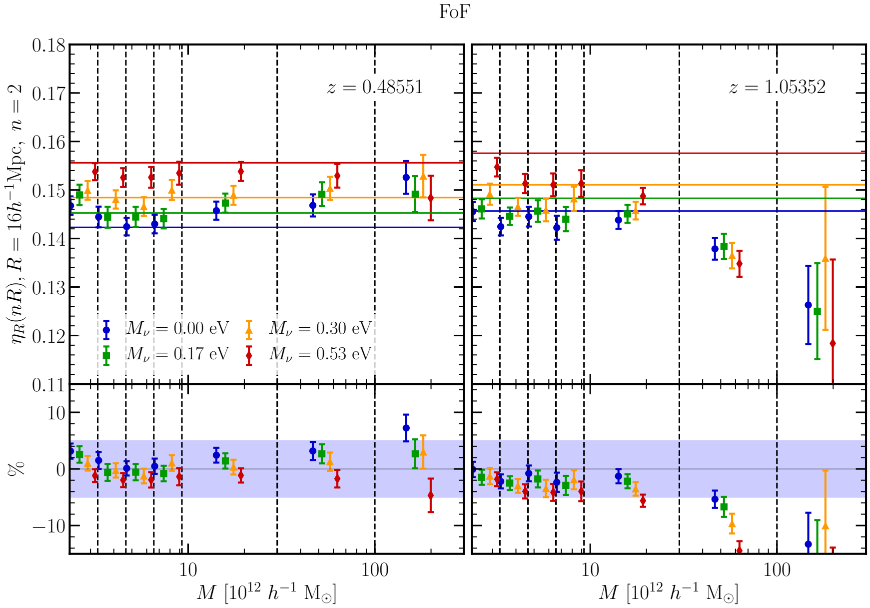

Figure 3.4: The clustering ratio at fixed scale (smoothing $R = 16\ h^{-1}$ Mpc and correlation $r = 2R = 32\ h^{-1}$ Mpc) as a function of the mass of the tracer, for friends of friends, at redshift $z = 0.48551$ (on the left) and $z = 1.05352$ (on the right). Different colors correspond to the different cosmologies, with $M_\nu = \{0, 0.17, 0.3, 0.53\}$ eV. In the upper panel, measures are compared to the theoretical prediction (straight lines). In the lower panel, it is shown the percentage difference between measures and predictions. The shaded region corresponds to a 5% discrepancy. Points are slightly horizontally displaced around the center of the bin in order not to overlap.

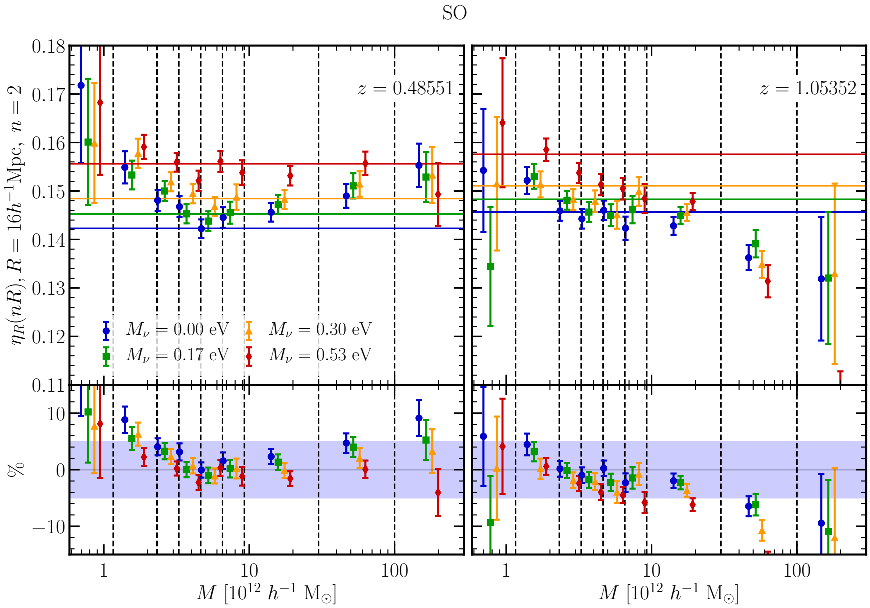

Figure 3.5: Same as Fig. 3.4, but for spherical overdensities.

the displacement

$$r_z^s = r_z + \frac{v_z\,(1 + z_{\rm box})}{H(z_{\rm box})}, \tag{3.36}$$

where v_z is the z component of the velocity of the object and $z_{\rm box}$ the cosmological redshift of the comoving output of the simulation (snapshot).

Fig. 3.6 shows the clustering ratio measured in real and redshift space, and their ratio, for the reference ΛCDM cosmology and the cosmology with $M_\nu = 0.53$ eV, at redshift $z = 0.48551$ and 1.05352. The case with $M_\nu = 0$ eV had already been studied in Bel and Marinoni (2014). Here I find the independence from redshift space distortions confirmed on all scales to better than 3% level, which is in agreement with the results of said paper. Also for the case with massive neutrinos, the independence of the clustering ratio from redshift space distortions, on these same scales, is confirmed at 3% level at $z \sim 0.5$. At $z \sim 1$ it reaches 1% level on scales larger than $R = 16\ h^{-1}$ Mpc. The higher accuracy at higher redshift is caused by structures growing in a less nonlinear regime.

The clustering ratio is therefore confirmed as being very weakly dependent on redshift-space distortions, and even less so in cosmologies with massive neutrinos. As a matter of fact, as neutrinos tend to reduce the velocity dispersion, in cosmologies with $M_\nu \neq 0$ redshift-space distortions appear in a more linear regime, making the agreement between the clustering ratio in real and redshift space even better.

3.3 Optimization

One of the most delicate points in the clustering ratio is the choice of smoothing scale R and correlation length r, the latter being usually expressed as a multiple of the former,

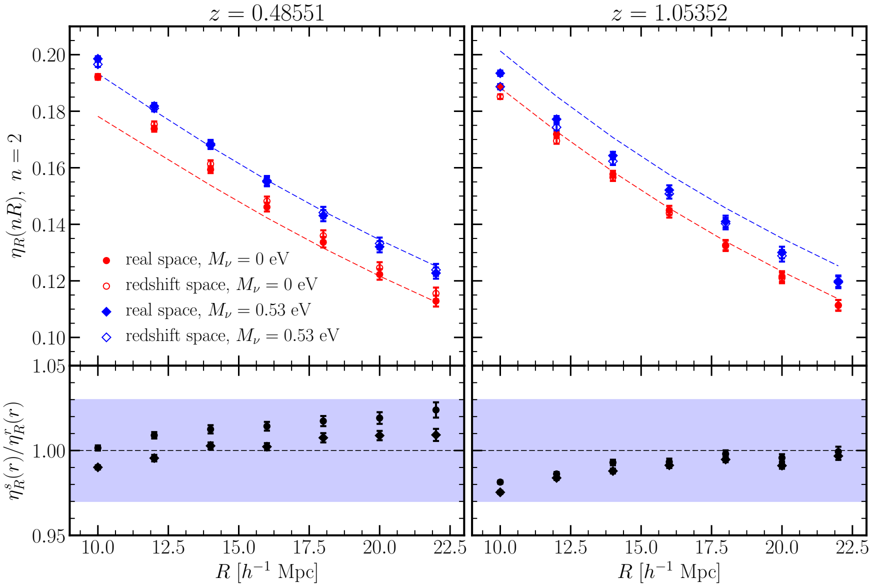

Figure 3.6: *Upper panels:* the clustering ratio in real and redshift space (filled and empty markers respectively) measure in the ΛCDM simulation (red circles) and in the $M_\nu = 0.53$ eV simulation (blue diamonds). Dashed lines represent the predicted clustering ratio in the two cosmologies, using the nonlinear power power spectrum (halofit). *Lower panels:* the ratio between the clustering ratio in redshift and real space. The shaded area marks a 3% mismatch. Again, circles are for ΛCDM and diamonds for $M_\nu = 0.53$ eV.

$r = nR$. One must find the combination of these parameters that minimizes noise and uncertainty and maximizes cosmological information.

The smoothing scale, the radius of the spheres used for the smoothing, controls the scale under which we make the clustering ratio blind to perturbations. A sufficiently large smoothing scale allows us to screen undesired nonlinear effects, that would compromise the effectiveness of the clustering ratio. On the other hand, choosing a smoothing scale that is excessively large would result in very noisy measurements, since in the same volume we could accommodate fewer spheres. Moreover, if R is too large, most of the information is screened and the measurement becomes little interesting.

Also for the correlation length, choosing small values implies coping with small-scale nonlinearities, which risks to invalid the identity expressed in Eq. 3.15. Large values of r, however, make it difficult to accommodate the entire motif of spheres require for the measurement in a given volume.

An additional constraint to consider is the fact that if $r < 2R$ the spheres of the motif would overlap. This results in a shot-noise that would affect the correlation function. For this reason I choose, in this work, to only allow values of $n \geq 2$.

The information we want to extract, in this case, is primarily the effect of neutrinos, in particular the neutrino total mass. This can be quantified as an effective signal to noise ratio, defined as

$$S/N = \frac{\eta_R(r,\nu) - \eta_R(r,\Lambda\mathrm{CDM})}{\sigma_\eta(\Lambda\mathrm{CDM})}, \tag{3.37}$$

where $\eta_R(r,\nu)$ is the clustering ratio measured in a simulation with neutrino mass M_ν, $\eta_R(r,\Lambda\mathrm{CDM})$ is measured in the reference ΛCDM simulation and $\sigma_{\eta_R}(\Lambda\mathrm{CDM})$ is the error measured in the ΛCDM simulation. This quantity measures how much a neutrino cosmology is distinguishable from a ΛCDM, given the typical errors on the measures of the clustering ratio for the specific box, redshift and for the current choice of R and n.

Fig. 3.7 shows the (n, R) plane, constructed as a grid of correlation lengths $n \in [2, 2.75]$, with step $\Delta n = 0.05$ and smoothing scales $R \in [15\ h^{-1}\ \mathrm{Mpc}, 30\ h^{-1}\ \mathrm{Mpc}]$, with step $\Delta R = 1\ h^{-1}\ \mathrm{Mpc}$. For each point on this grid the value of the S/N is represented with a color. The effects of massive neutrinos are more appreciable on small scales (both small R and small n), corresponding to larger difference between the two cosmologies combined with smaller errors.

While we want to maximizes the S/N quantity, we want to minimize errors. In particular we can define a theoretical error that measures the mismatch between the measured clustering ratio and the prediction, like in

$$\delta_{\mathrm{th}} = \frac{\eta_R(r) - \eta_R^{\mathrm{th}}(r)}{\sigma_\eta}, \tag{3.38}$$

where $\eta_R(r)$ is the clustering ratio measured in a given cosmology, $\eta_R^{\mathrm{th}}(r)$ the prediction in that cosmology and σ_η the uncertainty on the measurement. In this case we want to select the regions in the (n, R) plane where such theretical error is minimum, which are the choices of n and R that guarantee that the identity 3.15 is satisfied.

Fig. 3.8 shows the theoretical error computed in the same (n, R) parameter space. Here small values of R and n are associated with the highest mismatch between measures and theory, since on such small scales, where nonlinearities are quite important, the assumptions made on the bias break down.

It is seminal, at this point, to find a way of estimating the optimal combination of (n, R), since to maximize neutrino effects we should look at small scales while to minimize errors we should avoid them. In order to find a sweet-spot I define here a combined

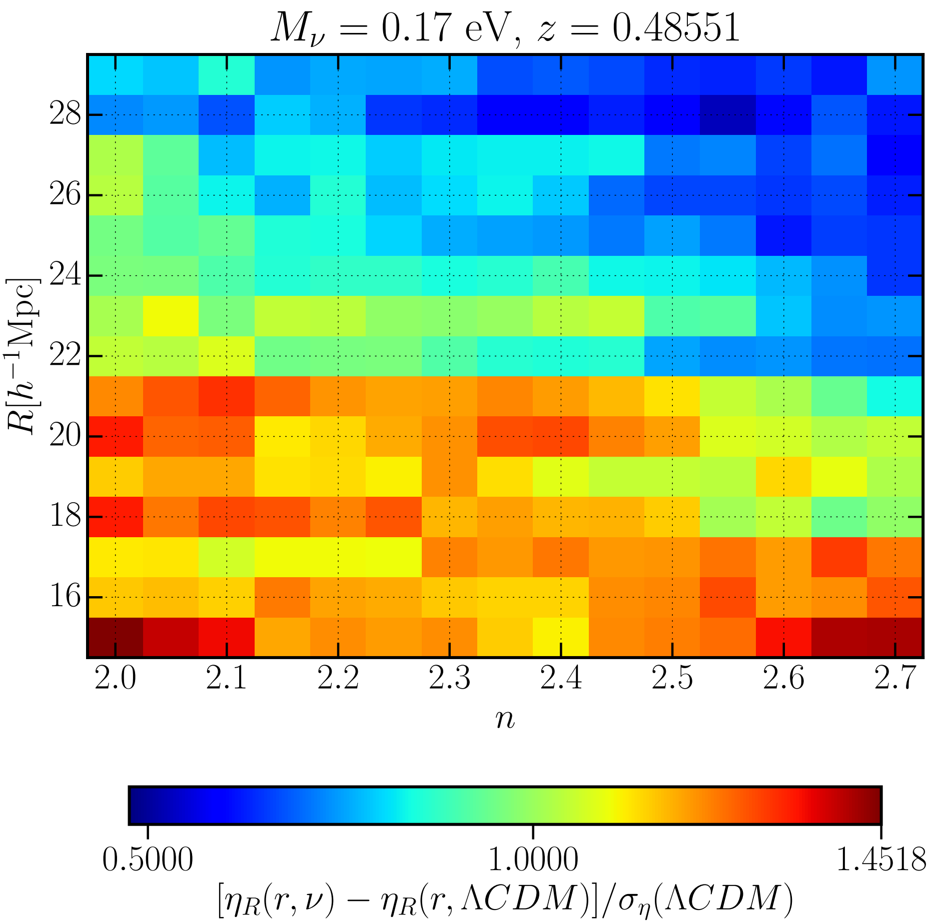

Figure 3.7: The effective signal-to-noise measures the distance between the clustering ratio in a massive neutrino cosmology (in this case $M_\nu = 0.17$ eV) and in a ΛCDM cosmology, in terms of the error on the measure in the ΛCDM case. The regions in the (n, R) plane that exhibit the reddest colour are the ones where distinguishing the effects of neutrinos is easiest (large difference and/or small errors).

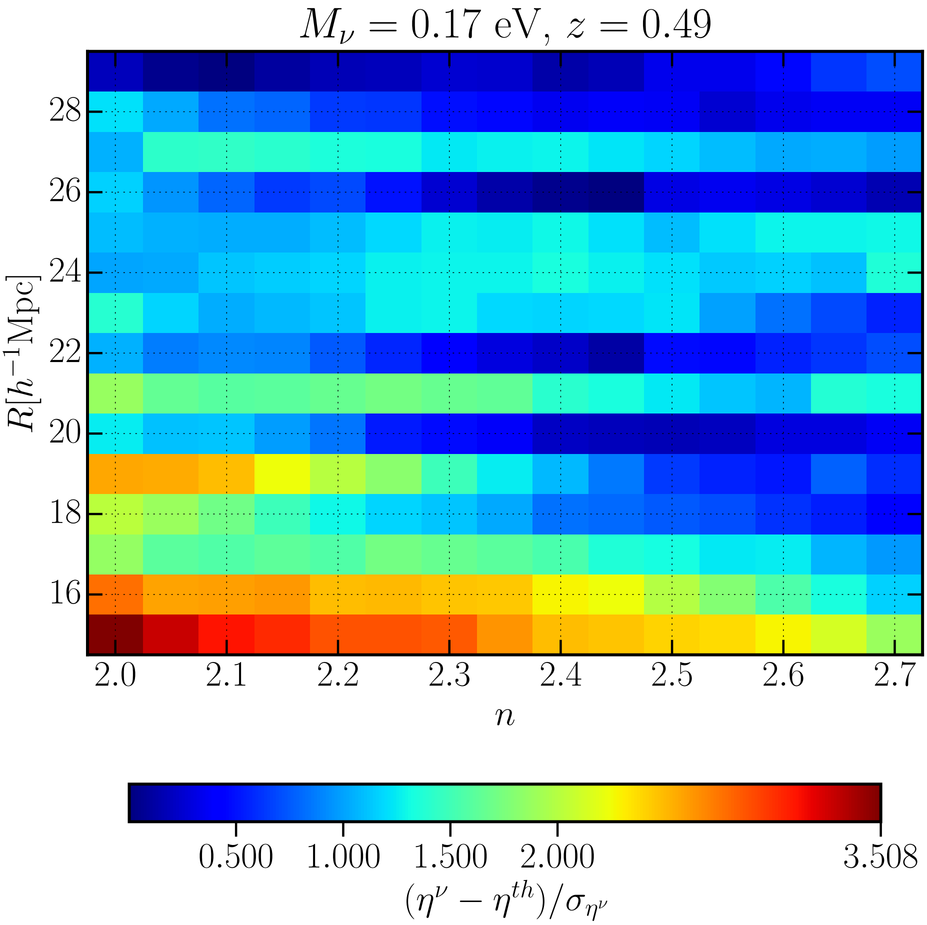

Figure 3.8: The theoretical error measures the mismatch between the measured clustering ratio and it prediction, normalized to the error on the measurement. The blue regions represent the choices of n and R that minimize it.

percentage error, which accounts both for statistical errors and systematic ones, and assumes the form

$$\delta_{\text{combined}} = \left\{ \frac{\eta_R^{\nu}(r) - \eta_R^{\nu,\text{th}}(r)}{\eta_R^{\nu}(r) - \eta_R^{\Lambda\text{CDM}}(r)} \right\} \left\{ \frac{\sigma_{\eta}^{\Lambda\text{CDM}}}{\eta_R^{\nu}(r) - \eta_R^{\Lambda\text{CDM}}(r)} . \right\} \tag{3.39}$$

The quantity in the first parentheses is related to how much the statistical error is important with respect to the effects of neutrinos, while the second parenthesis is a weight that accounts for the typical uncertainty on the measure in a bin of R and n.

We want to minimize this combined error and maximize the effective signal-to-noise ratio defined in 3.37. Let

$$C = \frac{S/N}{\max(S/N)} - \frac{\delta_{\text{combined}}}{\max(\delta_{\text{combined}})} \tag{3.40}$$

be the *neutrino contrast*, then the optimal situation is the one in which $C \sim 1$.

Fig 3.9 shows the neutrino contrast in the usual parameter space, for a cosmology with $M_\nu = 0.17$ eV, at redshift $z = 0.48551$. I have repeated the same analysis for all the available cosmologies ($M_\nu = \{0.17, 0.3, 0.53\}$ eV) and for different redshifts from $z = 0.48551$ to $z = 2.05053$. As a result, the most viable candidate is the choice $R = 22\ h^{-1}$ Mpc and $n = 2.1$.

3.4 Parameter estimation

The final goal of this work is, once the properties of the clustering ratio have been confirmed also in the presence of massive neutrinos, to employ it to constrain cosmological parameter, in particular the total neutrino mass M_ν and/or the dark energy equation of state w.

The idea is to fully exploit the identity

$$\eta_{g,R}^{s}(r) \equiv \eta_R(r), \tag{3.41}$$

comparing the clustering ratio measured in a galaxy survey (unavoidably in redshift space) to the predictions for matter in real space. In particular, the constraining power comes from the different dependence these two quantities have on cosmological parameters.

The measured clustering ratio depends on the parameters that regulate the conversion of redshifts into distances, namely the matter density parameter Ω_m, the dark energy fraction Ω_Λ and the Hubble function $H(z)$.

The predicted clustering ratio depends on the full set of parameters of the adopted cosmological model. I will consider a baseline model with six free parameters, the Hubble parameter today H_0, the CDM density parameter $\Omega_{cdm}h^2$, the baryon density parameter $\Omega_b h^2$, the optical depth τ, the spectral index of scalar perturbations n_s, and A_s, the amplitude of scalar perturbations at the epoch of the CMB at a pivotal scale $k_{\text{pivot}} = 0.05\, h\, \text{Mpc}^{-1}$. Altogether, they for the vector of parameter of the baseline model

$$\boldsymbol{p}_{\text{baseline}} = \{H_0, \Omega_{cdm}h^2, \Omega_b h^2, \tau, n_s, A_s\}. \tag{3.42}$$

On top of this vector, I consider two additional free parameters: the total neutrino mass M_ν and the dark energy equation of state w. In all cases I will assume the universe to be flat, fixing $\Omega_k = 0$.

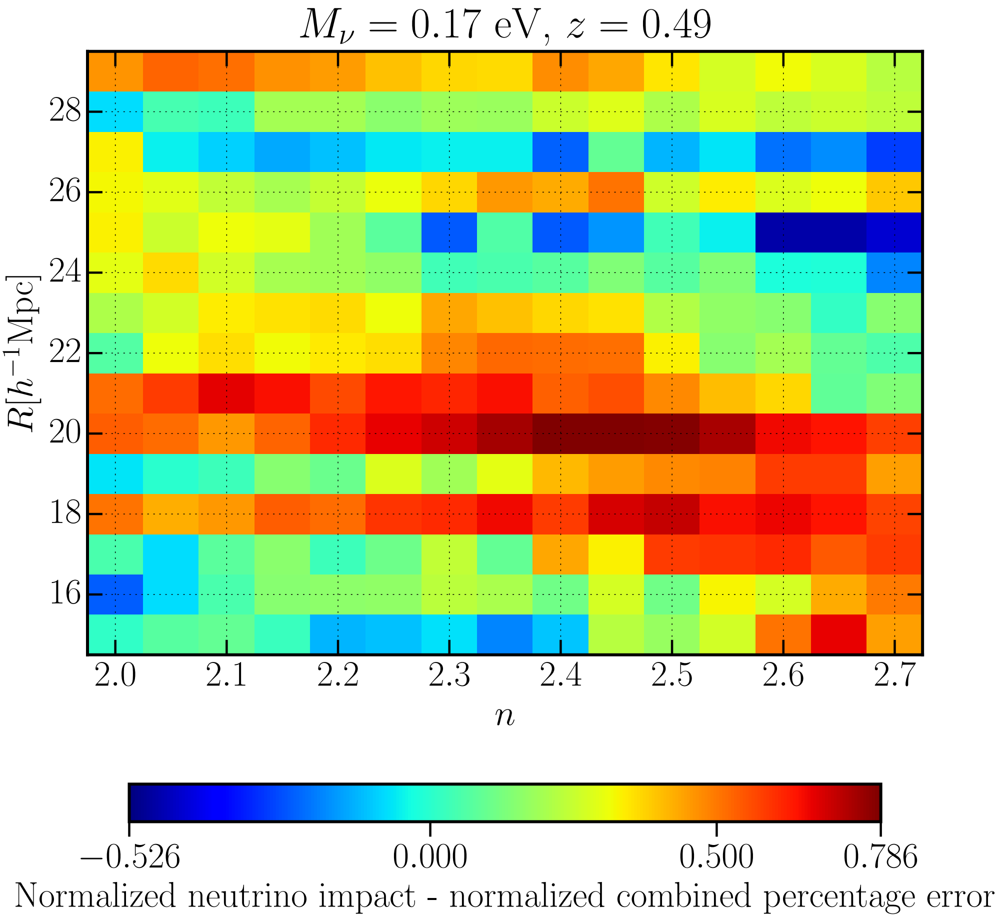

Figure 3.9: Neutrino contrast in the (n, R) parameter space. The contrast is obtained as the normalized effective signal-to-noise ratio minus the normalized combined error, and is optimal when approaches 1.

I will explore the posterior distribution of the parameters of the model. In general, given the vector of parameters $\boldsymbol{\vartheta}$ and a set of observations $\boldsymbol{x}$, realizations of a random variable X, the posterior distribution $p(\boldsymbol{\vartheta}|\boldsymbol{x})$ is the probability of the considered set of parameters $\boldsymbol{\vartheta}$ given the observations $\boldsymbol{x}$, and is computed as

$$p(\boldsymbol{\vartheta}|\boldsymbol{x}) = \frac{p(\boldsymbol{x}|\boldsymbol{\vartheta})\, p(\boldsymbol{\vartheta})}{p(\boldsymbol{x})}, \tag{3.43}$$

where $p(\boldsymbol{x}|\boldsymbol{\vartheta})$ is the likelihood, *i.e.* the probability of the observations given the parameters, and $p(\boldsymbol{\vartheta})$ is our prior belief about the parameters. Finally $p(\boldsymbol{x})$ is the probability of the observations, which is intrinsically not known. To work around our ignorance of $p(\boldsymbol{x})$ one can adopt an MCMC approach, in which, independently of the specific algorithm of choice, the parameter space is explored in terms of the ratio of the likelihood in couples of points. Since the prior is known and the probability of the data $p(\boldsymbol{x})$ is independent on the choice of parameters, the ratio of the likelihoods is equivalent to the ratio of the posterior in the considered points. For this reason, MCMC chains converge to the true posterior distribution, even if we do not know the intrinsic probability distribution of the data.

In Bel and Marinoni (2014) the likelihood obtained from the clustering ratio has been shown to be Gaussian to very good approximation. Here I repeat this analysis to make sure neutrino effects do not spoil this property.

While in the ΛCDM case many mock catalogues are available to repeat the measure in different, independent realizations of the same cosmology, for the case with neutrinos I only have access to the DEMNUni simulations. Fortunately, they are large enough that 64 jackknife resamplings can be performed, each time subtracting a large enough volume to affect the measures while, at the same time, keeping enough volume to have a robust statistics.

Figures 3.10 and 3.11 show 64 measurements of the clustering ratio at different smoothing scales and correlation length, the former in a ΛCDM cosmology and the latter in a cosmology with $M_\nu = 0.53$ eV. In all cases, I have tested the hypothesis the data are gaussianly distributed. To do so, I chose a Pearson's χ^2 test. To perform it, the data must be binned (here 9 bins are employed). In each bin B_i one can measure the observed frequency

$$O_i = \sum_{j \in B_i} 1, \tag{3.44}$$

and predict a expected frequency, according to the hypothesis we are testing,

$$E_i = N \int_{B_i} \mathrm{d}x \; p(x), \tag{3.45}$$

where N is the total number of observations and $p(x)$ is the probability density function corresponding to the probability law considered (in this case a Normal distribution). The Pearson's variable is defined as

$$\mathcal{P} = \sum_i^n \frac{(O_i - E_i)^2}{O_i}, \tag{3.46}$$

where n is the number of bins. A property of such variable is that, as the rank of the sample tends to infinity, it converges to a χ^2 distribution with $n-1$ degrees of freedom. For this reason, we can fix a significance level of the test (in this case $\alpha = 0.05$) and compare

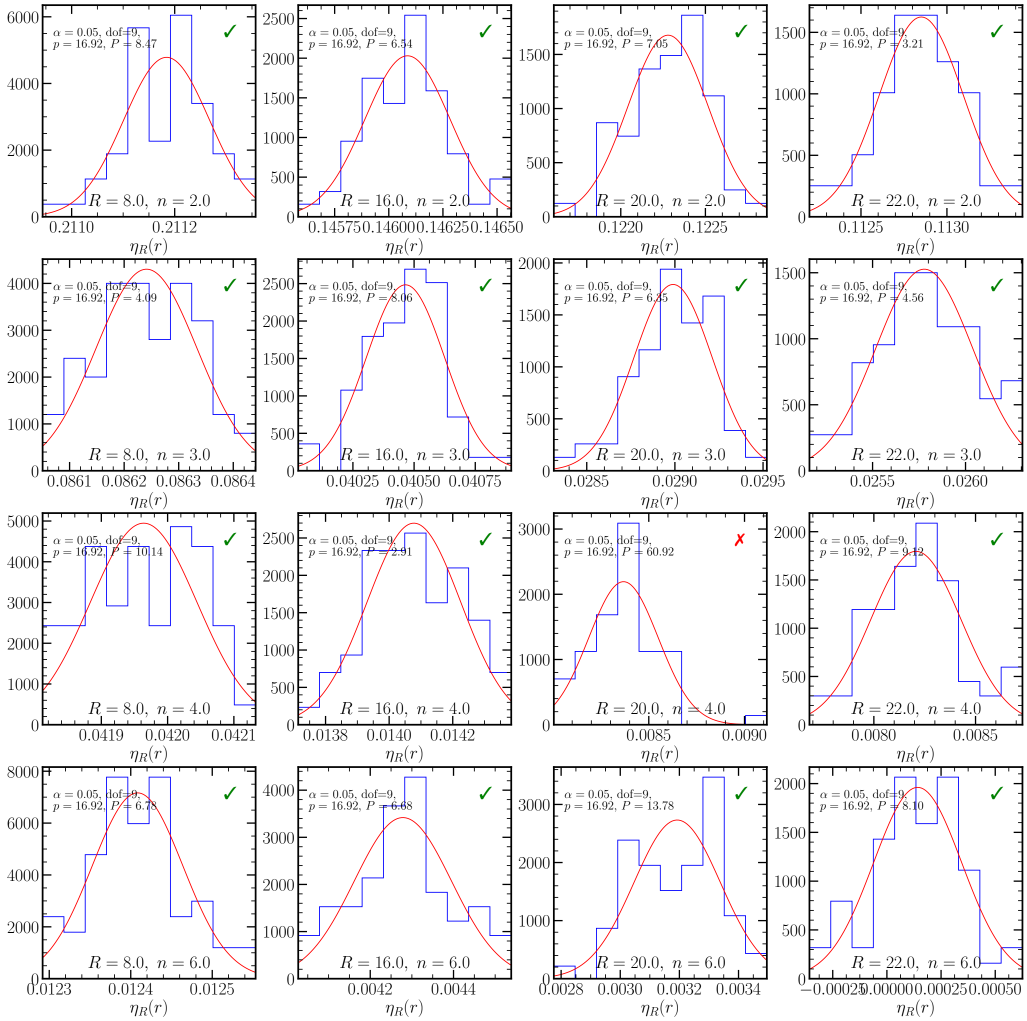

Figure 3.10: CR gaussianity

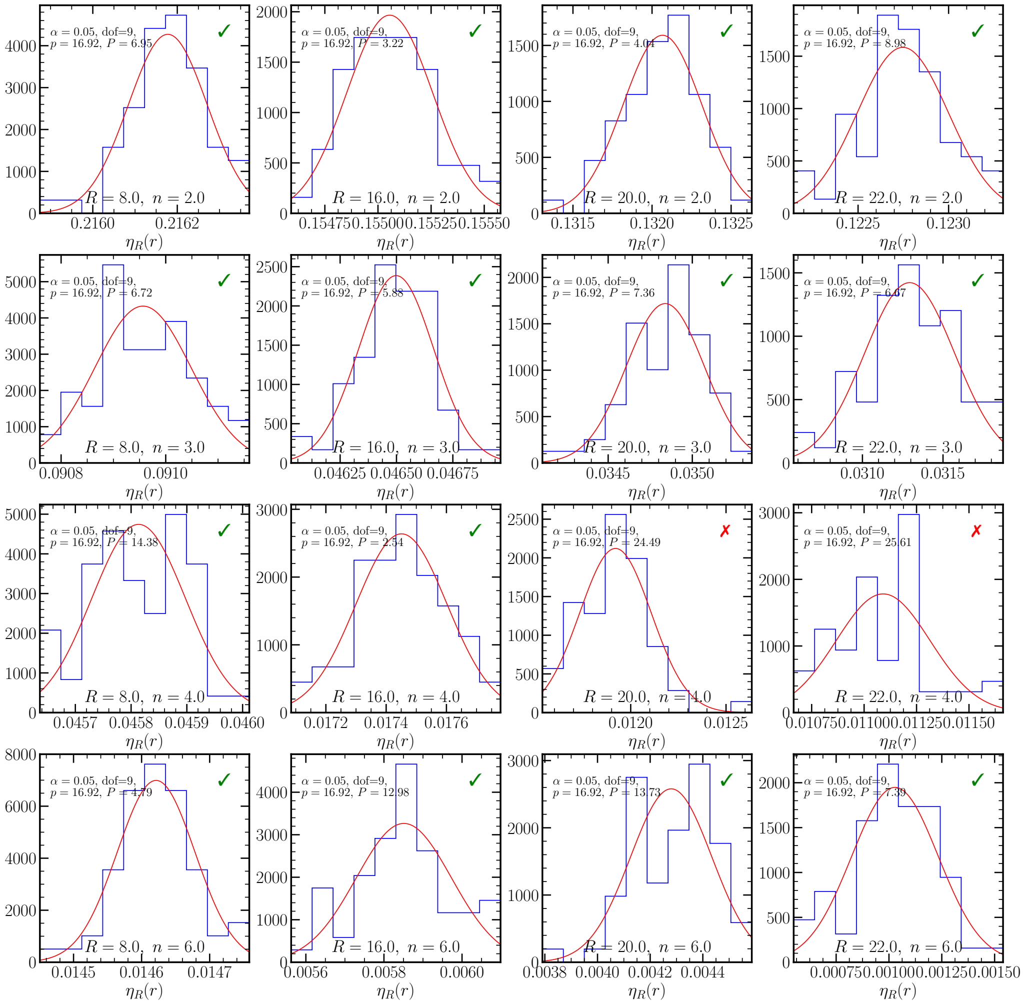

Figure 3.11: CR gaussianity

the Pearson's variable obtained with the p-value of a χ^2 distribution with significance α. Hence we have

$$p(\mathcal{P} > \chi^2_{1-\alpha}(n-1)) = \alpha. \tag{3.47}$$

In Fig.s 3.10-3.11 the Pearson's variable is compared to $\chi^2_{0.95}(8) = 16.92$, and when the hypothesis of gaussianity is accepted a green tick is drawn in the plot, while otherwise a red mark appears. Only on very large scales, $R = 20\ h^{-1}\ \mathrm{Mpc}, r = 80 - 88\ h^{-1}\ \mathrm{Mpc}$, the test does not confirm the gaussianity of the distribution, probably due to the sparseness of the sample. In all other cases, the hypothesis of gaussianity cannot be rejected at 5% significance level.

I therefore approximate the true likelihood with a Gaussian. For simplicity (and mainly for computational reasons) I will work in terms of the log-likelihood $\mathcal{L}$, which corresponds to the χ^2,

$$\chi^2(\boldsymbol{\vartheta}) = -2\mathcal{L}(\boldsymbol{\vartheta}) = \sum_i \frac{[\eta_{iR}(r,\boldsymbol{\vartheta}) - \eta^{\mathrm{th}}_{iR}(r,\boldsymbol{\vartheta})]^2}{\sigma^2_{\eta_i}}, \tag{3.48}$$

where i spans all the measurements of the clustering ratio considered. For measurements taken at different redshifts, I will neglected the covariance between the different redshift bins.

3.4.1 Alcock-Pacziński effect

Since the redshift to distance conversion depends on the choice of cosmological parameters, it becomes important to model this dependence, to understand how the measure would change if performed in a different cosmology.

One approach consists in choosing a reference cosmology, in which the measurement is performed. This cosmology becomes the *fiducial cosmology*, with parameters $\boldsymbol{\vartheta}_F$. Now we want to know how the measure would change under a generic choice of parameters $\boldsymbol{\vartheta}$. The Alcock-Pacziński effect describes exactly how parallel and transverse distances differ in different cosmologies (Alcock and Paczyński, 1979).

The modification of a regular volume induced by a different choice of cosmological parameters is given by

$$V = \alpha^3_{\mathrm{AP}} V^F, \tag{3.49}$$

where V^F is the volume in the fiducial cosmology, and α_{AP} is a correction factor that can be written as (Eisenstein et al., 2005)

$$\alpha_{\mathrm{AP}} = \left[\frac{E^F(z)}{E(z)} \left(\frac{D_A}{D_A^F} \right)^2 \right]^{1/3} . \tag{3.50}$$

In appendix C I present a derivation of this formula.

The clustering ratio only depends on distances through the smoothing scale R (the correlation length being taken to be a multiple of the latter, $r = nR$). For this reason, the only requirement to scale the measure of the clustering ratio in a cosmology different from the fiducial one, is to correct the smoothing scale $R = \alpha_{\mathrm{AP}} R^F$.

In this work I will always fix the fiducial cosmology to compute the measured clustering ratio. I will compare measures obtained assuming this cosmology to predictions (obtained leaving the cosmological parameters free) that assume the same redshift to distance relation. The comparison therefore becomes between

$$\eta_{g,R^F}(nR^F) \equiv \eta_{\alpha_{\mathrm{AP}}R}(n\alpha_{\mathrm{AP}}R). \tag{3.51}$$

3.4.2 Constraints using SDSS data

I have explored the likelihood of the vector of parameters defined in Eq. 3.42 in the parameter space, using the clustering ratio measured in the 7^{th} (Abazajian et al., 2009) and 12^{th} (Alam et al., 2015) data release of the Sloan Digital Sky Survey (SDSS).

Details on the computation of the clustering ratio and its errors in the SDSS can be found in Bel et al. (2015). The sample is divided into three redshift bins with $\bar{z} = \{0.29, 0.42, 0.60\}$. The first redshift bin comes from the DR7 catalogue, while the other two from the DR12, after removing the objects already present in the other bin.

The fiducial cosmology in which measures are performed has $H_0 = 67\,\mathrm{km\ s^{-1}\ Mpc^{-1}}$, $\Omega_m = 0.32$, and Ω_k is forced to be zero, imposing $\Omega_\Lambda = 1 - \Omega_r - \Omega_m$. The choice of smoothing radius and correlation length follows from the previous section, §3.3, devoted to the optimization of the clustering ratio, *i.e.* $R = 22\ h^{-1}$ Mpc and $r = nR$, with $n = 2.1$.

The measures obtained are

$$\begin{aligned} 0.15 \le \bar{z} \le 0.43, &\quad \eta_{g,R}(r) = 0.0945 \pm 0.0067\ , \\ 0.30 \le \bar{z} \le 0.53, &\quad \eta_{g,R}(r) = 0.0914 \pm 0.0055\ , \\ 0.53 \le \bar{z} \le 0.67, &\quad \eta_{g,R}(r) = 0.1070 \pm 0.0110\ . \end{aligned} \tag{3.52}$$

The posterior distribution obtained using these data, compared to the predictions of the clustering ratio, is shown in Fig. 3.12. The set of free parameters is the one presented in 3.42, however only four, relevant parameters are shown in this figure. In this figure we can see by eye that the constraints on the total neutrino mass do not improve significantly when we add the clustering ratio to the CMB data, while the most significant improvement is on the cold dark matter density parameter $\Omega_c h^2$.

Besides the baseline parameter set, I have also computed the posterior distribution leaving also the equation of state of dark energy w as a free parameter. This is because this parameter is known to be strongly degenerate with the other parameters when only CMB data are used, since, at the time the CMB photons decoupled, the energy density of the dark energy fluid was negligible. Therefore, it is interesting to check if a geometrical probe such as the clustering ratio, which is sensitive to the universe at later times, is capable of breaking such degeneracies. This additional posterior distribution is shown in Fig. 3.13. Already by eye, it is clear that adding the clustering ratio indeed breaks the degeneracy of w with the other parameters, favouring a universe with $w \sim -1$. Also the constraints on the other parameters significantly improve once this degeneracy has been broken.

Moreover, also the combination with other cosmological observables can help breaking degeneracies and tightening the constraints on the parameters. In particular, I am going to compare the constraining power of the clustering ratio with two other probes, the position of the BAO peak in the correlation function measured by the BOSS collaboration (Anderson et al., 2014) and the lensing of the CMB signal due to the intervening matter between the last-scatter surface and us (Planck Collaboration et al., 2016). In the latter case, the amplitude of the lensing potential has been fixed so that $A_L = 1$. Table 3.3 shows the mean, 68% and 95% levels of the marginalized posterior distribution for all the free parameters in the eight different probe combinations considered: CMB and clustering ratio with the baseline free parameters, and CMB, clustering ratio, CMB lensing and BAOs with the additional free parameter w.

To better show the behaviour of the clustering ratio with respect to the other probes considered, Fig.s 3.14 and 3.15 particularly focus on w, M_ν and H_0.

In general, adding the clustering ratio considerably improves on the constraints obtained with CMB data alone, especially when also w is free to vary. In particular, the

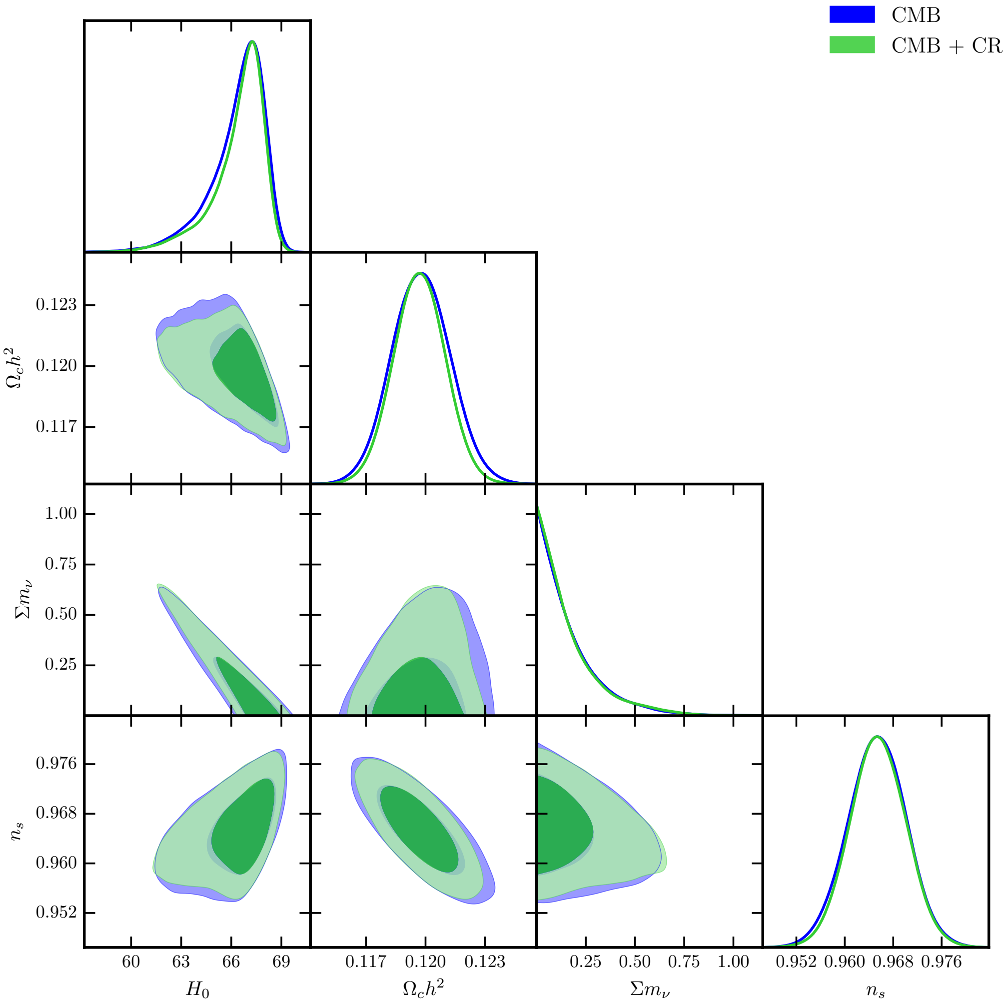

Figure 3.12: The 2D contours of the posterior distribution obtained using jointly the clustering ratio measured in the SDSS DR7 and DR12 and Planck's temperature and polarization anisotropies (TTTEEE). In green blue, the result obtained using only Planck's data is shown for reference. Only four of the seven free parameters are shown here. Inner, solid regions correspond to 68% contours, semi-transparent regions correspond to 95% contours.

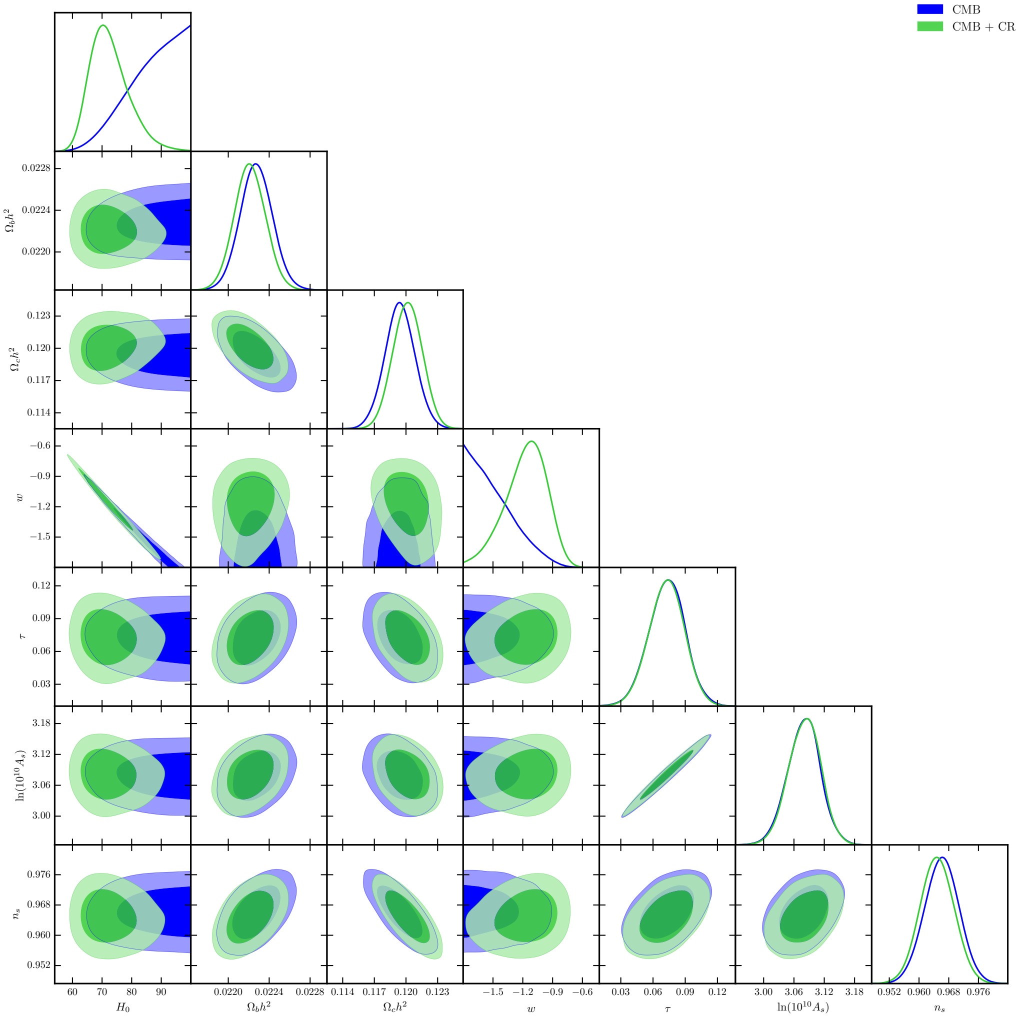

Figure 3.13: The 2D contours of the posterior distribution obtained using jointly the clustering ratio measured in the SDSS DR7 and DR12 and Planck's temperature and polarization anisotropies (TTTEEE). In green blue, the result obtained using only Planck's data is shown for reference. In this case the free parameters are $\boldsymbol{p} = \{H_0, \Omega_{cdm}h^2, \Omega_b h^2, \tau, n_s, A_s, w\}$. Inner, solid regions correspond to 68% contours, semi-transparent regions correspond to 95% contours.

	$\Omega_b h^2$			$\Omega_c h^2$		
Pl (fixed w)	0.02222	±0.00017	±0.00033	0.11978	±0.00147	±0.00291
Pl + CR (fixed w)	0.02222	±0.00016	±0.00031	0.11972	±0.00128	±0.00255
Pl	0.02222	±0.00016	±0.00034	0.11971	±0.00142	±0.00281
Pl + CR	0.02216	±0.00017	±0.00033	0.12042	±0.00149	±0.00290
Pl + CLens	0.02217	±0.00017	±0.00035	0.11967	±0.00153	±0.00299
Pl + BAO	0.02225	±0.00015	±0.00030	0.11949	±0.00134	±0.00263
Pl + CLens + CR	0.02213	±0.00016	±0.00032	0.12026	±0.00145	±0.00288
Pl + BAO + CR	0.02223	±0.00015	±0.00030	0.11965	±0.00132	±0.00261
	τ			M_ν		
Pl (fixed w)	0.07851	±0.01713	±0.03355	0.16722	< 0.19150	< 0.49402
Pl + CR (fixed w)	0.07801	±0.01744	±0.03330	0.15795	< 0.18088	< 0.47835
Pl	0.07737	±0.01793	±0.03483	0.22153	< 0.26698	< 0.60851
Pl + CR	0.07469	±0.01754	±0.03403	0.20304	< 0.24510	< 0.53081
Pl + CLens	0.06927	±0.01749	±0.03420	0.32882	±0.19711	< 0.67219
Pl + BAO	0.07728	±0.01705	±0.03304	0.11571	< 0.14235	< 0.30423
Pl + CLens + CR	0.06909	±0.01681	±0.03237	0.29440	±0.17524	< 0.59471
Pl + BAO + CR	0.07731	±0.01666	±0.03147	0.10844	< 0.13143	< 0.28339
	w			$\ln(10^{10} A_s)$		
Pl (fixed w)	-1.00000	–	–	3.09167	±0.03332	±0.06510
Pl + CR (fixed w)	-1.00000	–	–	3.09042	±0.03375	±0.06497
Pl	-1.68615	±0.29543	±0.59285	3.08881	±0.03490	±0.06751
Pl + CR	-1.25376	±0.24254	±0.52000	3.08537	±0.03368	±0.06550
Pl + CLens	-1.67628	±0.35984	±0.66750	3.07148	±0.03387	±0.06578
Pl + BAO	-1.05867	±0.07959	±0.16354	3.08846	±0.03305	±0.06428
Pl + CLens + CR	-1.22298	±0.23981	±0.51234	3.07259	±0.03189	±0.06176
Pl + BAO + CR	-1.05267	±0.07749	±0.15731	3.08903	±0.03209	±0.06098
	n_s			H_0		
Pl (fixed w)	0.96531	±0.00478	±0.00951	66.36205	$^{+1.93320}_{-0.79827}$	±3.14533
Pl + CR (fixed w)	0.96550	±0.00456	±0.00906	66.47015	$^{+1.72753}_{-0.68157}$	±2.93440
Pl	0.96500	±0.00473	±0.00953	86.91446	$^{+12.41268}_{-4.70920}$	±15.59971
Pl + CR	0.96389	±0.00487	±0.00967	73.04263	±6.83317	±14.51362
Pl + CLens	0.96452	±0.00502	±0.00978	84.62450	$^{+14.64438}_{-5.54025}$	±16.85512
Pl + BAO	0.96612	±0.00451	±0.00886	68.60048	±1.67361	±3.36935
Pl + CLens + CR	0.96385	±0.00493	±0.00946	71.08454	±6.31034	±13.48706
Pl + BAO + CR	0.96595	±0.00453	±0.00888	68.42143	±1.63637	±3.26416

Table 3.3: Mean, 68% and 95% levels for each parameter of the marginalised posterior.

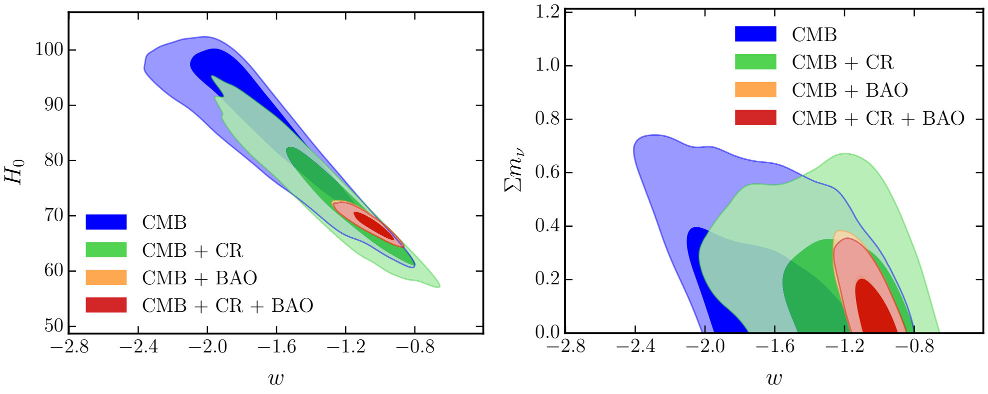

Figure 3.14: The degeneracy between H_0 and w (left) and between $\sum m_\nu$ and w (right) using the posteriors obtained employing only Planck's data (blue) or adding the clustering ratio (green), BAOs (orange) and both (red). The 68% and 95% contours are shown.

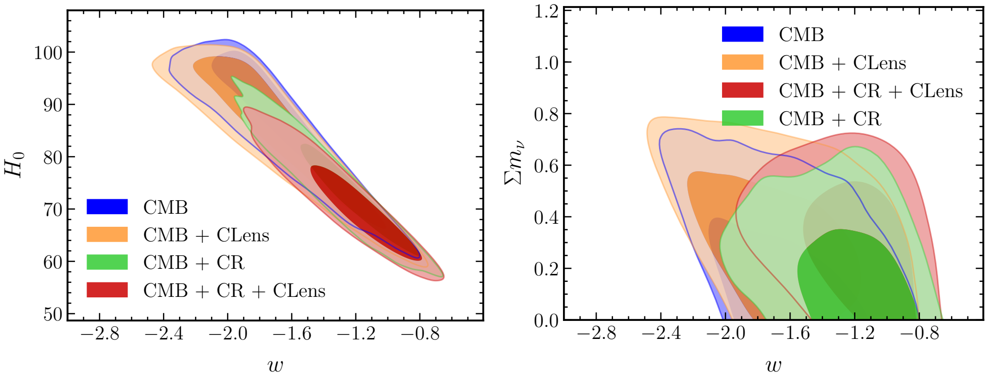

Figure 3.15: The degeneracy between H_0 and w (left) and between $\sum m_\nu$ and w (right) using the posteriors obtained employing only Planck's data (blue) or adding the lensing of the CMB (green), the clustering ratio (orange) and both (red). The 68% and 95% contours are shown.

	$\Omega_b h2$			$\Omega_c h^2$		
Pl	0.02244	± 0.00016	± 0.00034	0.11948	± 0.00157	± 0.00314
Pl + CR	0.02242	± 0.00015	± 0.00030	0.11950	± 0.00136	± 0.00265
	τ			M_ν		
Pl	0.09332	± 0.01644	± 0.03291	0.20477	< 0.26441	< 0.42993
Pl + CR	0.09199	± 0.01659	± 0.03229	0.20843	± 0.11909	< 0.41013
	w			$\ln(10^{10} A_s)$		
Pl	-1.00000	–	–	3.05893	± 0.03169	± 0.06381
Pl + CR	-1.00000	–	–	3.05620	± 0.03264	± 0.06422
	n_s			H_0		
Pl	0.95937	± 0.00518	± 0.01015	66.65175	± 1.43657	± 2.67394
Pl + CR	0.95969	± 0.00458	± 0.00918	66.60347	± 1.23252	± 2.41851

Table 3.4: Joint posterior obtained using Planck temperature and polarization data and the clustering ratio. Bestfits here are fixed, errors for Planck come from the publicly available covariance matrix, error on the clustering ratio have been compute in SDSS DR7 and 12.

clustering ratio is able to break the degeneracy between w and the other cosmological parameters that affects the constraints drawn with the sole CMB data. On the other hand, the clustering ratio does not seem to improve much on the constraints on M_ν obtained both by the CMB lensing and BAO peak position.

The clustering ratio proves to be extremely sensitive to the cold dark matter fraction Ω_{cdm}, as adding the clustering ratio information to the CMB analysis results in a 12% improvement on the 95% confidence level.

To improve the level of understanding of these results, however, it is important to check how well the clustering ratio is able to recover a known cosmology. To do so, I use the measures of the clustering ratio in one of the DEMNUni simulations, the one with $M_\nu = 0.17$ eV, which represents the closest case to the current available constraints on the neutrino total mass. The clustering ratio is measured in the simulation at the same redshift, and with the same binning, as in the SDSS data. The error on the measurements here is the one from the SDSS measures.

For the CMB data, in this case, I approximate the likelihood with a gaussian covariance matrix and I fix the best fits to match the cosmological parameters of the simulation.

The posterior distribution obtained with this exercise is shown in Fig. 3.16. Table 3.4 sums up the constraints from the marginalised posterior.

The clustering ratio is able to recover the bestfits of the known cosmology very precisely. The errors on the parameters, however, are compatible with the ones obtained from the real data, and the neutrino mass upper limit does not particularly improve. This points towards the idea that the uncertainties on the SDSS measures are too large for the clustering ratio to significantly tighten the constraint on the total neutrino mass. Smaller uncertainties, like the ones expected from future galaxy surveys, could in principle lead to more robust neutrino constraints. In the next section, I test this hypothesis, applying the clustering ratio to a Euclid-like synthetic galaxy survey.

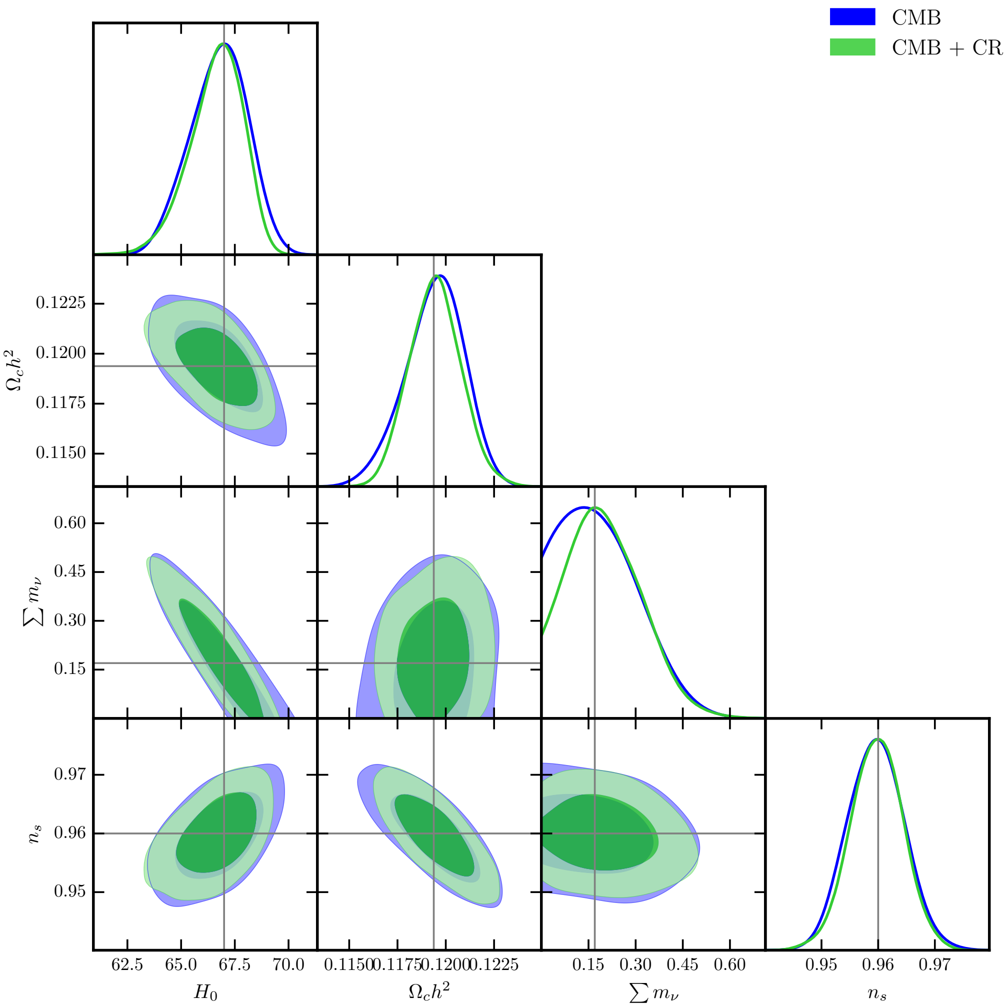

Figure 3.16: The 2D contours of the posterior distribution obtained fixing a known cosmology. Planck data are taken to be in a cosmology with same parameters as the $M_\nu = 0.17$ eV simulation, with errors given by the covariance matrix provided by the Planck collaboration. The clustering ratio has been measured in the simulation with $M_\nu = 0.17$ eV. Only four of the six free parameters are shown. Inner, solid regions correspond to 68% contours, semi-transparent regions correspond to 95% contours.

$\bar{z}$	$V\ [h^{-3}\ \mathrm{Mpc}^3]$	N
0.7	2.75625346×10^9	3.65142000×10^6
0.8	3.20219789×10^9	6.54721800×10^6
0.9	3.60913887×10^9	7.09283850×10^6
1.0	3.97413794×10^9	7.23869700×10^6
1.1	4.29687503×10^9	7.09319550×10^6
1.2	4.57872089×10^9	6.76143750×10^6
1.3	4.82206481×10^9	6.40477650×10^6
1.4	5.02984405×10^9	5.58098550×10^6
1.5	5.20522534×10^9	4.65646350×10^6
1.6	5.35139703×10^9	3.46346250×10^6
1.7	5.47143942×10^9	2.31274650×10^6
1.8	5.56824925×10^9	2.21206050×10^6
1.9	5.64450058×10^9	1.34057400×10^6
2.0	5.70262958×10^9	7.46419500×10^5

Table 3.5: Mean redshift, volume of the bin and number of galaxies contained in each bin for the synthetic, Euclid-like survey

3.4.3 Forecasts for a Euclid-like galaxy redshift survey

To forecast the expected constraining power of the clustering ratio with future, Euclid-like data, first of all I have chosen a Euclid-like redshift range, from $z = 0.7$ to $z = 2$. I have divided it into 14 redshift bins of width $\Delta z = 0.1$. Tab. 3.5 shows the mean redshift, the comoving volume and the number of galaxies for each of such bins.

In each bin, the clustering ratio is computed taking the expected value (obtained integrating a power spectrum produced by a Boltzmann code) and adding a small random noise (within 1 sigma).

For the errors to associate to the measures, I started from the errors measured in the same redshift bins in the simualation with $M_\nu = 0.17$ eV. I then rescaled these errors following the scaling relation used in Bel et al. (2015), that accounts for the difference in volume and number density between the simulation and the synthetic survey. Such scaling relation has the form

$$\frac{\delta\eta}{\eta} = A\, V^{-1/2}\ \exp\left\{0.14\left[\ln\rho - \frac{\ln^2\rho}{2\ \ln(0.02)}\right]\right\}, \tag{3.53}$$

where V is the volume expressed in $h^{-3}\mathrm{Mpc}^3$, ρ is the object number density in $h^3\mathrm{Mpc}^{-3}$ and A is a normalization factor (obtained from the reference volume and number density).

	$\Omega_b h^2$			$\Omega_c h^2$		
Pl	0.02243	±0.00016	±0.00031	0.11942	±0.00146	±0.00290
Pl + CR	0.02245	±0.00013	±0.00026	0.11926	±0.00084	±0.00167
	τ			M_ν		
Pl	0.09335	±0.01747	±0.03445	0.20513	±0.12382	< 0.43157
Pl + CR	0.09422	±0.01655	±0.03298	0.17749	±0.11133	< 0.37693
	w			$\ln(10^{10}A_s)$		
Pl	-1.00000	–	–	3.05859	±0.03378	±0.06670
Pl + CR	-1.00000	–	–	3.06008	±0.03262	±0.06476
	n_s			H_0		
Pl	0.95983	±0.00491	±0.00964	66.66588	±1.38464	±2.62998
Pl + CR	0.96046	±0.00443	±0.00854	66.98261	±1.12263	±2.18365

Table 3.6: Mean, 68% and 95% levels of the marginalised likelihoods. Note that in this case bestfits have been fixed to the ones of the fiducial cosmology, errors for Planck are obtained from the publicly available Planck parameter covariance matrix and error for the clustering ratio are the ones predicted for a Euclid-like galaxy survey, following the procedure described in the text.

Thanks to this procedure, the synthetic data for $R = 22\ h^{-1}$ Mpc and $r = 2.1\ R$ are

$$\begin{aligned}
\eta_R(r, z = 0.74658) &= 0.0977 \pm 0.0023,\\
\eta_R(r, z = 0.81056) &= 0.1009 \pm 0.0024,\\
\eta_R(r, z = 0.87688) &= 0.0982 \pm 0.0021,\\
\eta_R(r, z = 0.99958) &= 0.1000 \pm 0.0020,\\
\eta_R(r, z = 1.12875) &= 0.1004 \pm 0.0020,\\
\eta_R(r, z = 1.24679) &= 0.9799 \pm 0.0020,\\
\eta_R(r, z = 1.32910) &= 0.0956 \pm 0.0019,\\
\eta_R(r, z = 1.39368) &= 0.0981 \pm 0.0020,\\
\eta_R(r, z = 1.45825) &= 0.1008 \pm 0.0020,\\
\eta_R(r, z = 1.59455) &= 0.1003 \pm 0.0021,\\
\eta_R(r, z = 1.73842) &= 0.0956 \pm 0.0023,\\
\eta_R(r, z = 1.81435) &= 0.0988 \pm 0.0021,\\
\eta_R(r, z = 1.89027) &= 0.0970 \pm 0.0024,\\
\eta_R(r, z = 2.05053) &= 0.1004 \pm 0.0027.
\end{aligned} \tag{3.54}$$

Using this data, in combination with the Planck covariance matrix, with best fits fixed to the ones of the reference cosmology, I obtain the posterior distribution shown in Fig. 3.17. Table 3.6 shows the means, 68% and 95% limits for the free parameters.

In this case there is a much larger improvement on all the constraints. The neutrino total mass improves by 14% on the 2-σ limit with respect to using Planck alone. Most notably, the constraint on the cold dark matter density parameter, $\Omega_{cdm}h^2$, improves by over 40%. Also the spectral index n_s shows a 10% improvement and the constraint on the Hubble constant H_0 improves by 20%.

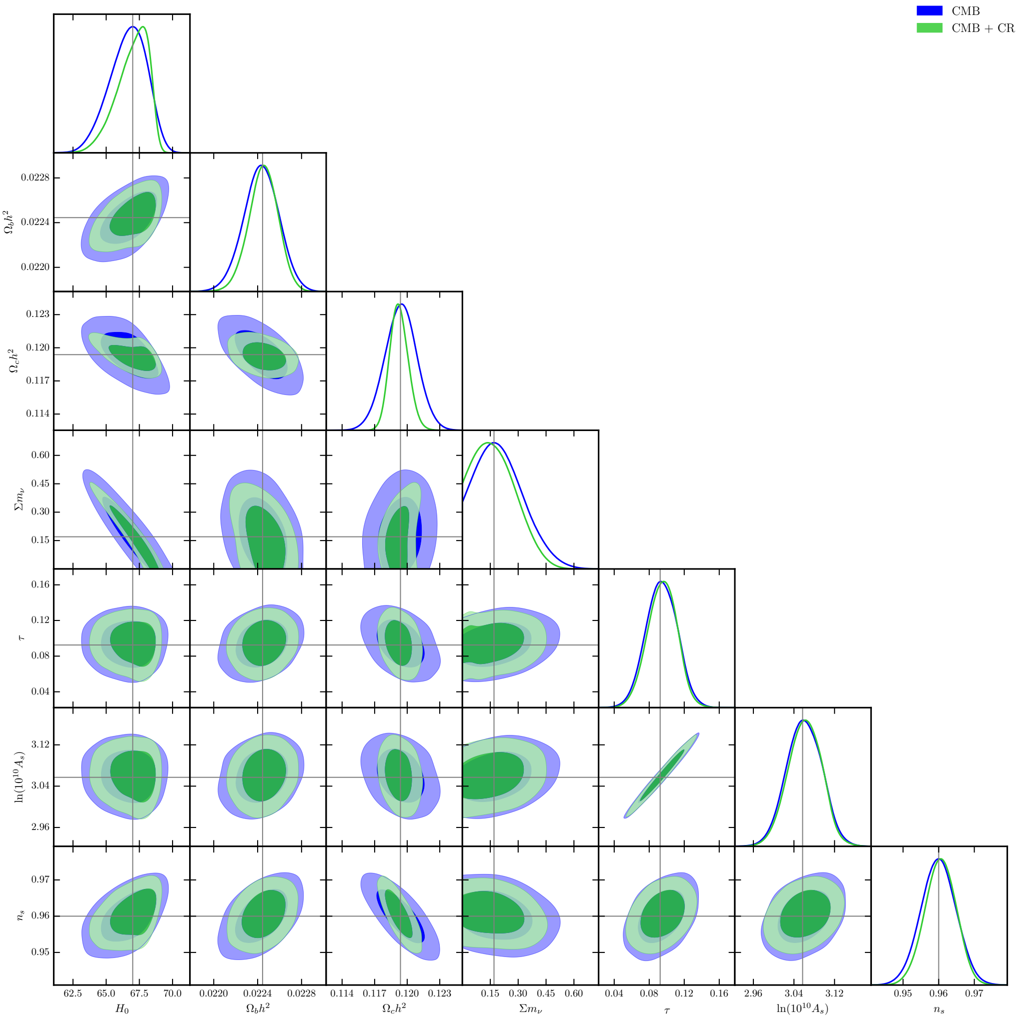

Figure 3.17: The 2D contours of the posterior distribution obtained using jointly the clustering ratio expected for a Euclid-like galaxy survey and Planck's temperature and polarization anisotropies (TTTEEE). In blue, the result obtained using only Planck's data is shown for reference. Inner, solid regions correspond to 68% contours, semi-transparent regions correspond to 95% contours.

This means that, when new data, covering a larger volume, will be available, the clustering ratio is expected to contribute to a significant improvement on the constraints on the parameters of the cosmological model.

Note also that, as more different observations are carried out, it becomes very interesting to enhance the constraining power of the clustering ratio also combining its measurements in different datasets. This can be easily done since the clustering ratio is a single measure, thus scarcely dependent on the survey geometry.

CHAPTER 4

Effects of neutrinos on the galaxy power spectrum

In the previous chapter, I addressed the problem of describing the galaxy-matter biasing function choosing a smoothed cosmological observable, the clustering ratio, that on certain scales is blind to bias and to nonlinear effects. However, this approach precludes the information coming from the small scale clustering of galaxies. A complementary approach, aimed at exploiting the large amount of information encompassed in the small scale range, is to model the galaxy power spectrum in the fully nonlinear regime. This task is not simple since the galaxy-matter relation and the galaxy formation details are in large part unknown. Moreover, when we add new parameters to describe the nonlinear galaxy bias, we incur the risk that they can mimic neutrino effects. In this case, the degeneracy between bias parameters and the neutrino total mass might undermine the constraining power of the galaxy power spectrum.

To model the nonlinear clustering of galaxies, once again we need simulations. Hydrodynamical simulations, which evolve at the same time both the dark matter and the baryonic (gas) components, can be used to study the processes of galaxy formation inside dark matter haloes (one recent example being given by the BAHAMAS simulations, McCarthy et al., 2017). However, such simulations, being quite expensive, often do not cover large volumes.

Another approach, which nevertheless benefits from calibration with hydrodynamical simulations, is to search for models to populate the dark matter haloes of a N-body simulation with galaxies. One of the fundamental frameworks in which such models can be developed is the Halo Occupation Distribution (HOD), which is naturally defined within the formalism of the Halo Model (Press and Schechter, 1974; Cooray and Sheth, 2002; Berlind and Weinberg, 2002; Zheng et al., 2005). In the HOD approach the galaxy population is split into centrals and satellites. The number of central and satellite galaxies in each halo only depends on the mass of the host halo itself. On top of that, within the framework of semi-analytic models, we try to develop recipes, calibrated on some physical observables (such as the angular correlation function), to describe galaxy formation processes and assign sensible characteristics to these galaxies, such as luminosities, colors, stellar populations, star formation rates and so on (see, for example, the review by Baugh, 2006).

Finally, yet a different approach is represented by the Sub-Halo Abundance Matching (SHAM). This is a class of models that place galaxies in the deepest wells of the gravitational potential, employing a matching between a galaxy property and a halo property. For example, Vale and Ostriker (2004) assumed galaxy luminosities to be a monotonic function of halo mass, or Guo et al. (2010) showed that the stellar mass of a galaxy is well described by a function of the maximum mass ever attained by its halo. More recent implementations of SHAM flavours have subsequently been developed, for example by matching the luminosity function of galaxies to the circular velocity of sub-haloes (Trujillo-Gomez et al., 2011). One interesting point about the SHAM approach is that many galaxy properties (such as positions and velocities, but also the number of satellites in a dark matter halo) directly come from the simulation itself, and are not assigned ad-hoc.

In this chapter, I will employ the sub-halo abundance matching technique to populate the first set of the DEMNUni simulations with galaxies. To this purpose I will use the sub-haloes produced by C. Carbone by post-processing these simulations with the `subfind` code, which is part of the `GADGET` suit (Springel, 2005). This code analyses haloes found with a Friend-of-Friends algorithm and determines the sub-haloes corresponding to local minima in the potential. While haloes in the DEMNUni simulations are composed of a minimum number of particles $N^h_{\mathrm{p,min}} = 32$, sub-haloes are formed at least of $N^{sh}_{\mathrm{p,min}} = 20$. After producing the galaxy catalogues, I will study the galaxy power spectrum in the presence of neutrinos, comparing it to some popular models of galaxy bias.

4.1 Sub-Halo Abundance Matching

Sub-Halo Abundance Matching is a technique employed to populate a dark matter simulation with galaxies. Its basic idea is to connect properties of a dark matter sub-halo with properties of the galaxy living in it. In practice, the dark matter sub-halo acts as a proxy of the depth and shape of the potential well, so that galaxies, in the SHAM formalism, are placed in the center-of-mass of such sub-haloes and inherit their velocities.

One of the most common choices is to place galaxies according to the maximum of the Newtonian circular velocity of sub-haloes at a given redshift,

$$v_{\mathrm{circ,max}} = \max\left[\sqrt{\frac{G\,M(<R)}{R}}\right], \tag{4.1}$$

which is sensible both to the depth and to the shape of the profile of local minima in the gravitational potential.

There exist also other possible flavours of SHAM, which differ in the choice of the proxy for the potential wells. Chaves-Montero et al. (2016) thoroughly examines many possible choices, investigating their consequences by comparing to hydrodynamic simulations.

In this work, I populate the first set of the DEMNUni simulations with galaxies, using the SHAM technique and choosing the maximum of the circular velocity defined in Eq. 4.1 as the SHAM parameter. I force the galaxy population to match three different choices of number density, namely $\bar{n} = \{1\times10^{-3}, 3\times10^{-4}, 1\times10^{-4}\}\ h^3\ \mathrm{Mpc}^{-3}$. Each of these choices is not a randomly sparser sample, but a more biased sampling of the original population, since each of them correspond to a higher cut in $v_{\mathrm{circ,max}}$. The mass function of sub-haloes with the different cuts in $v_{\mathrm{circ,max}}$ is shown in Fig. 4.1. Indeed, as the number density decreases, the low-mass end is depleted, meaning that we are selecting more biased objects.

As a result of the selection, we expect the three samples to represent complete galaxy populations, each of them reproducing a specific HOD model, with given number of central and satellite galaxies per halo mass. Fig. 4.2 shows the number of sub-haloes per halo of a given mass, for the three different samples. As the number density decreases,

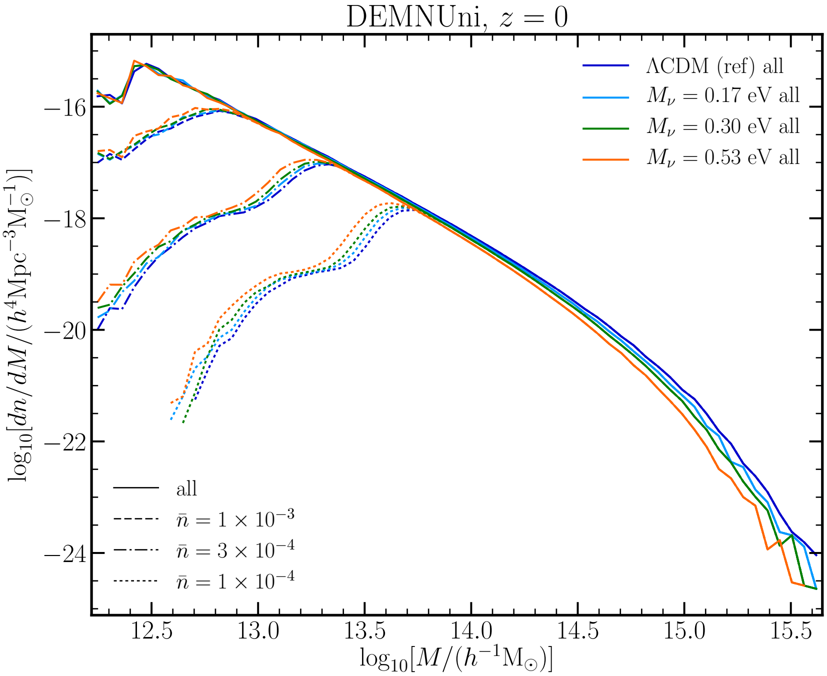

Figure 4.1: Mass function of sub-haloes selected adopting different cuts in the maximum circular velocity $v_{\mathrm{circ,max}}$. The cuts correspond to number densities of $\bar{n} = \{1 \times 10^{-3}, 3 \times 10^{-4}, 1 \times 10^{-4}\}\ h^3\ \mathrm{Mpc}^{-3}$.

the minimum mass needed to form a central galaxy increases. Moreover, forcing cosmologies with and without massive neutrinos to have the same number density, introduces a scatter in the number of satellite per halo. As a matter of fact, to reach the same number density, in a cosmology with massive neutrinos a higher number of satellites needs to be assigned to a halo of a given mass, with respect to the standard ΛCDM case.

These galaxy catalogues allow for measuring the fully nonlinear galaxy power spectrum from simulations with different neutrino masses. Moreover, even if at this stage I have not assigned physical properties to the galaxies, the three arbitrary cuts in number densities provide us with samples characterized by different bias properties.

4.2 Galaxy constraining power

The main goal of this work, which exploits the galaxy catalogues created from the DEMNUni simulations in the fashion described in the previous section, is to assess the question whether the galaxy power spectrum is informative about the value of the total mass of neutrinos, or the parameters introduced to describe the galaxy-matter bias are degenerate with neutrino effects.

To this purpose, I measure the power spectra of the galaxy samples with $\bar{n} = 10^{-3} h^3\ \mathrm{Mpc}^{-3}$ and $\bar{n} = 10^{-4} h^3\ \mathrm{Mpc}^{-3}$. To measure these power spectra I employ the code presented in Sefusatti et al. (2016) and publicly available[1]. Since the direct summation method is computationally very expensive when dealing with a large number of objects, I choose

---

[1] `https://github.com/sefusatti/PowerI4`

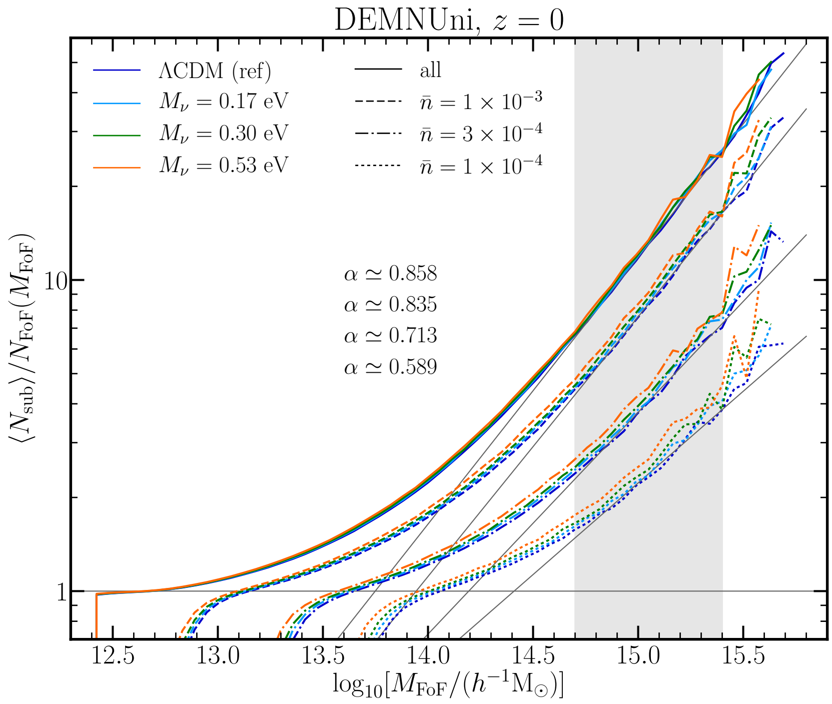

Figure 4.2: Each sub-halo sub-set, selected to reproduce a different number density, corresponds to a different HOD. The minimum mass required to have a central galaxy increases as the sample gets sparser. Moreover, forcing the models with and without massive neutrinos to have the same number density, introduces a scatter in the number of satellites that is not present when the entire sample is used (solid lines).

to compute power spectra assigning particles to a density grid in real space, that is subsequently Fourier transformed. The fourth order mass assignment scheme provided in this code minimizes grid effects, and the interlacing of two grids alleviates the aliasing due to the finite size of the grid.

The error on the estimation of the power spectrum should in principle account for the covariance among the different k bins, according to Eq. 1.112.

The non-Gaussian part of the covariance matrix can be important when nonlinearities are considered, as they introduce a coupling between different wavemodes. However, at this stage, I approximate the covariance considering only its Gaussian part, and neglecting the trispectrum. Blot et al. (2015) showed that this approach leads to an underestimation of the error on the fitted cosmological parameters. However, the goal of this work is investigating the degeneracy between nonlinear bias parameters and neutrino effects: Therefore I will leave the quantification of the impact on the parameter constraints to a future work. In the remaining part of this chapter I will present Gaussian errors on the power spectrum, which correspond to the diagonal terms of the covariance matrix.

I will consider different biasing models. In all cases with non-zero neutrino mass, I will assume the galaxy power spectrum to be connected to the underlying linear cold matter power spectrum (CDM + baryons), as

$$P_{\rm g} = F(P^L_{cb}). \tag{4.2}$$

The fact that the power spectrum of structures depends on the power spectrum of the cold component only is justified, in the case of dark matter haloes, in Castorina et al. (2015). Arguably, on the scale where galaxy formation is effective, neutrino perturbations are negligible (they enter only as long wavelength modes), and the matter distribution is dominated by CDM and baryons, as can be seen in Fig. 4.3. Moreover, I choose here to define the bias with respect to the linear theory prediction, even if, from the simulations, I have access to the fully nonlinear cold matter distribution. This choice relies on two reasons: first it is an attempt to proceed as in the analysis of real data, when the information on the underlying field is not accessible; second, nonlinear effects are described as a function of the variance of the linear power spectrum, usually smoothed on a $8\ h\ \mathrm{Mpc}^{-1}$ scale, thus making the linear prediction the quantity of interest in this analysis. For the time being, moreover, I will limit my analysis to the real space power spectrum, which serves as a proof-of-concept of the method, while I plan to extend this analysis in the future to the multipoles of the power spectrum in redshift space.

To assess the goodness of the fit of a model to the measured power spectrum, I compute the χ^2, in the Gaussian-error approximation, with the estimator

$$\hat{\chi}^2 = \sum_i^N \frac{[P_{\rm gg}(k_i) - P_{\rm model}(k_i)]^2}{C_{ii}}. \tag{4.3}$$

Note that this quantity follows a χ^2 distribution with $N - N_p$ degrees of freedom, N_p being the number of parameters of the model. A goodness of fit test with significance $\alpha = 0.05$ can therefore be performed stating that

$$P(\hat{\chi}^2 > \chi^2_{1-\alpha}(N - N_p)) = \alpha, \tag{4.4}$$

where $\chi^2_{1-\alpha}(N - N_p)$ is given by

$$1 - \alpha = \int_0^{\chi^2_{1-\alpha}(N-N_p)} \mathrm{d}\chi^2\ \chi^2(N - N_p)\ . \tag{4.5}$$

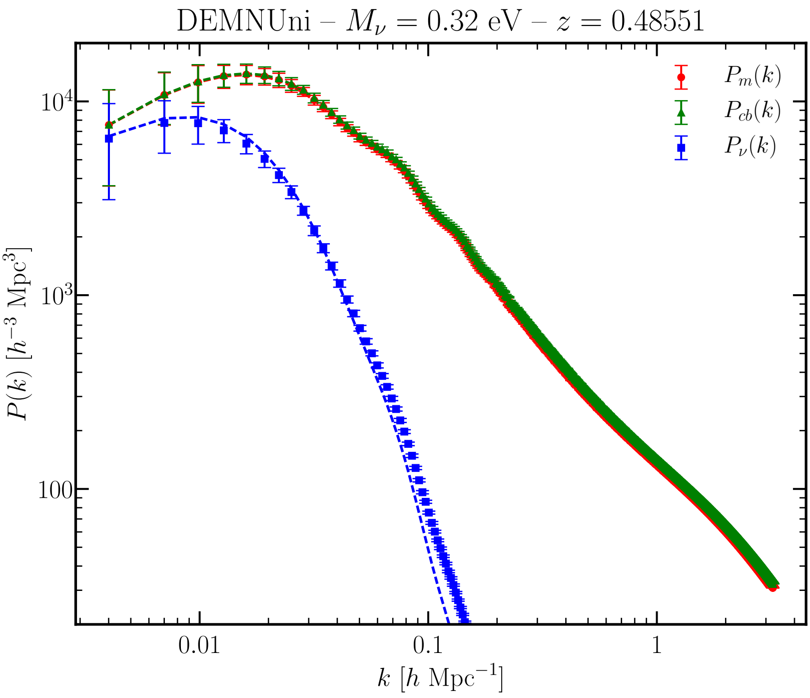

Figure 4.3: The power spectrum of total matter, $P_m(k)$, of cold matter, $P_{cb}(k)$, and of neutrinos, $P_\nu(k)$, in the DEMNUni simulation with $M_\nu = 0.32$ eV, at redshift $z = 0.48551$. The Gaussian errors on the measured power spectrum are shown in the plot. Dashed lines correspond to the nonlinear prediction for the matter power spectrum, the nonlinear prediction for the cold power spectrum and the linear prediction for the neutrino power spectrum. For wavemodes $k \gtrsim 0.1h\ \mathrm{Mpc}^{-1}$ nonlinearities in the total matter power spectrum are induced by the growth of dark matter perturbations (CDM+baryons) while the contribution of neutrino perturbations is negligible.

As a consequence, if $\hat{\chi}^2 > \chi^2_{1-\alpha}(N - N_p)$ the model is rejected, otherwise it is not rejected.

For each of the nonlinear biasing models I will first show the minimum scale that can be included in the fit without rejecting the model. Then, I will try to fit the measurement of the galaxy power spectrum in the ΛCDM simulation, computing the model assuming different neutrino masses. In this way I aim at investigating whether this models can reject a wrong hypothesis (*i.e.* a total neutrino mass different from the one in the measured power spectrum) or, on the contrary, the parameters introduced to describe the biasing model can mimic the effect of neutrinos and decrease the constraining power of the galaxy power spectrum.

The fits are performed using `emcee`, a fast python library that runs MCMC chains adopting a Goodman-Weare algorithm to explore the posterior (Foreman-Mackey et al., 2013). I have tested these results against an MCMC C-code developed by me, which adopts a Metropolis-Hastings algorithm (which is in principle more prone to get stuck on a local maximum of the likelihood). The two codes give compatible results, and the ones presented here come from `emcee`, which can easily be integrated directly in the plotting routines. In all cases I check the convergence of the chains applying a Gelman-Rubin test. This is a statistical test that compares the variance of the single chains and the variance of their combination to provide a rough criterion of convergence.

4.2.1 Linear bias

The first model is the simple linear bias model,

$$P_g(k) = b_1^2 \, P_{cb}^L(k), \tag{4.6}$$

in which the galaxy-galaxy power spectrum differs from the auto power spectrum of cold matter only by a multiplicative factor.

Fig. 4.4 shows the galaxy power spectra measured in the simulations with different neutrino masses, compared to linear predictions for the cold matter, along with the bias inferred from the comparison, at redshifst $z = 0$ and $z \sim 0.5$, for the case with $\bar{n} = 1 \times 10^{-3} \ h^3 \ \mathrm{Mpc}^{-3}$.

In particular, the first row shows the ratio to the ΛCDM case of the cold matter power spectra in cosmologies with $M_\nu = \{0, 0.17, 0.30, 0.53\}$ eV. The measured ratio follows the linear prediction on large scales, while for $k \gtrsim 0.2 \ h \ \mathrm{Mpc}^{-1}$ departures appear due to nonlinearities. In general, the asymptotic small-scale suppression induced by neutrinos on the cold matter clustering is expected to be of order 10% for the lightest neutrino choice, and of order 25% for the heaviest (in linear theory). Moreover, this figure shows the characteristic shape of the scale dependence introduced by neutrinos.

The second row in Fig. 4.4 shows the ratio to the ΛCDM case of the galaxy power spectrum. Since different neutrino cosmologies can exhibit a different bias, the relative amplitudes of these power spectra does not correspond to those of the cold matter. I also recall that the same number density was imposed to the galaxy samples in the different cosmologies, which justifies the scatter among the lines visible on small-scales. As a consequence, the asymptotic small-scale neutrino suppression is no longer clearly visible. However, the characteristic scale dependence is still present. Therefore, the comparison of the entire range of scales seems to help in distinguishing the effect of neutrinos.

The third row in Fig. 4.4 presents the linear bias. From this figure we can observe that the larger the total neutrino mass, the larger the bias. This is expected, since haloes of a given mass are rarer in a cosmology with $M_\nu \neq 0$ than in a ΛCDM one (Massara et al., 2014).

Finally, the last row shows the ratio to the ΛCDM case of the linear bias. In the presence of neutrinos, it does not show a particularly significant scale dependence with respect to the linear bias in the ΛCDM cosmology. However, on small-scales, nonlinearities induce a small deviation.

I fit these galaxy power spectra with the linear bias model, with the purpose of finding the minimum scale that the model can reach without being rejected with the χ^2 test presented in 4.4. I found that the largest k_{max} not rejected by the test, both for the sparse and the dense sample, is $k \sim 0.1 \ h \ \mathrm{Mpc}^{-1}$.

The values of the large-scale ($k < 0.1 \ h \ \mathrm{Mpc}^{-1}$), linear bias obtained at $z \sim 0.5$ for this galaxy sample are

$$\begin{aligned} b_1(M_\nu = 0) &= 1.5492 \pm 0.0047, \\ b_1(M_\nu = 0.17) &= 1.6104 \pm 0.0047, \\ b_1(M_\nu = 0.30) &= 1.6659 \pm 0.0050, \\ b_1(M_\nu = 0.53) &= 1.7738 \pm 0.0052 \, . \end{aligned} \tag{4.7}$$

Performing the same analysis for the galaxy sample with $\bar{n} = 1 \times 10^{-4} \ h^3 \ \mathrm{Mpc}^{-3}$, leads to similar conclusions. Fig. 4.5 shows the linear bias of this sample, which is in general

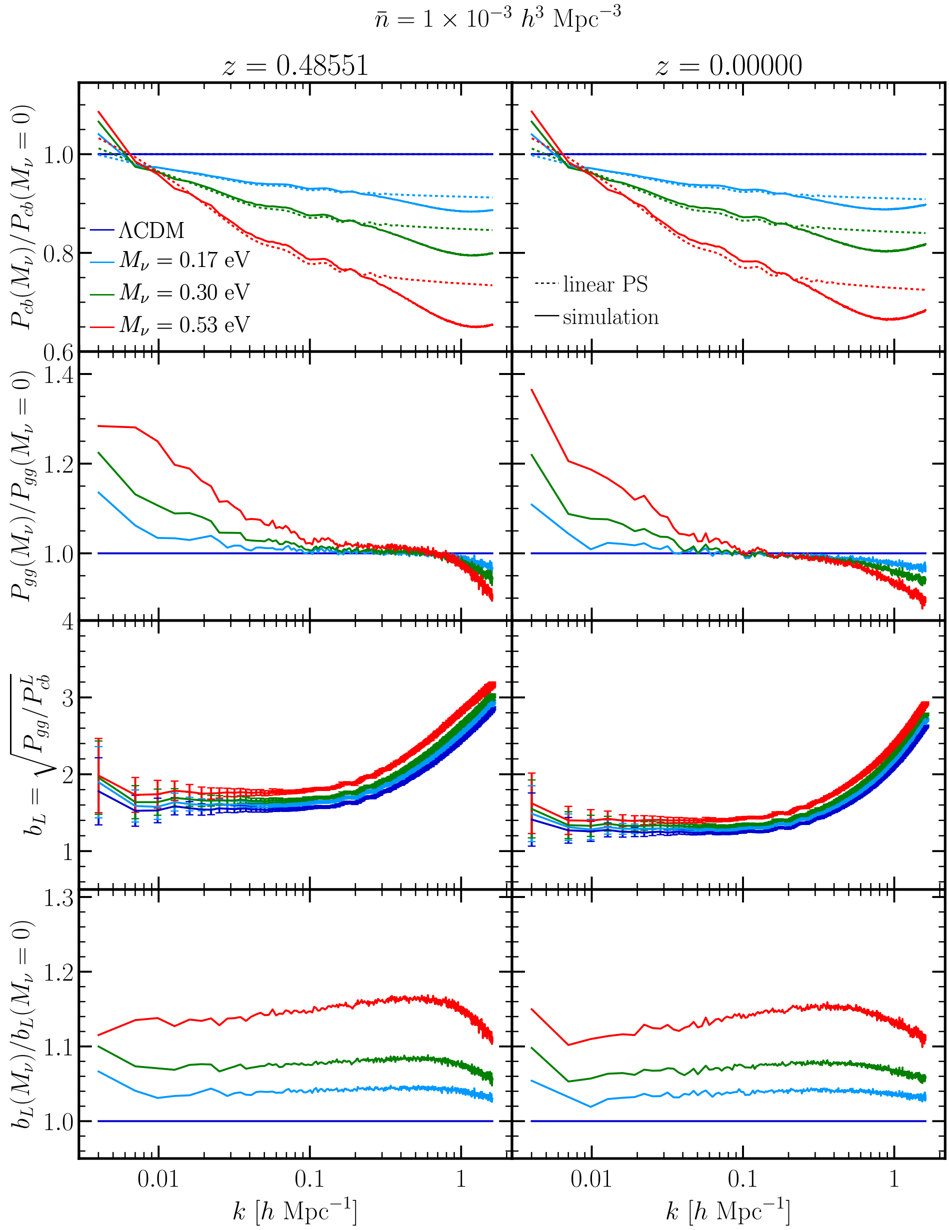

Figure 4.4: *Top panels:* ratio of the cold matter power spectrum measured in the neutrino simulations to the ΛCDM case (solid lines), and the same ratio obtained with linear predictions (dotted lines); the effect of neutrinos appears as a scale-dependent small-scale suppression, enhanced, for $k > 0.2\ h\ \mathrm{Mpc}^{-1}$, by nonlinearities. *Second row:* ratio of the galaxy power spectrum measured in the neutrino simulations to the ΛCDM case; the typical neutrino scale dependence is still present, even if the relative amplitudes are not conserved. *Third row:* the linear bias defined as the ratio between the galaxy power spectrum and the linear cold matter prediction; massive neutrinos enhance the bias. *Bottom panel:* ratio between the linear bias in the different cosmologies and the linear bias in ΛCDM; neutrinos only introduce a slight scale dependence in the bias.

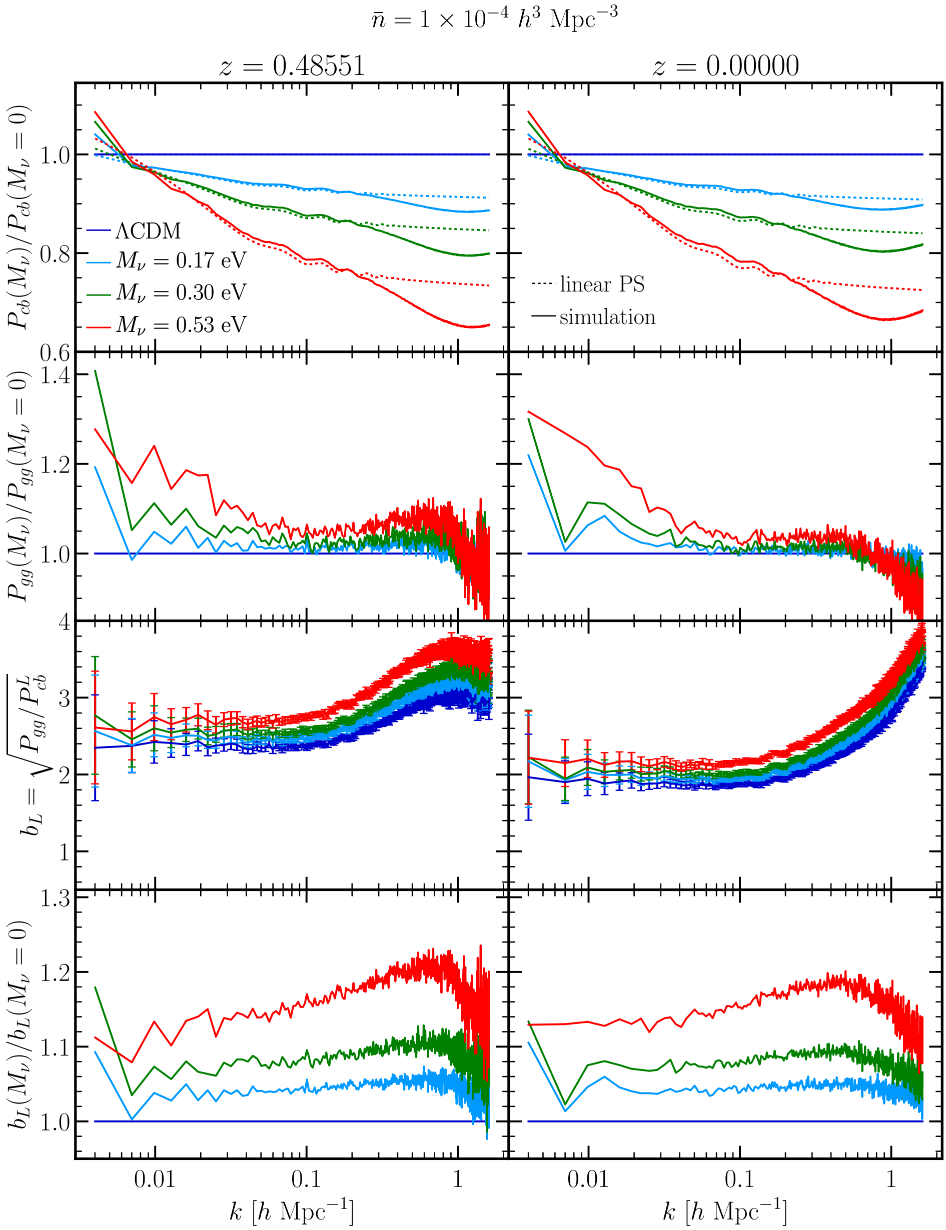

Figure 4.5: Same as Fig. 4.4, but for the more biased sample, with number density $\bar{n} = 1 \times 10^{-4}\ h^3\ \mathrm{Mpc}^{-3}$.

larger than the previous ones. The values of the large-scale linear bias in this case are

$$\begin{aligned} b_1(M_\nu = 0) &= 2.3603 \pm 0.0084, \\ b_1(M_\nu = 0.17) &= 2.4570 \pm 0.0087, \\ b_1(M_\nu = 0.30) &= 2.5464 \pm 0.0095, \\ b_1(M_\nu = 0.53) &= 2.7110 \pm 0.0100\ . \end{aligned} \tag{4.8}$$

As a matter of fact these objects have been selected to have larger circular velocities, and are therefore placed in deeper potential wells.

4.2.2 Q-model

This model was presented for the first time in Cole et al. (2005). The connection between the cold matter power spectrum and the galaxy power spectrum reads

$$P_{\rm g}(k) = b_1^2 \left(\frac{1+Qk^2}{1+Ak}\right) P^L_{\rm cb}(k), \tag{4.9}$$

where $b_1,\ A$ and Q are free parameters. Note that in the original article b_1 was determined independently and only afterwards A and Q were fitted. The original result, with 2dFGRS data, was $A = 1.7,\ Q = 9.6$ (real space) and $A = 1.4,\ Q = 4$ (redshift space).

First of all, I investigate the minimum scale that can be described using this model applied to the power spectrum of a galaxy population with $\bar{n} = 1 \times 10^{-3}\ h^3\ \mathrm{Mpc}^{-3}$, at redshift $z \sim 0.5$. This is shown in Fig. 4.6 for both the ΛCDM case and the case with $M_\nu = 0.53$ eV. The goodness-of-fit test cannot reject the fits performed setting the minimum scale down to $k \sim 0.4\ h\ \mathrm{Mpc}^{-1}$. As the fit is pushed towards smaller scales, it is rejected with 0.05 significance. These results are shown also in Tab 4.1, where the bestfit, mean and 68% limits are shown for each parameter, along with their χ^2 and the result of the goodness-of-fit test.

The value of the large-scale linear bias obtained limiting the fit to $k < 0.1\ h\ \mathrm{Mpc}^{-1}$ (in the ΛCDM case at $z \sim 0.5$) is

$$b_1 = 1.5782^{+0.0569}_{-0.0493}, \tag{4.10}$$

which is compatible with the linear bias found in the previous session.

Fig. 4.7 assesses the determination of the minimum scale of the fit in the sparse galaxy sample, with $\bar{n} = 1 \times 10^{-4}\ h^3\ \mathrm{Mpc}^{-3}$. Such galaxies constitute a more biased sample, and are generally more massive objects. For this reason, they trace more closely the distribution of large dark matter haloes. In this case the fit is able to describe the galaxy power spectrum up to $k \sim 0.8\ \ h\ \mathrm{Mpc}^{-1}$ in the ΛCDM case, and up to $k \sim 0.6\ h\ \mathrm{Mpc}^{-1}$ in the case with $M_\nu = 0.53$ eV.

However, the sensitivity of the power spectrum on the neutrino mass not only depends on the minimum scale of the fit, but also on the maximum scale (*i.e.* on $k_{\rm min}$). Including large scales can alleviate some possible degeneracies between models with different σ_8, which would be degenerate limiting the analysis to small scales. Fig.s 4.8 and 4.9 show the dependency of the fit on the choice of $k_{\rm min}$ for the case with $\bar{n} = 1 \times 10^{-3}\ h^3\ \mathrm{Mpc}^{-3}$ and $\bar{n} = 1 \times 10^{-4}\ h^3\ \mathrm{Mpc}^{-3}$ respectively. Each figure includes two plots: one shows the measures of the galaxy power spectrum in the ΛCDM simulation, fitted with the Q-model in a ΛCDM cosmology, for different choices of $k_{\rm min}$; the other shows the galaxy power spectrum in the ΛCDM simulation fitted with the model computed in a cosmology with $M_\nu = 0.53$ eV, again for different $k_{\rm min}$. For each choice of

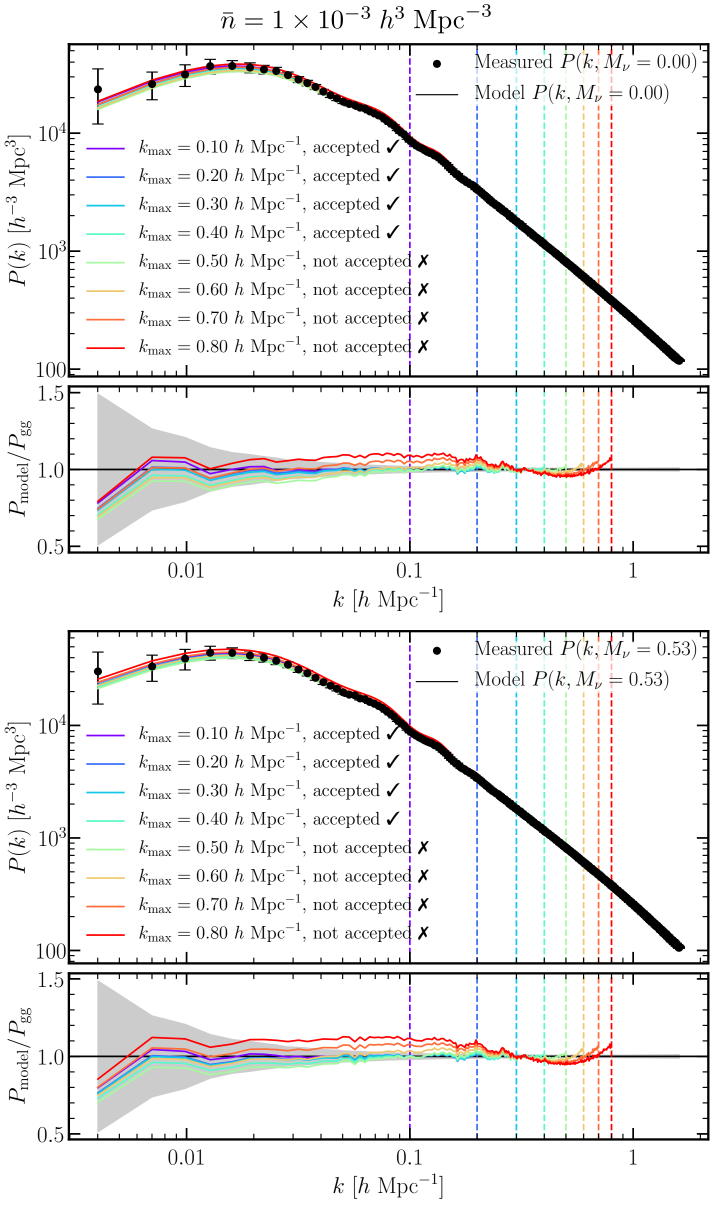

Figure 4.6: Q-model with the bestfit values obtained with different cuts in k_{max} for the galaxy sample with $\bar{n} = 1 \times 10^{-3}\ h^3\ \mathrm{Mpc}^{-3}$ at redshift $z = 0.48551$. Dashed vertical lines mark the different values of k_{max}. For each fit, the result of a χ^2 goodness-of-fit test is displayed, denoting whether the hypothesis assumed to compute the model is rejected or not. This model can describe the real space nonlinear power spectrum both in the ΛCDM case (upper figure) and in the most extreme massive neutrino model considered, $M_\nu = 0.53$ eV (lower figure), up to $k \sim 0.4\ h\ \mathrm{Mpc}^{-1}$. The fit is rejected for larger values of k_{max}.

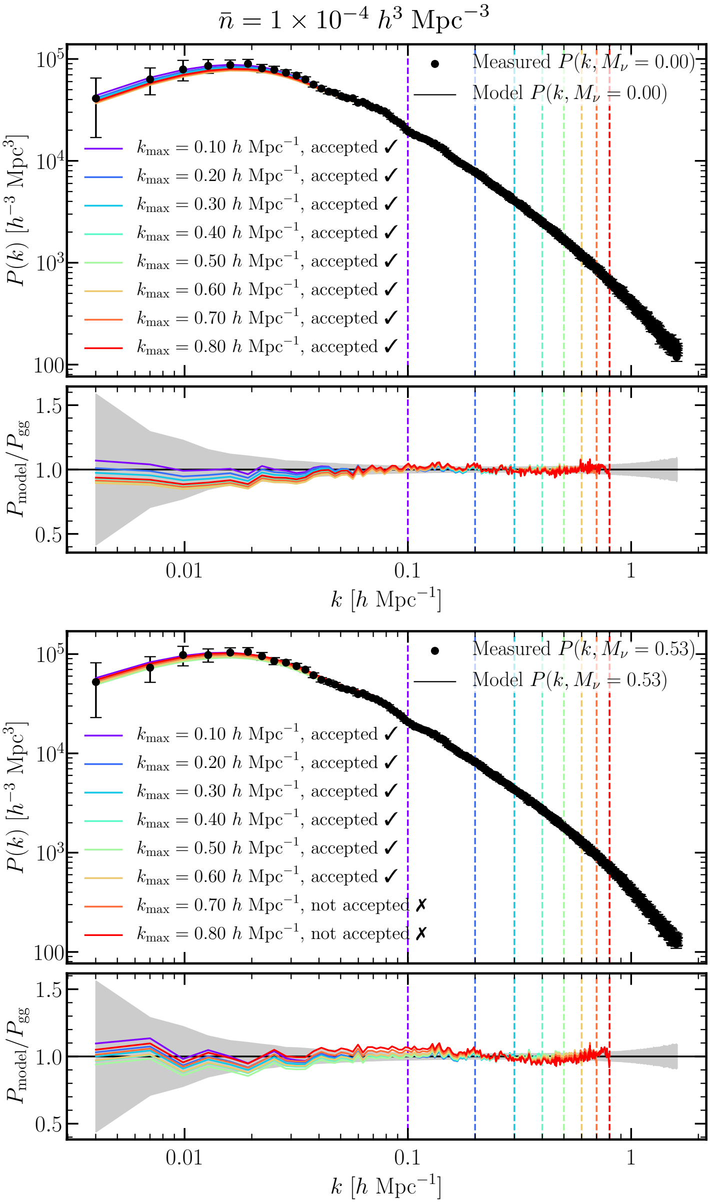

Figure 4.7: Same as in Fig 4.6, but for the sample with $\bar{n} = 1 \times 10^{-4}\ h^3\ \mathrm{Mpc}^{-3}$ at $z = 0.48551$, for the ΛCDM case (above) and a case with $M_\nu = 0.53$ eV (below). In this case the Q-model gives a good description of the galaxy power spectrum down to $k \sim 0.8h\ \mathrm{Mpc}^{-1}$ in the ΛCDM case ($k \sim 0.6h\ \mathrm{Mpc}^{-1}$ for $M_\nu = 0.53$ eV). This sample, as a matter of fact, only selects the most massive galaxies, which follow more closely the evolution of large haloes, less affected by nonlinearities.

$k_{\max}$	b_1 [bf/mean/68%]	Q [bf/mean/68%]	A [bf/mean/68%]	χ^2	#dof	
0.0975	1.5782 / 1.5971 / $^{+0.0569}_{-0.0493}$	16.2383 / 22.2505 / $^{+17.2934}_{-15.3071}$	1.8334 / 2.7137 / $^{+2.6914}_{-2.1491}$	1.9061	28	✓
0.1979	1.5376 / 1.5414 / $^{+0.0199}_{-0.0189}$	4.2462 / 4.6427 / $^{+1.9793}_{-1.8766}$	0.1132 / 0.2057 / $^{+0.4660}_{-0.4294}$	28.5332	60	✓
0.2985	1.5242 / 1.5251 / $^{+0.0115}_{-0.0114}$	2.7904 / 2.8513 / $^{+0.6947}_{-0.6825}$	-0.2152 / -0.1982 / $^{+0.1972}_{-0.1913}$	79.7779	92	✓
0.3990	1.4910 / 1.4916 / $^{+0.0082}_{-0.0080}$	0.3750 / 0.4070 / $^{+0.3717}_{-0.3599}$	-0.8428 / -0.8337 / $^{+0.1100}_{-0.1044}$	129.5881	124	✓
0.4995	1.4596 / 1.4601 / $^{+0.0064}_{-0.0061}$	-1.5030 / -1.4828 / $^{+0.2456}_{-0.2379}$	-1.3416 / -1.3359 / $^{+0.0707}_{-0.0671}$	230.8439	156	✗
0.5969	1.4772 / 1.4777 / $^{+0.0035}_{-0.0034}$	-1.5299 / -1.5120 / $^{+0.1256}_{-0.1221}$	-1.3100 / -1.3045 / $^{+0.0377}_{-0.0366}$	726.7698	187	✗
0.6974	1.5289 / 1.5293 / $^{+0.0027}_{-0.0027}$	-0.5598 / -0.5499 / $^{+0.0877}_{-0.0847}$	-0.9528 / -0.9493 / $^{+0.0300}_{-0.0289}$	2.1374×10^3	219	✗
0.7980	1.5815 / 1.5817 / $^{+0.0026}_{-0.0025}$	0.2984 / 0.3056 / $^{+0.0719}_{-0.0714}$	-0.5845 / -0.5818 / $^{+0.0280}_{-0.0274}$	4.4028×10^3	251	✗

Table 4.1: Galaxy sample with $\bar{n} = 1 \times 10^{-3}\ h^3\ \mathrm{Mpc}^{-3}$, constraints of the parameters of the Q-model for varying $k_{\max}$ (expressed in $[h\ \mathrm{Mpc}^{-1}]$). For each parameter the bestfit, mean and 68% limits are shown. The last 3 columns report the χ^2, the number of degrees of freedom and the result of a χ^2 test with significance 0.05 (✓ if not rejected, ✗ if rejected).

$k_{\min}$	b_1 [bf/mean/68%]	Q [bf/mean/68%]	A [bf/mean/68%]	χ^2	#dof	
0.0040	1.6263 / 1.6274 / $^{+0.0077}_{-0.0076}$	-2.5230 / -2.4749 / $^{+0.3492}_{-0.3439}$	-1.6686 / -1.6569 / $^{+0.0853}_{-0.0830}$	132.5858	124	✓
0.0098	1.6265 / 1.6273 / $^{+0.0079}_{-0.0074}$	-2.5141 / -2.4746 / $^{+0.3478}_{-0.3291}$	-1.6664 / -1.6569 / $^{+0.0857}_{-0.0793}$	132.2196	122	✓
0.0160	1.6267 / 1.6273 / $^{+0.0077}_{-0.0074}$	-2.5070 / -2.4757 / $^{+0.3520}_{-0.3325}$	-1.6647 / -1.6569 / $^{+0.0856}_{-0.0804}$	131.9298	120	✓
0.0317	1.6271 / 1.6283 / $^{+0.0080}_{-0.0077}$	-2.4911 / -2.4344 / $^{+0.3561}_{-0.3476}$	-1.6608 / -1.6470 / $^{+0.0876}_{-0.0838}$	131.5586	115	✓
0.0567	1.6243 / 1.6253 / $^{+0.0086}_{-0.0082}$	-2.6055 / -2.5657 / $^{+0.3895}_{-0.3651}$	-1.6888 / -1.6789 / $^{+0.0949}_{-0.0875}$	130.6748	107	✓
0.1100	1.6004 / 1.6026 / $^{+0.0111}_{-0.0105}$	-3.5897 / -3.4936 / $^{+0.4811}_{-0.4510}$	-1.9240 / -1.9019 / $^{+0.1128}_{-0.1033}$	119.3814	90	✗
0.2074	1.5743 / 1.6141 / $^{+0.0644}_{-0.0361}$	-4.6561 / -3.1327 / $^{+2.3081}_{-1.3717}$	-2.1653 / -1.8131 / $^{+0.6035}_{-0.3188}$	77.0048	59	✓

Table 4.2: Galaxy sample with $\bar{n} = 1 \times 10^{-3}\ h^3\ \mathrm{Mpc}^{-3}$, constraints of the parameters of the Q-model for varying $k_{\min}$ (expressed in $[h\ \mathrm{Mpc}^{-1}]$). For each parameter the bestfit, mean and 68% limits are shown. The last 3 columns report the χ^2, the number of degrees of freedom and the result of a χ^2 test with significance 0.05 (✓ if not rejected, ✗ if rejected).

$k_{\min}$, the corresponding result of the goodness-of-fit test is shown. Tables 4.2 and 4.3 show the bestfits, means, 68% limits and χ^2 of these fits, along with the result of the goodness-of-fit test, for the dense and the sparse sample respectively.

In the dense, less biased sample, when trying to fit the ΛCDM galaxy power spectrum with a model that assumes $M_\nu = 0.53$ eV, the χ^2-test never rejects the model (apart from a single case). This means that the nonlinear bias parameters are able to absorb the effects of neutrinos, thus lowering the constraining power of the model.

On the other hand, when using the spars, more biased galaxy sample, the χ^2-test correctly rejects the wrong hypothesis for all choices of $k_{\min} < 0.1\ h\ \mathrm{Mpc}^{-1}$. Arguably, the reason resides in the fact that, since with using this sample $k_{\max}$ can be pushed down to smaller scales, the combination of large and small scales in more efficient in breaking the degeneracy between the nonlinear bias parameters and neutrino effects. If $k_{\min} > 0.1\ h\ \mathrm{Mpc}^{-1}$, however, the lack of large-scale information restores this degeneracy, and the χ^2 test fails in rejecting the wrong hypothesis.

4.2.3 Nonlocal nonlinear model

This model has been proposed for the first time in McDonald and Roy (2009). More recently, it has then been employed for the analysis of the galaxy power spectrum measured within the BOSS collaboration (Beutler et al., 2014; Gil-Marín et al., 2015).

In Eq. 3.3 I introduced the local Eulerian bias, expanded with bias parameters $b_0, b_1, \ldots, b_n$, proposed by Fry and Gaztanaga (1993). However, the bias can in principle be a nonlocal function. For example, Chan et al. (2012) showed that the gravitational evo-

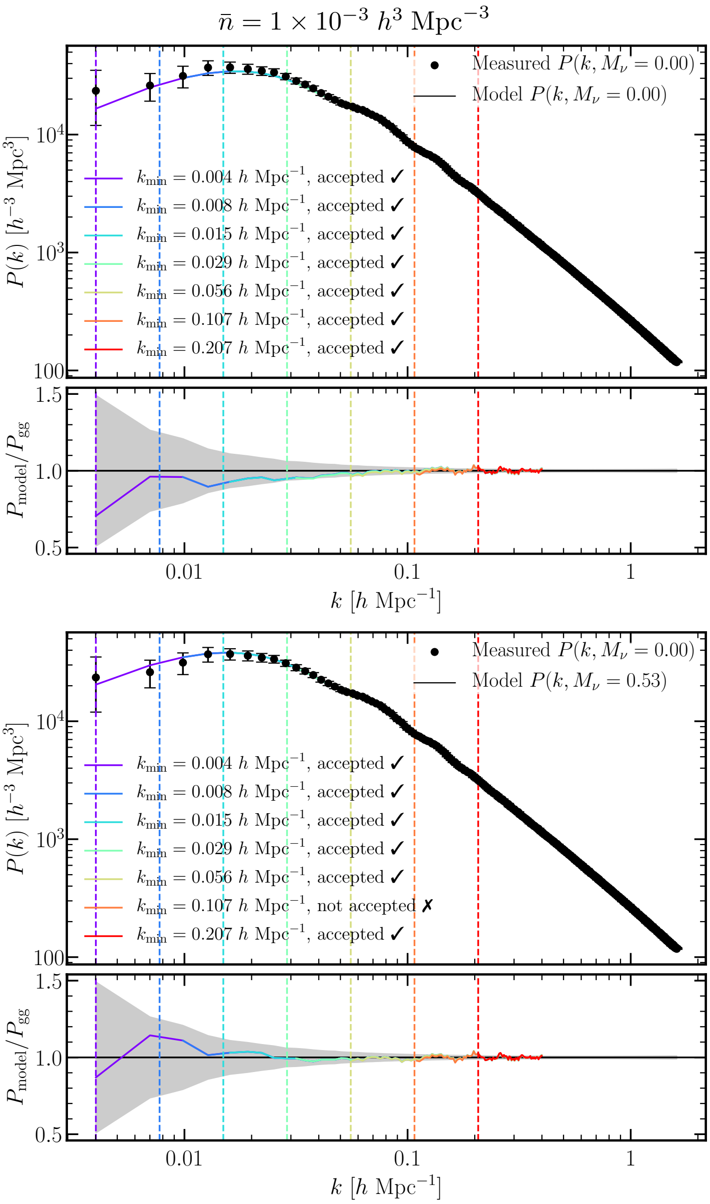

Figure 4.8: Dependence on the maximum scale of the fit for the Q-model, with different bestfit values obtained with different cuts in $k_{\rm min}$. *Upper figure:* the galaxy power spectrum in the ΛCDM simulation is fitted with the Q-model in ΛCDM. *Lower figure:* the galaxy power spectrum in the ΛCDM simulation is fitted with the model computed *assuming a non-zero neutrino mass*, namely $M_\nu = 0.53$ eV. For each choice of $k_{\rm min}$ the result of the χ^2 test with significance 0.05 is reported, showing whether the hypothesis on the value of neutrino mass assumed when computing the model is or is not rejected. In the upper figure, the test correctly never rejects the hypothesis. In the lower figure, the wrong hypothesis is never rejected (apart from the bin $k_{\rm min} \sim 0.1\ h$ Mpc^{-1}. In this case, the nonlinear bias parameters are degenerate with the total neutrino mass, whose effects are therefore masked.

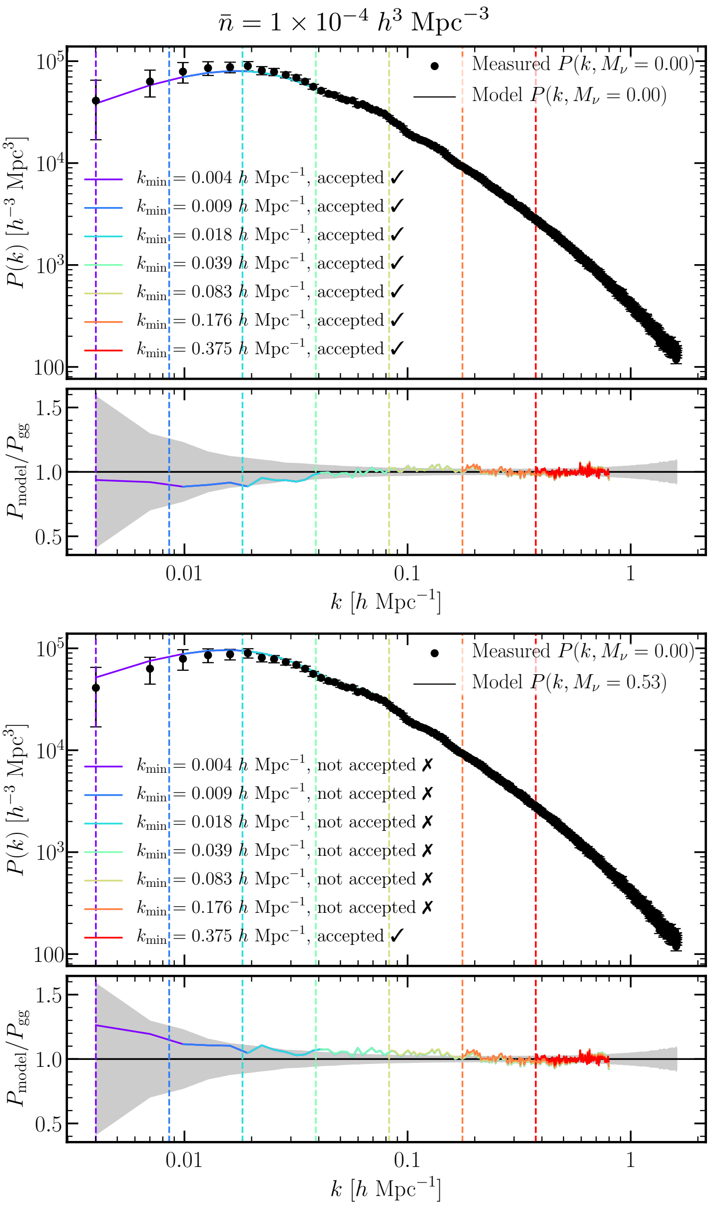

Figure 4.9: Same as in figure 4.8, but for the sample with $\bar{n} = 1 \times 10^{-4}\ h^3\ \mathrm{Mpc}^{-3}$. In this case, when the wrong hypothesis is assumed in the model (lower figure) the χ^2 test correctly rejects it with significance 0.05 for all $k_{\rm min} < 0.2\ h\ \mathrm{Mpc}^{-1}$, while does not reject it for larger $k_{\rm min}$. Arguably, the reason resides in the fact that, with this sample of more massive objects whose growth is more linear, the fit can be extended to higher wavemodes. As a consequence, the combination of large and small scales breaks the degeneracy between the nonlinear bias parameters and the effects of massive neutrinos.

$k_{\min}$	b_1 [bf/mean/68%]	Q [bf/mean/68%]	A [bf/mean/68%]	χ^2	#dof	
0.0040	2.5899 / 2.5906 / $^{+0.0030}_{-0.0029}$	-1.5220 / -1.5191 / $^{+0.0112}_{-0.0100}$	-1.2304 / -1.2291 / $^{+0.0050}_{-0.0045}$	421.3859	251	✗
0.0098	2.5900 / 2.5904 / $^{+0.0029}_{-0.0028}$	-1.5217 / -1.5195 / $^{+0.0111}_{-0.0098}$	-1.2302 / -1.2292 / $^{+0.0049}_{-0.0044}$	420.7467	249	✗
0.0192	2.5900 / 2.5906 / $^{+0.0030}_{-0.0029}$	-1.5215 / -1.5189 / $^{+0.0112}_{-0.0101}$	-1.2302 / -1.2290 / $^{+0.0050}_{-0.0046}$	419.2585	246	✗
0.0410	2.5905 / 2.5912 / $^{+0.0030}_{-0.0029}$	-1.5206 / -1.5179 / $^{+0.0115}_{-0.0100}$	-1.2297 / -1.2285 / $^{+0.0052}_{-0.0045}$	414.2243	239	✗
0.0849	2.5950 / 2.5955 / $^{+0.0032}_{-0.0032}$	-1.5112 / -1.5083 / $^{+0.0129}_{-0.0114}$	-1.2253 / -1.2240 / $^{+0.0057}_{-0.0051}$	376.2291	225	✗
0.1791	2.6189 / 2.6198 / $^{+0.0050}_{-0.0049}$	-1.4486 / -1.4440 / $^{+0.0241}_{-0.0208}$	-1.1959 / -1.1938 / $^{+0.0108}_{-0.0093}$	237.6218	195	✗
0.3770	2.7273 / 2.7395 / $^{+0.0318}_{-0.0266}$	-1.0805 / -1.0268 / $^{+0.1292}_{-0.1098}$	-1.0130 / -0.9855 / $^{+0.0687}_{-0.0562}$	75.0572	132	✓

Table 4.3: Galaxy sample with $\bar{n} = 1 \times 10^{-4}\ h^3\ \mathrm{Mpc}^{-3}$, constraints of the parameters of the Q-model for varying $k_{\min}$ (expressed in $[h\ \mathrm{Mpc}^{-1}]$). For each parameter the bestfit, mean and 68% limits are shown. The last 3 columns report the χ^2, the number of degrees of freedom and the result of a χ^2 test with significance 0.05 (✓ if not rejected, ✗ if rejected).

lution of the matter field inevitably introduces nonlocality, even if the bias is local at some early time. Supposing that the bias is local at early times can be approximated imposing locality in Lagrangian space. Doing so, and comparing against perturbation theory results, leads to finding that the bias in Eulerian space not only depends on the density in one point, but also on the tidal field. In a region where the tidal field is particularly high, it can significantly contrast the growth of structures, making them rarer. The nonlocal term comes from the tidal tensor $s^2(\boldsymbol{x}) = s_{ij}(\boldsymbol{x})s_{ij}(\boldsymbol{x})$, where $s_{ij}(\boldsymbol{x}) = \partial_i\partial_j\Phi(\boldsymbol{x}) - \delta^{\mathrm{Kr}}_{ij}\delta(\boldsymbol{x})$, and Φ is the gravitational potential. In Chan et al. (2012) it has been shown that the most important contribution to nonlocality comes from the second order nonlocal bias expansion.

However, in the modelling adopted by the BOSS collaboration (Beutler et al., 2014; Gil-Marín et al., 2015) also part of the third order contribution is retained, following the discussion in McDonald and Roy (2009). This contribution depends on a combination of terms in δ^3, δs^2, and $s^3 \equiv s_{ij}s_{jk}s_{ki}$. Adding these third order contributions, we can write

$$\begin{aligned}\delta_{\mathrm{g}}(\boldsymbol{x}) = b_1\delta(\boldsymbol{x}) &+ \frac{b_2}{2}\left[\delta^2(\boldsymbol{x}) - \sigma^2\right] + \frac{b_{s^2}}{2}\left[s^2(\boldsymbol{x}) - \langle s^2\rangle\right] \\ &+ \frac{b_3}{6}\left[\delta^3(\boldsymbol{x}) - \left\langle\delta^3(\boldsymbol{x})\right\rangle\right] + \frac{b_{s^2,\delta}}{2}\left[s^2\delta - \left\langle s^2\delta\right\rangle\right] + \frac{b_{s^3}}{6}\left[s^3 - \left\langle s^3\right\rangle\right] + \ldots\end{aligned} \tag{4.11}$$

Note anyway that s^3 has been shown to be zero. I do not report the entire derivation of the third order term, but I only mention that the third order contributions can be grouped together and described with an effective bias parameter b_{3nl}.

By Fourier transforming Eq. 4.11, one can compute $\langle\delta_{\mathrm{g}}(\boldsymbol{k}_1)\delta_{\mathrm{g}}(\boldsymbol{k}_2)\rangle$ to understand how the galaxy power spectrum can be written in terms of the (cold) matter power spectrum in real space. The result is

$$\begin{aligned}P_{\mathrm{g},\delta\delta}(k) = b_1^2P_{\delta\delta}(k) &+ 2b_1b_2P_{b_2,\delta}(k) + 2b_1b_{s^2}P_{b_{s^2},\delta}(k) + 2b_1b_{3\mathrm{nl}}\sigma_3^2(k)P^{\mathrm{lin}}(k) \\ &+ b_2^2P_{b_2^2}(k) + 2b_2b_{s^2}P_{b_2s^2}(k) + b_{s^2}^2P_{b_{s^2}^2}(k),\end{aligned} \tag{4.12}$$

where the different terms are

$$\begin{aligned}
P_{b_2\delta}(k) &= \int \frac{\mathrm{d}^3q}{(2\pi)^3} P^l(q) P^l(|\boldsymbol{k}-\boldsymbol{q}|)\mathcal{F}_2^{\mathrm{SPT}}(\boldsymbol{q},\boldsymbol{k}-\boldsymbol{q}), \\
P_{b_{s^2}\delta}(k) &= \int \frac{\mathrm{d}^3q}{(2\pi)^3} P^l(q) P^l(|\boldsymbol{k}-\boldsymbol{q}|)\mathcal{F}_2^{\mathrm{SPT}}(\boldsymbol{q},\boldsymbol{k}-\boldsymbol{q}) S_2(\boldsymbol{q},\boldsymbol{k}-\boldsymbol{q}), \\
P_{b_2 s^2}(k) &= -\frac{1}{2}\int \frac{\mathrm{d}^3q}{(2\pi)^3} P^l(q)\left[\frac{2}{3}P^l(q) - P^l(|\boldsymbol{k}-\boldsymbol{q}|) S_2(\boldsymbol{q},\boldsymbol{k}-\boldsymbol{q})\right], \\
P_{b^2_{s^2}}(k) &= -\frac{1}{2}\int \frac{\mathrm{d}^3q}{(2\pi)^3} P^l(q)\left[\frac{4}{9}P^l(q) - P^l(|\boldsymbol{k}-\boldsymbol{q}|) S_2^2(\boldsymbol{q},\boldsymbol{k}-\boldsymbol{q})\right], \\
P_{b_2^2}(k) &= -\frac{1}{2}\int \frac{\mathrm{d}^3q}{(2\pi)^3} P^l(q)\left[P^l(q) - P^l(|\boldsymbol{k}-\boldsymbol{q}|)\right], \\
\sigma_3^2(k) &= \int \frac{\mathrm{d}^3q}{(2\pi)^3} P^l(q)\left[\frac{5}{6} + \frac{15}{8} S_2(\boldsymbol{q},\boldsymbol{k}-\boldsymbol{q}) S_2(-\boldsymbol{q},\boldsymbol{k}) - \frac{5}{4} S_2(\boldsymbol{q},\boldsymbol{k}-\boldsymbol{q})\right],
\end{aligned} \tag{4.13}$$

and we have recalled the (symmetrised) kernel introduced in Eq. 1.60

$$\mathcal{F}_2^{\mathrm{SPT}}(\boldsymbol{k}_1,\boldsymbol{k}_2) = \frac{5}{7} + \frac{1}{2}\frac{\boldsymbol{k}_1\cdot\boldsymbol{k}_2}{k_1 k_2}\left[\frac{k_1}{k_2} + \frac{k_2}{k_1}\right] + \frac{2}{7}\left[\frac{\boldsymbol{k}_1\cdot\boldsymbol{k}_2}{k_1 k_2}\right]^2. \tag{4.14}$$

In order to numerically solve Eq.s 4.13 it is useful to exploit the symmetries of the power spectrum and turn them into 2-dimensional integrals.

Fig 4.10 shows the contributions of the different terms that enter this model. The matter power spectrum $P_{\delta\delta}$ is the leading term on large scales, while the other terms become important on small scales. The correction scheme is not trivial, as different terms have different signs, both adding and removing power.

Eq.s 4.12-4.13 can be implemented in a code to compute the model to be compared to the galaxy power spectrum with the aim of studying the likelihood of the parameters of the model given the data.

However, not all the bias parameters are independent, which allows us to reduce the number of free parameters in the model. If we assume that the galaxy bias, even if nonlocal in Eulerian space, is perfectly local in Lagrangian space (see eg Chan et al., 2012; Baldauf et al., 2012), then the second-order nonlocal bias parameters can be linked to the local linear bias as

$$b_{s^2} = -\frac{4}{7}(b_1 - 1). \tag{4.15}$$

However, this is quite a strong assumption, and tests with simulations have shown that even in Lagrangian space there can be departures from locality, which modify this equation. For example already Chan et al. (2012) propose a different fitting function

$$b_{s^2} = -\frac{4}{7}(b_1 - 1.43), \tag{4.16}$$

while more recently Bel et al. (2015) found

$$b_{s^2} = -\frac{4}{7}(b_1 - 0.8). \tag{4.17}$$

I will start assuming the approximate $b_{s^2} - b_1$ relation, derived assuming a local Lagrangian bias, and discuss the effect of the fitting formula presented here at the end of the section.

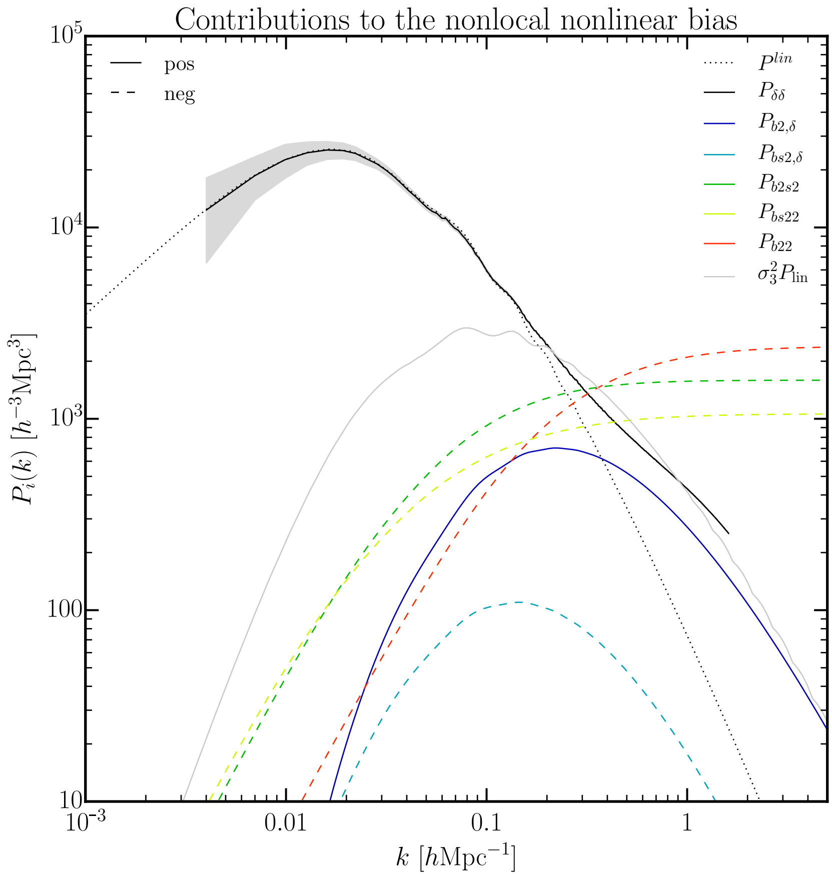

Figure 4.10: The contributions of the different terms that enter the non-local, nonlinear bias. Negative values are represented by dashed lines. The leading term on large scales is the matter power spectrum (here the solid line is the measured matter power spectrum in the simulation), while the other terms become important on small scales.

$k_{\rm max}$	b_1 [bf/mean/68%]	b_2 [bf/mean/68%]	χ^2	#dof	
0.0975	1.5503 / 1.5494 / $^{+0.0100}_{-0.0103}$	-0.011 / 0.0151 / $^{+0.2822}_{-0.2452}$	1.4028	29	✓
0.1979	1.5560 / 1.5558 / $^{+0.0042}_{-0.0042}$	-0.1362 / -0.1350 / $^{+0.0248}_{-0.0250}$	4.6103	61	✓
0.2985	1.5603 / 1.5603 / $^{+0.0026}_{-0.0027}$	-0.1642 / -0.1640 / $^{+0.0080}_{-0.0081}$	13.1030	93	✓
0.3990	1.5668 / 1.5668 / $^{+0.0019}_{-0.0020}$	-0.1881 / -0.1879 / $^{+0.0038}_{-0.0038}$	37.5035	125	✓
0.4995	1.5733 / 1.5733 / $^{+0.0015}_{-0.0015}$	-0.2045 / -0.2046 / $^{+0.0022}_{-0.0022}$	80.7503	157	✓
0.5969	1.5804 / 1.5804 / $^{+0.0013}_{-0.0013}$	-0.2182 / -0.2182 / $^{+0.0015}_{-0.0015}$	164.0548	188	✓
0.6974	1.5873 / 1.5873 / $^{+0.0011}_{-0.0011}$	-0.2289 / -0.2289 / $^{+0.0010}_{-0.0010}$	288.7572	220	✗
0.7980	1.5918 / 1.5918 / $^{+0.0010}_{-0.0010}$	-0.2348 / -0.2348 / $^{+0.0008}_{-0.0008}$	373.7237	252	✗

Table 4.4: Galaxy sample with $\bar{n} = 1 \times 10^{-3}\ h^3\ \mathrm{Mpc}^{-3}$, constraints of the parameters of the nonlocal nonlinear model for varying $k_{\rm max}$ (expressed in $[h\ \mathrm{Mpc}^{-1}]$). For each parameter the bestfit, mean and 68% limits are shown. The last 3 columns report the χ^2, the number of degrees of freedom and the result of a χ^2 test with significance 0.05 (✓ if not rejected, ✗ if rejected).

Also for the third order nonlocal bias parameter a relation can be established with the linear local bias. For example Beutler et al. (2014); Saito et al. (2014) find

$$b_{3\rm nl} = \frac{32}{315}(b1 - 1). \tag{4.18}$$

Once again, I start from determining the minimum scale that can be described using this model. In Fig. 4.11 and 4.12 I fit the model to the galaxy power spectrum ($\bar{n} = 1 \times 10^{-3}\ h^3\ \mathrm{Mpc}^{-3}$, $z \sim 0.5$), letting $k_{\rm max}$ vary in the range $[0.1, 0.8]\ h\ \mathrm{Mpc}^{-1}$, for galaxies measured in cosmologies with $M_\nu = \{0, 0.17, 0.30, 0.53\}$ eV. Tab. 4.4 shows the results of the fit in the ΛCDM case, displaying the bestfit, mean and 68% limits of each parameter, along with the χ^2 and the result of the χ^2 test.

For the sparse case with $\bar{n} = 1 \times 10^{-4}\ h^3\ \mathrm{Mpc}^{-3}$ Fig. 4.13 shows the fit in the ΛCDM case, the parameter constraints being reported in Tab. 4.5. The minimum scale allowed for the fit when $M_\nu \neq 0$ is the same as the ΛCDM one.

This model can be pushed down to smaller scales than the Q-model analysed in the previous section. In particular, for the dense sample the maximum $k_{\rm max}$ for which the χ^2 test does not reject the model is $0.6\ h\ \mathrm{Mpc}^{-1}$. Once again, for the sparse, more biased galaxy sample the minimum scale can be pushed even more towards small scales, up to $k_{\rm max} \sim 0.8\ h\ \mathrm{Mpc}^{-1}$.

Using these values of $k_{\rm max}$, I now study the dependence on $k_{\rm min}$, *i.e.* the largest scale included in the fit. In the same fashion adopted in the previous section, I fit the galaxy power spectrum measured in the ΛCDM simulation with the model computed assuming $M_\nu = \{0, 0.17, 0.3, 0.53\}$ eV. The goal is to verify in which cases the χ^2-test is able to correctly reject the wrong hypothesis.

The fits with the model assuming different neutrino masses are shown in Fig.s 4.14 and 4.15 for the galaxy sample with $\bar{n} = 1 \times 10^{-3}\ h^3\ \mathrm{Mpc}^{-3}$. The constraints on the parameters of the model (bestfit, mean, 68% limits, χ^2 and result of the χ^2 test) are reported only for the most extreme case (measures in ΛCDM and model assuming $M_\nu = 0.53$ eV) in Tab. 4.6. Moreover, Fig. 4.16 and Tab. 4.7, show the results of the fit for the sparse sample, only in the most extreme case.

Both in the sparse and in the dense cases, the χ^2 test is able to reject the wrong hypothesis of neutrino mass $M_\nu = 0.30$ ans 0.53 eV, when scales $k_{\rm min} < 0.03\ h\ \mathrm{Mpc}^{-1}$ and

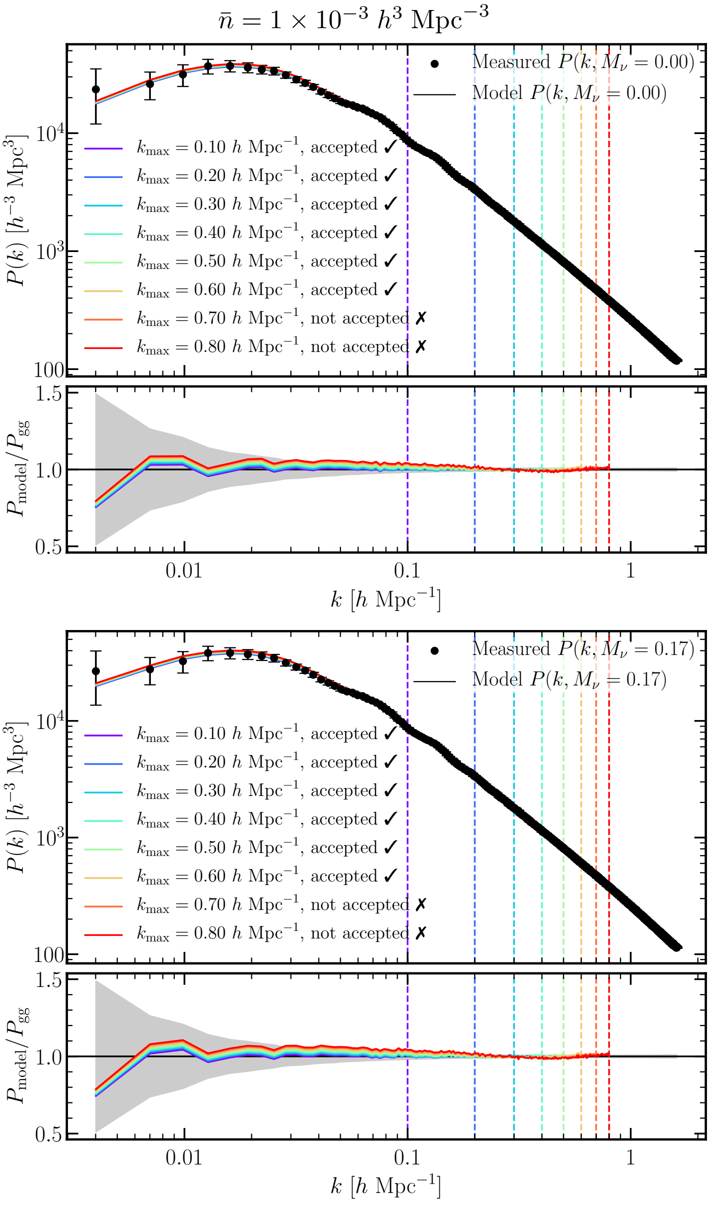

Figure 4.11: Nonlocal, nonlinear model with the bestfit values obtained with different cuts in $k_{\rm max}$ for the galaxy sample with $\bar{n} = 1 \times 10^{-3}\ h^3$ Mpc^{-3} at redshift $z = 0.48551$. Dashed vertical lines mark the different values of $k_{\rm max}$. For each fit, the result of a χ^2 goodness-of-fit test is displayed, denoting whether the hypothesis assumed to compute the model is rejected or not. This model can describe the real space nonlinear power spectrum both in the ΛCDM case (upper figure) and in the massive neutrino case with $M_\nu = 0.17$ eV (lower figure), up to $k \sim 0.6\ h$ Mpc^{-1}. The fit is rejected for larger values of $k_{\rm max}$.

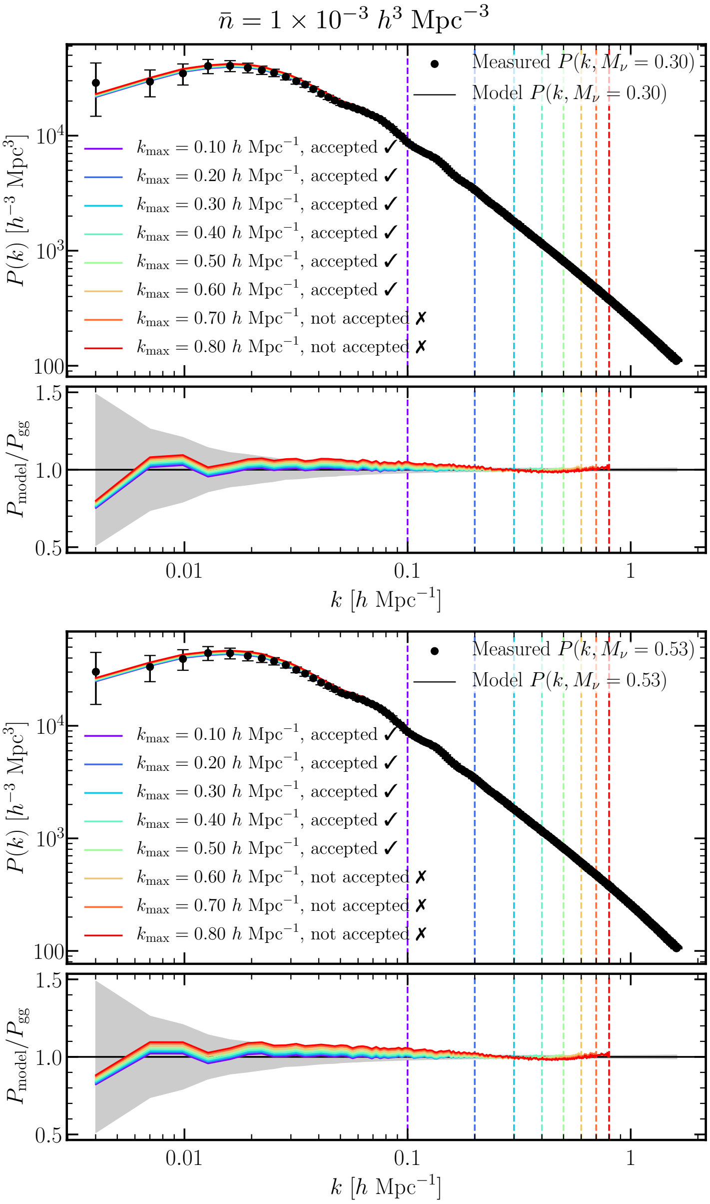

Figure 4.12: Same as in Fig. 4.11, but for the $\bar{n} = 1 \times 10^{-3}\ h^3\ \mathrm{Mpc}^{-3}$ sample. The model can describe the real space nonlinear power spectrum up to $k \sim 0.6\ h\ \mathrm{Mpc}^{-1}$ in the massive neutrino case with $M_\nu = 0.30$ eV (upper figure) and to $k \sim 0.5\ h\ \mathrm{Mpc}^{-1}$ in the case with $M_\nu = 0.53$ eV (lower figure). The fit is rejected for larger values of $k_{\rm max}$. This agrees with what found for $M_\nu = 0$ and 0.17 eV.

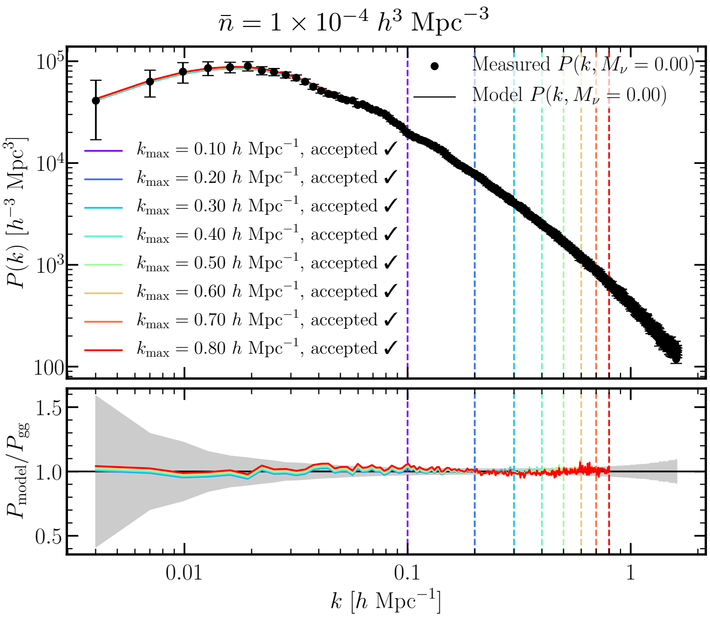

Figure 4.13: Nonlocal, nonlinear model with the bestfit values obtained with different cuts in $k_{\max}$ for the galaxy sample with $\bar{n} = 1 \times 10^{-4}\ h^3\ \mathrm{Mpc}^{-3}$ at redshift $z = 0.48551$. Dashed vertical lines mark the different values of $k_{\max}$. For each fit, the result of a χ^2 goodness-of-fit test is displayed, denoting whether the hypothesis assumed to compute the model is rejected or not. This model can describe the real space nonlinear power spectrum in the ΛCDM case up to $k \sim 0.8\ h\ \mathrm{Mpc}^{-1}$. Once again, this sample results less affected by nonlinearities, and the model can therefore pushed down to rather small scales.

$k_{\max}$	b_1 [bf/mean/68%]	b_2 [bf/mean/68%]	χ^2	#dof	
0.0975	2.3679 / 2.3667 / $^{+0.0182}_{-0.0180}$	-0.3548 / -0.3264 / $^{+0.3954}_{-0.3657}$	4.3885	29	✓
0.1979	2.3627 / 2.3622 / $^{+0.0086}_{-0.0085}$	-0.2508 / -0.2482 / $^{+0.0466}_{-0.0462}$	11.9365	61	✓
0.2985	2.3662 / 2.3661 / $^{+0.0058}_{-0.0058}$	-0.2626 / -0.2623 / $^{+0.0169}_{-0.0167}$	29.2056	93	✓
0.3990	2.3769 / 2.3770 / $^{+0.0046}_{-0.0046}$	-0.3034 / -0.3034 / $^{+0.0088}_{-0.0087}$	52.5292	125	✓
0.4995	2.3874 / 2.3874 / $^{+0.0040}_{-0.0040}$	-0.3324 / -0.3324 / $^{+0.0056}_{-0.0055}$	86.0188	157	✓
0.5969	2.3971 / 2.3971 / $^{+0.0035}_{-0.0035}$	-0.3527 / -0.3528 / $^{+0.0039}_{-0.0038}$	128.3500	188	✓
0.6974	2.4034 / 2.4033 / $^{+0.0032}_{-0.0031}$	-0.3636 / -0.3635 / $^{+0.0028}_{-0.0029}$	166.8112	220	✓
0.7980	2.4054 / 2.4053 / $^{+0.0029}_{-0.0029}$	-0.3664 / -0.3663 / $^{+0.0022}_{-0.0022}$	178.0375	252	✓

Table 4.5: Galaxy sample with $\bar{n} = 1 \times 10^{-4}\ h^3\ \mathrm{Mpc}^{-3}$, constraints of the parameters of the nonlocal nonlinear model for varying $k_{\max}$ (expressed in $[h\ \mathrm{Mpc}^{-1}]$). For each parameter the bestfit, mean and 68% limits are shown. The last 3 columns report the χ^2, the number of degrees of freedom and the result of a χ^2 test with significance 0.05 (✓ if not rejected, ✗ if rejected).

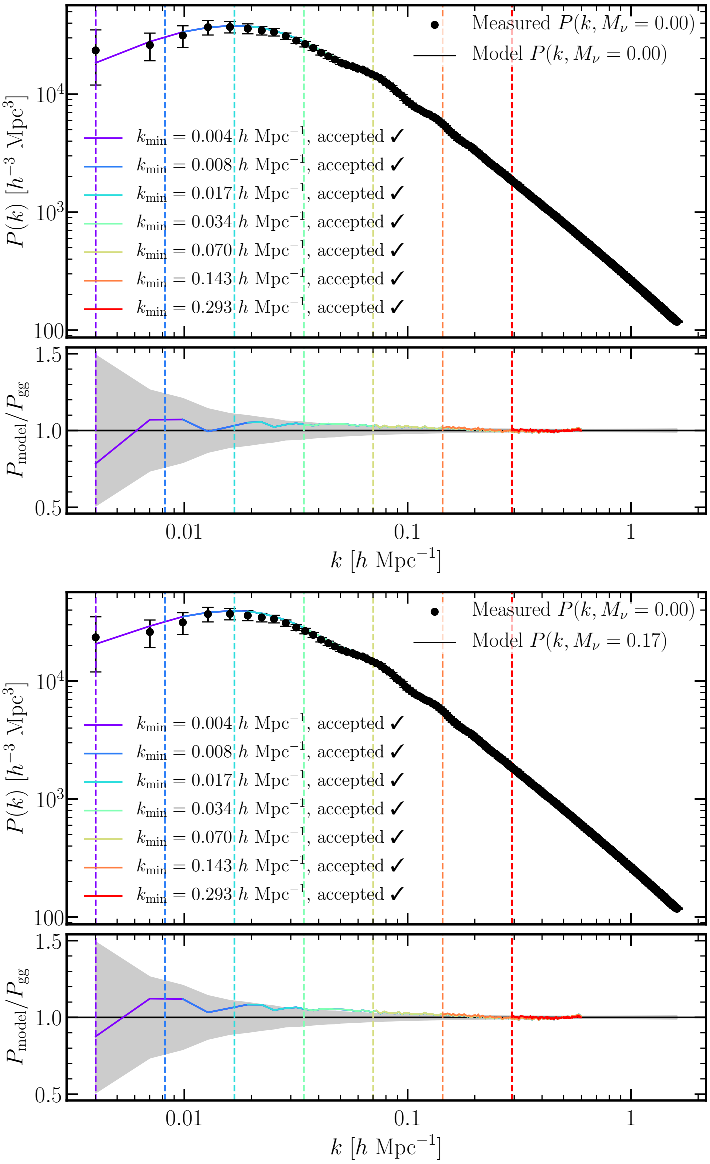

Figure 4.14: Dependence on the maximum scale of the fit for the nonlocal, nonlinear model, with different bestfit values obtained with different cuts in $k_{\rm min}$. *Upper figure:* the galaxy power spectrum in the ΛCDM simulation is fitted with the model computed assuming a ΛCDM cosmology. *Lower figure:* the galaxy power spectrum in the ΛCDM simulation is fitted with the model computed assuming $M_\nu = 0.17$ eV. For each choice of $k_{\rm min}$ the result of the χ^2 test with significance 0.05 is reported, showing whether the hypothesis on the value of neutrino mass assumed when computing the model is or is not rejected. In the upper figure, the test correctly never rejects the hypothesis. In the lower figure, the wrong hypothesis is never rejected. In this case, the nonlinear bias parameters are degenerate, within the errorbars, with the total neutrino mass, whose effects are therefore masked. Fig. 4.15 presents the same test with $M_\nu = 0.30$ and 0.53 eV.

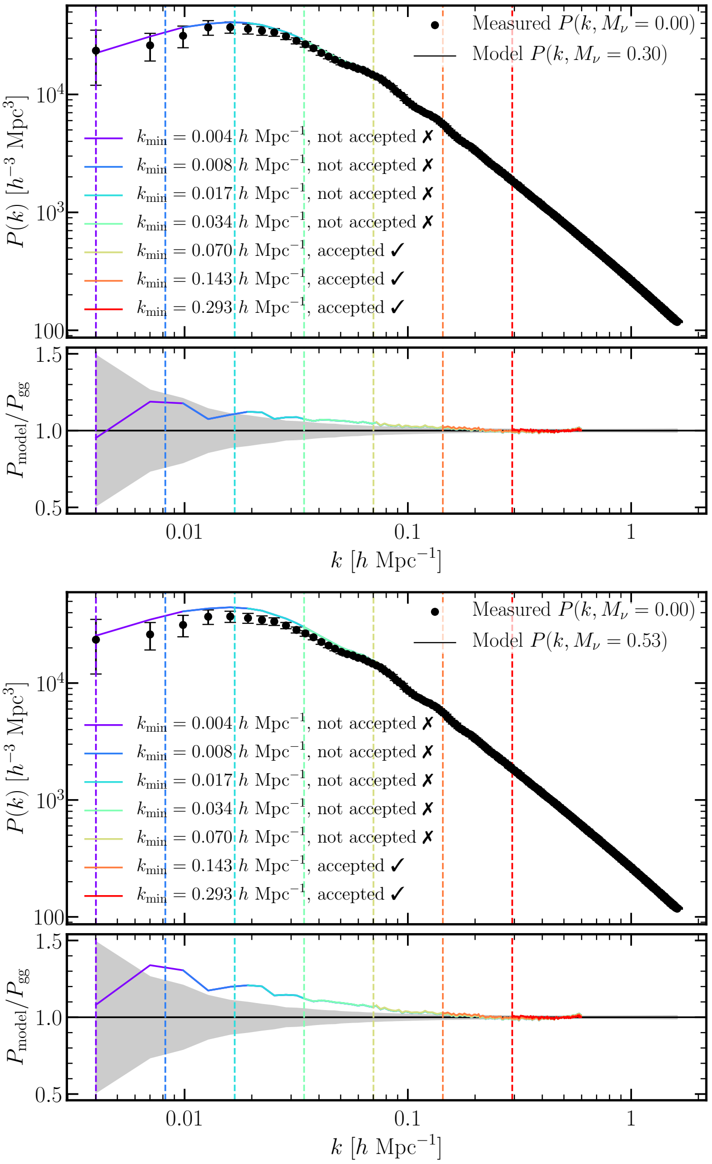

Figure 4.15: Same as in Fig. 4.14, but the wrong hypothesis tested in this case are $M_\nu = 0.30$ eV (upper figure) and $M_\nu = 0.53$ eV (lower figure). Unlike the case with $M\nu = 0.17$ eV, presented in Fig. 4.14, in this case both neutrino masses have effects large enough to be detected. As a matter of fact, with $M_\nu = 0.30$ eV, the wrong hypothesis is rejected for all $k_{\rm min} < 0.035\ h\ {\rm Mpc}^{-1}$, and, with $M_\nu = 0.53$ eV, it is rejected for all $k_{\rm min} < 0.07\ hmpc$. For these choices of maximum and minimum scale of the fit, the combination of large and small scales is able to break the degeneracy between nonlinear bias parameters and massive neutrino effects.

$k_{\rm min}$	b_1 [bf/mean/68%]	b_2 [bf/mean/68%]	χ^2	#dof	
0.0040	1.7809 / 1.7809 / $^{+0.0016}_{-0.0016}$	−0.1392 / −0.1392 / $^{+0.0023}_{-0.0022}$	377.5786	188	✗
0.0098	1.7810 / 1.7809 / $^{+0.0015}_{-0.0015}$	−0.1392 / −0.1392 / $^{+0.0023}_{-0.0023}$	375.8991	186	✗
0.0192	1.7811 / 1.7811 / $^{+0.0015}_{-0.0016}$	−0.1394 / −0.1393 / $^{+0.0023}_{-0.0022}$	368.9647	183	✗
0.0347	1.7816 / 1.7816 / $^{+0.0015}_{-0.0015}$	−0.1400 / −0.1401 / $^{+0.0023}_{-0.0022}$	343.1870	178	✗
0.0723	1.7840 / 1.7840 / $^{+0.0015}_{-0.0016}$	−0.1433 / −0.1432 / $^{+0.0023}_{-0.0022}$	267.5744	166	✗
0.1446	1.7918 / 1.7919 / $^{+0.0017}_{-0.0017}$	−0.1534 / −0.1535 / $^{+0.0024}_{-0.0023}$	152.8032	143	✓
0.2953	1.8129 / 1.8129 / $^{+0.0029}_{-0.0029}$	−0.1784 / −0.1784 / $^{+0.0035}_{-0.0036}$	42.0083	95	✓

Table 4.6: Galaxy sample with $\bar{n} = 1 \times 10^{-3}\ h^3\ {\rm Mpc}^{-3}$, constraints of the parameters of the non-local nonlinear model for varying $k_{\rm min}$ (expressed in $[h\ {\rm Mpc}^{-1}]$). For each parameter the bestfit, mean and 68% limits are shown. The last 3 columns report the χ^2, the number of degrees of freedom and the result of a χ^2 test with significance 0.05 (✓ if not rejected, ✗ if rejected).

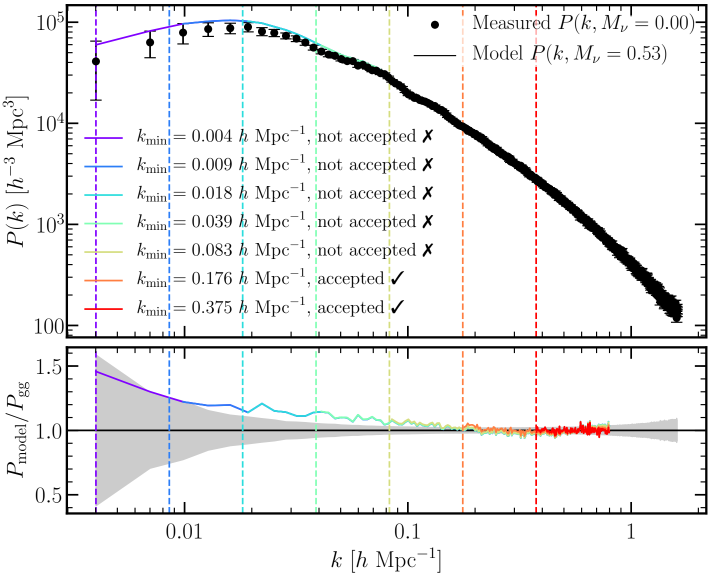

Figure 4.16: Same as in Fig.s 4.14 and 4.15, but for the sparsest sample with $\bar{n} = 1 \times 10^{-4} h^3\ {\rm Mpc}^{-3}$. This time, only the most extreme case is shown (ΛCDM galaxy power spectrum, $M_\nu = 0.53$ eV assumed in the model). The wrong hypothesis is rejected for all $k_{\rm min} < 0.08\ hmpc$. For these choices of maximum and minimum scale of the fit, the combination of large and small scales is able to break the degeneracy between nonlinear bias parameters and massive neutrino effects.

$k_{\rm min}$	b_1 [bf/mean/68%]	b_2 [bf/mean/68%]	χ^2	#dof	
0.0040	2.7303 / 2.7303 / $^{+0.0034}_{-0.0033}$	-0.3291 / -0.3291 / $^{+0.0032}_{-0.0031}$	436.2728	252	✗
0.0098	2.7304 / 2.7305 / $^{+0.0034}_{-0.0034}$	-0.3291 / -0.3292 / $^{+0.0032}_{-0.0032}$	434.6227	250	✗
0.0192	2.7307 / 2.7306 / $^{+0.0033}_{-0.0033}$	-0.3293 / -0.3292 / $^{+0.0030}_{-0.0032}$	429.3541	247	✗
0.0410	2.7325 / 2.7325 / $^{+0.0034}_{-0.0034}$	-0.3307 / -0.3306 / $^{+0.0032}_{-0.0032}$	401.4248	240	✗
0.0849	2.7417 / 2.7418 / $^{+0.0035}_{-0.0035}$	-0.3376 / -0.3376 / $^{+0.0032}_{-0.0032}$	307.7749	226	✗
0.1791	2.7718 / 2.7719 / $^{+0.0043}_{-0.0043}$	-0.3587 / -0.3587 / $^{+0.0036}_{-0.0036}$	143.4567	196	✓
0.3770	2.8077 / 2.8075 / $^{+0.0088}_{-0.0087}$	-0.3809 / -0.3808 / $^{+0.0056}_{-0.0056}$	63.2133	133	✓

Table 4.7: Galaxy sample with $\bar{n} = 1 \times 10^{-3}\ h^3\ {\rm Mpc}^{-3}$, constraints of the parameters of the nonlocal nonlinear model for varying $k_{\rm min}$ (expressed in $[h\ {\rm Mpc}^{-1}]$). For each parameter the bestfit, mean and 68% limits are shown. The last 3 columns report the χ^2, the number of degrees of freedom and the result of a χ^2 test with significance 0.05 (✓ if not rejected, ✗ if rejected).

$k_{\rm min} < 0.07\ h\ {\rm Mpc}^{-1}$ respectively are included in the fit. However, when $M_\nu = 0.17$ eV is wrongly assumed in the model, the test does not reject the hypothesis, for both the galaxy samples.

If we relax the assumption that the bias is perfectly local in Lagrangian space, we can slightly modify Eq. 4.15. I have repeated this analysis (for the sparsest galaxy sample) assuming the fitting formula 4.16, which allows for pushing $k_{\rm max}$ to $\sim 0.5\ h\ {\rm Mpc}^{-1}$ in ΛCDM, and gives very similar results as obtained with the local-Lagrangian relation. If instead I assume Eq. 4.17, the minimum scale that can be included in the fit moves to the smallest one allowed in the present analysis, $k_{\rm max} \sim 0.8\ h\ {\rm Mpc}^{-1}$, implying that this fitting formula better captures the relation between nonlocal and local parameters. However, the results in rejecting the wrong hypothesis do not change, and only $M_\nu = 0.30$ and 0.53 eV are rejected, while $M_\nu = 0.17$ eV is still not rejected. Nonetheless, it is important to note that with all the three assumptions on the relation between nonlocal and linear bias considered the wrong hypothesis with $M_\nu \geq 0.30$ eV is still rejected, implying that, the approach chosen to describe the nonlocal bias does not significantly spoil the constraining power of the model.

4.3 Future prospects

In this chapter I have presented the galaxy catalogues I have produced through the SHAM technique, starting from the first set of the DEMNUni simulations. I have used them to study the linear galaxy bias in the presence of neutrinos. As expected, it is larger for larger neutrino masses. Moreover, it presents a slight scale dependence, with respect to the ΛCDM case, induced by neutrino free-streaming.

I have then fitted these galaxy power spectra with two popular models of the nonlinear power spectrum, concluding that in both cases the parameters of the model can be degenerate with the effects induced by neutrinos. In general, we need a model able to describe scales smaller than $0.5\ h\ {\rm Mpc}^{-1}$, so that the combination with large scales ($k < 0.03 - 0.06\ h\ {\rm Mpc}^{-1}$) breaks such degeneracy. I have tested when this happens employing a χ^2 goodness of fit test.

This kind of analysis is, however, not complete. To robustly assess the possible degeneracies between the parameters of the models and neutrino effects, an MCMC approach, leaving all these parameters free, would be required. This is indeed the direction towards which my work is moving, and I will implement this line-of-work in the near future. Moreover, the same analysis needs to be extended to redshift space. This is rather important as recent works (see eg. Villaescusa-Navarro et al., 2017) have shown that some degeneracies between cosmological parameters (such as σ_8 and M_ν) can be alleviated by looking at the quadrupole of the galaxy power spectrum. Such effects, as well, need to be included in the analysis.

Another path to follow, starting from this work, is to better characterize the galaxies obtained with the SHAM technique. As a matter of fact, one can apply some recipes to match luminosity functions and colour distribution of galaxies to observations (see, eg., Carretero et al., 2015, and references therein). In this way, the past light-cone can be populated with a realistic distribution of galaxies, from which either mock catalogues or all-sky 2D maps can be extracted. These tools are of paramount importance to study galaxy clustering and dynamics in non-standard cosmologies, as well as to study the cross correlations between signals such as the CMB lensing, weak lensing or the Integrated Sachs Wolf effect and the Large Scale Structure (Carbone et al., 2016). Being these probes sensitive to different systematics, their cross-correlation is expected to be extremely powerful in breaking parameter degeneracies and tightening the constraints on the cosmological parameters.

Conclusions

In this thesis I presented my work on the effects of massive neutrinos on the large scale structure of the universe (LSS). This is a rather active field in contemporary cosmology, as the neutrino mass has recently entered the standard cosmological picture. In fact, properly accounting for their presence not only leads to more accurate constraints on the parameters describing the underlying cosmological model, but also, even more importantly, provides us with unique information about the nature of these elusive, but fundamental, particles. Given their effects on the evolution of cosmic structure, it comes as no surprise that the most stringent bounds on the total neutrino mass come indeed from cosmology.

The field being rather wide, I have tackled three main topics: on the cosmological simulation side, I developed a code for setting initial conditions that avoid systematics introduced by some approximations commonly assumed in simulations including massive neutrinos; on the modelling side, I extended the clustering ratio (the ratio of the correlation function over the variance of an overdensity field) to cosmologies with massive neutrinos, measuring the galaxy clustering ratio from real data, and constraining the parameters of the cosmological model; finally, I have devoted the last part of my work to study the effects of neutrinos on the galaxy power spectrum, employing the so-called SHAM technique.

Within my work on systematics in neutrino simulations, I have shown that starting a simulation with a matter power spectrum, computed with a Boltzmann solver (`camb`, `class`) at the initial redshift of the simulation, introduces order 10% discrepancies in the simulation matter power spectrum at low redshift and large scales. This is due to the lack of horizon crossing and radiation perturbations in simulations implementing Newtonian dynamics. Moreover, neglecting radiation in the background evolution introduces a scale independent systematic effect at the 4% level in the matter power spectrum at redshift $z = 0$. Finally, neglecting the neutrino scale dependence in the growth rate introduces a sub-percent error. The combination of many of these approximations can lead to important systematic departures from predictions in the output of N-body simulation, which instead need to reach 1% accuracy for correct modelling in view of upcoming galaxy surveys, such as Euclid.

By employing a two fluid, Newtonian approximation, I developed a code to rescale the redshift $z = 0$ matter power spectrum to the initial redshift of the simulation, accounting for the growth rate scale dependence introduced by neutrino free streaming, and correcting for relativistic effects unavoidably missing in the dynamics of simulations in the Newtonian limit. Employing this method, I was able to reach the same level of accuracy in neutrino simulations as in the massless neutrino ΛCDM case, usually taken as a reference in cosmological analyses.

In addition, I applied this method to produce the initial cold-matter and neutrino power spectra, together with the corresponding growth rates, needed to generate the initial conditions of the new set of the DEMNUni simulations by C. Carbone. These simulations explore many combinations of neutrino masses, and dynamical dark energy parameters w_0 and w_a. As some combinations of these parameters are degenerate with a massless neutrino ΛCDM cosmology, the analysis of such simulation is of paramount importance for accurate LSS modelling and parameter degeneracy breaking.

My work on the clustering ratio was aimed at extending this formalism to cosmological scenarios with massive neutrinos. The clustering ratio, $\eta_R(r) = \xi_R(r)/\sigma_R^2$, is the ratio of the smoothed correlation function over the smoothed variance of a overdensity field. By properly choosing the smoothing scale R and the correlation length r, such ratio can be considered unbiased, independent from redshift-space distortions, and very weakly dependent on redshift. For this reason, on such scales, the clustering ratio measured from galaxies in redshift space can be directly compared to its theoretical prediction for matter in real space. Besides being very easy to measure and model, the clustering ratio is also very sensitive to the shape of the matter power spectrum, making it a good candidate to be used for setting cosmological parameter constraints.

I tested with N-body simulations that these features of the clustering ratio hold also in cosmologies including massive neutrinos. I also optimized the combination of smoothing radius and correlation length that maximizes the effect of neutrinos on this observable, while minimizing statistical errors, within the range of scales of applicability of the clustering ratio. Finally, I used the clustering ratio measured in the SDSS DR7 and DR11 samples to draw constraints on the parameters of the cosmological model, considering a baseline model (assumed geometrically flat) parameterized by the Hubble parameter H_0, the CDM and baryon densities $\Omega_{cdm}h^2, \Omega_b h^2$, the primordial amplitude and spectral index of scalar perturbation A_s, n_s, and the optical width of the universe at reionization τ, with two extensions given by the total neutrino mass M_ν and the equation of state of dark energy, w.

I found that, using the current data, the clustering ratio is able to break the degeneracy between w and the other parameters, which is present when only CMB temperature and polarization anisotropies are considered. Moreover, it improves the constraint obtained from CMB data alone on the cold dark matter density parameter by nearly 12%. However, I have not found any appreciable improvement on the neutrino mass constraint. By applying the same parameter fitting pipeline to simulations, I showed that this occurs because errors on the clustering ratio measured in current data are still too large and spoil, therefore, its constraining power, especially on the neutrino total mass parameter. Motivated by this consideration, I have forecast the constraining power of the clustering ratio expected from the Euclid galaxy survey, applying it to a synthetic galaxy catalogue. In this case, the constraint on the cold dark matter density parameter improves by over 40% with respect to the results of the Planck collaboration alone, and the constraint on the total neutrino mass improves by 14%. In addition, I found a 10% improvement on the constraint of the primordial spectral index n_s, and a 20% improvement for the Hubble parameter H_0.

For the last part of my Ph.D. project, I populated the first set of the DEMNUni simulations with galaxies, using a SHAM technique. First, I studied the linear bias of this sample of galaxies, in the presence of massive neutrinos. I found that, consistently with expectations and previous works, to higher values of the neutrino mass correspond higher values of the galaxy bias. Moreover, I observed that the different bias induced by neutrinos, which modifies the overall amplitude of the galaxy power spectrum, can make cosmologies with different neutrino masses degenerate, when analysis is limited to small scales. Adding the large scale information, however, reintroduces the scale dependence that is a unique feature of the presence of massive neutrinos, and that depends on the total neutrino mass itself.

I fitted the fully nonlinear galaxy power spectrum obtained from the simulations using two popular models of the nonlinear bias, the Q-model by Cole et al. (2005) and the nonlocal nonlinear model by McDonald and Roy (2009). I applied them to two galaxy samples, one sparser and more biased, and one denser and less biased. For both the models, I studied which maximum wavemode (minimum scale) I could include in the fit, employing a χ^2 test to evaluate the goodness of the fit. Once I found this minimum scale, I investigated if these models are sensitive enough to reject a wrong assumption on the value of the neutrino mass M_ν. To this purpose I fitted the galaxy power spectrum measured in the massless neutrino ΛCDM cosmology with the models computed assuming a non-zero neutrino mass, $M_\nu = \{0.17, 0.3, 0.53\}$ eV. I found that, in general, the models are able to reject the wrong hypothesis on the neutrino mass when two conditions are satisfied, namely if the model can be pushed down to very small scales $k \gtrsim 0.6\ h\ \mathrm{Mpc}^{-1}$, and the fit can be extended to include large scales $k \lesssim 0.03 - 0.06\ h\ \mathrm{Mpc}^{-1}$, depending on the neutrino mass.

Using the Q-model model, I was able to reach this optimal conditions only with the sparse, more biased sample. Even in this case, the model correctly rejected $M_\nu = 0.3$ and 0.53 eV, while the case with the lightest neutrino mass ($M_\nu = 0.17$ eV) was degenerate with the massless case. On the other hand the nonlocal nonlinear model was able to satisfy these conditions also with the dense, less biased galaxy sample. However, also in this case, I could not break the degeneracy between $M_\nu = 0.0$ and $M_\nu = 0.17$ eV.

This last part of my work is still ongoing. In particular, to assess the degeneracies between the parameters of the nonlinear bias models and those of the cosmological model, I plan to repeat the analysis with an MCMC approach, leaving also the latter free. Moreover, I plan to extend this work to redshift space and exploit the quadrupole of the power spectrum, which will add information for breaking parameter degeneracies.

About the characterization of the galaxy population much more can be done. Employing techniques that have been presented and studied in the literature, I am moving towards assigning luminosities, colours and fluxes to the galaxies in the simulations, hence creating a more realistic realization of structures in non-standard cosmologies. This work will lead to the construction of mock galaxy catalogues that can be used to study galaxy properties in the presence of massive neutrinos and dynamical dark energy. In addition, it will also allow us to build all-sky maps of the large scale structure of the universe, using well known box-stacking and pixellization techniques (Calabrese et al., 2015). Such maps can be cross correlated with maps of CMB lensing, weak lensing or Integrated Sachs-Wolfe effect, extracted via ray-tracing codes from the same simulations. The strength of this approach resides in these different observables probing different epochs and scales, and being affected by different systematic effects, which can be minimized through as many as possible cross combinations.

As new, large galaxy surveys are expected to start in the very next future, aiming at measuring cosmological parameters with unprecedented precision and accuracy, it is now time to include all possible effects in our analyses, going in the direction of comparing more precise data to more accurate models. In this respect, the study of the cosmological effects of massive neutrinos on the LSS is undoubtedly a field worth exploring.

APPENDIX A

Neutrino decoupling

To the end of obtaining the correct neutrino to photon temperature ratio today, and to compute the correct number of relativistic species in the early universe, we need to model the process of decoupling of neutrinos.

In Eq. 1.72 I showed the redshift at which we expect neutrinos to decouple, *i.e.* when their interaction rate falls below the expansion rate of the universe.

Before decoupling neutrinos are at equilibrium with the hot, primeval plasma, composed of photons, neutrinos, electrons and positrons. In general, what we expect is that, after neutrinos decouple, their momentum distribution function is frozen as well as their temperature, since they can no longer exchange heat. Neutrino temperature, from this moment on, only decreases due to the expansion of the universe, with $T_\nu \propto a^{-1}$. In this case, if nothing else happens to the photon temperature, neutrinos, even if decouple, would end up having the same temperature as photons today.

However, soon after neutrino decoupling, the background temperature approaches the the rest-mass energy of electrons, 511 keV, allowing electrons and positrons to annihilate. This process frees energy (and entropy), which goes into heating the photon gas. As a consequence, even if before $e^\pm$ annihilation the temperature of neutrinos and photons was still the same, $T_\gamma \sim T_\nu$, after this process the temperature of photons increases, while the decoupled neutrinos remain unaffected, leaving us with $T_\gamma > T_\nu$.

The simplest way to compute by how much $T_\gamma > T_\nu$ is to model neutrino decoupling as an instantaneous process, which is completely over when $e^\pm$ annihilation happens. In the rest of this appendix I will make this assumption and derive T_γ/T_ν.

On the other hand, I want to underline right now that in no way neutrino decoupling is an instantaneous process. In fact, when $e^\pm$ annihilation starts a tail of neutrinos is still coupled to the background plasma. As a consequence a fraction of neutrinos gets heated as well as photons before decoupling, thus lessening the difference in temperature between the two species. At the end of this appendix I will mention a common approach to overcome this issue.

Following the second law of Thermodynamics, the entropy of a system is given by

$$\mathrm{d}S = \frac{\mathrm{d}[\rho(T)V] + p(T)\mathrm{d}V}{T}, \tag{1.1}$$

where T is the temperature of the background at equilibrium, p its pressure and V the volume. The entropy density (entropy per volume unit) is obtained by integrating the latter equation, and reads

$$s(T) = \frac{\rho(T) + p(T)}{T}. \tag{1.2}$$

In a gas at statistical equilibrium, the densities of the different species are

$$\rho_{\mathrm{eq}} = \begin{cases} \dfrac{\pi^2}{30}\, g\, T^4 & \text{for Bose-Einstein species} \\ \dfrac{7}{8}\,\dfrac{\pi^2}{30}\, g\, T^4 & \text{for Fermi-Dirac species.} \end{cases} \tag{1.3}$$

Being this plasma still relativistic at the time, the pressure of all these species is simply given by $p_{\mathrm{eq}}(T) = \rho_{\mathrm{eq}}(T)/3$. Therefore, we can conveniently rewrite Eq. 1.2 as

$$s(T) = \frac{2\pi^2}{45}\, g_\star\, T^3, \tag{1.4}$$

where $g_\star$ is summed over all the species present in the universe,

$$g_\star = \sum_{i\in\mathrm{bosons}} g_i \left(\frac{T_i}{T}\right)^3 + \sum_{i\in\mathrm{fermions}} \frac{7}{8} g_i \left(\frac{T_i}{T}\right)^3, \tag{1.5}$$

each species being at temperature T_i whereas the background temperature is T.

Since the expansion of the universe is expected to be adiabatic, entropy in a given comoving volume is conserved. In other words, the entropy density must remain constant, which implies

$$g_\star\, T^3 = \text{constant}. \tag{1.6}$$

Under the assumption that all neutrinos are already decoupled when $e^\pm$ annihilation happens, that they still share the same temperature of the background plasma before it happens, and that they do not change their temperature due to it, we can write that

$$T_{\gamma,\mathrm{before}} = T_{\nu,\mathrm{before}} = T_{\nu,\mathrm{after}}. \tag{1.7}$$

Enforcing entropy density conservation we have

$$\frac{T_{\gamma,\mathrm{after}}}{T_{\gamma,\mathrm{before}}} = \left(\frac{g_{\star,\mathrm{before}}}{g_{\star,\mathrm{after}}}\right)^{1/3}, \tag{1.8}$$

which can be recast as

$$T_{\gamma,\mathrm{after}} = \left(\frac{g_{\star,\mathrm{before}}}{g_{\star,\mathrm{after}}}\right)^{1/3} T_{\nu,\mathrm{after}}. \tag{1.9}$$

Now we just need to compute the ratio $g_{\star,\mathrm{before}}/g_{\star,\mathrm{after}}$.

Before $e^\pm$ annihilation, the species in the system, all sharing the same temperature T, are photons, electrons, positrons and neutrinos. Therefore

$$g_{\star,\mathrm{before}} = g_\gamma + \frac{7}{8}(g_{e^-} + g_{e^+} + g_\nu + g_{\bar\nu}) = \frac{43}{4}. \tag{1.10}$$

After $e^\pm$ annihilation, we are left with photons and neutrinos, but this time the temperature of neutrinos is no longer that of the background plasma. As a consequence

$$g_{\star,\mathrm{after}} = g_\gamma + \frac{7}{8}(g_\nu + g_{\bar\nu}) \left(\frac{T_{\nu,\mathrm{after}}}{T_{\gamma,\mathrm{after}}}\right)^3 = 2 + \frac{21}{4}\left(\frac{T_{\nu,\mathrm{after}}}{T_{\gamma,\mathrm{after}}}\right)^3. \tag{1.11}$$

We can now write

$$T_{\gamma,\mathrm{after}} = \left(\frac{11}{4}\right)^{1/3} T_{\nu,\mathrm{after}}. \tag{1.12}$$

The neutrino to photon temperature ratio is therefore defined as

$$\Gamma_\nu = \frac{T_\nu}{T_\gamma} = \left(\frac{4}{11}\right)^{1/3} \simeq 0.7137659 \tag{1.13}$$

in the limit of instantaneous decoupling, and gives a neutrino temperature today of $T_{\nu,0} = \Gamma_\nu \, T_{\gamma,0} = 1.9454\,\mathrm{K}$.

APPENDIX B

Redshift-space distortions in the Kaiser limit

In general, the position of a galaxy in redshift space can be obtained from the original position in real space, if the peculiar velocity of the galaxy is known. To link positions in redshift space to the original ones, we can consider three different observers, ø1, ø2 and ø3. They are defined such that

- $\mathcal{O}_1$ is a fundamental observer in the origin $\mathbf{0}$;
- $\mathcal{O}_2$ is a fundamental observer, located in a point $\boldsymbol{p}$;
- $\mathcal{O}_3$ is an observer located in $\boldsymbol{p}$, comoving with the galaxy in $\boldsymbol{p}$.

When $\mathcal{O}_2$ observes the galaxy in $\boldsymbol{p}$, it sees it moving according to its peculiar velocity, projected along the line of sight connecting them, $v_{\mathrm{pec}\,\parallel}$. The spectrum of the light emitted by the object in $\boldsymbol{p}$ is measured by $\mathcal{O}_3$ in the rest frame. $\mathcal{O}_2$, on the other hand, sees a shifted spectrum, the shift being determined by the Doppler effect,

$$1 + z_{\mathrm{pec}} = \frac{\lambda_{\mathcal{O}_2}}{\lambda_{\mathcal{O}_1}} = \sqrt{\frac{1 + z_{\mathrm{pec}}/c}{1 - z_{\mathrm{pec}}/c}} \simeq 1 + \frac{v_{\mathrm{pec}\,\parallel}}{c}. \tag{2.1}$$

When $\mathcal{O}_1$ looks at the motion of $\boldsymbol{p}$, it sees the combined effect of the expansion of the universe (given by the ratio between the wavelength measured by $\mathcal{O}_2$ and by $\mathcal{O}_1$) and the Doppler stretching of the spectrum (given by the ratio of the wavelengths measured by $\mathcal{O}_3$ and $\mathcal{O}_2$). The redshift observed by $\mathcal{O}_1$ is therefore

$$1 + z_{\mathrm{obs}} = \frac{\lambda_{\mathcal{O}_1}}{\lambda_{\mathcal{O}_3}} = \frac{\lambda_{\mathcal{O}_1}}{\lambda_{\mathcal{O}_2}} \frac{\lambda_{\mathcal{O}_2}}{\lambda_{\mathcal{O}_3}} = (1 + z_{\mathrm{cos}})(1 + z_{\mathrm{pec}}). \tag{2.2}$$

By combining the two previous equations one obtains

$$z_{\mathrm{obs}} = z_{\mathrm{cos}} + \frac{v_{\mathrm{pec}\,\parallel}}{c}(1 + z_{\mathrm{cos}}). \tag{2.3}$$

The comoving radial distance between the origin $\mathbf{0}$ and $\boldsymbol{p}$ is given by

$$\boldsymbol{r}(z_{\mathrm{obs}}) = \int_0^{z_{\mathrm{obs}}} \frac{c\,\mathrm{d}z}{H(z)}\,\hat{\mathbf{n}}, \tag{2.4}$$

where $\hat{\mathbf{n}}$ is the versor directed along the line of sight connecting $\mathbf{0}$ and $\boldsymbol{p}$. which can be split into

$$\int_0^{z_{\mathrm{obs}}} \frac{c\,\mathrm{d}z}{H(z)} = \int_0^{z_{\mathrm{cos}}} \frac{c\,\mathrm{d}z}{H(z)} + \int_{z_{\mathrm{cos}}}^{z_{\mathrm{cos}} + \frac{v_{\mathrm{pec}\,\parallel}}{c}(1 + z_{\mathrm{cos}})} \frac{c\,\mathrm{d}z}{H(z)}. \tag{2.5}$$

While the first two integrals are just the comoving distances from an observer today to a point located at the observed and at the cosmological redshift respectively, to carry out the last integral we need to introduce some assumptions. In particular, we can note that, as long as the modification to the observed redshift induces by peculiar velocities is way smaller than the cosmological redshift of the observed object, the Hubble function between $z_{\rm cos}$ and $z_{\rm pec}$ does not change significantly. Therefore we approximate the last integral by considering the Hubble function *at* the cosmological redshift, $H(z_{\rm cos})$, obtaining

$$r(z_{\rm obs}) = r(z_{\rm cos}) + \frac{c}{H(z_{\rm cos})}\left[z_{\rm cos} + \frac{v_{\rm pec\,\shortparallel}}{c}(1+z_{\rm cos}) - z_{\rm cos}\right]. \tag{2.6}$$

In the end we are left with

$$\boldsymbol{r}(z_{\rm obs}) = \boldsymbol{r}(z_{\rm cos}) + \frac{v_{\rm pec\,\shortparallel}\,(1+z_{\rm cos})}{H(z_{\rm cos})}\,\hat{\mathbf{n}}\,, \tag{2.7}$$

which, following the convention of naming positions in redshift space with $\boldsymbol{s}$ and in real space with $\boldsymbol{r}$, can be written as

$$\boldsymbol{s} = \boldsymbol{r} + \frac{v_{\rm pec\,\shortparallel}\,(1+z)}{H(z)}\,\hat{\mathbf{n}}\,. \tag{2.8}$$

The number density in real space in the point $\boldsymbol{r}$ is given by

$$\delta(\boldsymbol{r}) = \frac{n_r(\boldsymbol{r})}{\bar{n}_r} - 1, \tag{2.9}$$

while in redshift space it is

$$\delta(\boldsymbol{s}) = \frac{n_s(\boldsymbol{s})}{\bar{n}_s} - 1. \tag{2.10}$$

Even if they are not necessarily the same, the number of objects (or the mass) is conserved, meaning that

$$[1+\delta(\boldsymbol{s})]\,\mathrm{d}^3\boldsymbol{s} = [1+\delta(\boldsymbol{r})]\,\mathrm{d}^3\boldsymbol{r}. \tag{2.11}$$

We need to impose this condition while recalling that the peculiar velocity, in linear theory, is simply linked to overdensities through

$$\nabla\cdot\boldsymbol{v}_{\rm pec} = -\frac{\partial\delta}{\partial t} = -a\,f(a)\,H(a)\delta, \tag{2.12}$$

where a is the scale factor and $f \equiv \mathrm{d}\log D/\mathrm{d}\log a$ is the growth rate. To take care of the divergence, it is convenient to pass in Fourier space, so that we can write

$$\hat{\delta}^s(\boldsymbol{k}) = (1+f\mu^2)\,\hat{\delta}^r(\boldsymbol{k}), \tag{2.13}$$

where, on the left-hand side, we have the Fourier transform of the overdensity in redshift space, while on the right-hand side the Fourier transform of the overdensity in configuration space, modulated by the so called Kaiser factor. Here f is the growth rate, and

$$\mu = \frac{\hat{\boldsymbol{v}}_{\rm pec}\cdot\boldsymbol{k}}{|\hat{\boldsymbol{v}}_{\rm pec}\cdot\boldsymbol{k}|} = \cos\vartheta \tag{2.14}$$

is the cosine of the angle between the Fourier transform of the peculiar velocity vector and the considered wavemode.

As a consequence, the power spectrum in redshift space has the form

$$P^s(\boldsymbol{k}) = [1 + f\mu^2]^2 \, P^r(k), \tag{2.15}$$

which explicitly depends on the direction of the vector $\boldsymbol{k}$, and therefore it is no longer isotropic even on linear scales.

However, one can recover isotropy giving up a certain part of the information contained in the power spectrum. As a matter of fact, taking the angular average of the power spectrum, hence its monopole, it is possible to remove the dependence on the angle,

$$P^s_0(k) = \frac{1}{2}\int_{-1}^{+1} P^s(\boldsymbol{k}) \, \mathrm{d}\mu = \left[1 + \frac{2}{3}f + \frac{1}{5}f^2\right] \, P^r(k). \tag{2.16}$$

APPENDIX C

Alcock-Pacziński correction

Assuming different cosmological parameters leads to different relations linking the observable quantities (redshift and angles) to distances. To understand how distances transform under a change of cosmological parameters, we need to start from the quantities that do not depend on the model, namely redshifts and angles. We need to link them to parallel and transverse distances. I recall the FLRW line element (defined in Eq. 1.2), which is

$$\mathrm{d}s^2 = -c^2\mathrm{d}t^2 + a^2(t)\left\{\mathrm{d}r^2 + \mathcal{S}_k^2(r)(\mathrm{d}\vartheta^2 + \sin^2\vartheta\mathrm{d}\varphi^2)\right\}, \tag{3.1}$$

where the Gaussian curvature, is

$$k = -\frac{Kc^2}{a_0^2} = H_0^2\Omega_{k,0}\ , \quad \text{with} \quad K = \{-1, 0, 1\}\ , \tag{3.2}$$

and therefore

$$\mathcal{S}_k(r) = \begin{cases} \sin(\sqrt{|k|}r)/\sqrt{|k|} & \text{if } K = -1 \\ r & \text{if } K = 0 \\ \sinh(\sqrt{k}r)/\sqrt{k} & \text{if } K = +1. \end{cases} \tag{3.3}$$

The comoving radial distance, given by Eq. 1.6, is

$$r = \int_{t_e}^{t_o} \frac{c\,\mathrm{d}t}{a(t)} = \int_0^{z_e} \frac{c\,\mathrm{d}z}{H(z)}, \tag{3.4}$$

where t_e and z_e are the time end redshift at which a signal was emitted, and t_o and $z_o = 0$ are present day time and redshift.

The angular diameter distance is given by

$$D_A = \frac{\mathcal{S}_k(r)}{1+z}, \tag{3.5}$$

which, in a flat universe, reduces to

$$D_A = \frac{r}{1+z}. \tag{3.6}$$

To link these quantities to redshifts and angles, we need some assumptions. The two working assumptions I will introduce now are small redshift intervals and small angles. If the redshift interval is not large, we can safely assume that the Hubble function does not vary much, and transform the comoving radial distance integral into

$$\delta r_{\parallel} \simeq \frac{c}{H(z)}\,\delta z, \tag{3.7}$$

where I have explicitly marked this as the distance parallel to the line of sight. The angular diameter distance, if angles are not to big, can be written as

$$\delta r_\perp = D_A\, \delta\vartheta, \tag{3.8}$$

where $\delta_\perp$ denotes the transverse distance.

The quantities δz and δ_ϑ do not depend on the model, while $\delta r_\parallel$ and $\delta r_\perp$ do. For this reason, considering both the fiducial cosmology and a generic one, it must be valid that

$$\begin{aligned} \delta z &= \frac{H_0 E^F(z)}{c}\, \delta r^F_\parallel = \frac{H_0 E(z)}{c}\, \delta r_\parallel \\ \delta\vartheta &= \frac{\delta r^F_\perp}{D^F_A} = \frac{\delta r_\perp}{D_A}\,. \end{aligned} \tag{3.9}$$

This leads to linking a generic cosmology to the fiducial one with

$$\begin{aligned} \delta r_\parallel &= \frac{E^F(z)}{E(z)}\, \delta r^F_\parallel\,, \\ \delta r_\perp &= \frac{D_A}{D^F_A}\, \delta^F_\perp\,. \end{aligned} \tag{3.10}$$

Regular volumes, therefore, change under a change of cosmology, as

$$V = \delta r_\parallel \delta r^2_\perp = \left[\frac{E^F(z)}{E(z)} \left(\frac{D_A}{D^F_A}\right)^2\right] \delta r^F_\parallel (\delta r^F_\perp)^2 = \alpha^3_{\mathrm{AP}} V^F. \tag{3.11}$$

Hence, the Alcock-Pacziński correction is given by

$$\alpha_{\mathrm{AP}} = \left[\frac{E^F(z)}{E(z)} \left(\frac{D_A}{D^F_A}\right)^2\right]^{1/3}, \tag{3.12}$$

which is indeed the factor introduced in chapter 3 to correct the considered smoothing scale.

Bibliography

K. N. Abazajian, J. F. Beacom, and N. F. Bell. Stringent constraints on cosmological neutrino-antineutrino asymmetries from synchronized flavor transformation. *Phys. Rev. D*, 66(1):013008, July 2002. doi: 10.1103/PhysRevD.66.013008. URL `http://adsabs.harvard.edu/abs/2002PhRvD..66a3008A`.

K. N. Abazajian, J. K. Adelman-McCarthy, M. A. Agüeros, S. S. Allam, C. Allende Prieto, D. An, K. S. J. Anderson, S. F. Anderson, J. Annis, N. A. Bahcall, and et al. The Seventh Data Release of the Sloan Digital Sky Survey. *Astrophys. J. Suppl.*, 182:543-558, June 2009. doi: 10.1088/0067-0049/182/2/543. URL `http://adsabs.harvard.edu/abs/2009ApJS..182..543A`.

S. Agarwal and H. A. Feldman. The effect of massive neutrinos on the matter power spectrum. *Mon. Not. R. Astron. Soc.*, 410:1647–1654, January 2011. doi: 10.1111/j.1365-2966.2010.17546.x. URL `http://adsabs.harvard.edu/abs/2011MNRAS.410.1647A`.

S. Alam, F. D. Albareti, C. Allende Prieto, F. Anders, S. F. Anderson, T. Anderton, B. H. Andrews, E. Armengaud, É. Aubourg, S. Bailey, and et al. The Eleventh and Twelfth Data Releases of the Sloan Digital Sky Survey: Final Data from SDSS-III. *Astrophys. J. Suppl.*, 219:12, July 2015. doi: 10.1088/0067-0049/219/1/12. URL `http://adsabs.harvard.edu/abs/2015ApJS..219...12A`.

C. Alcock and B. Paczyński. An evolution free test for non-zero cosmological constant. *Nature*, 281:358, October 1979. doi: 10.1038/281358a0. URL `http://adsabs.harvard.edu/abs/1979Natur.281..358A`.

Yacine Ali-Haïmoud and Simeon Bird. An efficient implementation of massive neutrinos in non-linear structure formation simulations. *Mon. Not. R. Astron. Soc.*, 428:3375–3389, February 2013. doi: 10.1093/mnras/sts286. URL `http://adsabs.harvard.edu/abs/2013MNRAS.428.3375A`.

L. Anderson, É. Aubourg, S. Bailey, F. Beutler, V. Bhardwaj, M. Blanton, A. S. Bolton, J. Brinkmann, J. R. Brownstein, A. Burden, C.-H. Chuang, A. J. Cuesta, K. S. Dawson, D. J. Eisenstein, S. Escoffier, J. E. Gunn, H. Guo, S. Ho, K. Honscheid, C. Howlett, D. Kirkby, R. H. Lupton, M. Manera, C. Maraston, C. K. McBride, O. Mena, F. Montesano, R. C. Nichol, S. E. Nuza, M. D. Olmstead, N. Padmanabhan, N. Palanque-Delabrouille, J. Parejko, W. J. Percival, P. Petitjean, F. Prada, A. M. Price-Whelan, B. Reid, N. A. Roe, A. J. Ross, N. P. Ross, C. G. Sabiu, S. Saito, L. Samushia, A. G. Sánchez, D. J. Schlegel, D. P. Schneider, C. G. Scoccola, H.-J. Seo, R. A. Skibba, M. A. Strauss, M. E. C. Swanson, D. Thomas, J. L. Tinker, R. Tojeiro, M. V. Magaña, L. Verde, D. A. Wake, B. A. Weaver, D. H. Weinberg, M. White, X. Xu, C. Yèche, I. Zehavi, and

G.-B. Zhao. The clustering of galaxies in the SDSS-III Baryon Oscillation Spectroscopic Survey: baryon acoustic oscillations in the Data Releases 10 and 11 Galaxy samples. *Mon. Not. R. Astron. Soc.*, 441:24–62, June 2014. doi: 10.1093/mnras/stu523. URL `http://adsabs.harvard.edu/abs/2014MNRAS.441...24A`.

R. E. Angulo and A. Pontzen. Cosmological N-body simulations with suppressed variance. *Mon. Not. R. Astron. Soc.*, 462:L1–L5, October 2016. doi: 10.1093/mnrasl/slw098. URL `http://adsabs.harvard.edu/abs/2016MNRAS.462L...1A`.

A. W. Appel. An Efficient Program for Many-Body Simulation. *SIAM Journal on Scientific and Statistical Computing, vol. 6, no. 1, January 1985, p. 85-103.*, 6:85–103, January 1985. URL `http://adsabs.harvard.edu/abs/1985SJSSC...6...85A`.

T. Baldauf, U. Seljak, V. Desjacques, and P. McDonald. Evidence for quadratic tidal tensor bias from the halo bispectrum. *Phys. Rev. D*, 86(8):083540, October 2012. doi: 10.1103/PhysRevD.86.083540. URL `http://adsabs.harvard.edu/abs/2012PhRvD..86h3540B`.

A. Banerjee and N. Dalal. Simulating nonlinear cosmological structure formation with massive neutrinos. *ArXiv e-prints*, June 2016. URL `http://adsabs.harvard.edu/abs/2016arXiv160606167B`.

J. Barnes and P. Hut. A hierarchical O(N log N) force-calculation algorithm. *Nature*, 324: 446–449, December 1986. doi: 10.1038/324446a0. URL `http://adsabs.harvard.edu/abs/1986Natur.324..446B`.

C. M. Baugh. A primer on hierarchical galaxy formation: the semi-analytical approach. *Reports on Progress in Physics*, 69:3101–3156, December 2006. doi: 10.1088/0034-4885/69/12/R02. URL `http://adsabs.harvard.edu/abs/2006RPPh...69.3101B`.

J. Bel and C. Marinoni. Second-order matter fluctuations via higher order galaxy correlators. *Mon. Not. R. Astron. Soc.*, 424:971–992, August 2012. doi: 10.1111/j.1365-2966.2012.21257.x. URL `http://adsabs.harvard.edu/abs/2012MNRAS.424..971B`.

J. Bel and C. Marinoni. Determination of the abundance of cosmic matter via the cell count moments of the galaxy distribution. *Astron. Astrophys.*, 563:A36, March 2014. doi: 10.1051/0004-6361/201321941. URL `http://adsabs.harvard.edu/abs/2014A%26A...563A..36B`.

J. Bel, K. Hoffmann, and E. Gaztañaga. Non-local bias contribution to third-order galaxy correlations. *Mon. Not. R. Astron. Soc.*, 453:259–276, October 2015. doi: 10.1093/mnras/stv1600. URL `http://adsabs.harvard.edu/abs/2015MNRAS.453..259B`.

A. A. Berlind and D. H. Weinberg. The Halo Occupation Distribution: Toward an Empirical Determination of the Relation between Galaxies and Mass. *Astrophys. J.*, 575: 587–616, August 2002. doi: 10.1086/341469. URL `http://adsabs.harvard.edu/abs/2002ApJ...575..587B`.

F. Bernardeau, S. Colombi, E. Gaztañaga, and R. Scoccimarro. Large-scale structure of the Universe and cosmological perturbation theory. *Physics Reports*, 367:1–248, September 2002. doi: 10.1016/S0370-1573(02)00135-7. URL `http://adsabs.harvard.edu/abs/2002PhR...367....1B`.

F. Bernardeau, M. Crocce, and R. Scoccimarro. Multipoint propagators in cosmological gravitational instability. *Phys. Rev. D*, 78(10):103521, November 2008. doi: 10.1103/PhysRevD.78.103521. URL `http://adsabs.harvard.edu/abs/2008PhRvD..78j3521B`.

F. Beutler, S. Saito, H.-J. Seo, J. Brinkmann, K. S. Dawson, D. J. Eisenstein, A. Font-Ribera, S. Ho, C. K. McBride, F. Montesano, W. J. Percival, A. J. Ross, N. P. Ross, L. Samushia, D. J. Schlegel, A. G. Sánchez, J. L. Tinker, and B. A. Weaver. The clustering of galaxies in the SDSS-III Baryon Oscillation Spectroscopic Survey: testing gravity with redshift space distortions using the power spectrum multipoles. *Mon. Not. R. Astron. Soc.*, 443: 1065–1089, September 2014. doi: 10.1093/mnras/stu1051. URL `http://adsabs.harvard.edu/abs/2014MNRAS.443.1065B`.

S. Bird, M. Viel, and M. G. Haehnelt. Massive neutrinos and the non-linear matter power spectrum. *Mon. Not. R. Astron. Soc.*, 420:2551–2561, March 2012. doi: 10.1111/j.1365-2966.2011.20222.x. URL `http://adsabs.harvard.edu/abs/2012MNRAS.420.2551B`.

Simeon Bird, Matteo Viel, and Martin G. Haehnelt. Massive neutrinos and the non-linear matter power spectrum. *Mon. Not. R. Astron. Soc.*, 420:2551–2561, March 2012. doi: 10.1111/j.1365-2966.2011.20222.x. URL `http://adsabs.harvard.edu/abs/2012MNRAS.420.2551B`.

D. Blas, M. Garny, T. Konstandin, and J. Lesgourgues. Structure formation with massive neutrinos: going beyond linear theory. *Journal of Cosmology and Astroparticle Physics*, 11:039, November 2014. doi: 10.1088/1475-7516/2014/11/039. URL `http://adsabs.harvard.edu/abs/2014JCAP...11..039B`.

L. Blot, P. S. Corasaniti, L. Amendola, and T. D. Kitching. Non-Linear Matter Power Spectrum Covariance Matrix Errors and Cosmological Parameter Uncertainties. *ArXiv e-prints*, December 2015. URL `http://adsabs.harvard.edu/abs/2015arXiv151205383B`.

J. R. Bond, G. P. Efstathiou, and Joseph Silk. Massive neutrinos and the large-scale structure of the universe. *Physical Review Letters*, 45:1980–1984, December 1980. doi: 10.1103/PhysRevLett.45.1980. URL `http://adsabs.harvard.edu/abs/1980PhRvL..45.1980B`.

J. Brandbyge and S. Hannestad. Grid based linear neutrino perturbations in cosmological N-body simulations. *Journal of Cosmology and Astroparticle Physics*, 5:002, May 2009. doi: 10.1088/1475-7516/2009/05/002. URL `http://adsabs.harvard.edu/abs/2009JCAP...05..002B`.

J. Brandbyge, S. Hannestad, T. Haugbølle, and B. Thomsen. The effect of thermal neutrino motion on the non-linear cosmological matter power spectrum. *Journal of Cosmology and Astroparticle Physics*, 8:020, August 2008. doi: 10.1088/1475-7516/2008/08/020. URL `http://adsabs.harvard.edu/abs/2008JCAP...08..020B`.

J. Brandbyge, S. Hannestad, T. Haugbølle, and Y. Y. Y. Wong. Neutrinos in non-linear structure formation - the effect on halo properties. *Journal of Cosmology and Astroparticle Physics*, 9:14, September 2010. doi: 10.1088/1475-7516/2010/09/014. URL `http://adsabs.harvard.edu/abs/2010JCAP...09..014B`.

M. Calabrese, C. Carbone, G. Fabbian, M. Baldi, and C. Baccigalupi. Multiple lensing of the cosmic microwave background anisotropies. *Journal of Cosmology and Astroparticle Physics*, 3:049, March 2015. doi: 10.1088/1475-7516/2015/03/049. URL `http://adsabs.harvard.edu/abs/2015JCAP...03..049C`.

C. Carbone, M. Petkova, and K. Dolag. DEMNUni: ISW, Rees-Sciama, and weak-lensing in the presence of massive neutrinos. *ArXiv e-prints*, May 2016. URL `http://adsabs.harvard.edu/abs/2016arXiv160502024C`.

J. Carretero, F. J. Castander, E. Gaztañaga, M. Crocce, and P. Fosalba. An algorithm to build mock galaxy catalogues using MICE simulations. *Mon. Not. R. Astron. Soc.*, 447:646–670, February 2015. doi: 10.1093/mnras/stu2402. URL `http://adsabs.harvard.edu/abs/2015MNRAS.447..646C`.

E. Castorina, C. Carbone, J. Bel, E. Sefusatti, and K. Dolag. DEMNUni: the clustering of large-scale structures in the presence of massive neutrinos. *Journal of Cosmology* *and Astroparticle Physics*, 7:043, July 2015. doi: 10.1088/1475-7516/2015/07/043. URL `http://adsabs.harvard.edu/abs/2015JCAP...07..043C`.

K. C. Chan, R. Scoccimarro, and R. K. Sheth. Gravity and large-scale nonlocal bias. *Phys. Rev. D*, 85(8):083509, April 2012. doi: 10.1103/PhysRevD.85.083509. URL `http://adsabs.harvard.edu/abs/2012PhRvD..85h3509C`.

J. Chaves-Montero, R. E. Angulo, J. Schaye, M. Schaller, R. A. Crain, M. Furlong, and T. Theuns. Subhalo abundance matching and assembly bias in the EAGLE simulation. *Mon. Not. R. Astron. Soc.*, May 2016. doi: 10.1093/mnras/stw1225. URL `http://adsabs.harvard.edu/abs/2016MNRAS.tmp..893C`.

S. Cole, W. J. Percival, J. A. Peacock, P. Norberg, C. M. Baugh, C. S. Frenk, I. Baldry, J. Bland-Hawthorn, T. Bridges, R. Cannon, M. Colless, C. Collins, W. Couch, N. J. G. Cross, G. Dalton, V. R. Eke, R. De Propris, S. P. Driver, G. Efstathiou, R. S. Ellis, K. Glazebrook, C. Jackson, A. Jenkins, O. Lahav, I. Lewis, S. Lumsden, S. Maddox, D. Madgwick, B. A. Peterson, W. Sutherland, and K. Taylor. The 2dF Galaxy Redshift Survey: power-spectrum analysis of the final data set and cosmological implications. *Mon. Not. R. Astron. Soc.*, 362:505–534, September 2005. doi: 10.1111/j.1365-2966.2005.09318.x. URL `http://adsabs.harvard.edu/abs/2005MNRAS.362..505C`.

A. Cooray and R. Sheth. Halo models of large scale structure. *Physics Reports*, 372:1–129, December 2002. doi: 10.1016/S0370-1573(02)00276-4. URL `http://adsabs.harvard.edu/abs/2002PhR...372....1C`.

C. L. Cowan, Jr., F. Reines, F. B. Harrison, H. W. Kruse, and A. D. McGuire. Detection of the Free Neutrino: A Confirmation. *Science*, 124:103–104, July 1956. doi: 10.1126/science.124.3212.103. URL `http://adsabs.harvard.edu/abs/1956Sci...124..103C`.

M. Crocce and R. Scoccimarro. Renormalized cosmological perturbation theory. *Phys. Rev. D*, 73(6):063519, March 2006. doi: 10.1103/PhysRevD.73.063519. URL `http://adsabs.harvard.edu/abs/2006PhRvD..73f3519C`.

M. Crocce, P. Fosalba, F. J. Castander, and E. Gaztañaga. Simulating the Universe with MICE: the abundance of massive clusters. *Mon. Not. R. Astron. Soc.*, 403:1353–1367, April 2010. doi: 10.1111/j.1365-2966.2009.16194.x. URL `http://adsabs.harvard.edu/abs/2010MNRAS.403.1353C`.

Martín Crocce, Sebastian Pueblas, and Román Scoccimarro. Transients from initial conditions in cosmological simulations. *Mon. Not. R. Astron. Soc.*, 373:369–381, November 2006. doi: 10.1111/j.1365-2966.2006.11040.x. URL `http://adsabs.harvard.edu/abs/2006MNRAS.373..369C`.

K. S. Dawson, D. J. Schlegel, C. P. Ahn, S. F. Anderson, É. Aubourg, S. Bailey, R. H. Barkhouser, J. E. Bautista, A. Beifiori, A. A. Berlind, V. Bhardwaj, D. Bizyaev, C. H. Blake, M. R. Blanton, M. Blomqvist, A. S. Bolton, A. Borde, J. Bovy, W. N. Brandt, H. Brewington, J. Brinkmann, P. J. Brown, J. R. Brownstein, K. Bundy, N. G. Busca, W. Carithers, A. R. Carnero, M. A. Carr, Y. Chen, J. Comparat, N. Connolly, F. Cope, R. A. C. Croft, A. J. Cuesta, L. N. da Costa, J. R. A. Davenport, T. Delubac, R. de Putter, S. Dhital, A. Ealet, G. L. Ebelke, D. J. Eisenstein, S. Escoffier, X. Fan, N. Filiz Ak, H. Finley, A. Font-Ribera, R. Génova-Santos, J. E. Gunn, H. Guo, D. Haggard, P. B. Hall, J.-C. Hamilton, B. Harris, D. W. Harris, S. Ho, D. W. Hogg, D. Holder, K. Honscheid, J. Huehnerhoff, B. Jordan, W. P. Jordan, G. Kauffmann, E. A. Kazin, D. Kirkby, M. A. Klaene, J.-P. Kneib, J.-M. Le Goff, K.-G. Lee, D. C. Long, C. P. Loomis, B. Lundgren, R. H. Lupton, M. A. G. Maia, M. Makler, E. Malanushenko, V. Malanushenko, R. Mandelbaum, M. Manera, C. Maraston, D. Margala, K. L. Masters, C. K. McBride, P. McDonald, I. D. McGreer, R. G. McMahon, O. Mena, J. Miralda-

Escudé, A. D. Montero-Dorta, F. Montesano, D. Muna, A. D. Myers, T. Naugle, R. C. Nichol, P. Noterdaeme, S. E. Nuza, M. D. Olmstead, A. Oravetz, D. J. Oravetz, R. Owen, N. Padmanabhan, N. Palanque-Delabrouille, K. Pan, J. K. Parejko, I. Pâris, W. J. Percival, I. Pérez-Fournon, I. Pérez-Ràfols, P. Petitjean, R. Pfaffenberger, J. Pforr, M. M. Pieri, F. Prada, A. M. Price-Whelan, M. J. Raddick, R. Rebolo, J. Rich, G. T. Richards, C. M. Rockosi, N. A. Roe, A. J. Ross, N. P. Ross, G. Rossi, J. A. Rubiño-Martin, L. Samushia, A. G. Sánchez, C. Sayres, S. J. Schmidt, D. P. Schneider, C. G. Scóccola, H.-J. Seo, A. Shelden, E. Sheldon, Y. Shen, Y. Shu, A. Slosar, S. A. Smee, S. A. Snedden, F. Stauffer, O. Steele, M. A. Strauss, A. Streblyanska, N. Suzuki, M. E. C. Swanson, T. Tal, M. Tanaka, D. Thomas, J. L. Tinker, R. Tojeiro, C. A. Tremonti, M. Vargas Magaña, L. Verde, M. Viel, D. A. Wake, M. Watson, B. A. Weaver, D. H. Weinberg, B. J. Weiner, A. A. West, M. White, W. M. Wood-Vasey, C. Yeche, I. Zehavi, G.-B. Zhao, and Z. Zheng. The Baryon Oscillation Spectroscopic Survey of SDSS-III. *Astron. J.*, 145:10, January 2013. doi: 10.1088/0004-6256/145/1/10. URL `http://adsabs.harvard.edu/abs/2013AJ....145...10D`.

K. S. Dawson, J.-P. Kneib, W. J. Percival, S. Alam, F. D. Albareti, S. F. Anderson, E. Armengaud, É. Aubourg, S. Bailey, J. E. Bautista, A. A. Berlind, M. A. Bershady, F. Beutler, D. Bizyaev, M. R. Blanton, M. Blomqvist, A. S. Bolton, J. Bovy, W. N. Brandt, J. Brinkmann, J. R. Brownstein, E. Burtin, N. G. Busca, Z. Cai, C.-H. Chuang, N. Clerc, J. Comparat, F. Cope, R. A. C. Croft, I. Cruz-Gonzalez, L. N. da Costa, M.-C. Cousinou, J. Darling, A. de la Macorra, S. de la Torre, T. Delubac, H. du Mas des Bourboux, T. Dwelly, A. Ealet, D. J. Eisenstein, M. Eracleous, S. Escoffier, X. Fan, A. Finoguenov, A. Font-Ribera, P. Frinchaboy, P. Gaulme, A. Georgakakis, P. Green, H. Guo, J. Guy, S. Ho, D. Holder, J. Huehnerhoff, T. Hutchinson, Y. Jing, E. Jullo, V. Kamble, K. Kinemuchi, D. Kirkby, F.-S. Kitaura, M. A. Klaene, R. R. Laher, D. Lang, P. Laurent, J.-M. Le Goff, C. Li, Y. Liang, M. Lima, Q. Lin, W. Lin, Y.-T. Lin, D. C. Long, B. Lundgren, N. MacDonald, M. A. Geimba Maia, E. Malanushenko, V. Malanushenko, V. Mariappan, C. K. McBride, I. D. McGreer, B. Ménard, A. Merloni, A. Meza, A. D. Montero-Dorta, D. Muna, A. D. Myers, K. Nandra, T. Naugle, J. A. Newman, P. Noterdaeme, P. Nugent, R. Ogando, M. D. Olmstead, A. Oravetz, D. J. Oravetz, N. Padmanabhan, N. Palanque-Delabrouille, K. Pan, J. K. Parejko, I. Pâris, J. A. Peacock, P. Petitjean, M. M. Pieri, A. Pisani, F. Prada, A. Prakash, A. Raichoor, B. Reid, J. Rich, J. Ridl, S. Rodriguez-Torres, A. Carnero Rosell, A. J. Ross, G. Rossi, J. Ruan, M. Salvato, C. Sayres, D. P. Schneider, D. J. Schlegel, U. Seljak, H.-J. Seo, B. Sesar, S. Shandera, Y. Shu, A. Slosar, F. Sobreira, A. Streblyanska, N. Suzuki, D. Taylor, C. Tao, J. L. Tinker, R. Tojeiro, M. Vargas-Magaña, Y. Wang, B. A. Weaver, D. H. Weinberg, M. White, W. M. Wood-Vasey, C. Yeche, Z. Zhai, C. Zhao, G.-b. Zhao, Z. Zheng, G. Ben Zhu, and H. Zou. The SDSS-IV Extended Baryon Oscillation Spectroscopic Survey: Overview and Early Data. *Astron. J.*, 151:44, February 2016. doi: 10.3847/0004-6256/151/2/44. URL `http://adsabs.harvard.edu/abs/2016AJ....151...44D`.

W. Dehnen. A Very Fast and Momentum-conserving Tree Code. *Astrophys. J. Lett.*, 536: L39–L42, June 2000. doi: 10.1086/312724. URL `http://adsabs.harvard.edu/abs/2000ApJ...536L..39D`.

V. Desjacques, D. Jeong, and F. Schmidt. Large-Scale Galaxy Bias. *ArXiv e-prints*, November 2016. URL `http://adsabs.harvard.edu/abs/2016arXiv161109787D`.

A. D. Dolgov, S. H. Hansen, S. Pastor, S. T. Petcov, G. G. Raffelt, and D. V. Semikoz. Cosmological bounds on neutrino degeneracy improved by flavor oscillations. *Nuclear Physics B*, 632:363–382, June 2002. doi: 10.1016/S0550-3213(02)00274-2. URL `http://adsabs.harvard.edu/abs/2002NuPhB.632..363D`.

J. W. Eastwood, R. W. Hockney, and D. N. Lawrence. P3M3DP-the three-dimensional periodic particle-particle/particle-mesh program. *Computer Physics Communications*, 35, 1984. doi: 10.1016/S0010-4655(84)82783-6. URL `http://adsabs.harvard.edu/abs/1984CoPhC..35..618E`.

G. Efstathiou, M. Davis, S. D. M. White, and C. S. Frenk. Numerical techniques for large cosmological N-body simulations. *Astrophys. J. Suppl.*, 57:241–260, February 1985. doi: 10.1086/191003. URL `http://adsabs.harvard.edu/abs/1985ApJS...57..241E`.

D. J. Eisenstein, I. Zehavi, D. W. Hogg, R. Scoccimarro, M. R. Blanton, R. C. Nichol, R. Scranton, H.-J. Seo, M. Tegmark, Z. Zheng, S. F. Anderson, J. Annis, N. Bahcall, J. Brinkmann, S. Burles, F. J. Castander, A. Connolly, I. Csabai, M. Doi, M. Fukugita, J. A. Frieman, K. Glazebrook, J. E. Gunn, J. S. Hendry, G. Hennessy, Z. Ivezić, S. Kent, G. R. Knapp, H. Lin, Y.-S. Loh, R. H. Lupton, B. Margon, T. A. McKay, A. Meiksin, J. A. Munn, A. Pope, M. W. Richmond, D. Schlegel, D. P. Schneider, K. Shimasaku, C. Stoughton, M. A. Strauss, M. SubbaRao, A. S. Szalay, I. Szapudi, D. L. Tucker, B. Yanny, and D. G. York. Detection of the Baryon Acoustic Peak in the Large-Scale Correlation Function of SDSS Luminous Red Galaxies. *Astrophys. J.*, 633:560–574, November 2005. doi: 10.1086/466512. URL `http://adsabs.harvard.edu/abs/2005ApJ...633..560E`.

I. Esteban, M. C. Gonzalez-Garcia, M. Maltoni, I. Martinez-Soler, and T. Schwetz. Updated fit to three neutrino mixing: exploring the accelerator-reactor complementarity. *Journal of High Energy Physics*, 1:87, January 2017. doi: 10.1007/JHEP01(2017)087. URL `http://adsabs.harvard.edu/abs/2017JHEP...01..087E`.

D. J. Fixsen. The Temperature of the Cosmic Microwave Background. *Astrophys. J.*, 707:916–920, December 2009. doi: 10.1088/0004-637X/707/2/916. URL `http://adsabs.harvard.edu/abs/2009ApJ...707..916F`.

D. Foreman-Mackey, D. W. Hogg, D. Lang, and J. Goodman. emcee: The MCMC Hammer. *Publ. Astron. Soc. Pac.*, 125:306, March 2013. doi: 10.1086/670067. URL `http://adsabs.harvard.edu/abs/2013PASP..125..306F`.

D. V. Forero, M. Tórtola, and J. W. F. Valle. Neutrino oscillations refitted. *Phys. Rev. D*, 90(9):093006, November 2014. doi: 10.1103/PhysRevD.90.093006. URL `http://adsabs.harvard.edu/abs/2014PhRvD..90i3006F`.

J. N. Fry. The Galaxy correlation hierarchy in perturbation theory. *Astrophys. J.*, 279: 499–510, April 1984. doi: 10.1086/161913. URL `http://adsabs.harvard.edu/abs/1984ApJ...279..499F`.

J. N. Fry and E. Gaztanaga. Biasing and hierarchical statistics in large-scale structure. *Astrophys. J.*, 413:447–452, August 1993. doi: 10.1086/173015. URL `http://adsabs.harvard.edu/abs/1993ApJ...413..447F`.

H. Gil-Marín, J. Noreña, L. Verde, W. J. Percival, C. Wagner, M. Manera, and D. P. Schneider. The power spectrum and bispectrum of SDSS DR11 BOSS galaxies - I. Bias and gravity. *Mon. Not. R. Astron. Soc.*, 451:539–580, July 2015. doi: 10.1093/mnras/stv961. URL `http://adsabs.harvard.edu/abs/2015MNRAS.451..539G`.

M. C. Gonzalez-Garcia, M. Maltoni, and T. Schwetz. Updated fit to three neutrino mixing: status of leptonic CP violation. *Journal of High Energy Physics*, 11:52, November 2014. doi: 10.1007/JHEP11(2014)052. URL `http://adsabs.harvard.edu/abs/2014JHEP...11..052G`.

Q. Guo, S. White, C. Li, and M. Boylan-Kolchin. How do galaxies populate dark matter haloes? *Mon. Not. R. Astron. Soc.*, 404:1111–1120, May 2010. doi: 10.1111/j.1365-2966.2010.16341.x. URL `http://adsabs.harvard.edu/abs/2010MNRAS.`

`404.1111G`.

L. Guzzo, M. Scodeggio, B. Garilli, B. R. Granett, A. Fritz, U. Abbas, C. Adami, S. Arnouts, J. Bel, M. Bolzonella, D. Bottini, E. Branchini, A. Cappi, J. Coupon, O. Cucciati, I. Davidzon, G. De Lucia, S. de la Torre, P. Franzetti, M. Fumana, P. Hudelot, O. Ilbert, A. Iovino, J. Krywult, V. Le Brun, O. Le Fèvre, D. Maccagni, K. Małek, F. Marulli, H. J. McCracken, L. Paioro, J. A. Peacock, M. Polletta, A. Pollo, H. Schlagenhaufer, L. A. M. Tasca, R. Tojeiro, D. Vergani, G. Zamorani, A. Zanichelli, A. Burden, C. Di Porto, A. Marchetti, C. Marinoni, Y. Mellier, L. Moscardini, R. C. Nichol, W. J. Percival, S. Phleps, and M. Wolk. The VIMOS Public Extragalactic Redshift Survey (VIPERS). An unprecedented view of galaxies and large-scale structure at $0.5 \lesssim z \lesssim 1.2$. *Astron. Astrophys.*, 566:A108, June 2014. doi: 10.1051/0004-6361/201321489. URL `http://adsabs.harvard.edu/abs/2014A%26A...566A.108G`.

D. Inman, J. D. Emberson, U.-L. Pen, A. Farchi, H.-R. Yu, and J. Harnois-Déraps. Precision reconstruction of the cold dark matter-neutrino relative velocity from N -body simulations. *Phys. Rev. D*, 92(2):023502, July 2015. doi: 10.1103/PhysRevD.92.023502. URL `http://adsabs.harvard.edu/abs/2015PhRvD..92b3502I`.

J. H. Jeans. The Stability of a Spherical Nebula. *Royal Society of London Philosophical Transactions Series A*, 199:1–53, 1902. doi: 10.1098/rsta.1902.0012. URL `http://adsabs.harvard.edu/abs/1902RSPTA.199....1J`.

Y. P. Jing. Correcting for the Alias Effect When Measuring the Power Spectrum Using a Fast Fourier Transform. *Astrophys. J.*, 620:559–563, February 2005. doi: 10.1086/427087. URL `http://adsabs.harvard.edu/abs/2005ApJ...620..559J`.

N. Kaiser. Clustering in real space and in redshift space. *Mon. Not. R. Astron. Soc.*, 227: 1–21, July 1987. URL `http://adsabs.harvard.edu/abs/1987MNRAS.227....1K`.

A. A. Klypin and S. F. Shandarin. Three-dimensional numerical model of the formation of large-scale structure in the Universe. *Mon. Not. R. Astron. Soc.*, 204:891–907, September 1983. doi: 10.1093/mnras/204.3.891. URL `http://adsabs.harvard.edu/abs/1983MNRAS.204..891K`.

C. Kraus, B. Bornschein, L. Bornschein, J. Bonn, B. Flatt, A. Kovalik, B. Ostrick, E. W. Otten, J. P. Schall, T. Thümmler, and C. Weinheimer. Final results from phase II of the Mainz neutrino mass searchin tritium $\{\beta\}$ decay. *European Physical Journal C*, 40:447–468, April 2005. doi: 10.1140/epjc/s2005-02139-7. URL `http://adsabs.harvard.edu/abs/2005EPJC...40..447K`.

J. Lesgourgues. The Cosmic Linear Anisotropy Solving System (CLASS) I: Overview. *ArXiv e-prints 1104.2932*, April 2011a. URL `http://adsabs.harvard.edu/abs/2011arXiv1104.2932L`.

J. Lesgourgues. The Cosmic Linear Anisotropy Solving System (CLASS) III: Comparision with CAMB for LambdaCDM. *ArXiv e-prints*, April 2011b. URL `http://adsabs.harvard.edu/abs/2011arXiv1104.2934L`.

J. Lesgourgues and S. Pastor. Massive neutrinos and cosmology. *Physics Reports*, 429:307–379, July 2006. doi: 10.1016/j.physrep.2006.04.001. URL `http://adsabs.harvard.edu/abs/2006PhR...429..307L`.

J. Lesgourgues and S. Pastor. Neutrino mass from Cosmology. *ArXiv e-prints*, December 2012. URL `http://adsabs.harvard.edu/abs/2012arXiv1212.6154L`.

J. Lesgourgues and S. Pastor. Neutrino cosmology and Planck. *New Journal of Physics*, 16 (6):065002, June 2014. doi: 10.1088/1367-2630/16/6/065002. URL `http://adsabs.harvard.edu/abs/2014NJPh...16f5002L`.

J. Lesgourgues and T. Tram. The Cosmic Linear Anisotropy Solving System (CLASS)

IV: efficient implementation of non-cold relics. *Journal of Cosmology and Astroparticle Physics*, 9:032, September 2011. doi: 10.1088/1475-7516/2011/09/032. URL `http://adsabs.harvard.edu/abs/2011JCAP...09..032L`.

Antony Lewis, Anthony Challinor, and Anthony Lasenby. Efficient computation of cosmic microwave background anisotropies in closed friedmann-robertson-walker models. *Astrophys. J.*, 538:473–476, August 2000. doi: 10.1086/309179. URL `http://adsabs.harvard.edu/abs/2000ApJ...538..473L`.

Chung-Pei Ma and Edmund Bertschinger. Cosmological Perturbation Theory in the Synchronous and Conformal Newtonian Gauges. *Astrophys. J.*, 455:7–+, December 1995. doi: 10.1086/176550. URL `http://adsabs.harvard.edu/abs/1995ApJ...455....7M`.

C. Marinoni, J. Bel, and A. Buzzi. The scale of cosmic isotropy. *Journal of Cosmology and Astroparticle Physics*, 10:036, October 2012. doi: 10.1088/1475-7516/2012/10/036. URL `http://adsabs.harvard.edu/abs/2012JCAP...10..036M`.

E. Massara, F. Villaescusa-Navarro, and M. Viel. The halo model in a massive neutrino cosmology. *Journal of Cosmology and Astroparticle Physics*, 12:053, December 2014. doi: 10.1088/1475-7516/2014/12/053. URL `http://adsabs.harvard.edu/abs/2014JCAP...12..053M`.

I. G. McCarthy, J. Schaye, S. Bird, and A. M. C. Le Brun. The BAHAMAS project: calibrated hydrodynamical simulations for large-scale structure cosmology. *Mon. Not. R. Astron. Soc.*, 465:2936–2965, March 2017. doi: 10.1093/mnras/stw2792. URL `http://adsabs.harvard.edu/abs/2017MNRAS.465.2936M`.

P. McDonald and A. Roy. Clustering of dark matter tracers: generalizing bias for the coming era of precision LSS. *Journal of Cosmology and Astroparticle Physics*, 8:020, August 2009. doi: 10.1088/1475-7516/2009/08/020. URL `http://adsabs.harvard.edu/abs/2009JCAP...08..020M`.

S. P. Mikheyev and A. Y. Smirnov. Resonance enhancement of oscillations in matter and solar neutrino spectroscopy. *Yadernaya Fizika*, 42:1441–1448, 1985. URL `http://adsabs.harvard.edu/abs/1985YaFiz..42.1441M`.

B. O. Mummery, I. G. McCarthy, S. Bird, and J. Schaye. The separate and combined effects of baryon physics and neutrino free streaming on large-scale structure. *Mon. Not. R. Astron. Soc.*, 471:227–242, October 2017. doi: 10.1093/mnras/stx1469. URL `http://adsabs.harvard.edu/abs/2017MNRAS.471..227M`.

N. Palanque-Delabrouille, C. Yèche, J. Baur, C. Magneville, G. Rossi, J. Lesgourgues, A. Borde, E. Burtin, J.-M. LeGoff, J. Rich, M. Viel, and D. Weinberg. Neutrino masses and cosmology with Lyman-alpha forest power spectrum. *Journal of Cosmology and Astroparticle Physics*, 11:011, November 2015. doi: 10.1088/1475-7516/2015/11/011. URL `http://adsabs.harvard.edu/abs/2015JCAP...11..011P`.

P. J. E. Peebles. *The large-scale structure of the universe*. 1980. URL `http://adsabs.harvard.edu/abs/1980lssu.book.....P`.

M. Pellejero-Ibanez, C.-H. Chuang, J. A. Rubiño-Martín, A. J. Cuesta, Y. Wang, G.-b. Zhao, A. J. Ross, S. Rodríguez-Torres, F. Prada, A. Slosar, J. A. Vazquez, S. Alam, F. Beutler, D. J. Eisenstein, H. Gil-Marín, J. N. Grieb, S. Ho, F.-S. Kitaura, W. J. Percival, G. Rossi, S. Salazar-Albornoz, L. Samushia, A. G. Sánchez, S. Satpathy, H.-J. Seo, J. L. Tinker, R. Tojeiro, M. Vargas-Magaña, J. R. Brownstein, R. C Nichol, and M. D Olmstead. The clustering of galaxies in the completed SDSS-III Baryon Oscillation Spectroscopic Survey: double-probe measurements from BOSS galaxy clustering and Planck data – towards an analysis without informative priors. *ArXiv e-prints*, July 2016. URL `http://adsabs.harvard.edu/abs/2016arXiv160703152P`.

S. Perlmutter, G. Aldering, G. Goldhaber, R. A. Knop, P. Nugent, P. G. Castro, S. Deustua, S. Fabbro, A. Goobar, D. E. Groom, I. M. Hook, A. G. Kim, M. Y. Kim, J. C. Lee, N. J. Nunes, R. Pain, C. R. Pennypacker, R. Quimby, C. Lidman, R. S. Ellis, M. Irwin, R. G. McMahon, P. Ruiz-Lapuente, N. Walton, B. Schaefer, B. J. Boyle, A. V. Filippenko, T. Matheson, A. S. Fruchter, N. Panagia, H. J. M. Newberg, W. J. Couch, and T. S. C. Project. Measurements of Ω and Λ from 42 High-Redshift Supernovae. *Astrophys. J.*, 517:565–586, June 1999. doi: 10.1086/307221. URL `http://adsabs.harvard.edu/abs/1999ApJ...517..565P`.

Planck Collaboration, P. A. R. Ade, N. Aghanim, C. Armitage-Caplan, M. Arnaud, M. Ashdown, F. Atrio-Barandela, J. Aumont, C. Baccigalupi, A. J. Banday, and et al. Planck 2013 results. XVI. Cosmological parameters. *ArXiv e-prints*, March 2013. URL `http://adsabs.harvard.edu/abs/2013arXiv1303.5076P`.

Planck Collaboration, P. A. R. Ade, N. Aghanim, M. Arnaud, M. Ashdown, J. Aumont, C. Baccigalupi, A. J. Banday, R. B. Barreiro, J. G. Bartlett, and et al. Planck 2015 results. XIII. Cosmological parameters. *ArXiv e-prints*, February 2015. URL `http://adsabs.harvard.edu/abs/2015arXiv150201589P`.

Planck Collaboration, N. Aghanim, M. Arnaud, M. Ashdown, J. Aumont, C. Baccigalupi, A. J. Banday, R. B. Barreiro, J. G. Bartlett, N. Bartolo, and et al. Planck 2015 results. XI. CMB power spectra, likelihoods, and robustness of parameters. *Astron. Astrophys.*, 594: A11, September 2016. doi: 10.1051/0004-6361/201526926. URL `http://adsabs.harvard.edu/abs/2016A%26A...594A..11P`.

W. H. Press and P. Schechter. Formation of Galaxies and Clusters of Galaxies by Self-Similar Gravitational Condensation. *Astrophys. J.*, 187:425–438, February 1974. doi: 10.1086/152650. URL `http://adsabs.harvard.edu/abs/1974ApJ...187..425P`.

D. J. Price. splash: An Interactive Visualisation Tool for Smoothed Particle Hydrodynamics Simulations. *Publ. of the Astron. Soc. of Australia*, 24:159–173, October 2007. doi: 10.1071/AS07022. URL `http://adsabs.harvard.edu/abs/2007PASA...24..159P`.

A. G. Riess, A. V. Filippenko, P. Challis, A. Clocchiatti, A. Diercks, P. M. Garnavich, R. L. Gilliland, C. J. Hogan, S. Jha, R. P. Kirshner, B. Leibundgut, M. M. Phillips, D. Reiss, B. P. Schmidt, R. A. Schommer, R. C. Smith, J. Spyromilio, C. Stubbs, N. B. Suntzeff, and J. Tonry. Observational Evidence from Supernovae for an Accelerating Universe and a Cosmological Constant. *Astron. J.*, 116:1009–1038, September 1998. doi: 10.1086/300499. URL `http://adsabs.harvard.edu/abs/1998AJ....116.1009R`.

Graziano Rossi, N. Palanque-Delabrouille, A. Borde, Matteo Viel, C. Yèche, J. S. Bolton, J. Rich, and J.-M. Le Goff. Suite of hydrodynamical simulations for the Lyman-α forest with massive neutrinos. *Astron. Astrophys.*, 567:A79, July 2014. doi: 10.1051/0004-6361/201423507. URL `http://adsabs.harvard.edu/abs/2014A%26A...567A..79R`.

S. Saito, T. Baldauf, Z. Vlah, U. Seljak, T. Okumura, and P. McDonald. Understanding higher-order nonlocal halo bias at large scales by combining the power spectrum with the bispectrum. *Phys. Rev. D*, 90(12):123522, December 2014. doi: 10.1103/PhysRevD.90.123522. URL `http://adsabs.harvard.edu/abs/2014PhRvD..90l3522S`.

R. Scoccimarro. Redshift-space distortions, pairwise velocities, and nonlinearities. *Phys. Rev. D*, 70(8):083007, October 2004. doi: 10.1103/PhysRevD.70.083007. URL `http://adsabs.harvard.edu/abs/2004PhRvD..70h3007S`.

Román Scoccimarro. Transients from initial conditions: a perturbative analysis. *Mon. Not. R. Astron. Soc.*, 299:1097–1118, October 1998. doi: 10.1046/j.1365-8711.1998.01845.

x. URL `http://adsabs.harvard.edu/abs/1998MNRAS.299.1097S`.

Román Scoccimarro, Matias Zaldarriaga, and Lam Hui. Power spectrum correlations induced by nonlinear clustering. *Astrophys. J.*, 527:1–15, December 1999. doi: 10.1086/308059. URL `http://adsabs.harvard.edu/abs/1999ApJ...527....1S`.

E. Sefusatti, M. Crocce, R. Scoccimarro, and H. M. P. Couchman. Accurate estimators of correlation functions in Fourier space. *Mon. Not. R. Astron. Soc.*, 460:3624–3636, August 2016. doi: 10.1093/mnras/stw1229. URL `http://adsabs.harvard.edu/abs/2016MNRAS.460.3624S`.

Uros Seljak and Matias Zaldarriaga. A line-of-sight integration approach to cosmic microwave background anisotropies. *Astrophys. J.*, 469:437–+, October 1996. doi: 10.1086/177793. URL `http://adsabs.harvard.edu/abs/1996ApJ...469..437S`.

M. Shoji and E. Komatsu. Erratum: Massive neutrinos in cosmology: Analytic solutions and fluid approximation [Phys. Rev. D 81, 123516 (2010)]. *Phys. Rev. D*, 82(8):089901, October 2010. doi: 10.1103/PhysRevD.82.089901. URL `http://adsabs.harvard.edu/abs/2010PhRvD..82h9901S`.

R. E. Smith, J. A. Peacock, A. Jenkins, S. D. M. White, C. S. Frenk, F. R. Pearce, P. A. Thomas, G. Efstathiou, and H. M. P. Couchman. Stable clustering, the halo model and non-linear cosmological power spectra. *Mon. Not. R. Astron. Soc.*, 341:1311–1332, June 2003. doi: 10.1046/j.1365-8711.2003.06503.x. URL `http://adsabs.harvard.edu/abs/2003MNRAS.341.1311S`.

V. Springel. The cosmological simulation code GADGET-2. *Mon. Not. R. Astron. Soc.*, 364:1105–1134, December 2005. doi: 10.1111/j.1365-2966.2005.09655.x. URL `http://adsabs.harvard.edu/abs/2005MNRAS.364.1105S`.

R. Takahashi, M. Sato, T. Nishimichi, A. Taruya, and M. Oguri. Revising the Halofit Model for the Nonlinear Matter Power Spectrum. *Astrophys. J.*, 761:152, December 2012. doi: 10.1088/0004-637X/761/2/152. URL `http://adsabs.harvard.edu/abs/2012ApJ...761..152T`.

A. Taruya, F. Bernardeau, T. Nishimichi, and S. Codis. Direct and fast calculation of regularized cosmological power spectrum at two-loop order. *Phys. Rev. D*, 86(10): 103528, November 2012. doi: 10.1103/PhysRevD.86.103528. URL `http://adsabs.harvard.edu/abs/2012PhRvD..86j3528T`.

J. Tinker, A. V. Kravtsov, A. Klypin, K. Abazajian, M. Warren, G. Yepes, S. Gottlöber, and D. E. Holz. Toward a Halo Mass Function for Precision Cosmology: The Limits of Universality. *Astrophys. J.*, 688:709-728, December 2008. doi: 10.1086/591439. URL `http://adsabs.harvard.edu/abs/2008ApJ...688..709T`.

S. Trujillo-Gomez, A. Klypin, J. Primack, and A. J. Romanowsky. Galaxies in ΛCDM with Halo Abundance Matching: Luminosity-Velocity Relation, Baryonic Mass-Velocity Relation, Velocity Function, and Clustering. *Astrophys. J.*, 742:16, November 2011. doi: 10.1088/0004-637X/742/1/16. URL `http://adsabs.harvard.edu/abs/2011ApJ...742...16T`.

A. Upadhye, R. Biswas, A. Pope, K. Heitmann, S. Habib, H. Finkel, and N. Frontiere. Large-scale structure formation with massive neutrinos and dynamical dark energy. *Phys. Rev. D*, 89(10):103515, May 2014. doi: 10.1103/PhysRevD.89.103515. URL `http://adsabs.harvard.edu/abs/2014PhRvD..89j3515U`.

A. Vale and J. P. Ostriker. Linking halo mass to galaxy luminosity. *Mon. Not. R. Astron. Soc.*, 353:189–200, September 2004. doi: 10.1111/j.1365-2966.2004.08059.x. URL `http://adsabs.harvard.edu/abs/2004MNRAS.353..189V`.

M. Viel, M. G. Haehnelt, and V. Springel. The effect of neutrinos on the matter distribution as probed by the intergalactic medium. *Journal of Cosmology and Astroparticle Physics*, 6:015, June 2010. doi: 10.1088/1475-7516/2010/06/015. URL `http://adsabs.harvard.edu/abs/2010JCAP...06..015V`.

F. Villaescusa-Navarro, S. Bird, C. Peña-Garay, and M. Viel. Non-linear evolution of the cosmic neutrino background. *Journal of Cosmology and Astroparticle Physics*, 3:019, March 2013. doi: 10.1088/1475-7516/2013/03/019. URL `http://adsabs.harvard.edu/abs/2013JCAP...03..019V`.

F. Villaescusa-Navarro, A. Banerjee, N. Dalal, E. Castorina, R. Scoccimarro, R. Angulo, and D. N. Spergel. The imprint of neutrinos on clustering in redshift-space. *ArXiv e-prints*, August 2017. URL `http://adsabs.harvard.edu/abs/2017arXiv170801154V`.

S. D. M. White. Formation and Evolution of Galaxies: Les Houches Lectures. *ArXiv Astrophysics e-prints*, October 1994. URL `http://adsabs.harvard.edu/abs/1994astro.ph.10043W`.

S. D. M. White, C. S. Frenk, and M. Davis. Clustering in a neutrino-dominated universe. *Astrophys. J. Lett.*, 274:L1–L5, November 1983. doi: 10.1086/184139. URL `http://adsabs.harvard.edu/abs/1983ApJ...274L...1W`.

L. Wolfenstein. Neutrino oscillations in matter. *Phys. Rev. D*, 17:2369–2374, May 1978. doi: 10.1103/PhysRevD.17.2369. URL `http://adsabs.harvard.edu/abs/1978PhRvD..17.2369W`.

Y. Y. Wong. Analytical treatment of neutrino asymmetry equilibration from flavor oscillations in the early universe. *Phys. Rev. D*, 66(2):025015, July 2002. doi: 10.1103/PhysRevD.66.025015. URL `http://adsabs.harvard.edu/abs/2002PhRvD..66b5015W`.

Yvonne Y. Y. Wong. Higher order corrections to the large scale matter power spectrum in the presence of massive neutrinos. *Journal of Cosmology and Astroparticle Physics*, 10:035, October 2008. doi: 10.1088/1475-7516/2008/10/035. URL `http://adsabs.harvard.edu/abs/2008JCAP...10..035W`.

G. Xu. A New Parallel N-Body Gravity Solver: TPM. *Astrophys. J. Suppl.*, 98:355, May 1995. doi: 10.1086/192166. URL `http://adsabs.harvard.edu/abs/1995ApJS...98..355X`.

Y. B. Zel'dovich. Gravitational instability: An approximate theory for large density perturbations. *Astron. Astrophys.*, 5:84–89, March 1970. URL `http://adsabs.harvard.edu/abs/1970A%26A.....5...84Z`.

M. Zennaro, J. Bel, F. Villaescusa-Navarro, C. Carbone, E. Sefusatti, and L. Guzzo. Initial conditions for accurate N-body simulations of massive neutrino cosmologies. *Mon. Not. R. Astron. Soc.*, 466:3244–3258, April 2017. doi: 10.1093/mnras/stw3340. URL `http://adsabs.harvard.edu/abs/2017MNRAS.466.3244Z`.

Z. Zheng, A. A. Berlind, D. H. Weinberg, A. J. Benson, C. M. Baugh, S. Cole, R. Davé, C. S. Frenk, N. Katz, and C. G. Lacey. Theoretical Models of the Halo Occupation Distribution: Separating Central and Satellite Galaxies. *Astrophys. J.*, 633:791–809, November 2005. doi: 10.1086/466510. URL `http://adsabs.harvard.edu/abs/2005ApJ...633..791Z`.